Louisiana State University

LSU Scholarly Repository

March 2021

A Systematic Multiscale Investigation of Nanoparticle-Assisted CO2 Enhanced Oil Recovery (EOR) Process for Shale Oil Reservoirs

Dayo A. Afekare
Louisiana State University and Agricultural and Mechanical College

A SYSTEMATIC MULTISCALE INVESTIGATION OF NANOPARTICLE-ASSISTED CO₂ ENHANCED OIL RECOVERY (EOR) PROCESS FOR SHALE OIL RESERVOIRS

A Dissertation

Submitted to the Graduate Faculty of the
Louisiana State University and
Agricultural and Mechanical College
in partial fulfillment of the
requirements for the degree of
Doctor of Philosophy

in

The Craft & Hawkins Department of Petroleum Engineering

by
Dayo A. Afekare
BSc., University of Lagos, 2012
MSc., Heriot-watt University, 2015
May 2021

To my Parents, Taiwo Afekare and Temitope Afekare, my wife Melody Afekare, my daughter

Haven Afekare, and my in-laws for their absolute love and support all through the years and up

till today. They are instrumental to all my accomplishments till date, and I am immensely

grateful to God for them.

ACKNOWLEDGEMENTS

TABLE OF CONTENTS

ABSTRACT

Shale oil reservoirs are prolific on the short term due to hydraulic fracturing and horizontal drilling but experience significant production decline, leading to poor ultimate recovery and leaving billions of barrels of oil buried in the ground. In this study, a systematic multi-scale investigation of an enhanced oil recovery (EOR) process using relatively inexpensive silicon dioxide nanoparticles and carbon dioxide for shale oil reservoirs was conducted. Using the Tuscaloosa Marine Shale (TMS) as a case study, aqueous dispersions of nanosilica in conjunction with CO_2 were investigated at nano-to-core scales.

At the nanoscale, atomic force microscope was used to investigate the wettability modification performance of silica nanoparticles by measuring adhesion force between specific functional groups and pure minerals in nanofluid media. At the micron-scale, the roles of silica-based nanofluids in fluid/fluid interactions and rock/fluid interactions were distinguished by characterizing interfacial tension and advancing contact angle using optical tensiometer and the dual-drop-dual-crystal technique, respectively. Core-scale investigations consisted of: high-pressure CO_2 EOR coreflood experiment, reservoir rock/fluid characterization, physics-based modelling of capillary pressure and relative permeability using nano-to-core scale experimental data, and compositional simulation.

Results showed that hydrophilic silica nanoparticle (HNP) dispersions can effectively improve nanoscale wettability alteration (towards less oil-wet state) by decreasing adhesion force and work required to spontaneously desorb dominant functional groups in TMS crude oil from pure mineral surfaces. However, the grafting of aminosilanes on the surfaces of nanosilica generally increased adhesion force. At the micron-scale, HNP solutions showed great potential for enhancing oil recovery in TMS through wettability modification but not interfacial tension

reduction, whereas APTES-modified nanoparticle dispersions showed promising EOR potential through both mechanisms. At the core scale, coreflood experiment and compositional simulation showed that up to 30% of oil-in-place can be recovered with CO_2 EOR in TMS. The nano-to-micron scale mechanisms of silica-based nanofluids translated into a notable decrease in capillary pressure, an increase in oil relative permeability and a decrease in water relative permeability. However, the strongly-water state in TMS masked the synergistic effects of nanoparticle-assisted CO_2 EOR and thus helped revealed the initial wetting state as an important EOR screening criterion for shale oil reservoirs.

1. INTRODUCTION

1.1. Background

Oil production from unconventional shale oil reservoirs in the U.S. as of 2019 accounted for more than 60% of the nation's oil production, and currently, U.S. is the world's largest oil producer. Such growth metrics are expected to improve as shale exploration and production continues. Multi-stage hydraulic fracturing and horizontal drilling are the technologies responsible for the enormous success of shale oil field development. However, there are enormous challenges. Wells drilled in unconventional reservoirs suffer at least 70% decline in production after one or two years and reliable estimates in Bakken, Eagle Ford and Tuscaloosa show that only 3-10% of oil-in-place may be recovered. Second, hydraulic fracturing typically requires at least 4 million gallons of fresh water per well, equivalent to bath of 80, 000 people, stressing water supplies in American states and causing significant environmental concerns. In other words, should such enhanced shale oil recovery methods remain unfound, billions of oil barrels will be left buried in the ground at a time when conventional reservoirs around the world have been substantially depleted. As a result, EOR research efforts at lab-to-field scales have intensified.

The subsurface injection of CO_2 to improve oil production is an established EOR technique for conventional oil reservoirs, and while it is gaining significant attention in the shale oil industry, it remains fairly novel. At certain pressure and temperature conditions, CO_2 can become one with the oil phase by obtaining miscibility and eliminating interfacial tension. At the immiscible state, CO_2 can reduce oil viscosity and promote mass transfer to boost oil production. Yet, the reservoir containment of the gas and premature gas breakthrough especially in the presence of natural fractures in shale rocks present colossal challenges. To add, scientific understanding of oil

recovery mechanisms in shale oil is presently limited. Similarly, silica nanoparticle dispersions appear as a promising EOR alternative: silicon dioxide is one of earth's most abundant minerals and is environmentally friendly, with excellent material and chemical properties in the nanoparticle regime. Yet, nanofluid EOR remains a novel technique for oilfield recovery applications – for conventional and unconventional oil reservoirs – partly because there is no general consensus on fundamental oil release mechanisms across scales. Lastly, used herein as a shale oil reservoir case study, the Tuscaloosa Marine Shale (TMS) holds up to seven billion barrels of oil in recoverable reserves, but has experienced very few drilling and production activities, let alone EOR studies – either on lab or field scale.

1.2. Motivation

The motivation for this research is presented by summarizing the comprehensive review of literature, as follows:

- Micron-to-core scale measurements such as contact angle, Amott index, capillary pressure and relative permeability have been the focus of wettability studies for decades but these indicators give little or no information about the direct role of surface and intermolecular forces which govern wettability at the atomic to nano scales

- Capillary pressure and relative permeability are the main rock/fluid interaction parameters used in predicting recovery factor at the core-scale – and beyond – but the relationship between these properties in the context of shale oil recovery (primary production or EOR) are yet to be studied in great detail

- The potential of CO_2 EOR in tight oil reservoirs (studied from lab tests, numerical simulation and field pilot experiments) is promising but fairly novel, partly because the industry is just beginning to realize how much oil can be obtained from tight oil reservoirs

and fundamental scientific understanding such as impact of diffusion and capillary pressure in these types of reservoirs is not fully understood

- Nanofluid injection have been tested both at lab and field scales on high permeability (~ 200 mD) sandstone rocks and heavy oils, with optimistic results, but no significant studies on naturally fractured formations, low-permeability and ultra-low-permeability shale oil reservoirs. In what few cases have been reported in shale oil, scientific evidence of oil release mechanisms at the nanoscale are yet to be revealed

- Lab-to-field studies of nanofluid-assisted CO_2 EOR have been reported with optimistic results, but fundamental gaps in knowledge such as the impact of mineralogical composition and crude oil functional species as well as modelling of relative permeability and capillary pressure based on reliable experimental data appears missing

- Lastly, Tuscaloosa Marine Shale (TMS) which is the focus of this study holds up to seven billion barrels of oil recoverable reserves, but has experienced very few drilling and production activities, let alone EOR studies – either on lab or field scale

1.3. Research Objectives

Consequently, a systematic, multiscale investigation of nano-enhanced CO_2 recovery method for shale oil reservoirs was conducted, with a detailed case study of the Tuscaloosa Marine Shale. The main objectives of this research are listed as follows:

1. *Systematically investigate silica-based nanofluid as an EOR technique, at the nano-, micron - and core scales*: This was done using the atomic force microscope, scanning electron microscope, zeta potential measurements, interfacial tension measurements, precise contact angle measurements using the DDDC technique and analytical models.

Pure minerals, crude oil functional species as well as actual rocks and fluids from TMS were used.

2. *Methodically study immiscible CO_2 injection EOR, at the core scale:* This was accomplished by conducting high-pressure coreflood experiment and core-scale compositional simulation using TMS core as well as rock and fluid properties.

3. *Thoroughly examine the core-scale EOR potential of nanofluid EOR combined with CO_2 EOR for TMS:* This was conducted using key experimental data gathered from steps 1-2 in addition to characterizing TMS rocks and fluids, developing and implementing workflows to predict relative permeability and capillary pressure as function of micron-to-core scale data, and conducting core-scale compositional simulations

The following distinguishes this research from previous studies:

- Nanoscale investigation of silica nanofluid EOR using the atomic force microscope

- Precise wettability characterization measurements of contact angle in TMS rock/fluid system using the DDDC technique

- High-pressure coreflood and core-scale compositional simulation of CO_2 EOR in TMS

- Development and implementation of a new workflow to predict relative permeability and capillary pressure as a function of fluid/fluid interaction and rock/fluid interaction properties such as interfacial tension and DDDC-measured contact angle in shale oil rock/fluid system respectively

- Validation of core-scale capillary pressure and relative permeability models with well-scale petrophysical log data in shale oil reservoirs

The pyramid diagram below (Figure 1.1) further illustrates the multi-scale nature of this project. It is important to conduct investigations across length scales to clearly identify the consistency in the behavior of mechanisms (or lack thereof) of the nano-CO_2 EOR process and also the regularity of favorable conditions. Thus, from a length scale perspective, this research is split into specific components which are described in more detail in the next three sub-sections.
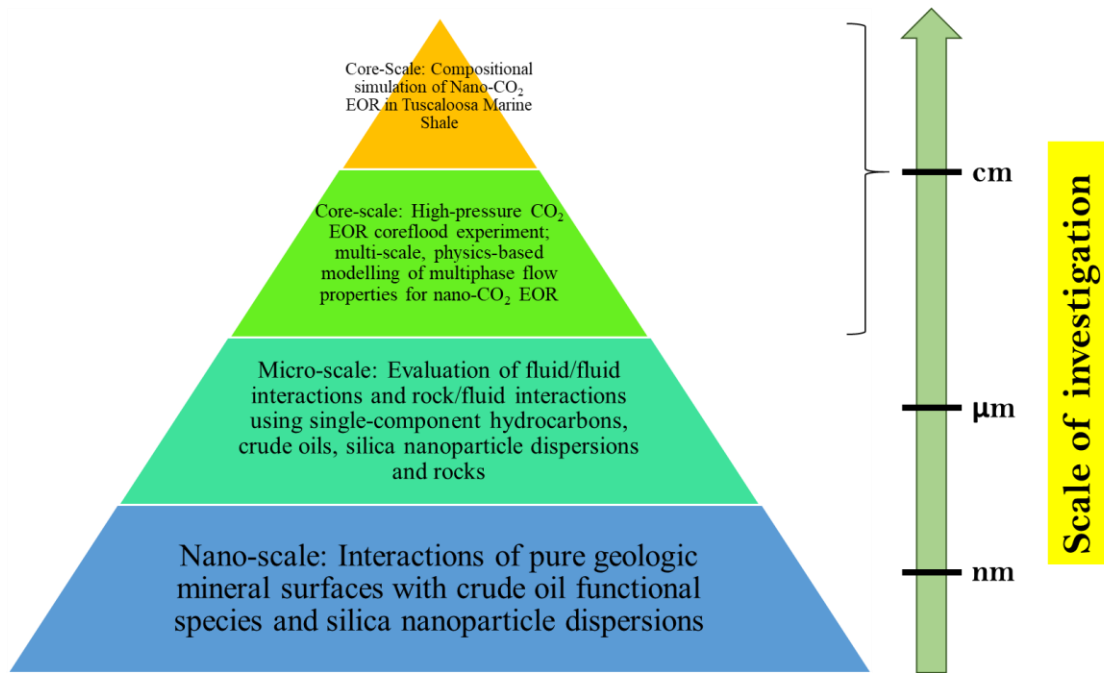
Figure 1.1. Diagrammatic illustration of research approach

1.3.1. Nanoscale Characterization of Nanofluid Enhanced Oil Recovery

The objective of this study is to investigate the wettability alteration performance of silicon dioxide nanoparticles at the nanoscale and expand current scientific understanding in the context of nanofluid EOR. Specifically, it addresses the following research questions:

- Which mechanisms indicate the EOR potential of silica nanoparticle dispersions at the nanoscale?

- How does rock mineralogical composition affect the performance of silica-based nanofluid EOR at the nanometer scale?

- Which type of crude oil functional species are responsive to silica-based nanofluid EOR at the surface level?

- What is the impact of surface functionalization of hydrophilic silica nanoparticles on nanoscale performance of silica-based nanofluid EOR?

Even though mechanisms of nanofluid EOR have been identified at the micron-to-field scales and in high permeability rocks (tens of mD), its oil displacement and mobilization potential at the nanoscale - which is the domain of tight rocks – is not well understood.

The atomic force microscope (AFM), a high-resolution analytical tool, was the main tool used to meet the objective of this study. Using AFM, adhesion force and the work of adhesion were characterized in nanofluid dispersions when mineral substrates were brought into contact with polar and non-polar functional groups. Two types of nanoparticles dispersed in 1 wt% NaCl were tested: untreated, hydrophilic silica nanoparticles (HNP) and surface-treated silica nanoparticles (NNP). This study was conducted as part of a research initiative to improve oil recovery in Tuscaloosa Marine Shale (TMS), so mineral substrates, chemical groups and brine formulation were based on TMS rock and fluid data. Further, the dynamics of nanoparticle adsorption is revealed.

1.3.2.   Micron-scale Characterization of Nanofluid Enhanced Oil Recovery

The previous section stated that the atomic force microscope is used to investigate the effects of hydrophilic and functionalized silica nanoparticles on adhesion force of alkane, aromatic and carboxylate compounds to muscovite mica and quart minerals. The changes in adhesion force, according to Young- Dupre (Young, 1805) equation can be identified from corresponding changes

in interfacial tension (IFT) and contact angle. At the nanoscale, it is difficult to evaluate and differentiate the role of nanofluids in fluid/fluid interactions (interfacial tension effects) from rock/fluid interactions (surface wettability changes). Therefore, this section is focused on evaluating both types of interactions to characterize nanofluid EOR at the micron-scale and expand the current fundamental understanding of adhesion forces measured at the nanoscale. Specifically, the following research questions are addressed:

- Which mechanisms indicate the EOR potential of silica nanoparticle dispersions at the micron-scale?

- Which type of crude oil functional species are responsive to silica-based nanofluid EOR in terms of interfacial tension?

- What is the impact of surface functionalization of hydrophilic silica nanoparticles on interfacial tension and contact angle measured at the micron-scale?

- How do micron-scale evidences of silica-based nanofluid EOR complement or contradict nano-scale observations?

Using the optical tensiometer, interfacial tension between nanofluids and different pure compounds such as alkane and ethylbenzene, as well between nanofluids and actual crude oil obtained from TMS formation were measured. Using the DDDC technique, the advancing and receding contact angles were measured between TMS rocks in the presence of nanofluids and TMS oil following a rigorous sample preparation procedure explained in the methodology section (Chapter 3). Contact angle and IFT measurements were performed at ambient conditions. The novelty of this work also lies in the fact that, to the best of my understanding, there is no publicly available report on wettability characterization of TMS rocks and application of EOR methods.

DDDC Contact angle measurements and IFT data served as input variables to determine important multiphase flow properties for compositional simulation of nanofluid-assisted CO_2 EOR process.

1.3.3. Core-scale Characterization of Nanofluid-assisted CO_2 Enhanced Oil Recovery

The objective of this study is to evaluate the microscopic efficiency of CO_2 injection augmented by silicon dioxide nanoparticle dispersions as a hybrid EOR technique for the Tuscaloosa Marine Shale. This study in particular addresses the following questions:

- What is the EOR potential of immiscible CO_2 injection EOR in TMS observed at the core-scale?

- For adequate simulation of nanofluid-assisted CO_2 EOR process, how can the dominant multiphase flow properties – namely capillary pressure and relative permeability – be modelled based on experimental data and information gathered at nano-to-core scale scales?

- How do core-scale evidences complement or contradict nano-to-micron scale observations in the context of nanofluid-assisted CO_2 EOR?

This study presents additional novel insights by using experimental data obtained from nano-to-micron scales in this study and elsewhere (Lohr and Hackley, 2018) in conjunction with analytical models to forecast the core-scale efficiency of nanofluid-CO_2 EOR. The core-scale characterization component of this work is split into an experimental part and a simulation part. The experimental part involved the evaluation of CO_2 injection EOR in a low-permeability TMS core using a high-pressure coreflood setup to simulate TMS subsurface conditions. For the simulation part, there were four main steps involved: reservoir fluid characterization, reservoir rock characterization, EOR characterization and model building. Reservoir fluid characterization involved gathering, analyzing, and matching experimental data obtained from industry source

(Australis Oil) with regression models using the Computer Modelling Group (CMG)'s WinProp industry package. Regarding reservoir rock characterization, TMS reservoir petrophysical parameters such as porosity, permeability, total organic content, and resistivity were obtained from industry source (Goodrich Petroleum & University of Louisiana Lafayette) and evaluated to identify the oil-bearing capacity of the reservoir and the zone of interest. With regards to EOR characterization, in addition to data obtained from industry source, the Leverett J Function and Purcell Model were adapted and coupled to derive relative permeability and capillary pressure curves as a function of interfacial tension and water-advancing contact angle for gas, oil and water phases measured at micron scales. Already published mercury injection capillary pressure data for TMS were used in the Leverett J Function (Lohr and Hackley, 2018). Significant experimental and modelling parameters served as input variables into a model built in CMG's 3-phase compositional simulator (GEM) to predict recovery efficiency. A Cartesian grid volumetrically similar to a synthetic core (cylindrical piece of rock) obtained from the TMS was created. The injector and producer well constraints, position and initial conditions were set based on a physical laboratory experimental setup used for evaluation for CO_2 EOR in TMS core. The main simulation results for the CO_2 EOR and nanofluid-assisted CO_2 EOR processes are the oil production rate, recovery factor and pressure drop. Results are discussed meaningfully and in the context of previous studies, after which the report is concluded.

1.4. Structure of the Dissertation

This dissertation consists of five chapters. The introduction to the work is presented in Chapter 1, including background, motivation and objectives of the research, and structure of the dissertation. Chapter 2 provides a comprehensive literature survey supporting the research motivations and objectives, starting from wettability in the context of enhanced oil recovery and wettability

characterization techniques across length scales. An overview of shale oil reservoirs and a background on the Tuscaloosa Marine Shale, followed by EOR techniques in shale oil reservoirs with specific focus on CO_2 EOR, nanofluid EOR, nanofluid-assisted CO_2 EOR are also presented in Chapter 2. In Chapter 3, materials and methodologies employed at each scale of investigation were described in detail. These include the materials, methodologies and workflow used for: atomic force microscope investigations at the nanoscale; optical tensiometer and the dual-drop dual-crystal technique at the micron-scale; high-pressure coreflood equipment design, reservoir fluid and rock characterization; analytical models of multiphase rock/fluid properties and compositional simulation at the core-scale; and analytical science and surface functionalization procedures employed across scales. Correspondingly, the results obtained from nano-to-core scale investigations were systematically presented and elaborately discussed in Chapter 4. These include: adhesion force maps and adhesion energy data which revealed the performance of silica nanoparticle dispersions at the nanoscale; interfacial tension, advancing contact angle and adhesion force calculations as indicators of silica-based nanofluid EOR potential at the micron-scale; and capillary pressure curves, relative permeability curves, coreflood and simulation recovery profiles of CO_2 EOR in TMS and simulation results of nanofluid-assisted CO_2 EOR at the core scale. Finally, the dissertation was concluded with a summary of significant findings and recommendations in view of future research directions.

2. LITERATURE REVIEW

2.1. Wettability

2.1.1. Overview

Wettability is one of the most significant phenomena in EOR because it describes the interactions of reservoir fluids, rocks and surrounding thermodynamic conditions. It is the tendency of one fluid to spread on or adhere to a rock surface when at least one other immiscible fluid is present (Anderson 1986; Craig 1971). A reservoir is said to be water-wet when it prefers to contact water in the presence of oil. Conversely, if oil for a presumably long time contacts and spreads over the rock surface in the presence of water, the reservoir is said to be oil wet. For a water-wet rock, pore doublet model explains that small pores tend to be occupied by water while the larger pores contain oil (Heshmati and Piri, 2018; Moore and Slobod, 1955). In this case, the pressure differential (known as capillary pressure) required to expel oil out of the pores will be relatively small, which makes residual oil saturation less, and recovery efficiency high. The reverse is true for oil-wet reservoirs: the preferential contact of the rock with oil will lead to formation of extensive, continuous oil films which makes oil easily occupy the small pores, with water occupying larger pores. Capillary pressure and residual oil saturation become high, even as the relative permeability of rock to water becomes low. This consequently leads to poor recovery factor. Therefore, the degree of alteration from oil-wet to water-wet is integral to improvement in oil recovery. It should be noted that the wettability types described above apply to homogeneous rock wettability – other classes such as neutral, intermediate and fractional wettability have also been identified but they are excluded from this discussion for the purpose of simplicity.

Until recently, wettability studies in the context of flow through porous media and enhanced oil recovery of petroleum reservoirs have mostly been at the micron and core scales, with

interfacial tension measurements, contact angle measurements and imbibition experiments being among the most popular approaches. Some of the main reasons are the industry's exclusive focus on conventional reservoirs (prior to success of shale exploration) and the reliability of imbibition experiments. Conventional sandstone and carbonate reservoirs have pore radii in the order of microns, which makes it reasonable to focus on micron-scale techniques. Forced and spontaneous imbibition experiments conducted on cores (usually centimeter-sized cylindrical rock plugs) have been highly dependable in demonstrating field scale potential of recovery techniques and deriving global parameters such as relative permeability and capillary pressure that help predict incremental oil recovery.

2.1.2.   Contact Angle

In historical context, traditional methods of characterizing wettability alteration are: contact angle (Treiber and Owens, 1972), Amott index (Amott, 1959) and USBM index (Donaldson et al., 1969), relative permeability and capillary pressure (Craig, 1971). The contact angle method is a wettability characterization technique as it is the angle (usually measured in the denser phase) that a fluid (drop phase) makes with a rock surface in the presence of another immiscible fluid (continuous phase). An increase in preferential contact between the surface and drop phase will lead to a lower contact angle (in degrees) and thus an indication of wettability change. The more widely accepted classifications of contact angle are 0−75°: water-wet; 75−115°: intermediate-wet; 115−180°: oil-wet (Afekare and Radonjic, 2017; Anderson, 1986); note that oil is usually the drop phase and water (or aqueous formulation) is continuous phase. Contact angle measurements on core discs and surfaces of centimeter-sized mineral plates are the most common because such measurements can easily be done under reservoir thermodynamic and fluid conditions; it is the least time-consuming; and it can be used to probe specific mineralogical effects on wettability.

Contact angles were measured using the sessile drop technique and the modified sessile drop technique until the dual-drop-dual-crystal (DDDC) technique was developed. The DDDC approach helped overcome the deficiencies in the earlier methods in terms of: honoring three-phase boundary, obtaining reproducible results, and requiring less aging time (Rao and Girard, 1996). The DDDC technique was used in the core-scale characterization component of this research and more details on the technique are available in the methodology section of this report.

Advanced research in the application of digital imaging for pore-scale characterization have led to discovery of measuring in-situ contact angle within rocks using X-Ray Computerized Tomography (CT). Andrew and colleagues (Andrew et al., 2014) first reported a new approach to measure contact angle in a CO_2/brine/carbonate system using micro-CT. They took CT images of the carbonate rock containing brine and where CO_2 appears as a trapped residual phase. Thousands of the rock sample projections were taken and reconstructed into a 3D volume. After filtering and correction of the 3D volume, the image was then segmented by an algorithm that generated a 2D histogram and studied to identify disconnected ganglion edges of the CO_2, brine and solid phases. The contact line was labelled as the intersection of the edges of all phases and the contact angle was measured by resampling data on a plane with a normal parallel to the contact line at a certain point. The resulting data is thus a histogram distribution of contact angle within the carbonate rock region imaged. This method has potential applicability to wide-ranging issues surrounding multiphase flow in porous media, including impact of surface roughness, mineralogical heterogeneity, and pore-scale modelling. Subsequently, similar approaches have been developed and implemented to study pore-scale occupancies and different wettability states which were otherwise difficult to investigate in the past (Al-Menhali et al., 2016; Alhosani et al., 2021; Mirchi, 2018).

2.1.3. Amott-Harvey Index

When conducting an Amott-Harvey imbibition test, a core sample flooded with oil at irreducible water saturation S_{wirr} is put in a graduated tube containing water. The water phase spontaneously imbibes the core – and raises the water saturation to say S_{w2} - for a considerably sufficient time to release oil. Afterwards, the core is placed in a flow cell or centrifuge for forced imbibition of water, additionally recovering oil and increasing the water saturation to S_{w4}. The sample is then at residual oil saturation level, and the process is repeated with an oil-filled tube and oil flow cell/centrifuge. This time the spontaneous imbibition of oil reduces the water saturation from S_{w4} to S_{w3} and the forced imbibition of oil takes the water saturation from S_{w3} back to S_{wirr}, if wettability effects due to flooding are assumed negligible. It then follows that the water and oil indices, I_w and I_o respectively, are mathematically described as (Abdallah et al., 2007):

$$I_w = \frac{S_{w2} - S_{wirr}}{S_{w4} - S_{wirr}}$$

2.1

$$I_o = \frac{S_{w4} - S_{w3}}{S_{w4} - S_{wirr}}$$

2.2

The Amott index, I_A is the difference between the water index and oil index, i.e.

$$I_A = I_w - I_o$$

2.3

A +1 index indicates a strongly water-wet system while –1 index indicates a strongly oil-wet system.

2.1.4.   US Bureau of Mines (USBM) index

The US Bureau of Mines (USBM) index is determined by plotting the aforementioned saturation paths S_{wirr} to S_{w4} on a capillary pressure curve; see previous section. In a USBM test, a core sample at S_{wirr} in a water-filled tube is placed in a centrifuge and spun at increasing speeds. After several periods of spins, the core reaches residual oil saturation and is put in a tube filled with oil for another set of measurements. To obtain Amott and UBSM indices, consider Figure 2.1 below. The steps to obtain the saturation points for the Amott index calculation were discussed as part of the explanations leading to equations 2.1 and 2.2. The USBM index is a logarithm of the ratio under the positive capillary pressure curves to that under the negative capillary pressure curves. Strongly oil-wet and water-wet systems are denoted by $-\infty$ and $+\infty$ USBM indices respectively, even though most results fall within -1 and +1 range (Abdallah et al., 2007).
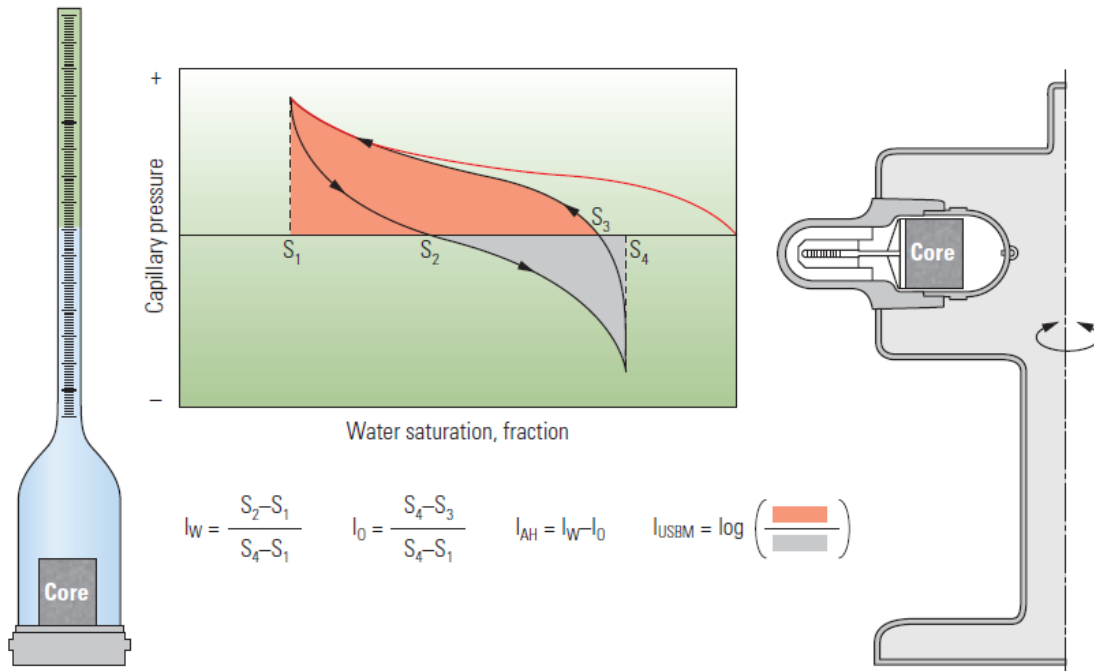
Figure 2.1. The Amott index (denoted I_{AH} in the third equation from the left) and USBM index (denoted I_{USBM} in the last equation from the left) are used to evaluate core-scale wettability and both parameters can be obtained from capillary pressure curves (graph) (Abdallah et al., 2007)

2.1.5. Capillary Pressure

Both the Amott and USBM indices can be explained in terms of capillary pressure curves, and capillary pressure is one of the most important parameters that describes wettability and multiphase flow in porous media. Hence the term "capillary pressure" is explicitly described as follows. Capillary pressure P_c is defined as the differential pressure between a non-wetting phase P_{nw} and a wetting-phase P_w, i.e.

$$P_c = P_{nw} - P_w \qquad\qquad 2.4$$

In the context of porous media in petroleum reservoirs, P_c is the pressure required to expel oil from small to larger pores in a water-wet reservoir and the pressure required to expel water from small to larger pores in an oil-wet reservoir. According to Young-Laplace formulation, capillary pressure can also be mathematically described as:

$$P_c = \frac{2\sigma_{ow} cos\theta}{r} \qquad\qquad 2.5$$

where σ_{ow} is oil/water interfacial tension; θ is advancing contact angle; and r is pore radius. Equation 2.5 signifies that capillary pressure is an indicator of wettability alteration and this reservoir rock/fluid property has been used for many decades to represent wetting effects at the core-to-field scales (Afekare and Radonjic, 2017). In the context of petroleum reservoir porous media, fluid saturation is significantly influenced by pore size distribution which makes P_c a function of fluid saturation. Consequently, a plot of P_c versus water saturation – known as capillary pressure curve – has become an established representation of fluid distribution in oil and gas reservoirs (Donaldson et al., 1969; Helset et al., 1998; Jahanbakhsh and Sohrabi, 2015; Li and Horne, 2006; Morrow, 1976; Purcell, 1949; Rücker et al., 2020). Some of the well-known capillary pressure measuring techniques are mercury injection porosimetry, porous diaphragm, dynamic

capillary pressure method and centrifuge method (Todd and Somerville, 2014). Capillary pressure is usually scaled up using the Young-Laplace equation – or other methods - for field applications.

2.1.6. Relative Permeability

The relative permeability of a rock to a fluid is the ability of the rock to transmit that fluid in the presence of at least one other immiscible fluid. According to Craig's rule of thumb (Craig, 1971), the wettability state of a reservoir can be classified in terms of residual oil saturation (how much oil is left after EOR) and relative permeabilities (see Figure 2.2; (IPE, 2005)). The initial water saturation for a water-wet system is usually greater than 20% while that of an oil-wet system is typically less than 15%. The crossover point between the water and oil relative permeability curves (point A in Figure 2.2) on the water saturation axis is greater than 50% for a water-wet system and less than 50% for an oil-wet system. Also, the relative permeability of the rock to water at residual oil saturation is less than 30% for a water-wet system and greater than 50% for an oil-wet system.

In a water-wet system, water forms extensive and continuous films across the reservoir pore network and imbibes through the smallest pores in the network, leaving oil in the large, fast-flowing pores. Consequently, the oil relative permeability is expected to slowly decrease as water saturation increases and the endpoint water relative permeability is low. Conversely, an oil-wet reservoir has oil in the smallest pores and water in large pores such that waterflooding will lead to a drastic reduction in oil relative permeability with a high endpoint water relative permeability. Therefore, a change in the preference of the rock to contact either fluid is indicated by changes in relative permeability curves – a widely established method of characterizing wettability at the core scale.

In water-wet system:
S_w mostly > 20%
At point A: $k_{ro} = k_{rw}$; S_w > 50%
k_{rw} at S_{or} / k_{ro} at W_{wi} < 30%

In oil-wet system:
S_w < 15%
At point A: $k_{ro} = k_{rw}$; S_w < 50%
k_{rw} at S_{or} / k_{ro} at S_{wi} > 50%
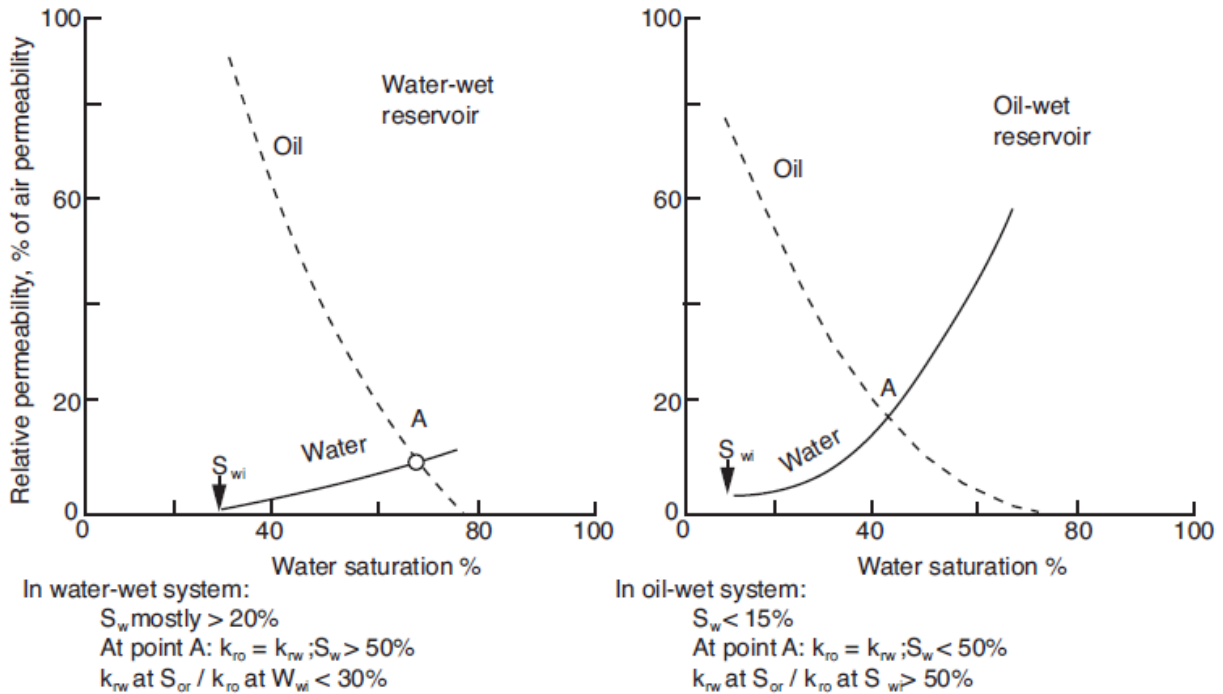
Figure 2.2. Relative permeability curves for a water-wet reservoir (left) and an oil-wet reservoir (right) according to Craig's rule of thumb (IPE, 2005)

Laboratory experiments on cores - such as steady and unsteady state methods - as well as analytical models – such as Brook and Corey and Stone's I and II models - are widely regarded techniques for obtaining relative permeability in conventional reservoirs (Brooks and Corey, 1966; Chen, 2007; Ghazanfari   M. H.   et al., 2006). However, there is no established method for determining relative permeability in unconventional reservoirs. This is mainly due to capillary forces, which makes obtaining steady state in low-permeability rocks at laboratory conditions mostly implausible. To add, it usually requires weeks to months for dense fluids to penetrate the cores during displacement experiments. As a result, research efforts on developing models to derive both relative permeability and capillary pressure for unconventional oil reservoirs have intensified.

2.1.7. Scaling: Relative Permeability & Capillary Pressure

Capillary pressure and relative permeability are the two main properties used for scaling different EOR techniques and wettability alteration effects from core to field scales but each has often been treated separately. In unconventional oil reservoirs, one of the ways in which the physics of multiphase flow can be adequately incorporated in the prediction of recovery factor is by coupling relative permeability and capillary pressure models. This approach is of merit because capillary pressure and relative permeability are heavily dependent on pore radii which are significantly smaller in unconventional rocks compared to conventional rocks. Therefore, evaluating relative permeability based on capillary pressure will introduce the dependence of pore size distribution on the transmissibility of the rocks to in-situ fluids. The determination of both parameters coupled is currently being researched (Helset et al., 1998; Jahanbakhsh and Sohrabi, 2015; Li and Horne, 2006; Purcell, 1949; Zhang et al., 2012). One of the ways in which both properties have been determined co-dependently is through history matching in conjunction with the power-law model and piece-wise model to fit the models to displacement data (Sun and Mohanty, 2005; Zhang et al., 2012). However, this approach suffers significant drawbacks. First, the power law model relies on the premise that the curves take a certain shape within the fluid saturation range and the piece-wise model dictates that the relative permeability and capillary pressure curves are interpolated, giving rise to non-unique solutions. Cumulative oil production from shale cores at lab conditions is also usually not sufficient to perform any meaningful analysis; the recovery factor are typically obtained by weighing method (Sheng et al., 2015).

Another approach to estimating capillary pressure and relative permeability concurrently is to determine the former using an established conventional technique such as mercury injection porosimetry or Young-Laplace equation and then obtain the latter using an analytical model

(Jahanbakhsh and Sohrabi, 2015; Li and Horne, 2006; Stimpson and Barrufet, 2017). This method is particularly valuable in tight oil reservoirs where multiphase flow data is limited due to low permeability and capillary forces. Stimpson and Barrufet (2017) used pore distribution of an Eagle Ford shale core and interfacial tension model to determine capillary pressure from Young-Laplace equation and later obtained relative permeability curves based on a model originally derived by Nakornthap and Evans (Nakornthap and Evans, 1986). In following this methodology, they reasonably incorporated nanopore effects, fluid-fluid interactions and rock-fluid interactions in their compositional simulation. However, their capillary pressure evaluation was based on the assumption of a perfectly oil-wet system with no supporting experimental data.

2.1.8.   Scaling: Dimensionless Numbers

Dimensionless numbers are ratios of forces that govern the mechanisms of displacement in porous media, and as such, they have been used in scaling different processes and wettability alteration, from core to field scales (Lake et al., 2014). The ratio of viscous forces to capillary forces is known as capillary number N_{ca}, a dimensionless group which has been prominently studied for decades (Helset et al., 1998; Sheng, 2013a). The viscosity, porosity and velocity of the displacing phase makes up the viscous forces whereas the interfacial tension and cosine of the advancing contact angle makes up the capillary forces. Wettability is a function of capillary forces and much of EOR research efforts have been targeted at overcoming these forces which trap oil in place and increase residual oil saturation. As a result, the relationship between capillary number and residual fluid saturation – known as capillary desaturation curve - have been extensively studied. With respect to capillary desaturation curve, it is known that both residual fluid saturation for the wetting and non-wetting phase are fairly constant at small N_{ca} or when capillary forces are dominant. This plateau region on the capillary desaturation curve is typical for waterfloods in conventional

reservoirs. However, at a certain critical N_{ca}, when the capillary forces are low, the residual fluid saturation begins to decrease until complete desaturation at the total desaturation capillary number. A large change in IFT and contact angle - possibly due to surface-acting chemicals – can substantially increase the capillary number and reduce residual oil saturation. Thus, capillary desaturation curves can be used to characterize different EOR techniques such as surfactant and low salinity EOR. The data points for these curves are usually gathered from forced imbibition experiments and field production data, so that the residual oil saturation obtained from coreflood for instance can give an idea of the incremental recovery obtainable at field scale at a certain EOR fluid injection rate, assuming all other properties are constant. Yet, even though capillary desaturation curves have been expansively studied for carbonates and sandstone reservoirs (Ehrlich et al., 1974; Gupta and Trushenski, 1979; Kamath et al., 2001; Taber, 1969), the same cannot be said for unconventional low-permeability oil reservoirs like shale oil and tight rocks because the industry is just beginning to realize how much of oil-in-place can be recovered.

The combination of the bond number – ratio of gravity to capillary forces – and the capillary number also gives rise to another dimensionless constant known as the trapping number N_{tr} which is often used in characterizing residual fluid saturation and scaling relative permeability in the context of EOR (Neshat and Pope, 2018; Pope et al., 2000; Sharma and Filoco, 2000). Trapping number becomes more significant when the impact of gravity segregation cannot be ignored. Similar to capillary desaturation curves, residual saturation of non-wetting phase and wetting phase are plotted as a function of N_{tr} with plateau regions and sloppy regions differentiated by a critical N_{tr} for the respective phases.

2.1.9.   Surface Force Measurements

2.1.9.1.   Overview

The importance of surface forces can be reviewed in the context of certain limitations that constrain the aforementioned wettability evaluation methods, especially in the context of shale oil recovery. First, wettability is a function of surface forces, but these previously described indices give little or no information about the direct role of intermolecular forces dominant at sub-micron- to atomic scales (Abdallah et al., 2007; Basu and Sharma, 1997; Israelachvii, 2009). Capillary forces are often misinterpreted as adhesion forces which quantify the chemical and electrostatic interactions in oil/fluid/rock systems. Exploring rock/oil adhesion mechanics in the context of wettability alteration may help expand our existing body of knowledge but quantifying adhesion has been difficult to achieve in the past. Second, the importance of nanopore confinement in tight oil reservoirs has in recent times been recognized because of the prolific near-term performance but elusive long-term potential of these type of formations (Alfarge et al., 2018; Li and Sheng, 2017). For such unconventional reservoirs, a significant portion of in-place hydrocarbons are adsorbed (or adhered) on pore walls, but adhesion in the context of tight oil recovery is poorly understood (Jin and Firoozabadi, 2016; Pathak, 2018). There is a pressing need to examine the role of surface forces in wettability alteration via EOR. Recently, this has been elaborately studied using the atomic force microscope (AFM).

2.1.9.2.   Atomic Force Microscope

Atomic force microscope is a high-resolution analytical tool that can be used to characterize surface forces (in the order of 10^{-9} to 10^{-12}N) in an aqueous environment (EOR injectant phase)

Section 2.1.9 was previously published as Afekare, D., Garno, J. and Rao, D., 2020a. Insights into Nanoscale Wettability Effects of Low Salinity and Nanofluid Enhanced Oil Recovery Techniques. Energies, 13(17). Reprinted by permission of Energies MDPI.

when geologic substrates are contacted with polar/non-polar moieties typically found in crude oils. The AFM follows the Hooke's law: a silicon nitride tip charged with certain functional species represents a "spring" which deflects from a surface in a manner proportional to the total interactive force sensed at the surface. Studies on the interfaces of rock and functional groups can be performed in liquid media to quantify their impact on wettability alteration at the nanoscale. In the past, AFM has been used to determine disjoining pressure (total adhesion force per unit area across the interface of two interacting bodies) and evaluate mixed wettability states in oil reservoirs (Basu and Sharma, 1997). The AFM has also been used to identify the correlation between crude oil composition and brine film thickness (Basu and Sharma, 1999) and investigate the role of cationic and anionic surfactants such as dodecyltrimethylammonium bromide and propoxylated sulfate respectively in wettability alteration in wettability alteration (Kumar et al., 2005). It has also been adopted to determine bitumen/water surface potential (Drelich et al., 2007); characterize nanoparticle size distribution (Hoo et al., 2008) and assess nanopores in shale gas rocks (Javadpour et al., 2012; Liu et al., 2016). Recently, AFM has been used to probe ionically tuned brine and effects on adhesion in petroleum reservoirs (Chandrasekhar and Mohanty, 2018; Hilner et al., 2016; Wu et al., 2017). There is also a body of literature on interpretations and broad applications of force measurements (Butt et al., 2005; Heinz and Hoh, 1999; Leite et al., 2012). Basu and Sharma (Basu and Sharma, 1997) used AFM to characterize brine film stability by comparing disjoining pressure data with calculations from DLVO theory, whereas Kumar and coworkers (Kumar et al., 2005) argued that the film stability criterion is tedious to derive due to the possibility of water suction and drainage during retraction and approach of AFM tip respectively. Consequently, the use of adhesion force measurement was proposed as a surface wettability characterization approach.

The application of AFM to perform adhesion force and energy measurements is known as chemical force microscopy (CFM). In CFM, a functionalized probe is used as a chemical sensor which when brought close to a surface can detect nanoscale forces (such as Van der Waal and structural forces) that are resolved in adhesion force measurements (Afekare et al., 2020b). The spatial characterization of adhesion force on a given sample area using CFM is referred to as chemical force mapping. The work of adhesion (to be described in the next section) can then be obtained from adhesion force using either an AFM-based mathematical expression (Butt et al., 2005) or existing adhesion mechanics' models (Derjaguin et al., 1975; Johnson et al., 1971).

2.1.9.3. Work of Adhesion, Adhesion Force and Wettability

For a rock/oil/fluid system at equilibrium, the wetting state can be described in terms of interfacial energies. Consider the configuration in Figure 2.3, where 1 represents oil; 2 rock and 3 nanofluid (or brine). Through force balance, it has been proven that the energy required for rock/oil interface to be penetrated by nanofluid (or brine), creating new oil/nanofluid (or oil/brine) and rock/nanofluid (or rock/brine) interfaces is (Israelachvii, 2009):

$$W_{132} = \Upsilon_{13} + \Upsilon_{23} - \Upsilon_{12} \qquad\qquad 2.6$$

1 – oil
2-rock
3-nanofluid/brine
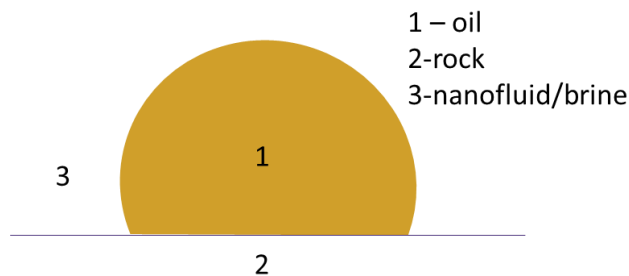
Figure 2.3. Illustration of a rock/oil/brine (or nanofluid) system at equilibrium

where Υ_{13} represents oil/nanofluid (or oil/brine) interfacial energy, Υ_{23} is rock/nanofluid (or rock/brine) interfacial energy, Υ_{12} is rock/oil interfacial energy and W_{132} is the three-phase oil/rock/fluid *work of adhesion*. It should be noted that the mathematical expression above only applies to a system in which the oil is the drop phase and water the continuous phase, but not vice versa. A negative W_{132} means that medium 3 will penetrate 1/2 interface and completely wet 2. On the other hand, if W_{132} is positive, there will be a partial spreading of both oil and nanofluid (or brine). Thus, degree of wettability alteration (towards water-wet) can be identified by a decrease in adhesion. As the work of adhesion decreases, the wetting phase tend to advance across the surface and stability of resulting film improves. However, this parameter has been difficult to measure in the past which has limited its adoption in wettability evaluation. Interestingly, with recent advances in AFM applications, the work of adhesion and adhesion force can be conveniently characterized (Chandrasekhar and Mohanty, 2018; Hassenkam et al., 2012).

In accordance with DLVO theory, adhesion force and work are a sum of different surface and intermolecular interactions – primarily electrostatic and non-electrostatic components (Israelachvili, 2009; Leite et al., 2012) . The force contributions can be identified using AFM force spectroscopy (see Figure 2.4). Raw force-displacement ($F(Z_{piezo})$) graphs may be used to qualitatively identify different intermolecular forces. On the other hand, quantitative analyses usually require force-distance ($F(D)$) curves and models that typically demand other experimentally derived parameters such as interfacial zeta potential values, dielectric constants, refractive index, absorption frequencies and surface charge densities (Hilner et al., 2016; Lorenz et al., 2017; Wu et al., 2017).

Van der Waals (vdW) forces and electrostatic repulsion (Figure 2.4a,b) may be sensed in the approach portion of the AFM force curve while non-electrostatic adhesion and structural forces

can be detected in the retraction portion (Figure 2.4c-e) of the force-displacement curve (Heinz and Hoh, 1999). Van der Waal forces (attractive or repulsive) apply to all discrete bodies (Leite et al., 2012) in the absence of long-range interactions, in a similar manner as gravitational forces apply to earthly bodies, and are indicated by a notable well in the force-displacement approach curve (circled red in Figure 2.4a). The vdW forces are largely unresponsive to pH and electrolyte concentration (Israelachvili, 2009) and although it is difficult to resolve it from electrostatic interactions (attractive, repulsive or both), a zero frequency of vdW usually implies a complete electric double layer effect (Leite et al., 2012). Regarding Figure 2.4b, the removal of critical divalent ions from brine may create a net repulsion between hydrophobic oil compounds and a negatively charged surface. Consequently, the electric double layer expands to promote a decrease in adhesion energy; growth of imbibing water films; and a change of surface wettability to a less oil-wet state. Hydrophilic silica nanoparticle dispersions also tend to promote double layer repulsion by creating more negative charges on mica and repelling polar species. The smaller the particle size, the larger the surface coverage which translates to larger electrostatic repulsion and a higher decrease in adhesion.

In the retract portion, a high non-electrostatic adhesion (attractive; circled blue in Figure 2.4c) may exist when hydrophobic groups interact with mineral substrates under high salinity conditions. The introduction of dispersed reagents can create a chemical potential gradient that significantly lowers adhesion (circled blue in Figure 2.4d). Another non-electrostatic and non-DLVO component known as structural force (Figure 2.4e) may arise when particles of similar sizes are confined in the nanometer range so that they are discretely ordered in multiple layers. This force contribution may be attractive, repulsive or oscillatory in nature and is not yet well understood (Israelachvili, 2009). A stepwise deflection of the cantilever to a zero baseline on the

retract force curve is due to the structural component of the adhesion force, which may be indicative of the number of particle layers formed at the solid/liquid interface (asterisk in Figure 2.4e) (Afekare et al., 2020b).
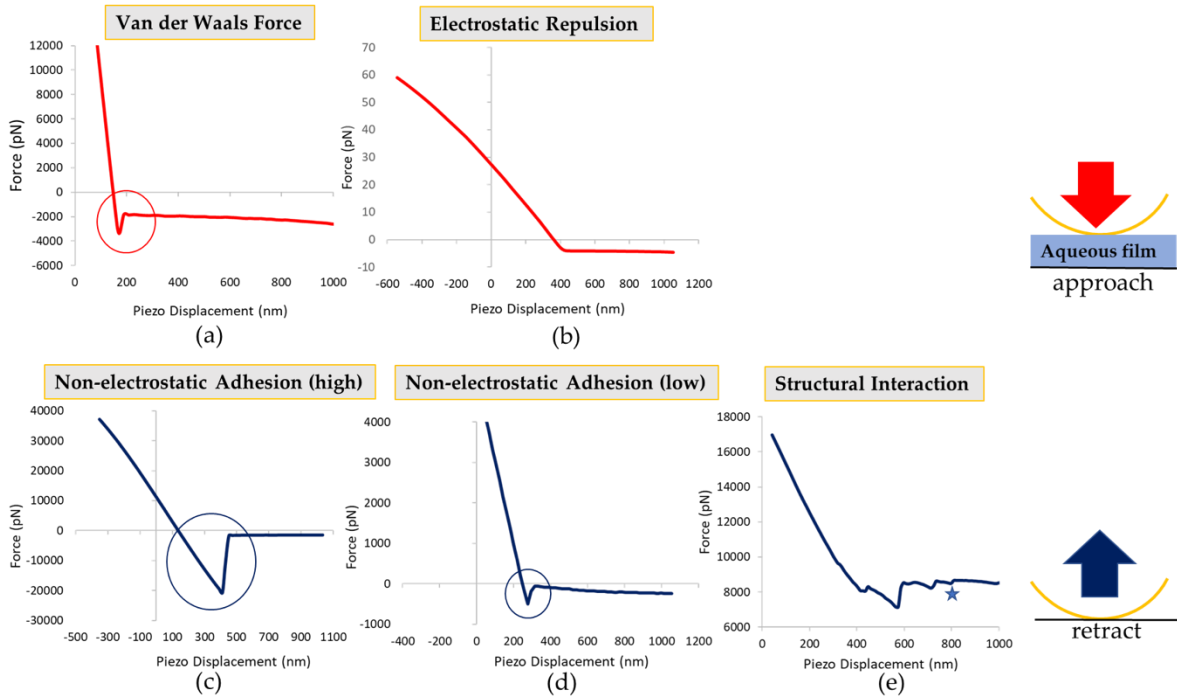
Figure 2.4. Force-displacement curves as the AFM tip approaches (a-b) and is retracted (c-e) from a surface: (a) Van der Waals (VDW) force, (b) electrostatic repulsion; (c & d) non-electrostatic adhesion and (e) structural force

It has been proposed that, at nanoscale (typically less than 100 nm), it is important to evaluate the total interactive force for a three-phase system (adhesion force) per unit area of separation between two approaching bodies – known as disjoining pressure - in the context of surface wettability (Israelachvili, 2009; Leite et al., 2012) . A negative disjoining pressure indicates an attractive force while positive disjoining pressure implies a repulsive force (Wu et al., 2017). Correspondingly, a decrease in the adhesion force due to repulsive effects will follow a change in disjoining pressure towards positive and increasing thickness of the wetting film. An increase in adhesion force due to attraction will tend to create a negative disjoining pressure and wetting film

collapse. Therefore, it can be said that adhesion force and energy reduction translate to creation of positive disjoining pressure which also results from non-electrostatic and electrostatic intermolecular interactions.

A number of theoretical models (Leite et al., 2012; Rao, 2003) have been used to estimate adhesion forces, most of which appear in the form:

$$F_{adh}/R = \text{KY}_{\text{LV}} \ (\cos\theta_r - \ \cos\theta_a) \qquad\qquad 2.7$$

where F_{adh}/R is adhesion force, R is radius of fluid-rock contact area, K is proportionality constant, γ_{LV} is liquid surface tension, and θ_a and θ_r are advancing and receding contact angles respectively. Using versions of the above expression and the Young dupre (Young, 1805) equation, some authors have estimated changes in force and work of adhesion based on interfacial tension and contact angle experimental data (Lashkarbolooki and Ayatollahi, 2018; Nguyen et al., 2017; Rao, 2003; Rao, 2004; Saini and Rao, 2009). For instance, with live oil, reservoir brine and pure minerals at elevated temperature (61°C - 96°C) and pressure (17.5 MPa – 25MPa), Rao (Rao, 2003) estimated adhesion forces (F/R) to be 12.05 mN/m equivalent to a water-wet system, 39.07 mN/m for intermediate-wet system and 60.37mN/m for oil-wet system. Tangparitkul and coworkers (Tangparitkul et al., 2018) also formulated contour maps of adhesion force, oil-water IFT and CA where they show that the highest adhesion force (400-500 µN) correspond with high CA (70°-90°) and IFT values (35-45 mN/m).

2.2. Shale Oil Reservoirs

2.2.1. Overview

Shale oil reservoirs are source rocks rich in organic matter (kerogen) and containing hydrocarbon accumulations which are in commercial quantities but are only recoverable through horizontal drilling and hydraulic fracturing. These reservoirs are also referred to as oil shales. For the purpose

of clarity, oil shale is the source rock containing the hydrocarbon accumulations known as shale oil. These reservoirs are low permeability (< 0.1 mD and often <0.01 mD) rocks containing predominantly clays, carbonates and siltstones with interconnected natural fractures in some cases. The oil shale industry was first mentioned in the seventeenth century, when a British Patent was issued to Martin Eale in 1694, who found a means of extraction. Since then, many countries including China, Brazil, Switzerland, and the US have developed an oil shale industry (Tissot and Welte, 1984). Even though the US contains the largest oil shale resource worldwide, the oil shale industry became largely successful only within the last decade, after more than 150 years since the first attempt to establish the industry. Because they cannot be produced by conventional drilling and extraction techniques, shale oil reservoirs are classified as unconventional reservoirs (Lin, 2016; Phillips et al., 2007; Shuler et al., 2011), as shown in Figure 2.5.
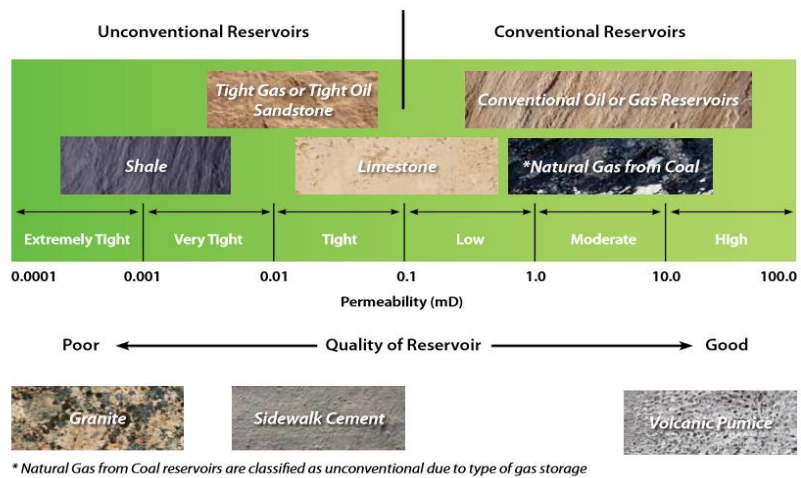
Figure 2.5. A general classification of petroleum reservoirs in terms of quality, mineralogy and permeability (Lin, 2016)

The type of kerogen in these unconventional reservoirs controls the quality of source rock and hence the shale oil reservoir. In terms of hydrocarbon potential, Type I kerogen refers to an oil-prone reservoir of lacustrine environment; Type II kerogen refers to an oil- and gas-prone reservoir of marine environment; Type III kerogen refers to a gas-prone reservoir of terrestrial

environment; and Type IV kerogen refers to a reservoir which is neither gas nor oil prone but contains carbonized material, of terrestrial environment (Borrok et al., 2019; Tissot and Welte, 1984). With varying total organic content (TOC), shale oil reservoirs are fine-grained sedimentary rocks which are generally brittle – a candidate feature for hydraulic fracturing – and fissile – meaning it can easily split along its planes (Jiang et al., 2016; Mousavi and Bryant, 2007). Another distinct feature is that, unlike conventional oil, shale oil experiences little or no migration within the source rock in which it was formed (Jiang et al., 2016). Other terminologies used in place of shale oil are: tight oil, low-permeability oil, tight sand, among others. The US shale industry has experienced significant boom in the last decade due to the largely successful exploration of different shale basins, notably Bakken, Eagle Ford and Barnett among others (Gong et al., 2013; Lin, 2016; Phillips et al., 2007; Shuler et al., 2011; Zhou et al., 2020). The Eagle ford formation in South Texas which is of the late Cretaceous age has since 2008 emerged as a major oil producing formation. With a thickness of 984 ft, it is a transgressive organic-rich shale with carbonates and siltstones (Bjørlykke, 2010). The Bakken formation in the Williston basin is another subsurface container of shale oil which is of the late Devonian age. It contains organic-rich mudstones and dolomite, has an average porosity of 5% with absolute permeability of 0.04 mD (Bjørlykke, 2010). The Tuscaloosa Marine Shale which is the reservoir of interest for this study is reviewed in the following sub section.

2.2.2.   Tuscaloosa Marine Shale (TMS)

2.2.2.1.   Geology & Production History

The Tuscaloosa marine shale (TMS) is of the gulfian Cretaceous age, lying between Upper and Lower Tuscaloosa sands with varied thickness from South west Mississippi to South east Louisiana. Figure 2.6 below shows the stratigraphic classification of Tuscaloosa sands (John et al.,

1997). Tuscaloosa Marine Shale is predominantly gray to black, sandy, and fissile (easily split) with fining upwards sequence. It is 500 ft. thick, increasing to 800 ft. in the south-central region of Washington parish, Louisiana. TMS is believed to be a source rock for most of the lower Tuscaloosa oil trapped in sand bars and this is substantiated by geochemical studies performed by the Basin Research Institute at Louisiana State University on fluid samples obtained from two wells, one in Gillsburg field and the other in Silvercreek field. Multiple wells drilled revealed strong presence of interconnected fractures, most of which might have been created through pressurization of hydrocarbon generation. Similar conclusions were made on Bakken shale (Meissner, 1991). According to a recent study, TMS contains Type II and III kerogen, and vitrinite reflectance data suggested that a significant number of wells are within the oil and wet gas window (Borrok et al., 2019). Findings from the study match well with previous indications that TMS is a self-sourced rock contributing hydrocarbons to neighboring Lower Tuscaloosa sands (John et al., 1997; Koons et al., 1974).
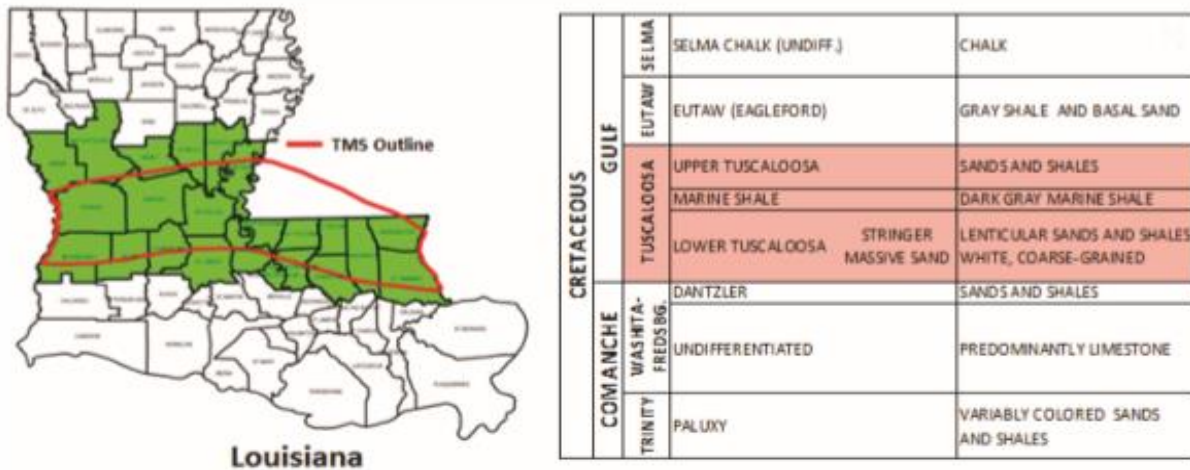
Figure 2.6. (a) Map showing outline of the TMS over Louisiana and Mississippi (State of Louisiana Department of Natural Resources) and (b) Stratigraphic column (John et al., 2006)

More than 100 cores were analyzed to obtain petrophysical properties and the results show that: permeability, porosity and water saturation were in the ranges of <0.01-0.06 mD, 0.023-0.08

31

and 0.32-0.88 respectively. These low porosity and permeability values could not account for 2,500 bbls of oil which was produced from the same interval. The delineated fractures were observed to increase with depth, being generally widespread between 11,000 ft and 11,055 ft, which would indicate the enhancement of flow and storage capacities. TMS was identified as overpressured: at 6200 psi, it lies between two sand bodies which ranged from 4400 to 5200 psi. In terms of reserves potential, an average payzone thickness of 93 ft was evaluated from well logs on the premise that 40% of the resistive TMS section contains fracture-driven porosity and permeability. Of this thickness interval, 37 ft could potentially produce oil, which amounts to seven billion barrels of recoverable oil (John et al., 1997).

In a recent TMS reservoir characterization study made using nuclear magnetic resonance (NMR), more than 60% of depth of investigation identified with clays such as illite and mixed-layer clays (Besov et al., 2017). Measured total organic content (TOC) was found to be 1.6%, most of which does not associate with porosity. Imbibition and pressure saturation experiments reveal that TMS is strongly water-wet and would not allow entry of hydrocarbons, which leads to the conclusion that much of the OIP is stored in fractures and inorganic pores.

2.2.2.2.   *Exploration and Production Activities*

TMS has been recognized as one of the most promising unconventional resource plays in the U.S. Crude oil production in TMS commenced several years ago through conventional drilling and horizontal drilling, during which thousands of barrels of oil have been produced. One of two vertical wells drilled about four decades ago produced up to 20,000 barrels within the first nineteen years while several wells recently drilled have initial production of at least 1,000 bopd and more than 200,000 bbls cumulative production in less than two years (Besov et al., 2017). Exploration activity using unconventional techniques began in TMS with the first successful well drilled in

1978 in Tangipahoa Parish, Louisiana (John et al., 2005). Activity then gradually increased in the successive years. From 2007 to 2016, around 80 horizontal wells drilled have produced at least 9 million barrels of oil (38-46 API) and 5 billion cubic feet of gas (IHS Energy Group 2016). Without supporting evidence, initial oil formation volume factor of 1.3 rb/stb has been reported.

Decline curve analyses of oil wells in TMS using publicly available production profile (SONRIS, 2018) showed that monthly production rate typically drops by 80-90% (even more in some cases) in the first year of production, leading to 5-9% ultimate recovery estimates (see Figure 2.7). Thus, should advanced and efficient EOR technologies remain undiscovered, 91-95% of in-place hydrocarbons in TMS will be left buried in the ground.
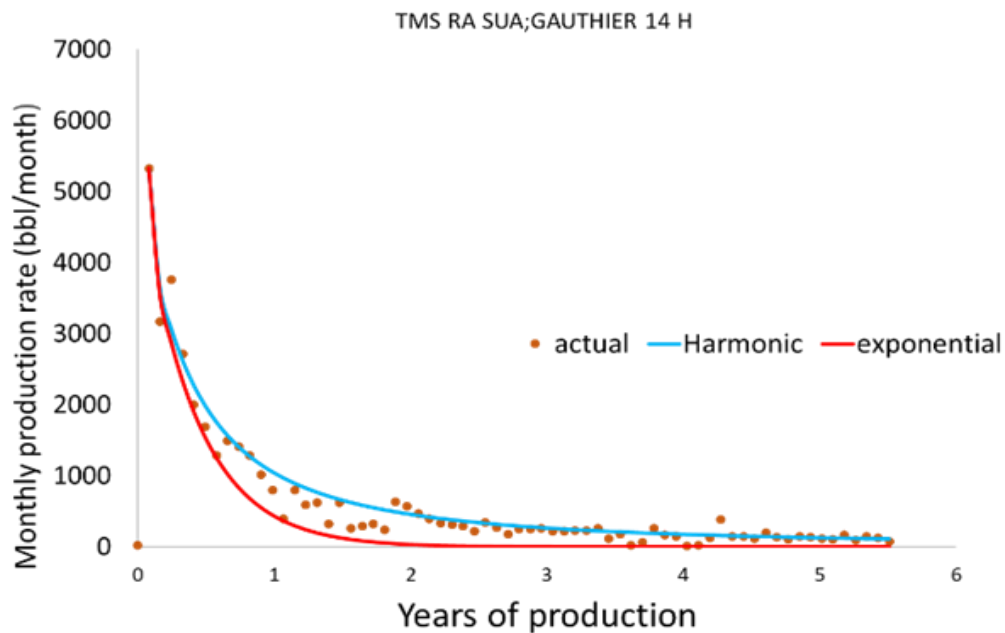
Figure 2.7. Production performance history match using decline curve analyses on TMS oil wells. These graphs show that more than production rate drops by more than 80-90% in the 1st year leading to 5-9% ultimate recovery estimates.

2.3. Enhanced Oil Recovery in Shale Oil Reservoirs

2.3.1. Overview

Oil production from unconventional shale oil reservoirs in the U.S. as of 2019 accounted for more than 60% of the nation's oil production and currently, U.S. is the world's largest oil producer. Such growth metrics (see Figure 2.8) are expected to improve as the shale exploration and production continues. Multi-stage hydraulic fracturing and horizontal drilling are the technologies responsible for the enormous success of shale oil field development (Sheng, 2017; Sheng et al., 2015). However, there are colossal challenges. Wells drilled in unconventional reservoirs suffer at least 70% decline in production after one or two years and reliable estimates in Bakken, Eagle Ford and Tuscaloosa show that only 3-10% of oil-in-place may be recovered (2018; Alharthy et al., 2018). Second, hydraulic fracturing typically requires at least 4 million gallons of fresh water (mixed with chemicals) per well, equivalent to bath of 80, 000 people, stressing water supplies in American states and causing significant environmental concerns (Gherabati et al., 2016; Reuters, 2013). In other words, should such enhanced shale oil recovery methods remain unfound, billions of oil barrels will be left buried in the ground at the time when conventional reservoirs around the world have been substantially depleted (Sorrell et al., 2009). To investigate EOR potential in tight oils, research studies – including experimental work and model development - and field pilot tests have been performed. The most popular techniques so far are gas injection and water injection – only a few chemical injection cases have been reported (Dong and Hoffman, 2013; Joslin et al., 2017; Kovscek et al., 2008; Sheng, 2014; Sheng, 2017; Sheng and Chen, 2014; Vega et al., 2010; Wang et al., 2010).

Oil and gas production in the United States
New Policies Scenario, 1980 - 2040
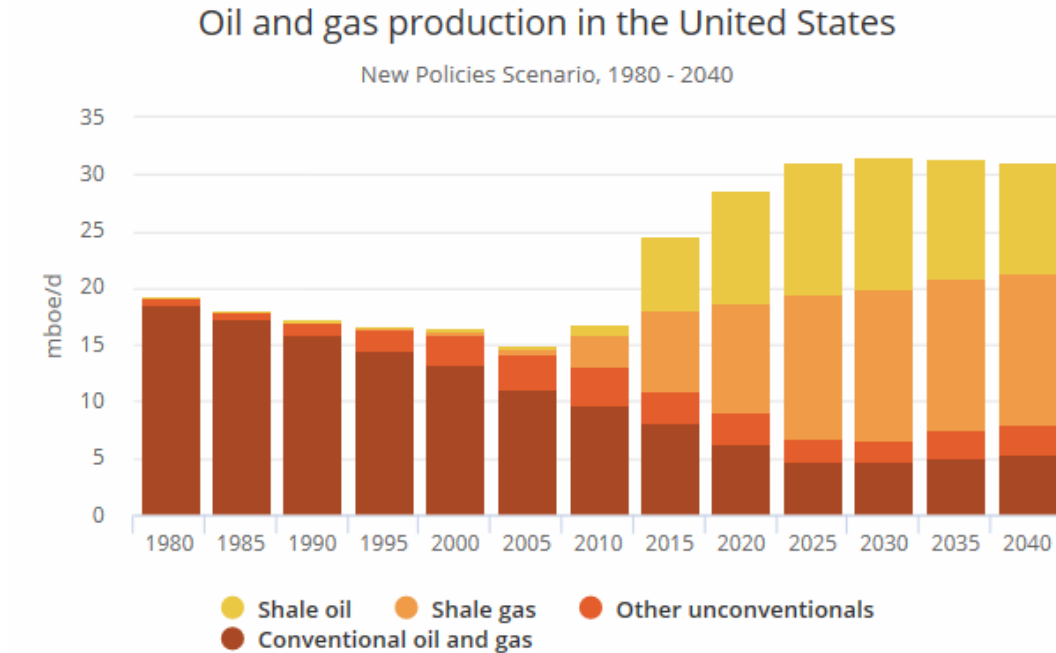
Figure 2.8. Oil and Gas Production in the United States from 1980 to 2040 (EIA, 2017)

Majority of research work and field tests involving gas injection have investigated continuous and huff-n-puff CO_2 injection. Water injection has also been tested both on lab and field scale, also in continuous and cyclic modes, but most continuous injection results have revealed poor recoveries due to injectivity issues (Todd and Evans, 2016), permeability reduction and formation damage (Duan et al., 2017; Morsy and Sheng, 2014), water break through and poor displacement efficiency (Wood and Milne, 2011). However, there have been some instances where water injected continuously promoted rock/fluid interactions and improved recovery. For example, it has been observed that water may aid creation of micro-fractures in the absence of confining pressure, but whether fractures may be induced to improve permeability during shale water injection EOR under confining stresses remains debatable (Morsy and Sheng, 2014; Morsy et al., 2013a; Morsy et al., 2013b; Morsy et al., 2013c; Sheng and Chen, 2014). Sheng and Chen (Sheng and Chen, 2014) reported that water injection fails to increase average pressure but only near-

wellbore localized pressure. Another group (Wood and Milne, 2011) summarized results from pilot tests performed in Bakken in Saskatchewan and North Dakota. In the Bakken case, peak oil rate increased in four wells from 75bbl/d to 500bbl/d with an estimated 5% incremental recovery over 50 years. The success of these tests was attributed to injection well pattern: horizontal injectors parallel to horizontal producers, with 100 m spacing. In the latter, 1 injector in the midst of 4 producers led to increased bottom hole pressure of 6000 psi with increased water flow rate but no improved oil production. Cyclic injection did not help either. In fact, water injection rate dropped with no additional oil produced. Water injection was subsequently switched to gas flooding.

Surfactant EOR has received substantial attention in the area of EOR for conventional reservoirs. Though its mechanisms have been extensively researched at lab scales (Chen et al., 2001; Hirasaki and Zhang, 2004; Sheng, 2013b) and field scales (Rilian et al., 2010; Sheng, 2013b; Sheng, 2017; Xie et al., 2005; Yang and Wadleigh, 2000), economics and environmental concerns has limited its potential for field implementations. Nonetheless, some surfactants now serve as fracturing fluid agents and are currently being applied for shale EOR applications. Some shale rock samples have been found to be oil-wet, which is logical because many factors including saturation history and crude oil composition affects rock surface wettability, even though clays are typically negatively charged and hydrophilic (Phillips et al., 2007; Wang et al., 2011). The mobilization and displacement of oil can be inhibited by oil wetness, which can be improved by surfactant injection through wettability improvement – making wettability alteration and spontaneous surfactant imbibition popular research areas in tight oil EOR (Ferno et al., 2012; Morsy and Sheng, 2014; Sheng, 2017; Shuler et al., 2011; Xu and Fu, 2012). Forced imbibition (such as fracking) has helped overcome the issue of low flow rates in long cores over the years

(Babadagli, 2001; Cuiec et al., 1994; Kazemi et al., 1992; Ma et al., 1995; Mattax, 1962). Zeng and co-workers (Zeng et al., 2018) examined application of surfactant blends in wettability alteration and spontaneous imbibition where they observed contact angle change from 175° to 28° and 20% recovery. In Wang et al.'s (Wang et al., 2012) work, Bakken shale cores were generally oil- or intermediate-wet and surfactants consistently changed wetting state towards water wetness. Surfactants provided 8% additional recovery compared to water injection and 20% recovery in total on average. Amott Harvey methods (Amott, 1959) were used for wettability measurements and spontaneous imbibition.

This section gave an overview of enhanced shale oil recovery methods, from mechanistic studies to field implementations. The next two subsections will review specific EOR methods proposed for this research.

2.3.2. CO$_2$ Enhanced Oil Recovery

2.3.2.1. Classifications of CO$_2$ EOR

Majority of EOR studies and tests performed on tight oil reservoirs recently have been based on gas injection due to its low density and high mobility. Multiple cases have experimented primarily CO$_2$ and natural gas in "huff-n-puff" mode, whereby gas is injected through a well, and the well is shut in to allow for soaking (days-weeks of soak time), thereby promoting interaction with crude oil. Subsequently, the well is put back on production. To add, application of CO$_2$ EOR meets a worldwide objective of carbon capture and sequestration to mitigate climate changes (Bachu et al., 2004; Manrique et al., 2007). Laboratory studies and numerical modeling have been performed on Bakken, Mancos (Alharthy et al., 2018), and Eagle Ford (Phi and Schechter, 2017) fields notably.

The overall recovery obtained with CO$_2$ injection EOR can be subdivided into macroscopic sweep efficiency (how much of reservoir volume is contacted relative to total volume) and

37

microscopic efficiency (how effective CO_2 is in mobilizing oil in areas where oil-contained rock has been contacted). Some of the factors affecting macroscopic sweep efficiency are: viscous fingering, gravity override and heterogeneity while those that affect microscopic displacement may include dispersion effects and distance travelled by injectant to attain miscibility. To curb these effects, different classes of CO_2 injection other than continuous injection have been applied. Some of these include: water-alternate-gas (WAG) and huff-n-puff (H/P) injection schemes. Adopting WAG using miscible and immiscible CO_2 has been tremendously effective in conventional reservoirs around the world, due to superior injectivity control, improved microscopic displacement and great synergistic effects of water flooding and gas injection (Christensen et al., 2001; Ghedan, 2009; Manrique et al., 2007; Smalley et al., 2018). In WAG, water is injected to sweep oil, and after some time gas is injected, and then the cycle is repeated. Yet, upward gas migration in WAG injection has been a concern and major cause of mismatch between experimental observations and field results of recovery efficiency. Gravity override is amplified by high vertical heterogeneity, large permeability streaks and high-pressure differential between gas (in this case CO_2) and oil phases. This has led to the emergence of gas-assisted gravity drainage (GAGD) where gas is injected from top as oil is being swept to a horizontal producer (Rao et al., 2004). As previously explained, the H/P type allows for enhanced interaction between injected CO_2 and in-situ hydrocarbons – especially the trapped oil globules.

During injection, CO_2 may either push oil from matrix into fractures – leading to diffusion, oil swelling and oil viscosity reduction - or vice versa which is typically unfavorable due to high capillary pressure in the low-permeability matrix. Zuloaga and co-authors (Zuloaga-Molero et al., 2016) conducted a simulation study on impact of fractures on CO_2 EOR in Bakken and found that, matrix permeability did not affect recovery performance during primary production but did during

CO2 injection. In a naturally fractured low-permeability (0.01 mD) reservoir, the fractures improved recovery performance with gas injection. Thus, appropriate models should be used for simulating CO2 injection in tight oil with low permeability and large natural fracture density. It is suggested that the case for huff and puff gas injection will be strengthened with thorough investigation into shale oil reservoirs with adequate geological characterizations (Jia et al., 2019).

2.3.2.2. *New Mechanisms of CO2 EOR in Tight Rocks*

The nanopores and mineralogy contained in tight rocks have given rise to new mechanisms of fluid flow and enhanced oil recovery process in the context of CO_2 injection. Convective flow and gravity drainage are known driving forces in conventional sandstone and carbonate reservoirs with high permeability and porosity. Whereas in shale rocks where pores are in the order of nm, mixing of fluids by virtue of their molecules' random movement through porous media and concentration gradient – otherwise called molecular diffusion – may dominate fluid flow from matrix. In turn, research have shown that molecular diffusion control CO_2/oil mixing process (Alfarge et al., 2018; Jia et al., 2019; Jin et al., 2017b). Tsau and co-authors (Bui et al., 2010; J., 2011) studied near-miscible CO_2 behavior in Arbuckle reservoir by examining swelling tests in conjunction with slim tube experiments. They showed that, at low pressures, CO_2 dissolves in oil with little oil-in-gas dissolution and this dissolution causes oil swelling. At high pressures (near miscibility conditions), oil is being substantially extracted into gas, as shown by significant color change in the swelling test system. They concluded by stating the importance of unidirectional diffusion in low pressure (below miscibility pressure) in low-pressure reservoirs and diffusion coefficient determination (binary or multicomponent). Ferno and colleagues (Fernø MA et al., 2015) performed a CO_2 flow visualization test on a fractured sandstone core (permeability of 1.2D and porosity of 0.22) using positron emission tomography (PET) and observed diffusive transport, with a 2.2 $\times 10^{-8}$ m^2/s

effective diffusion coefficient measured from dynamic distribution of CO_2. It was pointed out in their work that diffusive coefficient in shale do not follow Fick's Diffusion law due to non-inclusion of pore size and geometry as well as clay chemistry. Injection of CO_2 was done in the absence of fracking in cores of 0.9 micro-Darcy average permeability at high pressure (22.1 MPa) and temperature (60°C). With a 55% recovery, CO_2 was proposed to mobilize oil through a combination of viscous force and molecular diffusion. Injected CO_2 produced oil from pores without initiating fractures. Jia and co-workers (Jia et al., 2018) performed compositional simulation in CMG GEM and demonstrated that, during CO_2 EOR, molecular diffusion reduced gas-oil ratio, contributed 0.3% recovery in 500 days and extended production time. It was inferred that high level of heterogeneity supports oil recovery with high correlation length but may be of demerit with small correlation lengths, which tallies with Johns and Garmeh's (Johns and Garmeh, 2010) work on reservoir mixing and dispersivity. In the past, multiple empirical correlations of diffusion coefficient have been developed (da Silva and Belery, 1989; Sigmund, 1976a; Sigmund, 1976b; Wilke CR and P., 1955), most of which are based on few experiments under low pressure conditions, atypical of liquid-rich unconventional formations.

With respect to nanopore confinement, reservoir fluids (mainly hydrocarbons) and injected fluid (in this case CO_2) are under pseudosteady state in nanometer-sized pores which may lead to drastic shift in phase envelope. Many research groups have proven that this causes suppression of bubble point and increase in dew point pressure (Jin et al., 2017a; Lowry and Piri, 2018; Yang et al., 2018; Zarragoicoechea and Kuz, 2004). Zarragoicoechea and Kuz developed empirical correlations for critical properties between bulk and pore-confined phase where critical change was described in terms of collision diameter and pore size. Very good agreements were obtained for mesopores (2-50 nm) with minute changes at smaller pores due to possibility of multilayer

adsorption. CO_2 aims to reduce or eliminate capillary pressure (miscibility) by lowering IFT – both of which have recently shown to be pore size-dependent. In furtherance to existing efforts (Jin et al., 2013; Ma et al., 2013), Li and Sheng (Li and Sheng, 2017) examined nanopore confinement on capillary pressure in Wolfcamp shale oils and found that IFT reduces drastically as pore reduces below 100 nm, during which capillary pressure first increases then decreases at less than 5 nm. Low density difference between oil and gas also contributes to lower capillary pressure. Wang and colleagues (Wang et al., 2016) developed a compositional tight oil simulator that captures effect of capillary pressure and nanopore structure on rock and fluid properties. Capillary pressure was obtained from J function while modifications were made to stability and flash tests to factor capillarity as pore size reduced from 50 to 10 nm, bubble point pressure dropped by 300 psi at 80°F while cumulative production increased from 5600 bbls to 6600 bbls with capillary effects (smaller pores contain lighter fluids with lower viscosity which may favor oil extraction). In unconventional reservoirs, adsorbed crude oil is known to significantly contribute to fluids-in-place volumes and can be displaced by CO_2 injection. Through molecular dynamics simulation, mass transport of CO_2 through shale inorganic pores was studied and it was seen that CO_2 adsorption capacity increased close to pore walls (Wang et al., 2016). CO_2 had more adsorption than alkanes in organic pores, which favors carbon sequestration and enhanced recovery. Higher temperatures also promoted flow capacity and reduced adsorption. This branch of shale characterization has received significant research attention recently (Jiang et al., 2008; Zhang et al., 2018) but with less physical experimental evidence.

2.3.2.3.   *CO_2 Injection Experiments in Shale Rocks*

Laboratory tests of CO_2 injection in tight rocks have been designed in different ways and several mechanisms have been addressed: from miscibility to diffusion. For the most popular method

proposed by Tovar and colleagues (Tovar et al., 2014), a core is centralized in a cell where it may either be saturated with oil or preserved, while empty space or high permeability glass beads are used to simulate fractures. They performed two experiments – one at 3000 psi and the other at 1600 psi, with both at 150°F on sidewall cores. Glass beads were the high permeability media assumed as fractures and to ensure rock/CO_2 contact. The cores were soaked in CO_2 for days and intermittent production was allowed while saturation changes were monitored using CT. CO_2 penetrated the cores and dissolved in oil, recovering up to 55% OOIP. Mass exchange of rock during CO_2 injection was ascribed to adsorption of CO_2 on organic pores, which was observed in another work, where pore and surface diffusion were proposed as prevalent mechanisms for transport of gas molecules in shale (Kang et al., 2010). Jin and co-workers (Jin et al., 2017a; Jin et al., 2017b) experimentally and numerically evaluated CO_2 H/P in Lower Bakken, Middle Bakken and Three Forks by analyzing 21 preserved core samples. Injection pressure was kept constant at 5000 psi with reservoir temperature 230°F and 24 hrs production duration. A low flow rate of 1.5cm^3/min was maintained to allow dominance of diffusion mechanism. A 60% recovery factor was obtained for Lower and Upper Bakken. Using analyses of variance (ANOVA), TOC, pore size and water saturation were identified as the most dominant parameters in production. Reasons proposed are that kerogen in pore size is smaller than that in inorganic matrix, leading to high capillary pressure and that kerogen make pore oil wet which also promotes high capillary pressure, also affecting residual oil saturation and relative permeability.

Miscibility development during CO_2 injection have also been studied in different experiments and reported recently. Most results reveal strong impact of CO_2 miscibility on recovery and less miscibility requirements compared to other gases such as CH_4 and N_2. For example, miscibility was addressed in the work of Song and Yang (Song and Yang, 2017) where CO_2 was performed

in immiscible, near-miscible and fully miscible conditions where the latter two conditions contributed 19-20% increments beyond immiscible flood recovery with less number of cycles. Miscible CO_2 performed 1% less than near-miscible flood, and although no explanation was given, it was concluded that obtaining complete miscibility in CO_2 floods may not be obligatory to obtain best CO_2 EOR performance in shale oils.   In Hawthorne and colleagues work on MMP determination using VIT/capillary rise technique, CO_2 MMP was reported as 2524 psi at 230°F and 1279 psi at 108°F, whereas methane obtained miscibility at 4514 psia while Nitrogen gas MMP was reported as 22,365 psia (Hawthorne et al., 2016). Ethane MMP was lower than CO_2 MMP at the same temperature (1345 psia at 230°F) which is consistent across different studies (Ahmadi and Johns, 2008; Alharthy et al., 2018; Yellig and Metcalfe, 1980).

2.3.2.4.   *Numerical Simulation of CO2 EOR in Tight Oil Reservoirs*

In tight oil reservoirs, viscous and gravity forces are less dominant as CO_2 EOR mechanisms due to the effect of molecular diffusion. However, this phenomenon is a new subject waiting to be more thoroughly examined. Further, impact of key reservoir and fracture properties such as permeability, fracture half-length, complex nonplanar fractures, natural fractures, and reservoir heterogeneity on the effectiveness of CO_2-EOR have not been evaluated quantitatively. Majority of these parameters can be conveniently studied through numerical simulation.

The governing equation for reservoir multiphase flow simulation that describes the total mass balance for components in the oil and gas phases is expressed by the continuity equation, including accumulation term of component in rock and fluid phases as well as convection, dispersion, and molecular diffusion terms for all phases (Lashgari, 2014).The Sigmund correlation (Sigmund, 1976a) is often used to calculate the oil and gas diffusion coefficients (in cm^2/s) since it is valid for both oil and gas phases. Effects of diffusion coefficient, fracture complexity, reservoir

permeability, heterogeneity, and gas injection scenario in numerical studies of CO_2 EOR in unconventional oil reservoirs have been addressed in a comprehensive book chapter focused on CO2 EOR in Middle Bakken (Yu and Sepehrnoori, 2018). The authors performed compositional simulation CO_2 in Bakken and for the base case set up a basic reservoir model with four effective hydraulic fractures within one stage because of the expensive computational time for the entire well with multiple fractures. In this study, matrix permeability of 10 μD and initial water saturation of 25% are used and the reservoir is assumed to be homogeneous. Oil recovery factor at 30 years of production for the case with CO_2 injection and diffusion is the highest. The oil recovery factor was almost the same for the case without CO_2 injection and the case only with primary production. In addition, the recovery factor of the case with CO_2 injection but without diffusion was the lowest – even lower than primary production - illustrating that CO_2 diffusion plays an important role in simulating CO_2 injection for enhanced oil recovery. Without considering diffusion, large amount of CO_2 will backflow to the surface after the end of soaking time and impede oil production. This is tandem with another study performed elsewhere (Yu et al., 2015) which showed incremental oil recovery factor at 30 years of production to be 0.10%, 1.40%, and 3.25% corresponding to CO_2 diffusion coefficient of 0.0001, 0.001, and 0.01 cm^2/s. However, Sun and colleagues (Sun et al., 2016) concluded in their study that CO_2 H/P floods are insensitive to diffusion, soaking and capillary pressure. Reasons for this discrepancy remain unclear but it is likely that well control parameters such as injection rate and reservoir properties such as permeability and heterogeneity may cause such contrasting observations.

With respect to injection cycles, incremental oil recovery factor of 1.40%, 2.12%, and 2.43% after 1, 2, and 3 cycles respectively were observed during CO_2 injection in Middle Bakken on a 30-year production lifespan (Yu et al., 2015). This is in concordance with the work of Sun

and colleagues (Sun et al., 2016) which showed that increasing injection cycle from 2 to 3 can improve recovery from 6% to 11.4%. Fracture geometry poses superior effect on production by improving formation permeability near wellbore and expanding stimulated rock volume and is expected to impact CO_2 EOR likewise. Yu and colleagues (Yu et al., 2015) observed an increase in additional oil recovery from CO_2 injection from 1.4% to 2.8% when fracture half-length increased from 210 ft to 310 ft. Evidently, Bakken formation has been quite prolific due to huge presence and interconnectivity of natural fractures to matrix to hydraulic fractures (Mullen et al., 2010; Theloy and Sonnenberg, 2013).Wan and Liu (Wan T and H., 2018) examined impact of fracture complexity on CO_2 Huff/Puff in shale reservoirs and discovered that fracture network conductivity for CO_2-enhanced recovery depends on matrix permeability, reservoir fluid properties and fracture cluster spacing, at a given fracture conductivity. Further, they showed that CO_2 injection performs better in complex fractures than planar fractures. When Sun and co-workers (Sun et al., 2016) simulated CO_2 H/P using unstructured discrete fracture network (DFN) and dual-continuum modeling, they observed that DFN was more accurate because it handles stochastically distributed fracture networks well, which is not true with dual continuum models. It was also observed that incremental oil recovery is sensitive to matrix/fracture porosity and permeability, well controls, duration of gas injection and length of H/P cycles.

CO_2 Huff-n-Puff gas injection is a suitable technique for tight oil reservoirs because it allows additional time for CO_2/oil/rock interactions, as earlier mentioned. Yet, the soaking time required can be excessively long and thus be of huge demerit. It may lead to even poorer recovery than continuous injection. Zuloaga and colleagues (Zuloaga-Molero et al., 2016) compared both huff-n-puff and continuous injection scenarios: in CO_2 H/P, each cycle consisted of 1 year of CO_2 injection, 1 month of CO_2 soaking, and 47 months of back production. To fairly compare the

45

effectiveness of both, the total volume of CO_2 injection remained same, which was 5475 MMSCF for 18 years. The average recovery factor was obtained as 7.67% and 14.13% for CO_2 Huff-n-Puff and continuous CO_2 flooding, respectively. They also conducted sensitivity studies on well pattern and compared incremental oil recovery factor between the zipper well pattern and the aligned well pattern with 8 horizontal wells for both flooding types. A small difference between two well patterns of about 2% is obtained for CO_2 Huff-n-Puff scenario, while a big difference of about 10% is achieved for CO_2 flooding. The reason was revealed through comparison of CO_2 global mole fraction distribution. For CO_2 Huff-n-Puff, most of injected gas molecules are primarily concentrated near hydraulic fractures, resulting in similar contact area between molecules and reservoir for both well patterns. However, for continuous CO_2 flooding scenario, the zipper well pattern generated a larger contact area and longer CO_2 breakthrough time than the aligned well pattern, significantly improving CO_2 sweep efficiency. Hence, it implies that the zipper well pattern is a better candidate for implementing CO_2-EOR field project in tight oil reservoirs. Zipper "fracs" have demonstrated tremendous EOR potential elsewhere through investigation of fracture interference using analytical methods (Akinluyi and Hazlett, 2018). For the soaking time, there is no additional improvement of oil recovery when the time was longer than 1 month. This finding is fairly in concert with a recent study on CO_2 EOR in Bakken shale which demonstrated that 6 weeks is optimal soaking time considering in-situ liberation of light oil components. In this report, CO2 with liberation yielded recovery of 19% - 9% greater than primary depletion. (Mahzari et al., 2019).

2.3.3. Nanofluid Enhanced Oil Recovery

2.3.3.1.   Merits and Applications

The injection of carbon dioxide is likely to be an established EOR technique for unconventional oil reservoirs as more research studies and field implementations are conducted, but it suffers significant limitations, three of which are: early gas breakthrough, soaking time period and heterogeneous miscibility development. Previous studies both in conventional and tight rocks have shown that the implementation of CO_2 EOR at field scale in the presence of natural fractures and high permeability streaks promotes viscous fingering effects (Phi and Schechter, 2017; Todd and Evans, 2016), premature gas production (Todd and Evans, 2016), poor microscopic displacement efficiency and overall low recovery. Optimization studies on soaking time during CO_2 H/P reveals that additional production during puff may not justify shut in period for soaking, which may cause CO_2 injection to perform even less than primary production which is already too low. Miscible CO_2 eliminates IFT and capillary pressure, but this effect is most probably close to injection source and may not propagate into the far field where miscibility conditions are required for enhanced CO_2/oil interactions. Thus, the inclusion of a denser fluid (to address gas breakthrough and soaking time concerns) that may alter wettability states deep into the reservoir (to address rock/fluid interaction problem) to augment CO_2 flooding appears like a forward approach. Nanofluid injection using nanometer-sized silica nanoparticles promises a viable option to assist CO_2 injection.

The development and application of nanomaterials has been ongoing for many decades, spanning across several industries such as electronics, aviation, medicine and energy sectors (Haeri, 2018; Kaasa, 2013). Nanoparticles (NPs) can be manufactured with different specifications: shape, size, functionalities, solvent types, both synthetically and mechanically. These particles when dispersed in medium or solvent fluid like ethanol or water by interacting with the tail group give rise to nanofluids. In the oil industry, it has been used in exploration to obtain accurate reservoir information and downhole images; in drilling for thermal conductivity; in cementing and improved cement strength; in production for well flow assurance; at surface for oil droplet removal from produced water; and more recently in hydraulic fracturing and enhanced oil recovery for wettability improvement and reduced formation impairment (Khezrnejad et al., 2014; Kong and Ohadi, 2010; Li et al., 2015; Li and Torsæter, 2015a; Syfan et al., 2018; Tajmiri and Ehsani, 2016) Pertinent to EOR applications, different types of NPs exist: hydrophilic (promoting water wetness and soluble in polar solvents), hydrophobic (promoting oil wetness and soluble in non-polar solvents) and neutral-wet (possess hydrophobic and hydrophilic parts). They behave like surfactants - depending on adsorption/absorption capacity (Hendraningrat et al., 2013d; Ogolo et al., 2012). The thermal stability of NPs also make them a promising alternative for thermal EOR in heavy oils (Ding et al., 2018).

Pertinent to nanofluid EOR, silica (SiO_2) NPs are mostly preferred. Silica is a generic nomenclature for water-soluble and inorganic harmless ceramic mineral made of silicon dioxide and can be found in a wide range of other composite minerals, like quartz. Besides being the earth most abundant mineral, its high specific surface area (200 – 300 m^2/g), low bulk density (0.04-0.1g/cm^3), superior suspension ability, tailor-fit geometry, controllable chemistry and environmental safety makes it best suited for chemical EOR – especially in shale reservoirs. This

is in addition to its unique thermal properties (fast cooling, isolation), high mechanical strength, light adsorption and emission, and catalytic properties which expands its band of application (Haeri, 2018). This is substantiated with research outputs from academic and commercial laboratories, which showed incremental oil recovery correlated with contact angle change, IFT reduction and wettability alteration-with few discrepancies in some cases (Carpenter, 2015; Ghanaatian, 2014; Hendraningrat et al., 2013d; Maghzi et al., 2012; Sheshdeh, 2015).

2.3.3.2.   *Experimental Investigations of Nanofluid EOR*

Majority of the mechanistic studies relating to nanofluid EOR injection have been conducted in the lab, with few numerical modelling attempts. As Vad and Christian pointed (Bennetzen and Mogensen, 2014), some of these mechanisms are: viscosity reduction, foam stabilization, wettability alteration, conformance control and capillary trapping reduction (Hendraningrat et al., 2013a; Hendraningrat et al., 2013b; Hendraningrat et al., 2013c; Hendraningrat et al., 2013d; Hendraningrat et al., 2012; Torsater et al., 2012). Adsorption phenomenon is not fully understood and is an important component of NP mechanics. To capture this physics, it was proposed that Van der Waal interactions, electrostatic repulsion, Brownian motion, inertia forces, hydrodynamic forces, surface tension effects and gravity impact should be adequately studied.

Jiang and colleagues (Jiang et al., 2017) performed contact angle and IFT measurements of silica Nanofluids (in distilled water) in the presence of decane on calcite crystals to mimic carbonate rocks. They observed contact angle change from ∼75° to ∼50° in 0.5 wt% nanofluids, modest IFT reduction (50 to 45 mN/m), with an 8.7% improvement in oil recovery from corefloods. Ogolo and co-workers (Ogolo et al., 2012) tested a wide range of nanoparticles including silane-treated SiO_2 and hydrophobic SiO_2 NPs to verify incremental oil recovery, wettability changes, soaking effects and dispersant effects. While ethanol provided highest

recovery and distilled water provided the least, it was concluded that silane and hydrophobic NPs dispersed in ethanol showed tendency to improve recovery through wettability modification – particularly for oil-wet rocks. The optimistic performance of hydrophobic NPs may be contradictory, but it appears that both hydrophilic and hydrophobic NPs can reduce IFT and improve wettability. This is in tandem with an experimental investigation of polysilicon NP recovery: hydrophobic NP reduced IFT from 26.3 mN/m to 1.75mN/m, 130° to 95° contact angle reduction, corresponding to a ~32% recovery (Roustaei et al., 2012). In the same work, neutral wet NPs reduced IFT from 26.3 to 2.5mN/m, higher contact angle drop (130° to 80°) but slightly less recovery of ~29%. However, experimental studies on fine migration show that neutral-wet fines migrate to oil/water interface (possibly reducing IFT), while water-wet and oil-wet particles preferably remain in water and oil phases respectively (Muecke, 1979; Sarkar, 1988; Sarkar and Sharma, 1990).

Disjoining pressure is the most fundamental nanofluid EOR mechanism identified so far, and it was first discovered by Wasan and Nikolov (Wasan and Nikolov, 2003). In this work, they observed through video microscopy the ordering of nanospheres in water and their spreading behavior on glass, and they also analytically calculated disjoining pressure based on statistical mechanics. By extensive review of published reports, wettability alteration is the most recognized mechanism of nano-EOR but original scientific evidence at the nanoscale appears scarce in literature. Most studies have focused on characterizing globally lumped parameters such as contact angle and relative permeability which do not directly provide much information about the role of intermolecular interactions (Israelachvili, 2009). Yet, these lumped parameters are a result of the intermolecular forces and they are of more practical importance in engineering applications.

The search for the nanoscale wettability alteration mechanism in nanofluid EOR has now become crucial for cogent reasons. First, the dominance of nanopore confinement in tight rocks has recently been recognized due of the high near-term productivity but elusive long-term potential of these formations (Alfarge et al., 2018; Li and Sheng, 2017). For such reservoirs, a significant portion of in-place hydrocarbons are adsorbed (or adhered) on pore walls, but adhesion in the context of tight oil recovery is not well understood (Jin and Firoozabadi, 2016; Pathak, 2018). Second, fundamental understanding of EOR using SiO_2 nanoparticles at the molecular level offers a unique path for screening this method. The process of discovering, presenting, and linking nanoscale evidence to pore- and field-scale observations help to identify consistencies (or lack of) with regards to mechanistic insight into nanofluid EOR technology. Also, most studies in which a decrease in IFT was observed was due to the employment of surface-treated silica particles (Metin et al., 2012), whereas significant wettability alteration did not typically require surface functionalization (Haeri and Rao, 2019; Jiang et al., 2017). However, the role of crude oil chemistry and mineralogical composition in the context of nanofluid EOR have not been studied in detail. Also, the application of DDDC technique for precise wettability measurements in the context of nanofluid EOR has not been significantly explored.

2.3.3.3.   *Numerical Modeling and Simulation of Nanofluid EOR*

The application of nanofluids for enhanced oil recovery became recognized only recently – perhaps within the last two decades - thus there have been limited numerical modeling and simulation efforts. Majority of analytical models have incorporated relative permeability change, capillary pressure change, porosity change and permeability impairment rather than experimental data for capturing displacement mechanisms (El-Amin et al., 2017; El-Amin et al., 2013; Ju et al., 2006; Miranda et al., 2012). In the context of nanofluid EOR, Brownian motion – the random

movement of particle in a suspended medium - has been modeled based on Boltzmann constant, viscosity of NP dispersion, temperature and particle size (El-Amin et al., 2013). The formation damage model originally developed by Liu and Civan (Liu and Civan, 1993) which was based on laboratory data (Sarkar, 1988; Sarkar and Sharma, 1990) is the bedrock for most nanoparticle EOR injection models established so far. The model is based on the following assumptions:

1. Isothermal, 1D, horizontal flow (negligible gravity effects)

 2. Homogeneous isotropic and incompressible porous media

3. Incompressible fluids

4. Negligible viscosity and density changes due to particle suspensions

5. Negligible geochemical effect

6. Negligible variations in capillary pressure and relative permeability due to fines migration

Mass conservation equations are used to express oil and water flow, while the particle transport is modeled using an adsorption-convection-diffusion equation: the mass accumulation term defines rate change in water-dispersed NPs' flux; the convection term defines Darcy flow of NP dispersions while the diffusion term captures the diffusion of NP based on Stokes-Einstein equation. Dispersion effects were neglected in Liu and Civan's model since it was assumed that particle sizes are larger than 1 micron, whereas NP sizes are in nanometer range. According to El-Amin and co-authors (El-Amin et al., 2013), net rate loss of NP can be modeled based on Gruesbeck and Collin's formulation (Gruesbeck and Collins, 1982), in terms of entrapment and surface deposition. Porosity change is then modeled based on NP rate loss and permeability impairment is calculated from porosity modification, flow efficiency factor, fluid seepage and

power law exponent. Ju and colleagues (Ju et al., 2006) extended this model to study enhanced oil recovery using lipophobic and hydrophilic polysilicon NP with 10-500 nm and observed relative permeability shift indicating wettability alteration with reduction in permeability and porosity. Their results show that 2-3 wt% NPs may be sufficient to improve oil recovery. Later, Ju and Fan (Ju and Fan, 2009) used a Transmission Electron Microscope demonstrate wettability changes during NP flooding in sandstone and showed that water effective permeability improved by more than 1.5 times. They also obtained good match between experiment and modeled effective permeabilities. El-Amin and colleagues (El-Amin et al., 2013) also improved on the same model developed by Liu and Civan (Liu and Civan, 1993) to incorporate NP concentration-dependent relative permeability and capillary pressure but their model were not substantiated with laboratory measurements. The same research group later employed time-splitting technique (accounting for different time step for pressure and NP concentration calculations) to model NP transport through hydraulic fractures in tight rocks (El-Amin et al., 2017).

The EOR potential of nanofluids have also been studied at the molecular level, using molecular dynamic simulations (MDS). This approach provides an excellent means of performing nanoscale investigations on the effects of surface forces, molecular diffusion, viscosity and binding energies at typical reservoir conditions (temperature, pressure and brine salinity). Miranda and co-workers (Miranda et al., 2012) investigated the EOR application of bare silica NPs (dispersed in $CaCl_2$ and NaCl salts) using MDS at 300K and 0.1MPa. They adopted the CHARMM interatomic potential to define the interactions of silica nanoparticles. Their MDS snapshots and density profile results showed that aromatic molecules (benzene and toluene) accumulated on the NP surfaces (bare or modified) significantly while alkane molecules did not. The interfacial tension between bare silica NP and oil (mixture of alkanes and aromatics) calculated using Gibb's formulation to be 0.913

53

N/m whereas that between silica NP functionalized with polyethylene glycol and aromatics was 1.056 N/m. Also, the calculated nanoparticle-oil-brine contact angle using bare silica NP was 50° whereas that obtained with polyethylene glycolated NPs was 67°- signifying a tendency to stabilize oil/water emulsions better than bare nanosilica. However, they did not study density profiles, interfacial tension and contact angle between oil and a base dispersant such as water or brine (without nanoparticles), for comparison. In an MDS study, Liang and colleagues (Liang et al., 2019) investigated the effect of engineered SiO_2 nanoparticles on oil detachment from silica surface. They showed that silica nanoparticles with a mix of hydrophobic and hydrophilic chains (NP3) were the most effective in reducing oil/water interfacial tension and coherent energy of oil droplet (a measure of the difficulty to detach oil from silica surface) as well as recovery of adsorbed oil molecules from density profiles compared to hydrophobic silica nanoparticles (NP2) and hydrophobic silica nanoparticles (NP1). In pure water, oil/water interfacial tension was 60 mN/m, whereas IFT decreased to 48 mN/m, 46 mN/m and 31 mN/m using NP1, NP2 and NP3 nanoparticles, respectively. Similarly, the coherent energy obtained with NP3 was 230 Kcal/mole; compared to 380 Kcal/mole, 340 Kcal/mole and 400 Kcal/mole obtained with NP1, NP2 and pure water, respectively.

2.3.4. Nanofluid-assisted CO_2 Enhanced Oil Recovery

The application of carbon dioxide to improve production in conventional petroleum reservoirs is a well-established technique: its mechanisms are well known, and it has been deployed in many fields across the world for several years. As previously discussed, a literature survey on EOR in tight rocks has shown that CO_2 injection has received widespread interest from academic research and field test standpoints. In these unconventional oil reservoirs, supercritical CO_2 can obtain miscibility with the oil, eliminate interfacial tension and improve recovery significantly. However,

as discussed previously, presence of highly transmissive natural fractures – such as those found in TMS - impairs reservoir containment of CO_2, leading to viscous fingering and gas breakthrough. This is coupled with the fact that CO_2 huff-and-puff injection usually requires long soaking time to enhance interactions with the oil and rock. With the injection of nanoparticle dispersions, rock/fluid and fluid/fluid interactions are efficiently enhanced without the need for soaking and viscous fingering effects can be reduced – all of which presents benefits of oil recovery improvement. The benefits of injecting nanofluids and CO_2 for EOR purpose have been studied in the context of nanofluid-alternate-CO_2 injection and nanofluid-CO_2 co-injection. The former application preserves the mechanisms of nanoparticle dispersions and carbon dioxide separately while the latter combines both reagents to form stabilized foam and explore synergistic effects.

Al Matroushi and co-workers (Al Matroushi et al., 2015) conducted coreflood experiments using nanofluid-alternate-CO_2 EOR and modelled rock/fluid interactions. Following their history-matched results, they showed that nanofluid-alternate-CO_2 injection improved recovery by 48% compared to 35% obtained with conventional water-alternate-CO_2 injection. The recognized mechanism responsible for improved recovery was wettability alteration using nanoparticles which resulted in a shift in the oil/water and gas/oil relative permeability curves, indicating an improved mobility of the oil phase and reduced mobilities of water and gas phase. Zheng and colleagues (Zheng et al., 2020) investigated results from huff-n-puff field pilot implementation of nanofluid-alternate-CO_2 EOR in Eagle Ford shale. The field pilot test used 160 tons of CO_2 and 7000 gallons of surface-modified silica nanofluids in 11 nanofluid-alternate-CO_2 injection cycles. This process took less than 24 hours and the well was shut in for 5 days. The cumulative production obtained after 271 days was 8600 bbls; in comparison, only 3200 bbls was predicted to have been recovered in the same time span without nanofluid-alternate- CO_2 EOR. They also concluded that

the mechanisms of nanofluid EOR being wettability modification and interfacial tension reduction helped improve oil recovery while CO_2 injection acted as a carried fluid for the placement of the silica nanoparticles at the oil-water interface.

If nanofluids are co-injected with CO_2 (i.e. simultaneously), the resulting stabilized foams can provide an innovative means of ensuring mobility control because surface-engineered nanoparticles can adhere to the surface of CO_2 bubbles and prevent coalescence (Aminzadeh-Goharrizi et al., 2012; Espinoza et al., 2010; Qian et al., 2020; San et al., 2016). Espinoza and colleagues (Espinoza et al., 2010) studied stabilized foams of supercritical CO_2 and nanoparticles treated with polyethylene-glycol (PEG) and observed that the nanoparticle stabilized foam had to 2-18 times more resistance to flow than de-ionized water stabilized foams. They also observed that surface-treated nanoparticles could form stabilized foams at low salinity (as in De-ionized water) and higher salinity (as in 4 wt% NaCl) conditions. Similarly, PEG-coated silica nanoparticles were shown through CT images to slow the displacement front of nanofluid-stabilized CO_2 foams and smear the CO_2 injection flow paths to reduced viscous fingering and channeling, in Aminzadeh and co-workers' study (Aminzadeh-Goharrizi et al., 2012).

Despite promising results of nanofluid-assisted CO_2 EOR observed from literature, some fundamental research questions remain unanswered. For instance, besides relative permeability curves, effects of interfacial tension, contact angle and capillary pressure on recovery factor results with forced imbibition experiments and core-scale simulation have not been studied in detail. The synergistic effects of CO_2 EOR augmented with untreated silica nanoparticles in shale rock systems are also yet to be investigated in detail. Thus, these call for the need to characterize this EOR process across length scales for the Tuscaloosa Marine Shale which is the reservoir of interest for this study.

3. MATERIALS & METHODOLOGIES

3.1. Nanoscale Characterization of Nanofluid EOR

3.1.1. Mineral Samples

Muscovite mica was used as a rock substitute throughout this study because it closely resembles illite and kaolinite clay minerals which have been identified from X-Ray Diffraction (XRD) analyses on TMS cores in terms of the chemical composition and material properties. Quartz minerals were also employed based on XRD data which showed that the TMS section of interest contains primarily clays (44%) and quartz (43%), with other minerals such as calcite, pyrite, feldspars and anhydrite in small amounts (Afekare et al., 2020c). Mica sheets were purchased from Ward's Science (Rochester, NY), and were freshly cleaved before each experiment. Quartz substrates (purchased from VWR, Radnor, PA) were soaked in nitric acid for 20 mins and dried before use. All substrates have a minimum purity of 98%.

3.1.2. Nanofluids and Brine

To prepare nanofluids, 8 nm sized hydrophilic SiO_2 particles (purchased from US Research nanomaterials, Houston TX; see Figure 3.1) were dispersed in 1 wt% NaCl, and different concentrations (0, 0.05, 0.1 and 0.5 wt %) were prepared. Key properties of these dispersions are tabulated below (see Table 3.1). In a real-life scenario, fresh or de-ionized water will promote clay swelling and fines migration, hence the choice of 1 wt% NaCl dispersant.

Section 3.1.1 was previously published as Afekare, D., 2020. Enhancing Oil Recovery Using Aqueous Dispersions of Silicon Dioxide Nanoparticles: The Search for Nanoscale Wettability Alteration Mechanism, SPE Annual Technical Conference and Exhibition. Society of Petroleum Engineers, Virtual, pp. 19. Reprinted by permission of Society of Petroleum Engineers.

Section 3.1.2 was previously published as Afekare, D., Garno, J. and Rao, D., 2020a. Insights into Nanoscale Wettability Effects of Low Salinity and Nanofluid Enhanced Oil Recovery Techniques. Energies, 13(17). Reprinted by permission of Energies MDPI.

To simulate brine, a previously prepared brine formulation (AFB) based on TMS formation water geochemical analyses was used as base case (Afekare et al., 2020b). It contains 60000 ppm NaCl, 10000 ppm $CaCl_2$, 2650 ppm KCl, 250 ppm $MgSO_4$ and 150 ppm $MgCl_2$.

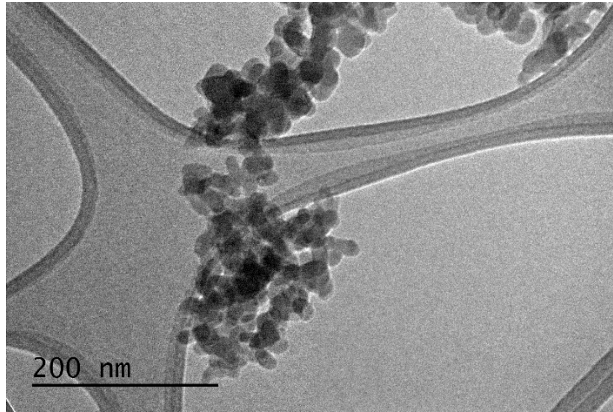Figure 3.1. Nanoparticles characterized under Transmission Electron Microscope

Table 3.1. Hydrophilic Silicon dioxide Nanoparticle dispersions, concentrations (wt %), pH and purity level

Nanofluids	Concentrations (wt% in 1 wt% NaCl)	pH	Purity (%)
Hydrophilic Silicon dioxide Nanoparticles (HNP)	0.05	7.66	99.99
	0.1	8.66	99.99
	0.5	8.28	99.99
	1	8.52	99.99

3.1.3. Thiol Solutions

The solutions used to represent alkanes and aromatic groups are 1-Undecanethiol and 2-phenylethanethiol respectively with key properties summarized in

Table 3.2. These thiols were purchased from Sigma Aldrich (St. Louis MO). Carboxylic acids are surface-active crude oil components typically found in both resins and asphaltene fractions, thus 11-mercaptoundecanoic acid was used to represent –COOH group. The acid thiol was purchased as powder.

Table 3.2. Thiol solutions used to functionalize AFM probes, and key properties.

Non-polar thiol solutions	Functional Group	Molecular Wt.(g/gmol)	Density (g/ml)	Purity (%)	Boiling Point (ºC)
1Undecanethiol - $CH_3(CH_2)_9CH_2SH$	Alkyl	188.37	0.841	98	103-104
2-Phenylethanethiol - $C_6H_5CH_2CH_2SH$	Phenyl	138.23	1.032	98	217-218
Polar thiol powder	Functional Group	Molecular Wt.(g/gmol)	Flash point (ºC)	Purity (%)	Melting point (ºC)
11-Mercaptoundecanoic acid - $COOH(CH_2)_9CH_2SH$	Carboxyl	218.36	> 110	95	46-50

Section 3.1.3 was previously published as Afekare, D., Garno, J. and Rao, D., 2020a. Insights into Nanoscale Wettability Effects of Low Salinity and Nanofluid Enhanced Oil Recovery Techniques. Energies, 13(17). Reprinted by permission of Energies MDPI.

3.1.4.   Atomic Force Microscopy (AFM)

3.1.4.1.   Experimental Set-up for Chemical Force Microscopy

The atomic force Microscope (AFM) is a high-resolution scanning probe microscopy tool which was used in this work to characterize the total interaction force that exists between a functionalized tip and mineral substrate in aqueous media – known as the adhesion force. A schematic of the AFM setup is presented in Figure 3.2. As the functionalized tip gently approaches the surface, it senses surface properties and causes the cantilever to bend. The position of the laser spot reflected from the cantilever onto the photodiode detector changes in response and the resulting deflection is recorded by the detector. Depending on the tip-sample distance, the feedback controller either allows piezoelectric scanner to adjust the position of the tip or the data is transmitted through topography images and/or force maps.

The design for the liquid cell experiments is shown in Figure 3.3. The substrate which is muscovite mica or quartz is pinned onto the magnetic plate with the liquid cell before the test solution is introduced (Figure 3.3a). Afterwards, the cantilever is lowered into the liquid-filled cell by adjusting the piezo scanner and the system is allowed to equilibrate (Figure 3.3b). Note that this is an open cell design: the liquid level is open to air so the liquid can evaporate over time. Chemical force microscopy (CFM) was used to perform adhesion tests in liquids.

Section 3.1.4 was previously published as Afekare, D., Garno, J. and Rao, D., 2020a. Insights into Nanoscale Wettability Effects of Low Salinity and Nanofluid Enhanced Oil Recovery Techniques. Energies, 13(17). Reprinted by permission of Energies MDPI.
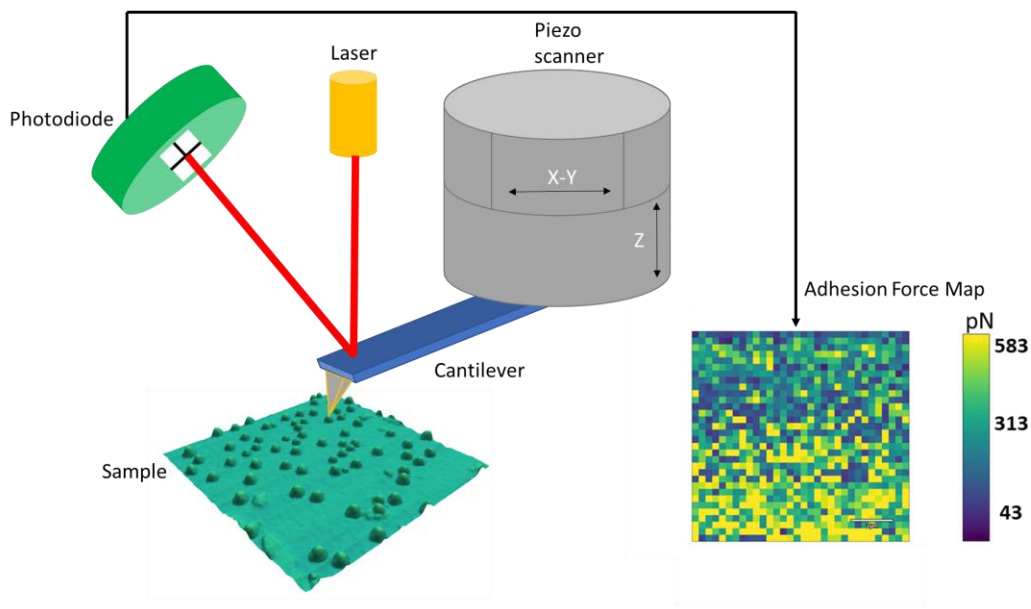
Figure 3.2. Schematic of AFM setup based on the Keysight 5500 Scanning probe microscope design used in this study

In CFM, a functionalized probe is used as a chemical sensor which when brought close to a surface can detect nanoscale forces (such as Van der Waal and structural forces) that are resolved in adhesion force measurements (Afekare et al., 2020b). The spatial characterization of adhesion on a given sample area using CFM is referred to as chemical force mapping (Hassenkam et al., 2012). Studies with CFM have been reported previously (Chandrasekhar and Mohanty, 2018; Hassenkam et al., 2012; Hilner et al., 2016). Chemical force mapping was performed using a Keysight 5500 AFM (Santa Rosa, CA) using the force volume spectroscopy feature.
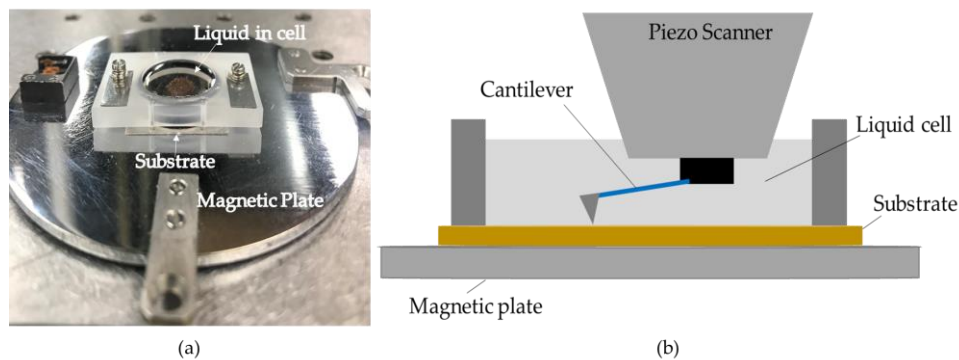
Figure 3.3. AFM liquid cell design: (a) an image of the cell containing test solution (brine or nanofluids) pinned with the substrate to a magnetic plate; and (b) a graphic of the overall setup as the tip scans the substrate area after equilibration.

3.1.4.2. *Thiolate Functionalization for Chemical Force Microscopy*

Gold-coated silicon nitride probes were employed for facile thiolate functionalization, which is a proven method to coat AFM probes for chemical force microscopy (Hassenkam et al., 2012; Hilner et al., 2016; Wu et al., 2017). A Pyrex PNP-TR-Au silicon nitride probe with a gold coated cantilever and tip of radius 28 nm and width of 3.3 µm was used (see Figure 3.4a). Analyses of crude oil can be tedious as it is a complex mixture, containing more than a thousand compounds. A convenient evaluation method is through saturate, aromatic, resin and asphaltene (SARA) analyses (Hackley et al., 2020) and the AFM tip can be treated with different solutions to represent these groups. The choice of functional groups studied was also based on Pressure-Volume-Temperature (PVT) tests performed on TMS oil samples (see Appendix A). The solutions used to represent alkanes and aromatic groups are 1-Undecanethiol and 2-Phenylethanethiol respectively (Figure 3.4b&c). These thiols were purchased from Sigma Aldrich (St. Louis MO). Carboxylic acids are surface-active crude oil components typically found in both resins and asphaltene fractions, thus 11-mercaptoundecanoic acid was used to represent –COOH group (Figure 3.4d). The acid thiol was purchased as powder.
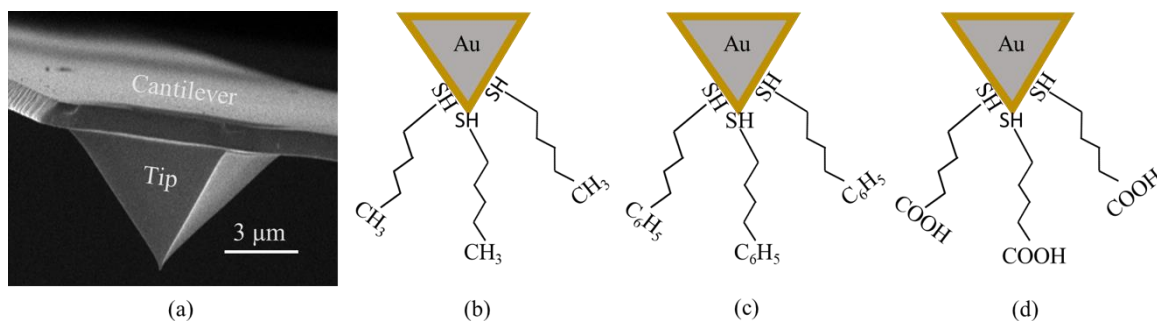
Figure 3.4. Scanning Electron Microscope (SEM) micrograph of AFM probe and conceptual schematic of functionalized tips. (a) A Pyrex PNP-TR-Au probe with gold coated cantilever and tip functionalized with (b) -CH$_3$, (c) -C$_6$H$_5$ and (d) -COOH groups

3.1.4.3. *Experimental Procedure*

Several aqueous media conditions were tested to determine an equilibrium adhesion time, i.e. the time after which there was no significant change in adhesion force (see Figure 3.5). Substantial variations were observed between 0 and 3 hrs compared to measurements taken after ≥ 8 hrs which were not significantly different from those observed after 3 hrs as shown. For the case of 1 wt% NaCl and 0.5 wt% HNP, evaporation effects might have caused substantial changes in adhesion force measurements after 3 hrs because the AFM fluid cell was not refilled over the course of the experiments. Nonetheless, it was determined that 3 hrs was sufficient time to obtain equilibrium adhesion, and this is in accordance with similar experiments performed elsewhere on brine composition effects on rock–oil interactions in carbonate reservoirs (Chandrasekhar and Mohanty, 2018). The short time frame makes force spectroscopy provides benefits of efficiency when compared to previous wettability evaluation methods that require days to weeks to obtain statistically tangible and reliable results (Hendraningrat et al., 2013d; Mascle et al., 2019).
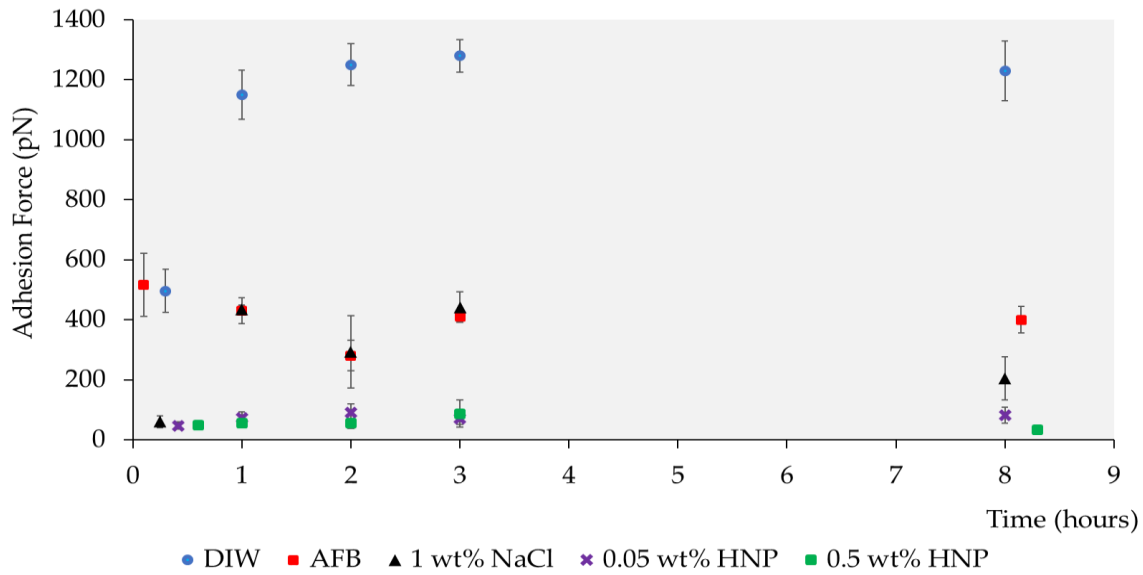
Figure 3.5. Graph of adhesion force as a function of time between a -CH$_3$ terminated tip and mica in de-ionized water (DIW); artificial formation brine (AFB); 1 wt% NaCl and solutions of 0.05 wt% and 0.5 wt% silica nanoparticles dispersed in 1 wt% NaCl.

Adsorption of nanoparticles is considered to be crucial for wettability improvement (Hendraningrat and Torsæter, 2015; Li and Torsæter, 2015b) and is related to nanoparticle concentration. The sequence of experiments was initiated with artificial formation brine and NaCl solution followed by low to high HNP concentrations, i.e. AFB > 1 wt%; NaCl > 0.05 wt%; HNP > 0.1 wt%; HNP > 0.5 wt%; HNP > 1 wt% HNP. The sequence was maintained for each experiment using functionalized probes. Force curves were taken with each test solution, collecting volume maps of adhesion force over a 5 μm x 5 μm scan area with 256 force curve measurements per map. After force volume maps were completed with a specific functionalized probe-substrate combination, the mineral substrate was replaced, and the test sequence was repeated. Results from AFM were processed using Gwyddion (version 2.55; released 2019-11-04), an open-source scanning probe microscopy data visualization and analysis tool (Nečas and Klapetek, 2012).

3.1.5. Experimental Workflow

Following the experimental details provided in this section, a user-friendly experimental flowchart displayed in Figure 3.6 illustrates the systematic nature of the research – including materials used, preparation steps, experimental procedure and data analysis and interpretation. As an original contribution of this work, a step-by-step guide on AFM force volume spectroscopy measurements using the Keysight 5500 Scanning Probe Microscope was prepared (see Appendix C).
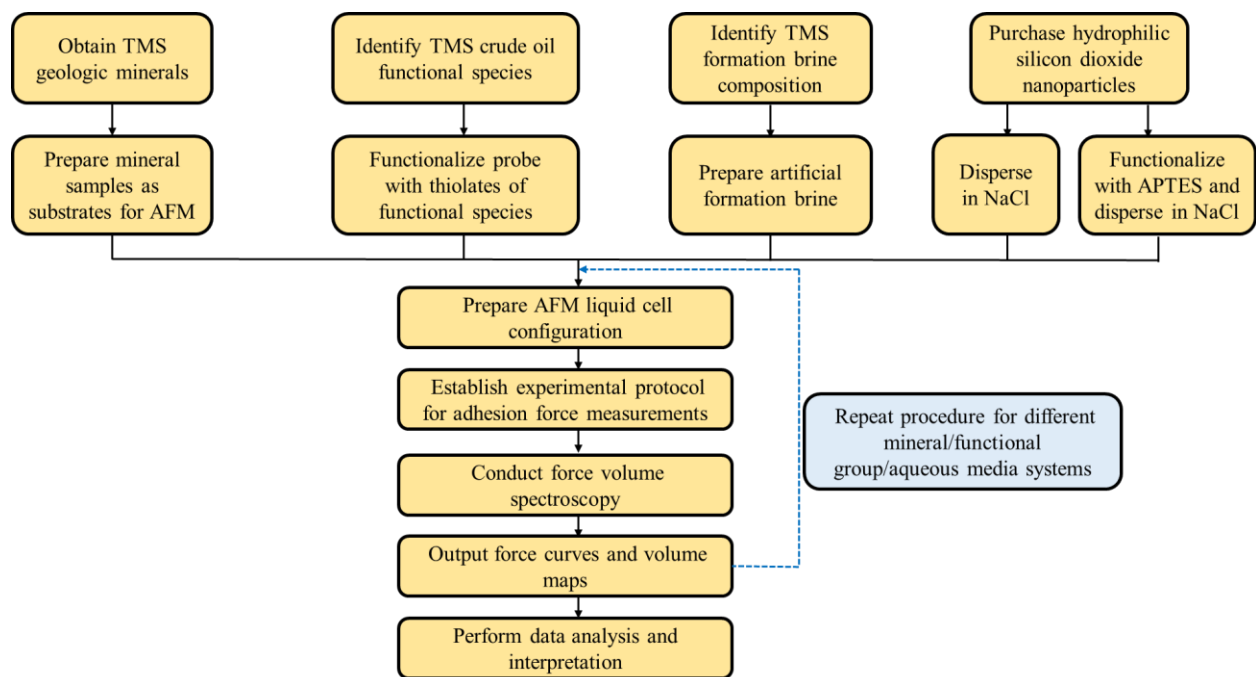
Figure 3.6. Flow chart highlighting the systematic nature of research – including materials used, preparation steps, experimental procedure and data analysis and interpretation.

3.2. Micron-scale Characterization of Nanofluid EOR

3.2.1. Materials

In addition to the aqueous solutions already prepared - such as artificial formation brine (AFB), sodium chloride (1 wt% NaCl) solution and nanofluids (HNP and NNP) - pure oil compounds such as ethylbenzene and undecane purchased from Sigma Aldrich (St. Louis MO) were employed to present phenyl and alkyl functional groups. Specifically, ethylbenzene was employed as a

compound carrying -C_6H_5 due to its similarity in chemical formula with 2-Phenylethanethiol used for nanoscale experiments (see Figure 3.7a&b). Likewise, undecane was used to present -CH_3 functional groups due to resemblance in chemical structure with 1-undecanethiol employed at the nanoscale level (see Figure 3.7c&d).

(a) Undecane   (b) 1-Undecanethiol

(c) Ethylbenzene   (d) 2-Phenylethanethiol
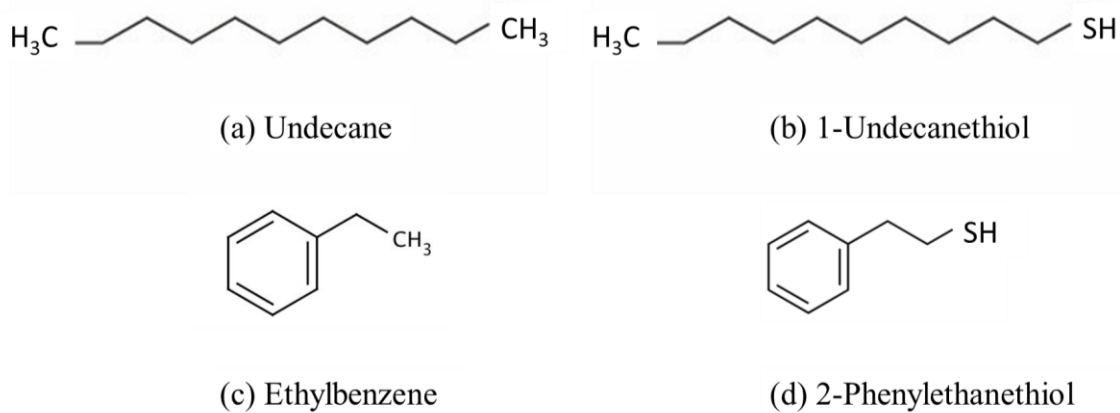
Figure 3.7. Different organic compounds employed in this study and their structural formulae :(a) Undecane (b) 1-Undecanethiol (c) Ethylbenzene (d) 2-Phenylethanethiol

Carboxylic acids are usually in powder form due to its melting point so a mixture of ethylbenzene and undecanoic acid was used to represent -COOH compound. Degassed crude oil samples retrieved from a well drilled in the Amite County portion of TMS (labelled TMS) was also employed in this study. The oil samples were pulled from the oil leg of a heater treater, so it is likely that they would have been separated from the gas component which comes out of another outlet. Key properties of undecane, ethylbenzene and undecanoic acid are presented in Table 3.3 while those of TMS are listed in Table 3.4 below.

Table 3.3. Selected organic compounds used for IFT tests and key properties

Chemical	Specific Gravity	Melting Point (°C)	Boiling Point (°C)	Molecular Weight (mg/mol)	Purity (%)
Undecane (-CH$_3$)	0.740	-26	196	156.31	$\geq$ 99
Ethylbenzene (-C$_6$H$_5$)	0.867	-95	136	106.17	99.8
Undecanoic acid (-COOH)	0.85	28-31	228	186.29	$\geq$ 99

Table 3.4. Key properties of TMS crude oil sample used for IFT and contact angle tests

Crude Oil Sample ID	API Gravity at 60°F	Viscosity (cP)	Asphaltene Content (wt%)	Sulfur Content (wt%)	Total Acid Number (mg KOH/g)
TMS	38.4	0.526	1.2	0.14	< 0.05

3.2.2. Optical Tensiometer

Interfacial tension (mN/m) between nanofluids and TMS crude oil as well as pure mineral oils such as undecane, ethylbenzene and a mixture of undecanoic acid and ethylbenzene were measured using the Attension optical tensiometer. A cuvette was filled with the continuous phase (brine or nanofluids) while a syringe with a 1.88 mm-diameter needle was used to form the oleic drop phase. Using the pendant drop technique, interfacial tension was obtained after ~2 hrs which was deemed sufficient for equilibration of the oil droplet in liquid based on stability of average IFT and standard deviation over time. The final IFT values reported are averages of five measurements. The optical

tensiometer system was calibrated by measuring IFT of standard solutions such as decane and ethylbenzene before each experiment. Calibration results in comparison with reference data (Jennings, 1967; NOAA, 1999) are tabulated below:

Table 3.5. Interfacial tension measurements obtained during optical tensiometer system calibration. The final IFT values reported are averages of five measurements.

Drop Phase	Continous Phase	Drop Image	Measured IFT, mN/m	Reference Value, mN/m (Literature Source)
Decane	De-Ionized Water		53.8 ± 0.9	51.2 (Jennings 1967)
Ethylbenzene	De-Ionized Water		33.97 ± 0.5	35.48 (NOAA 1999)

3.2.3. Dual-Drop-Dual Crystal (DDDC) Technique

The advancing contact angle of an injecting fluid phase (brine or nanofluids) over an area of a rock previously occupied by a bulk oil droplet can be precisely measured using the well-established DDDC technique (Haeri and Rao, 2019; Kafili Kasmaei and Rao, 2015; Rao and Girard, 1996) as shown in Figure 3.8. In the DDDC system, dynamic contact angles are measured using two oil droplets that are placed on two polished surfaces made from the reservoir rock. The rock surfaces and oil droplets are aged in a cell filled with brine (or nanofluids as used in this work). Then the lower rock is flipped and the oil droplets on both rock surfaces are merged (Figure 3.8a).
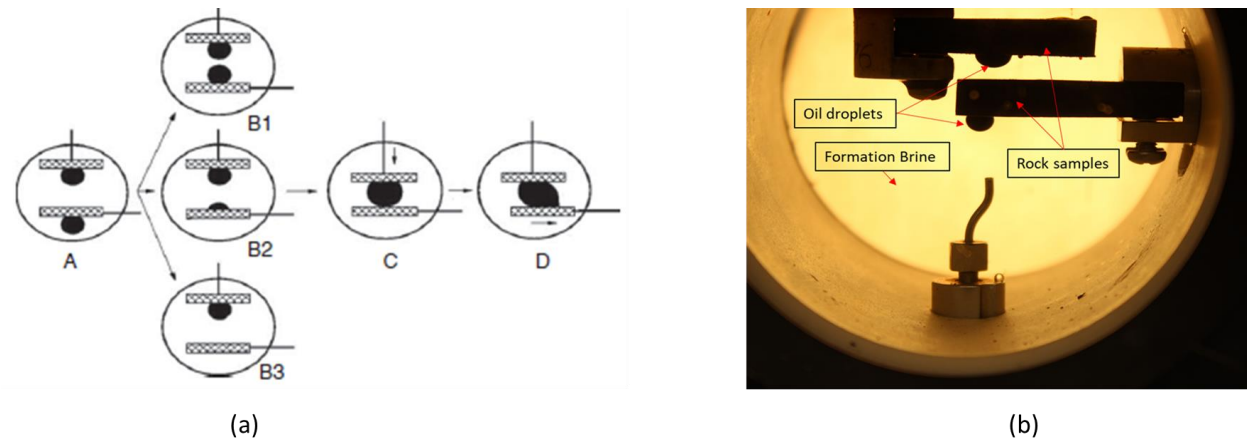
Figure 3.8. (a) Schematic depiction of DDDC technique and the steps to measure dynamic water advancing contact angle (Rao, 2002); and (b) an image of the DDDC set-up during a TMS wettability characterization experiment

At the stage of measuring the contact angle, the lower rock is gradually shifted while the three-phase-contact-line (TPCL) is monitored, as shown in Figure 3.9. Each time the side holder is shifted, the sheared oil droplet is given 30 mins to stabilize and the process continues until a change in three-phase contact-line or TPCL is observed. As seen in Figure 3.9, TPCL is normalized by dividing the distance from the lower left corner of the droplet to the edge of rock (l) by the initial distance of the right corner of the droplet to the edge of the rock (r_i). A change in TPCL is recognized when l/r_i or normalized TPCL is reduced, Once TPCL moved, the angle made by the droplet at the point of movement on the lower crystal in the water phase is measured as the dynamic water advancing angle.
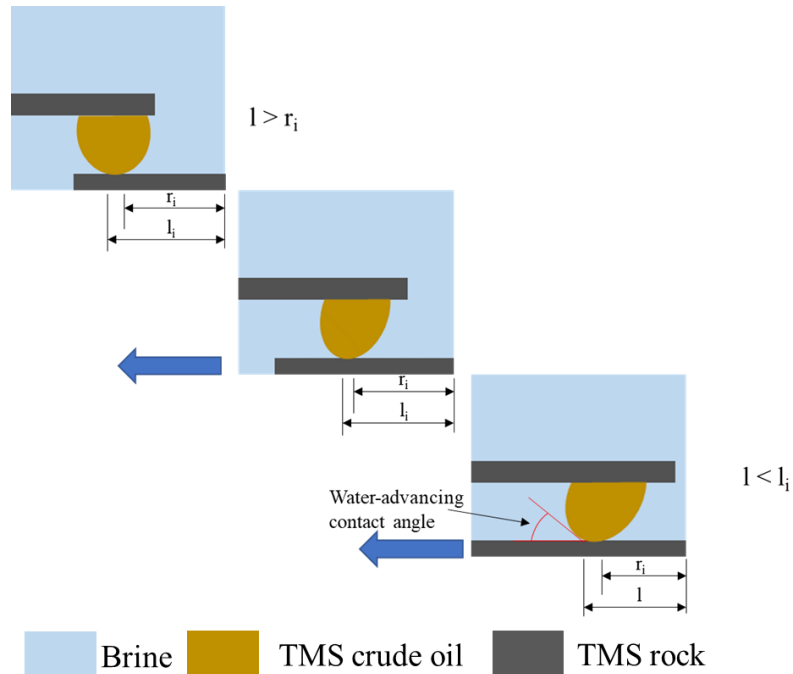
Figure 3.9 Monitoring of the three-phase contact line (TPCL) movement to measure water-advancing contact angle in the DDDC technique

Measurements of advancing and receding contact angles and how they relate to reservoir conditions are elaborately studied by Rao (Rao, 2002) (also see Figure 3.8a). The water receding angle mostly represents the native wettability of the reservoir when oil migrated and displaced the water. In the case of waterflooding, however, oil is expelled from the reservoir by water, which suggests that the water advancing contact angle is the correct indicator for wettability characterization of the system.

An image of the physical set-up during a TMS wettability experiment is shown in Figure 3.8b. In addition to TMS artificial formation brine, nanofluids and TMS oil samples, two well-polished rock samples cut out of TMS rocks are required. Blocks of rocks cut using a diamond milling machine and polishing pads were used to trim the samples into desired dimensions: 30 mm x 20 mm x 6 mm. Aluminum oxide polishing pads were used due to their non-reactivity with oil and water, and the rock samples were polished with pads of different mesh sizes (see Figure 3.10):

70

(a) 100; (b) 200; (c) 400; (d) 1000; and (e) 2000 grit. While polishing, the TMS rocks are allowed to rotate on the polishing pads which remain stationary. The process took between 30 s and 1 min per pad. No lubricating fluid is used when polishing the rock surfaces with pads of 100, 200 and 400 grits; however, about 0.2 ml of TMS brine is required when polishing with pads of 1000 and 2000 grits. The entire polishing process is also required for precise wettability characterization using DDDC: as will be shown subsequently, it helped confirm the true wetting state of TMS when comparing contact angle measurements with relative permeability curves. The polished TMS rock samples were fixed onto the rock holders and inserted into the optical cell. The dimension of the plate holder required trimming of the sample edges with polishing pads also. Next, the cell was filled with liquid – starting with AFB brine – and oil drops were introduced from the bottom of cell using a needle that was connected through a tubing to a syringe pump. Both the top and bottom rocks were aged with the oil droplets separately for 24 hrs in the surrounding aqueous media (brine or nanofluid) before images were captured and the advancing and receding contact angle values were obtained. The same procedure was repeated for HNP and NNP.
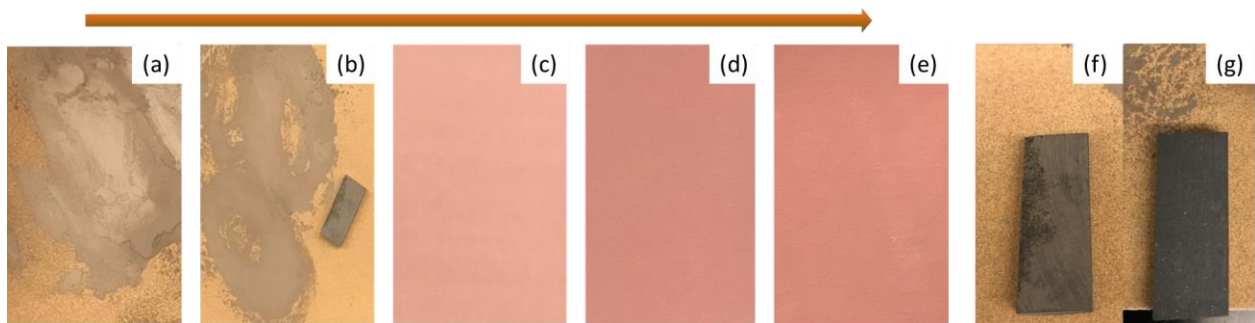
Figure 3.10. Polishing of TMS rock samples for DDDC experiments using Aluminum Oxide pads of: (a) 100; (b) 200; (c) 400; (d) 1000; and (e) 2000 grit. The final polished surface (g) has a shiny and smooth appearance compared to unpolished sample (f).

The exposure of the TMS rocks to elevated temperatures was avoided following an observation of cracks formed along the bedding planes when some pieces of rocks were gradually

heated in artificial formation brine (AFB); see Figure 3.11. This also explains why the rocks were not cleaned prior to contact angle experiments or corefloods and why high-pressure, high-temperature contact angle tests were not conducted. The rocks completely broke down when an attempt was made to clean in a Soxhlet extractor. It was observed in this study that the TMS rocks are very fissile.
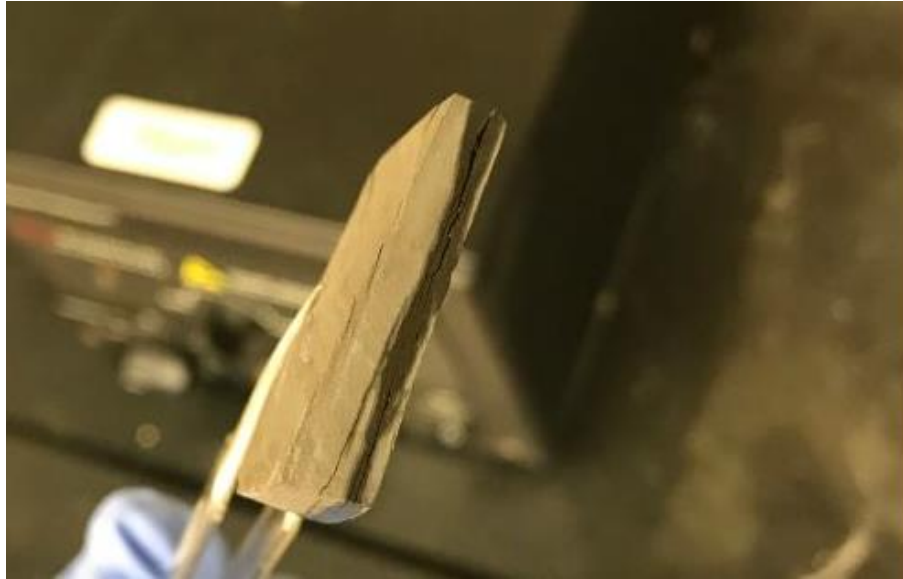
Figure 3.11. Cracks were formed along the bedding planes of TMS rocks due to exposure to heat in formation brine, which prevented the use of the rocks in high-temperature experiments.

3.2.4.   Experimental Workflow

Following the experimental details provided in this section, a user-friendly experimental flowchart displayed in Figure 3.12 illustrates the systematic nature of the research – including materials used, preparation steps, experimental procedure and data analysis and interpretation.
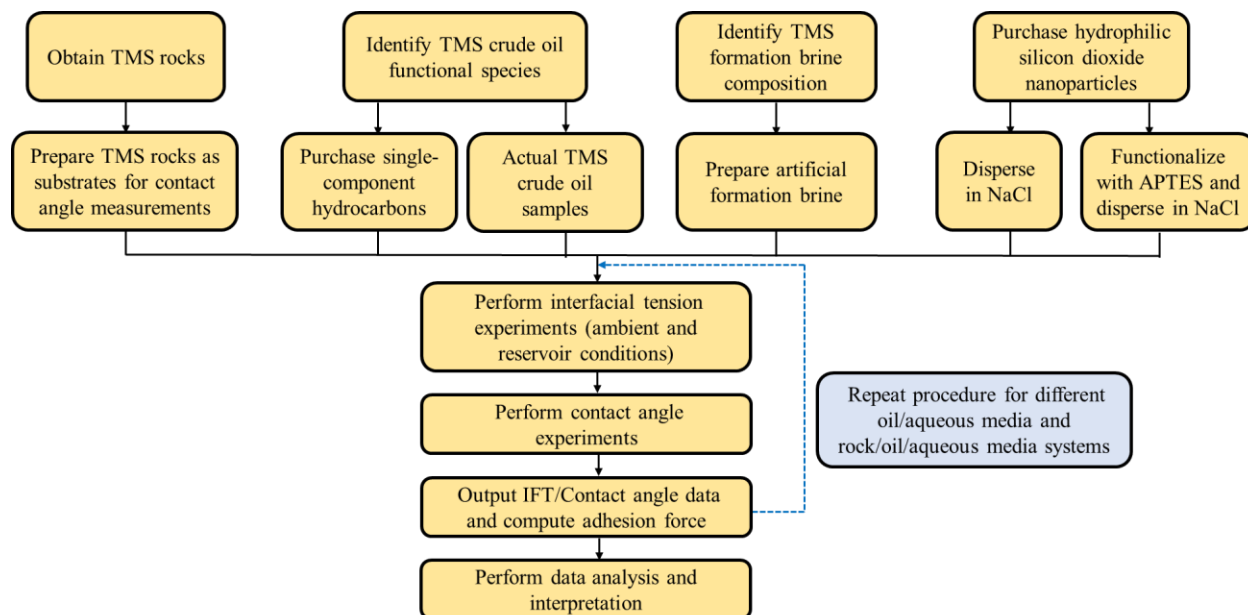
Figure 3.12. Flow chart highlighting the systematic nature of research – including materials used, preparation steps, experimental procedure and data analysis and interpretation.

3.3. Core-Scale Characterization of Nanofluid-assisted CO_2 EOR

3.3.1. Coreflood Experimental Setup

The coreflood system designed in this work as well as corresponding procedures followed were adopted from a water-alternating-gas EOR study conducted previously (Kulkarni and Rao, 2005), as presented in Figure 3.13. A 1 in diameter and 2 in length low-permeability TMS cylindrical piece of rock (or core) was cut from a larger core of 3 ft in length and 4 in diameter retrieved close to the TMS zone of interest, at a depth of interval of 15197.5' and 15200.84' TVD (see Figure 3.15a&b). The core has an effective porosity and matrix permeability of ~4% and 0.071 mD respectively. The original, dry weight of the 1" x 2" core was measured to be ~64.6g using a mass balance (Figure 3.15c). Due to the fissile nature of shale, the core was fixed tight in a heat shrinkage tube with two Berea sandstone cores placed at each end for pressure support, as shown in Figure 3.15. This approach was also adopted following a previous attempt to clean the cores which led to

73

complete disintegration upon cleaning in a Soxhlet extractor using a solvent mixture of methanol and ethylene glycol. Hence, the TMS core was used as received. The shrinkage tube (with cores) was then placed in the core holder and the system was subjected to a given confining pressure of 1500 psi using hydraulic oil and a hand pump. The coreholder was flooded with dead oil from TMS under a constant pressure of 1000 psi using Teledyne D-Series Isco Pump and room temperature. It took ~ 12 days of oil flooding for the upstream and downstream pressures to equilibrate to 1000 psi (see Figure 3.14), primarily due to low porosity and permeability of the rock. The pump was then shut off and the core was allowed to age in oil for an additional 30 days. CO_2 was injected at constant pressure of 1000 psi for 1 day.
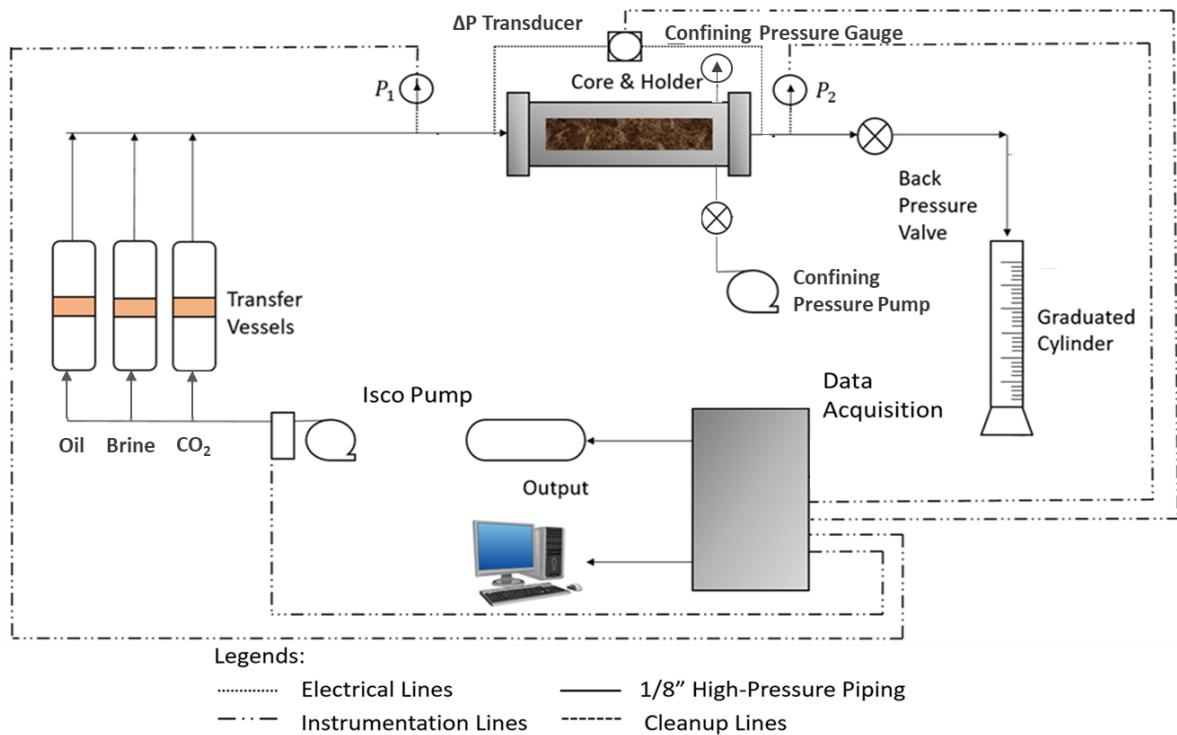
Figure 3.13. Laboratory coreflood design for core-scale EOR experiments conducted in this study (modified after Kulkarni and Rao (Kulkarni and Rao, 2005))
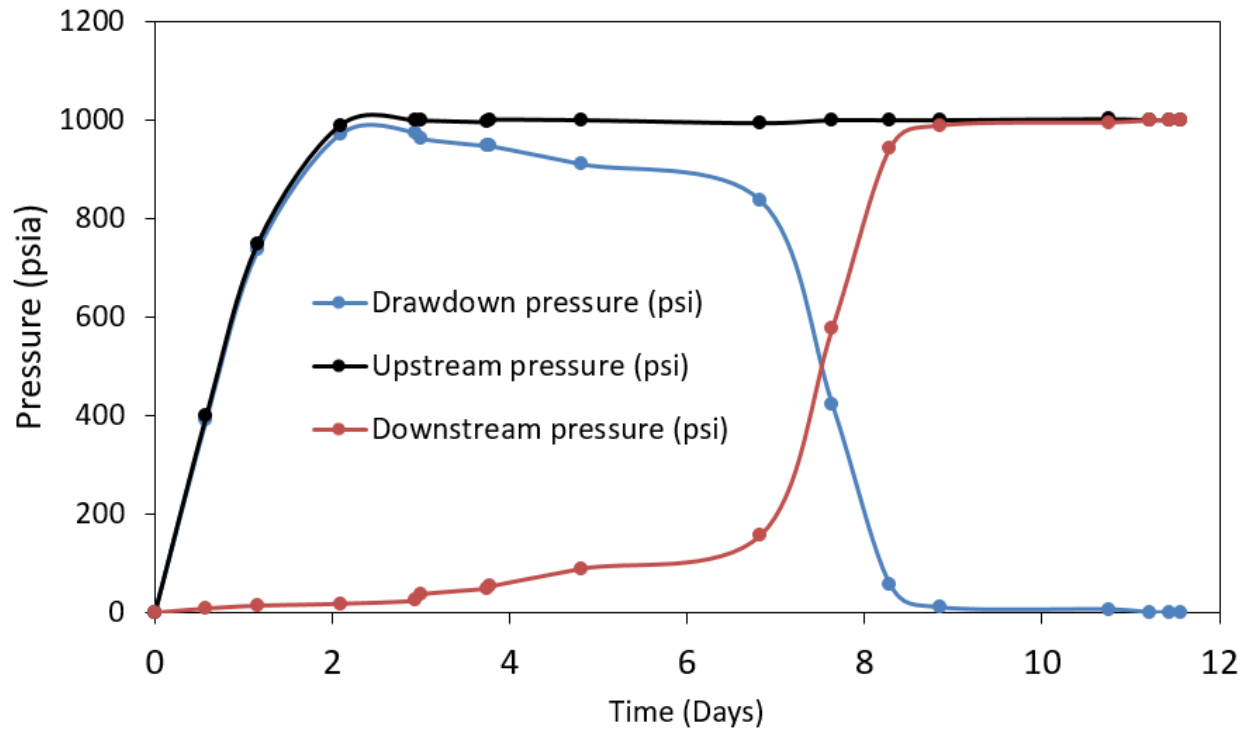
Figure 3.14 Upstream, downstream and drawdown pressure profiles obtained during the flooding of the low-permeability TMS rock with crude oil for CO_2 injection
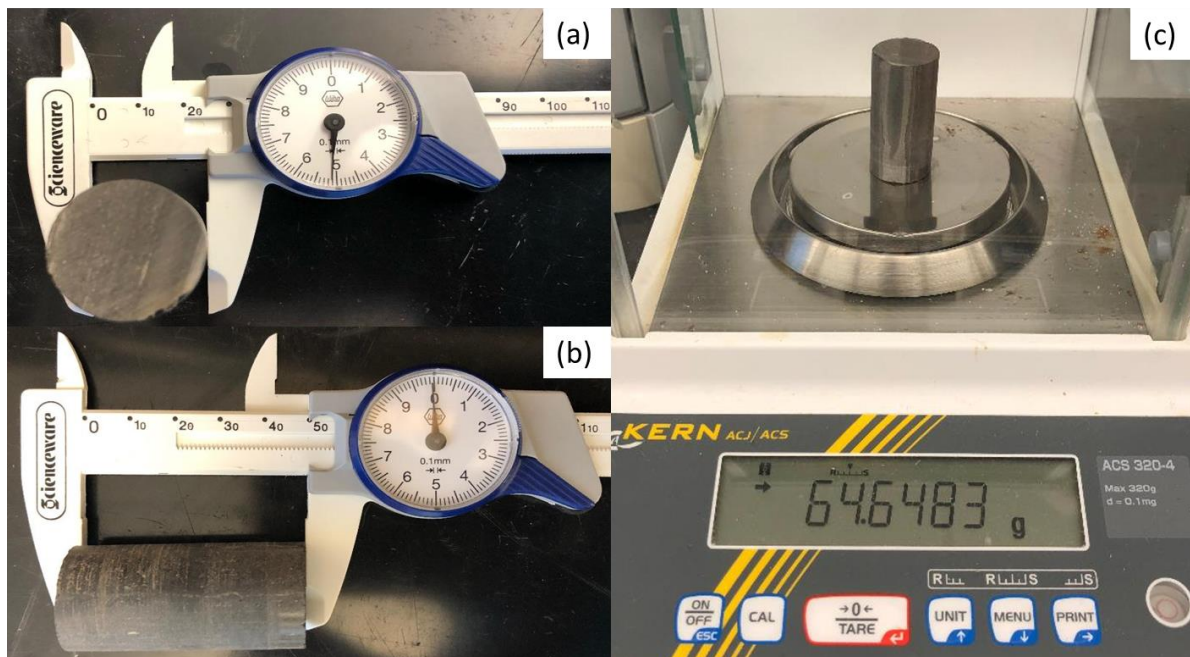
Figure 3.15. The diameter, length and weight of the TMS core used for CO_2 EOR injection experiment were measured to be: (a) 1 inch; (b) 2 inches; and (c)~64.6 g respectively

Figure 3.16. The TMS core was fixed tight in a heat shrinkage tube with two Berea sandstone cores placed at each end for pressure support

Next, the pressure profiles and flow rates were monitored over time. The recovery factor R_f was calculated by subtracting the final core weight (after injection) W_{final} from the initial weight of oil-saturated core (before injection) $W_{initial}$ and dividing by the difference between initial weight of oil-saturated core $W_{initial}$ and dry weight of core W_{dry}, i.e.

$$R_f = \frac{W_{final} - W_{initial}}{W_{initial} - W_{dry}}$$

3.1

3.3.2. Reservoir Fluid Characterization

Extensive reservoir fluid Pressure-Volume-Temperature (PVT) data (provided by Australis Oil) were analyzed and modeled using a compositional Equation-of-State tool known as Computer Modelling Group (CMG) WinProp package. Data from the following PVT tests were provided and used as input parameters for reservoir fluid characterization with CMG WinProp:

- Differential liberation (DL)

- Constant Composition Expansion (CCE)

- Reservoir fluid composition

- Flash expansion

- Separator Test

The reservoir initial pressure is 7497 psia, the reservoir temperature is 260°F and the saturation pressure is 1417 psia. The API gravity at 60°F is 38.4 and Gas-Oil Ratio is 610 scf/stb at or above saturation pressure, which implies that TMS is a black oil reservoir. Reservoir fluid characterization is important to properly model the compositional effects in TMS porous media multiphase flow and fluid/fluid interactions while modelling the core-scale potential of CO_2 EOR augmented with nanoparticle dispersions. Critical steps followed in CMG WinProp include: defining fluid composition, matching saturation pressure, EOS tuning using regression and lumping fluid into pseudo-components and predicting laboratory experiments such as DL and CCE. More details on the characterization process are found in the documentation package of CMG (version 2021).

3.3.3. Reservoir Rock Characterization

Well logging data and petrophysical properties – namely porosity and permeability – obtained from formation evaluation data were provided by Goodrich Petroleum & University of Louisiana Lafayette. From literature review (Hackley et al., 2020) and background information obtained from Goodrich & ULL, a formation interval called the high resistivity zone (HRZ) is the prolific part of the Tuscaloosa Marine Shale in terms of oil production and well deliverability. Thus, the HRZ in TMS is the focus of this study. A plot of absolute permeability versus porosity (K/Ø plot) for the entire well logging interval in Figure 3.17. The HRZ was delineated between from 15289.5' – 15467.5' TVD from well logs using the deep, medium and shallow resistivity logs as well as TOC (Figure 3.18). Using this depth information helped to identify the K/Ø profile for HRZ, as shown in Figure 3.17b. The petrophysical parameters in the zone of interest exhibits a good correlation,

with $R^2 = 0.8$, which limits the uncertainty in the reservoir quality of TMS. The K/Ø correlation is used as input variable in the J function.
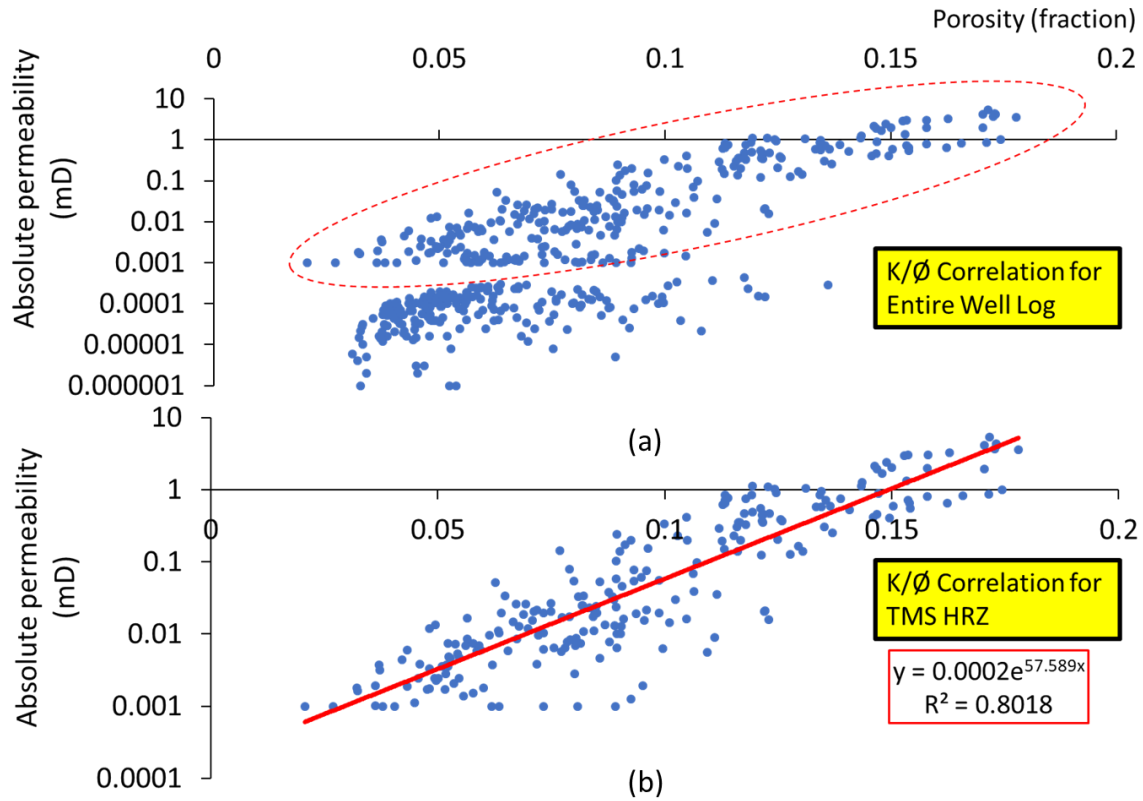
Figure 3.17. Permeability-porosity correlation obtained from the: (a) entire logged interval and (b) high resistivity zone (HRZ; also circled in top figure) in TMS. A correlation for TMS HRZ was obtained with $R^2 = 0.8018$

Analyses of bottom hole temperature profile as a function of depth revealed that the deviated or horizontal section of the well kicked off at ~15056 ft. The geothermal gradient obtained in the vertical section was 1.41°F/100ft.
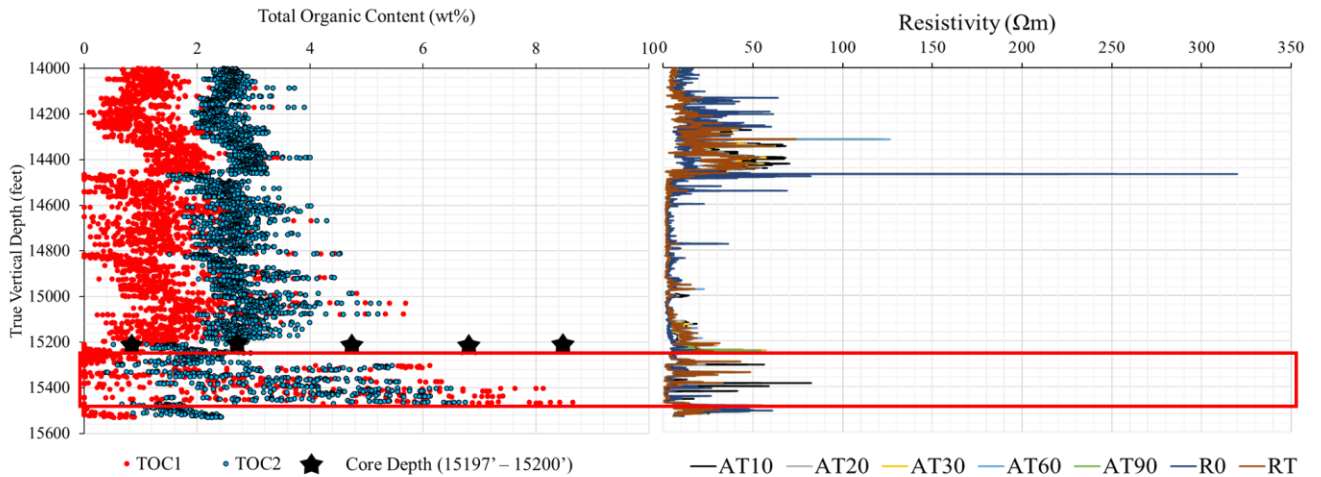
Figure 3.18. Logs of Total Organic Content (TOC) and formation resistivity in TMS were used to identify the high resistivity zone near the bottom of the well (boxed in red). The core samples used and analyzed in this study were obtained a few feet above the HRZ.

3.3.4.   Scaling: Capillary Pressure & Relative Permeability Modelling

3.3.4.1.   Capillary Pressure Modelling

As discussed in the literature review section, two of the most important parameters used to quantify the efficiency of an EOR process are relative permeability and capillary pressure. Capillary pressure curves are affected by rock pore size distribution, interfacial tension, contact angle and pore structure (Falode and Manuel, 2014; Ghazanfari M. H.   et al., 2006; Stimpson and Barrufet, 2017). A dimensionless scaling group called the Leverett J-function was used to account for these effects (Gonzalez et al., 2016b; Leverett, 1941) in the core-scale characterization of nanofluid-enhanced CO_2 EOR. The J-function is an important analytical tool used for interpolation of capillary pressure in a reservoir containing multiple immiscible phases. In this work, it was used to obtain capillary pressure curves for the TMS reservoir zone of interest (HRZ) based on available mercury/air injection pressure data on TMS HRZ characterized elsewhere (Lohr and Hackley, 2018). The petrophysical properties of the TMS HRZ cores used for mercury injection porosimetry

are displayed in Table 3.6 below and the resulting capillary pressure curves are shown in Figure

3.19.

Table 3.6. Properties of TMS HRZ cores obtained from petrophysical evaluations and mercury
injection porosimetry (Lohr and Hackley, 2018)

Sample ID	Porosity, Ø	Permeability, K (md)	Median pore throat (microns)	Pore radius (microns)	Air-Hg entry pressure (psi)
S20	0.0659	0.000168	0.00536	0.0334	3226
S21	0.0519	0.00011	0.00551	0.0334	3226
S22	0.0478	0.000059	0.004	0.0246	4380
S23	0.0578	0.000133	0.00548	0.0405	2660
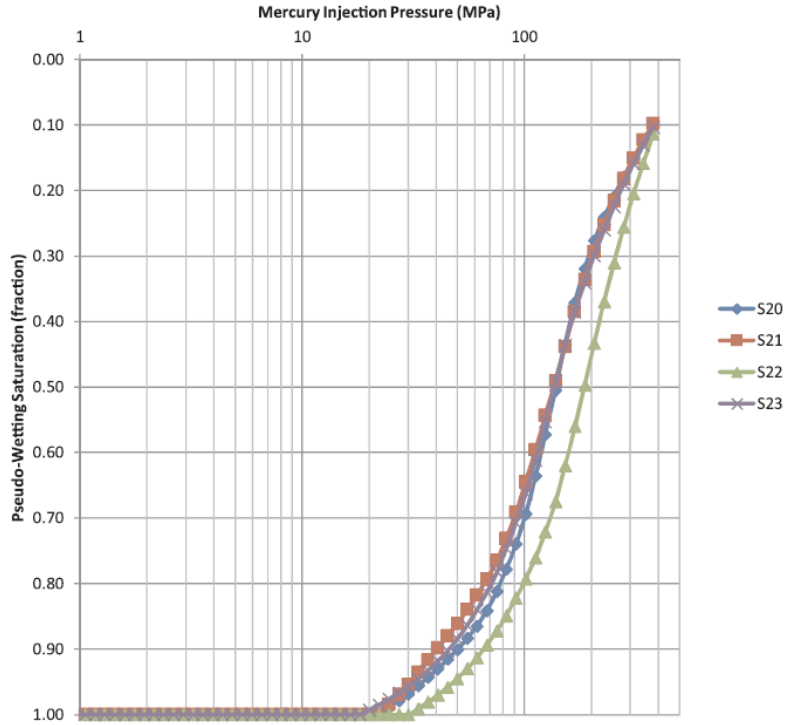
Figure 3.19. Tuscaloosa marine shale HRZ mercury-air capillary pressure curves obtained from core samples (Lohr and Hackley, 2018)

It has been established that a representative pore radius is directly proportional to the permeability/porosity ratio, which mathematically implies that:

$$R_{pore} \propto \frac{K_{abs}}{\emptyset} \qquad\qquad 3.2$$

Hence the J-function is given as (Gonzalez et al., 2016a; Leverett, 1941):

$$J[S_w] = \frac{P_c[S_w]}{\sigma \cos \theta} \left(\frac{K_{abs}}{\emptyset} \right)^{0.5} \qquad\qquad 3.3$$

Where Pc [S_w] = capillary pressure as a function of wetting phase saturation S_w (psia)

   K_{abs} = absolute permeability (mD)

   σ = interfacial tension (mN/m)

θ = water-advancing contact angle (°)

$\emptyset$ = porosity

The Hg-air capillary pressure can be rescaled to oil-water and gas-water capillary pressure using the following equations (Lohr and Hackley, 2018):

$$P_{c,o/w} = P_{c,Hg/air} \frac{(\sigma \cos \theta)_{o/w}}{(\sigma \cos \theta)_{Hg/air}} \qquad 3.4$$

$$P_{c,g/w} = P_{c,Hg/air} \frac{(\sigma \cos \theta)_{g/w}}{(\sigma \cos \theta)_{Hg/air}} \qquad 3.5$$

The oil-gas capillary pressure which is used for compositional simulation of CO_2 EOR is obtained by subtracting both equations (Chen, 2007) i.e.

$$P_{c,g/o} = P_{c,g/w} - P_{c,o/w} \qquad 3.6$$

The steps involved in obtaining capillary pressure curves are as follows:

a) Obtain air-H_g P_c [S_w] and K_{abs}/$\emptyset$ from Lohr and Hackley (2018)

b) Obtain $\sigma cos\theta$ from optical tensiometer and DDDC

c) Rescale air-H_g P_c [S_w] to oil-water, gas-water and oil-gas capillary pressures using equations 3.4-3.6.

d) Calculate J[S_w] from equation 3.3 using parameters from steps a-c

e) Obtain K_{abs}/$\emptyset$ using permeability-porosity correlation for TMS zone of interest

f) Re-compute the oil-water, gas-water and oil-gas capillary pressures using the J Function

3.3.4.2. Relative Permeability Modelling

The final capillary pressure profile obtained in the previous section can be used to derive relative permeability values since the latter is also a function of rock-fluid interactions and petrophysical properties (Haeri and Rao, 2019; Jahanbakhsh and Sohrabi, 2015; Kafili Kasmaei and Rao, 2015). The importance of coupling relative permeability and capillary pressure is greatly justified by the dominance of nanopores (1-100 nm) in shale oil reservoirs like TMS. The Young-Laplace equation shows how high the capillary pressure can be (in thousands of psi) when the pore radii are in the order of nm. Previous studies on core-scale potential of nanofluid EOR in conventional rock systems have neglected the impact of capillary pressure as well as effects of both contact angle and interfacial tension changes on relative permeability and capillary pressure. In unconventional rocks, these subject areas to the best of my understanding have not been studied in depth.

In this study, analytical relative permeability values were derived using the Purcell model (Purcell, 1949) which is recognized as of the most widely accepted models. In particular, it provides with a high-level accuracy fitting to experimental data of wetting-phase relative permeability when measured capillary pressure curves have the same residual oil saturation as relative permeability curve (Jahanbakhsh and Sohrabi, 2015; Li and Horne, 2006).

For a reservoir with a saturation range of $(1-S_{or})$ to $(1-S_{wi})$, the wetting- and non-wetting phase relative permeability values, namely K_{rw} and K_{rnw} can be determined as follows:

$$K_{rw} = \frac{\int_{S=0}^{S=S_{w'}} \frac{dS}{(P_c)^2}}{\int_{S=0}^{S=1} \frac{dS}{(P_c)^2}} \qquad 3.7$$

$$K_{rnw} = \frac{\int_{S=S_{w\prime}}^{S=1} \frac{dS}{(P_c)^2}}{\int_{S=0}^{S=1} \frac{dS}{(P_c)^2}} \qquad\qquad 3.8$$

The steps followed to derive these values are follows:

a. Obtain capillary pressure data P_c [S_w]

b. Plot the curve $1/P_c^2$ as a function of wetting phase saturation S_w

c. Find the area under the entire curve (denominator term in equations 3.7 and 3.8)

d. For a selected value of wetting phase saturation ($S_{w\prime}$, say), calculate the area under the $1/P_c^2$ curve from 0 to $S_{w\prime}$ (numerator term in equation 3.7). This gives the effective permeability to the wetting phase.

e. For the same value of wetting phase saturation ($S_{w\prime}$, say), calculate the area under the $1/P_c^2$ curve from $S_{w\prime}$ to 1 (numerator term in equation 3.8). This gives the effective permeability to the non-wetting phase.

f. Calculate the relative permeability of the rock to the wetting phase by dividing value obtained in step d by that obtained in step c (equation 3.7)

g. Calculate the relative permeability of the rock to the non-wetting phase by dividing value obtained in step e by that obtained in step c (equation 3.8)

3.3.4.3.   *Relative Permeability & Capillary Pressure Modelling Workflow*

The main steps used in deriving relative and capillary pressure using experimental data obtained from this study and elsewhere (Lohr and Hackley, 2018) coupled with Leverett J Function and Purcell Model are summarized in the workflow chart displayed in Figure 3.20.

Analyses of the permeability and porosity data along the TMS HRZ shows that this portion of the reservoir can be classified distinctly into two zones: tight matrix (<0.1 mD) and fractured

zone (≥ 0.1 mD), as seen in Figure 3.17b. The arithmetic average permeability and porosity for the

tight matrix portion are 0.02 mD and 0.08 respectively, while those of the fractured zone are 1 mD

and 0.13, respectively. Subsequently, capillary pressure and relative permeability curves for TMS

HRZ for the low and high permeability zones were obtained.
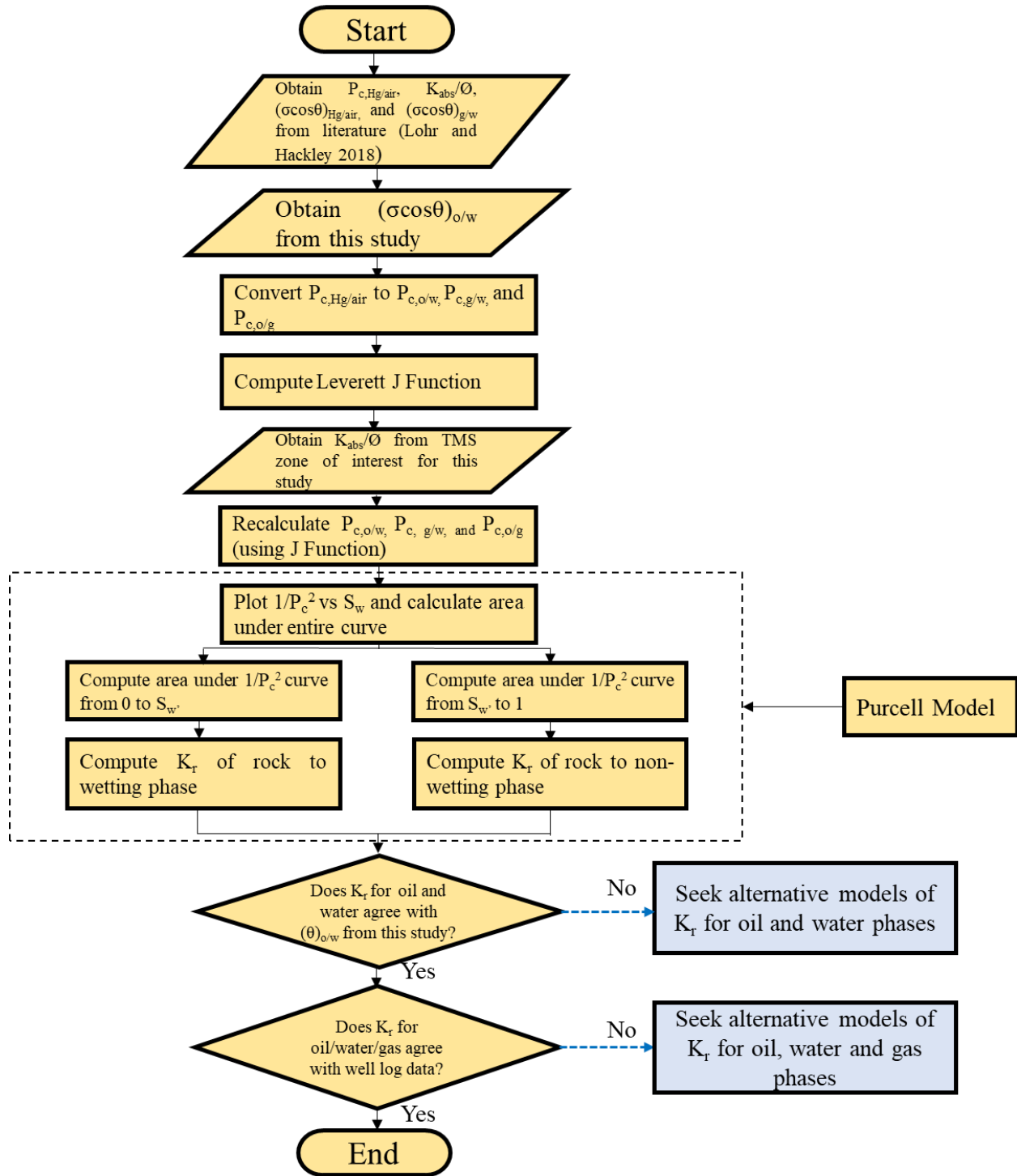
Figure 3.20. Workflow chart summarizing steps followed in computing relative and capillary pressure curves for matrix-dominated and fracture-dominated portions of TMS HRZ as a function of petrophysical parameters, contact angle and interfacial tension measurements

3.3.5. Model Building

The dimensions of the Cartesian grid adopted in CMG GEM for compositional simulation of CO_2 EOR and nanofluid-assisted CO_2 EOR were selected based on the dimensions of the TMS core used for high-pressure coreflood experiment, which was 2 in length x 1 in diameter. Subsequently, the grid dimensions are 0.167 ft (I direction) x 0.0739 ft (J direction) x 0.0739 ft (K direction).

Two models were built in CMG were developed: a low permeability system for CO_2 EOR study on the unfractured portion of the TMS HRZ and a high-permeability system as a representative elementary volume of the fractured region in TMS HRZ for nanofluid-assisted CO_2 EOR study. The main properties which served as input variables for both models are provided in Table 3.7. The relative permeability and capillary pressure curves for the in-situ fluids are specified as Region 1 under the rock/fluids tab while those of the injection fluids are in Region 2.

Table 3.7. Significant input variables used for compositional simulation of CO_2 EOR and nanofluid-assisted CO_2 EOR in CMG GEM

	Unfractured region of TMS HRZ	Naturally fractured region of TMS HRZ
Case Study	CO_2 EOR	Nanofluid-assisted CO_2 EOR
Porosity	0.04	0.13
Permeability (mD)	0.07	1
Reservoir depth (ft)	15200	15200
Oil-water contact (ft)	15300	15300
Initial reservoir pressure (psia)	1014.7	1014.7
Reservoir temperature ($^{\circ}$F)	260	260

Capillary pressure curves	This study	This study
Relative permeability curves	This study	This study
PVT properties	This study	This study
Number of grid blocks	15	15
Grid dimensions	0.167 ft x 0.0739 ft x 0.0739 ft	0.167 ft x 0.0739 ft x 0.0739 ft

The reference depth chosen was 15200 ft and oil-water contact assumed to be 15300 ft (since the entire core is in the oil zone). For CO_2 injection, the well injection pressure was set to 1000 psi and the duration of flow was set to a maximum of 7 days; in the lab, the injection pressure was held constant at 1000 psi and CO_2 EOR process lasted for 1 day. For nanofluid-assisted CO_2 injection, the well injection pressure for both injection phases was set to 1000 psi and the duration of flow was set to a maximum of 7 days each, making a total of 14 days of EOR injection. Hence, the Dirichlet boundary condition was set for the models since the pressure was prescribed as a function of location and time (Chen, 2007). The radii of both injector and producer wells were specified based on the size of each grid block.

With regards to the numerical parameters, most of the changes made were done to account for the small pressure, saturation and composition changes that are expected during a core flood simulation. All the parameters are an order of magnitude or two smaller than the default used by GEM. The maximum changes in simulation variables like pressure, saturation, composition are compared with the corresponding values for the normal variation per time step and the time step size is adjusted accordingly. I used large maximum changes per time step values to prevent time

step cuts on account of the changes in simulation variables exceeding the specified maximum value. The other parameters such as maximum newton iterations and threshold value improve numerical convergence. All of these parameters have been increased from the default to allow for more Newton and/or solver iterations that help with the convergence.

After the model was initialized, sensitivity analysis on the effect of grid coarsening and refinement was performed by conducting CO_2 EOR simulation with 3, 7, 15, 30, 60 and 120 grids. Figure 3.21 shows the changes in recovery factor with number of gridblocks. As shown, it appears that the optimum number of gridblocks is 15: using more grid blocks and less grid blocks both decreased recovery factor via CO_2 EOR in low-permeability TMS core. On this basis, 15 gridblocks were used for simulation, as seen in Figure 3.22.
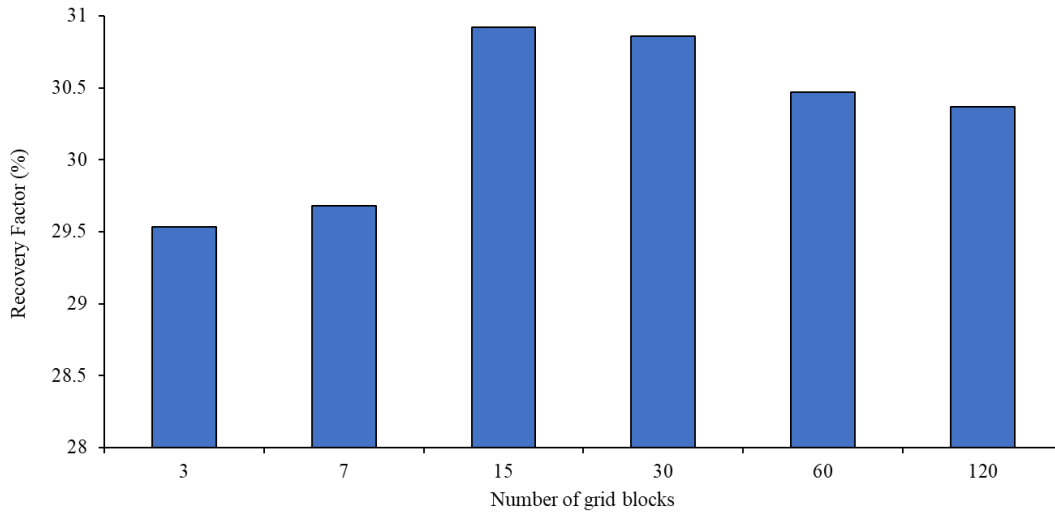
Figure 3.21. Effect of number of gridblocks on oil recovery factor CMG GEM during compositional simulation of CO_2 EOR in low-permeability TMS core
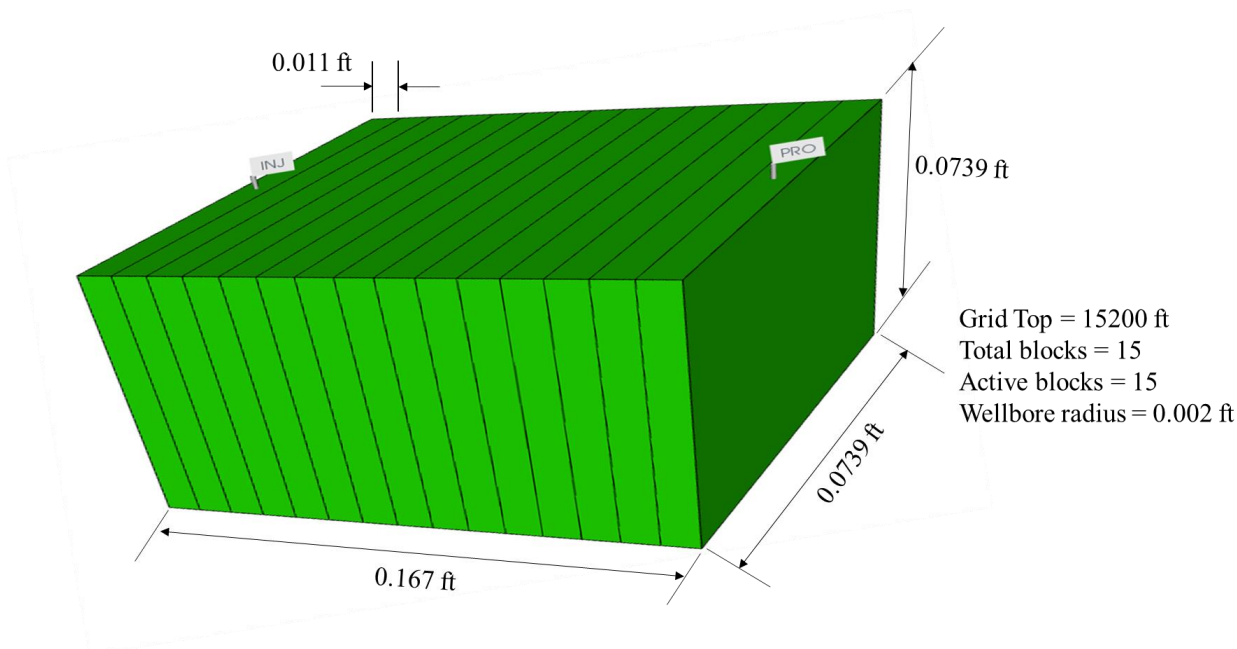
Figure 3.22. Cartesian grid used for TMS core-scale simulation in CMG GEM, with specific dimensions

3.4. Analytical Science & Surface Functionalization Procedures

This section describes the different analytical science tools used for material characterization and procedures followed in the surface functionalization of hydrophilic silica nanoparticles.

3.4.1. Zeta Potential Equipment

The zeta potential of the nanoparticle dispersions was measured to study the effect of surface chemistry and electrostatic interactions. To measure zeta potential, nanoparticle dispersions were

---

Section 3.4 was previously published as Afekare, D.A., Garno, J.C. and Rao, D.N., 2020c. Application of Force Spectroscopy to Evaluate Rock-Fluid Interactions at the Nanoscale, SPE/AAPG/SEG Unconventional Resources Technology Conference. Unconventional Resources Technology Conference, Virtual, pp. 20. Reprinted with permission from URTeC, whose permission is required for further use.

injected through a syringe into disposable capillary cells which was then placed in the Malvern Zetasizer Nano-ZS (Malvern Panalytical, Westborough, MA) equipment.

Before each experiment, the cells were rinsed with ultra-pure water twice. Nanofluid solutions containing 0, 0.05, 0.1, 0.5 and 1 wt% HNP (dispersed in 1 wt% NaCl) were tested. Three zeta potential measurements were performed on each sample, and all tests were at ambient conditions (25 ºC).

3.4.2. Scanning Electron Microscopy (SEM)

The Scanning Electron Microscope (SEM) was used in this study as a surface characterization technique to capture an image of the AFM tip and visualize the impact of nanoparticle adsorption on TMS rocks. For the visualization experiments, rock pieces were retrieved along bedding planes were trimmed into 0.5 cm x 0.5 cm which made it fit well onto the SEM mount. The original, unpolished samples were vacuumed for 10 minutes and then sputter-coated with platinum for 4 minutes to curb charging artifacts. Rock surfaces coated with hydrophilic (HNP) solutions were oven-dried for ~1 hr. at 51ºC. Using the Quanta 3D FEG Focused-Ion Beam (FIB) SEM available at Louisiana State University (LSU) Shared Instrumentation Facility (SIF), SEM images were obtained using 20 KV beam acceleration voltage and 3.3 pA probe current, at different magnifications: 20 000, 50 000, and 100 000 x.

3.4.3. X-Ray Diffraction (XRD) Analyses

The objective of XRD analyses was to identify the dominant minerals which, as shown in Figure 3.23, are clay minerals (43.9%) and quartz (43.3%), as shown in Table 3.8. The clay minerals identified are illite and kaolinite, and the mineralogical compositions are presented in Table 3.9. Rock chips from TMS cores (provided by Goodrich Petroleum and University of Louisiana) were crushed to powder for X-ray diffraction (XRD) study. All XRD results were obtained using

Malvern Panalytical High Score Plus V4.8 software, using the rietveld refinement technique. Other minerals such as calcite (5.4%), pyrite (3.1%), feldspars (2.6%) and anhydrite (1.7%) exist but appear to be in smaller amounts. This data was obtained from 3 different samples cored along the same section in the East Feliciana parish of the TMS formation where the cores were retrieved from, between 15197.95 ft and 15200.84 ft TVD (see Table 3.8). It is understood that there is significant mineralogical heterogeneity across TMS, as XRD data collected by several authors show (Borrok et al., 2019; Enomoto et al., 2018; Lu et al., 2011). Nonetheless, all referenced literature has identified the leading presence of clays and quartz in close to 100 wells in TMS.

Table 3.8. Mineralogical composition (in weight percentage) of TMS based on XRD data from three samples. N/D = not detected

Sample ID	Approximate Depth (ft TVD)	Clays (%)	Quartz (%)	Anhydrite (%)	Feldspars (%)	Calcite (%)	Pyrite (%)
TMS-1	15198.4	46.3	41.4	2.1	5.3	0.3	4.6
TMS-2	15199.4	45.4	39.8	1.0	N/D	10.4	3.3
TMS-3	15200.4	40.1	48.7	1.9	2.4	5.4	1.5

Table 3.9. Mineralogical composition (in weight percentage) of clays identified in TMS based on XRD data from three samples

Sample ID	Approximate Depth (ft TVD)	Illite (%)	Kaolinite (%)	Total percentage of clays in TMS (%)
TMS-1	15198.4	29.6	16.7	46.3
TMS-2	15199.4	25.4	20.0	45.4
TMS-3	15200.4	23.0	17.1	40.1
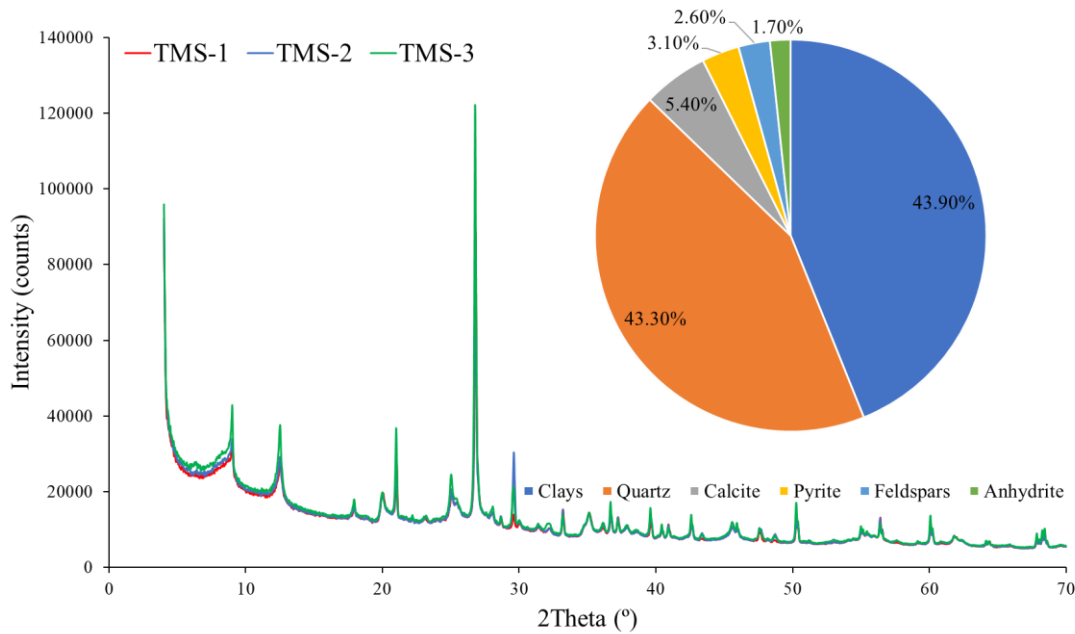
Figure 3.23. X-ray Diffraction Analyses of TMS rock samples. Pie chart on the right shows that the dominant minerals in the formation are clay minerals (43.9%) and quartz (43.3%). Other minerals identified are calcite (5.4%), pyrite (3.1%), feldspars (2.6%) and anhydrite (1.7%).

3.4.4. Silica Nanoparticle Silanization

Surface-modified, amino-treated nanoparticle (NNP) dispersions were prepared by functionalizing hydrophilic nanoparticles (HNP) with (3-Aminopropyl) triethoxysilane (APTES), following a widely accepted silanization procedure (Kneuer et al., 2000). In addition to HNP powder samples, materials used for this process include acetic acid (purchased from Sigma Aldrich), SnakeSkin™ Dialysis Tubing (10K MWCO, 35 mm; purchased from Sigma Aldrich), APTES (purchased from Sigma Aldrich). The following steps were taken in the functionalization process:

a. Mix 6g of HNP dry weight with 30g of water and 12 ml acetic acid

b. Heat mixture at 80°C for ~1 hr.: The mixture was heated using a Soxhlet extractor that was circulated with water to maintain constant temperature. A thermometer was used for temperature check every 10 mins.

c. Add ~0.8g of APTES and continue to heat for another 16 hrs, similar to step b.

d. Allow mixture to cool and pour into dialysis tubing.

e. Dialyze 5 times for a 24-hr period while rotating mixture at ~200 rpm at room conditions.

    To limit particle aggregation, a pH of ~4 was maintained during this timeframe using HCl.

After the steps were completed, the synthesis was confirmed by measuring zeta potential of 0.1 wt% NNP at pH of 2,4,6,8 and 10. An NNP solution concentration of 0.1 wt% was obtained by oven-heating the initial suspension to 150°C to obtain the original weight concentration of 0.48%, before dilution. Initial pH was also modified using 0.01M HCl and 0.1M NaOH for acid and base titration, respectively. The z-potential versus pH data obtained was then compared with Kneuer et al.'s (2000) results, as shown in Figure 3.24. As seen, the physiochemical behavior for NNP most closely resembles that of Si22E and Si10E which are amino-synthesized particles with 22 nm and 16 nm diameter, respectively. By interpolation (see Table 3.10), the isoelectric point (IEP) of NNP is 8.47 compared to 8.6 for Si22E and 8.1 for Si10E. Likewise, the z-potential of NNP at neutral pH (7.4) is 15.4 compared to 26 for Si22E and 17 for Si10E, which confirms the modification of surface charges via silanization.
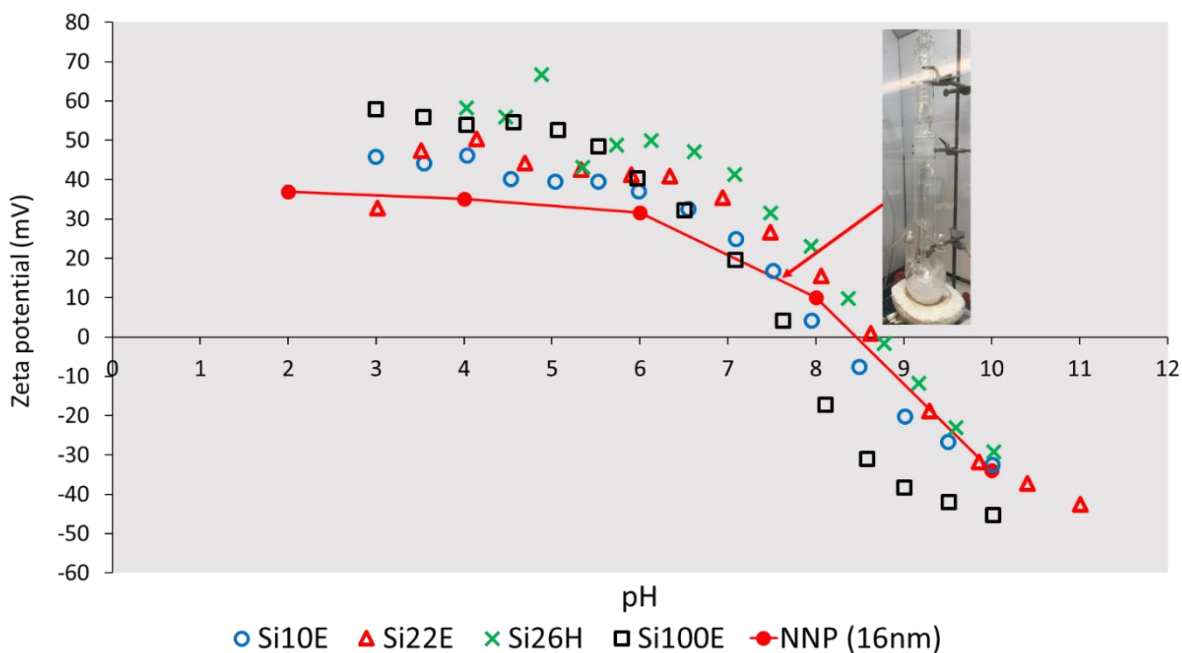
Figure 3.24. Zeta potential titration of synthesized nanoparticles in this study (scatter plot with red line and circular markers) in comparison with Kneuer et al.'s (2000) results

Table 3.10. Physicochemical parameters of synthesized particles obtained in this study compared to existing literature (Kneuer et al., 2000)

Particle	Diameter (nm)	IEP (pH)	Zeta potential at pH of 7.4 (mV)	Literature Source
NNP	16	8.47	15.4	This work
Si10E	10	8.1	17	(Kneuer et al., 2000)
Si22E	22	8.6	26	(Kneuer et al., 2000)
Si100E	100	7.7	7	(Kneuer et al., 2000)
Si26H	26	8.6	31	(Kneuer et al., 2000)

4. RESULTS AND DISCUSSION

4.1. Nanoscale Characterization of Nanofluid Enhanced Oil Recovery

4.1.1. Adhesion Force Characterization of Hydrophilic Silica-based Nanofluids

4.1.1.1. *Effect of Hydrophilic Silica-based Nanofluids on the Adhesion of Alkane (-CH₃), Aromatic (-C₆H₅) and Carboxylate (-COOH) Compounds to Mica*

Aqueous dispersions of silica nanoparticles can desorb molecules of non-polar alkane ($-CH_3$) and aromatic ($-C_6H_5$) compounds as well as polar carboxylic acid ($-COOH$) compounds from clay-rich rock surfaces (see Figure 4.1, Figure 4.2, and Figure 4.3). For the case of mica/$-CH_3$ group (Figure 4.3), mean adhesion force in synthetic TMS brine (AFB) and 1 wt% NaCl measured 400 pN and 442 pN respectively, from force maps. However, the adhesion force reduced to 84 pN with 0.05 wt% HNP, and successive increase in nanofluid concentration led to a reduction in surface energy, which signified further wettability improvement. The least adhesion force (29 pN) was attained with 0.5 wt% or 5000 ppm HNP, which represents a greater than 90% reduction compared to AFB. It appears, however, that there is an optimal silicon dioxide nanofluid concentration for wettability alteration such that a higher HNP concentration of 1 wt% HNP might actually lead to a rise in adhesion force and reverse wetting effects at the nanoscale. Nevertheless, decrease in adhesion force with increase in SiO_2 nanoparticle dispersions presents concrete, sub-pore scale evidence of nano-EOR potential in clay-rich reservoirs with predominantly alkane hydrocarbons.

Section 4.1.1 was previously published as Afekare, D., 2020. Enhancing Oil Recovery Using Aqueous Dispersions of Silicon Dioxide Nanoparticles: The Search for Nanoscale Wettability Alteration Mechanism, SPE Annual Technical Conference and Exhibition. Society of Petroleum Engineers, Virtual, pp. 19. Reprinted by permission of Society of Petroleum Engineers.

Figure 4.1. Adhesion force maps obtained over a 5 μm x 5 μm scan area of mica in the presence of –CH$_3$ compound and aqueous media such as brine and HNP solutions

In the case of during mica/-C$_6$H$_5$ experiments, the average adhesion force in AFB and 1wt% NaCl measured 544 pN and 735 pN respectively whereas adhesion force in 0.05 wt% HNP measured 99 pN – indicating a more than 80% decrease compared to AFB (Figure 4.2). Higher nanofluid concentrations decreased the adhesion force even further: the least adhesion force of 52 pN was measured in 0.5 wt% HNP which appeared to be the optimal concentration as it was in the case of mica/-CH$_3$ interactions. Adhesion force however increased from 52 pN to 75pN when switching from 0.5 wt% to 1 wt% HNP nanofluid media.

Figure 4.2. Adhesion force maps obtained over a 5 μm x 5μm scan area of mica in the presence of -C$_6$H$_5$ compound and aqueous media such as brine and HNP solutions

Carboxylate compounds typically found in resin and asphaltene fractions of crude oils such as those found in TMS are markedly surface-active. Thus, they tend to notably influence interfacial energies and respond to wettability effects via chemical EOR (Afekare and Radonjic, 2017; Andersen et al., 2016). The polarity of these organic compounds is reflected in high adhesion forces measured between –COOH "greased" AFM tip and mica substrate regardless of the

surrounding liquid media (see Figure 4.3). The adhesion force measured in TMS artificial brine AFB and 1wt% NaCl was 942 pN and 3279 pN respectively, which is about 5x the force attained in mica/$-C_6H_5$ system and 7x the adhesion force in mica/$-CH_3$ system at the same electrolyte conditions. Adhesion force decreased to 660 pN with 0.05 wt% HNP, however, suggesting that nanoscale wettability is shifted towards a less oil-wet state.

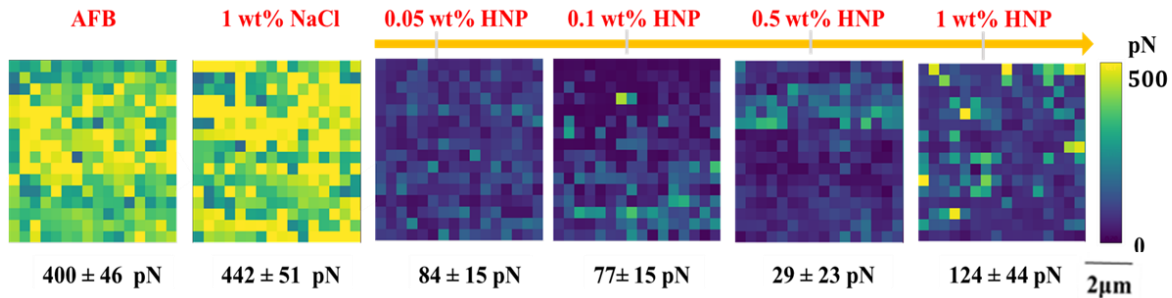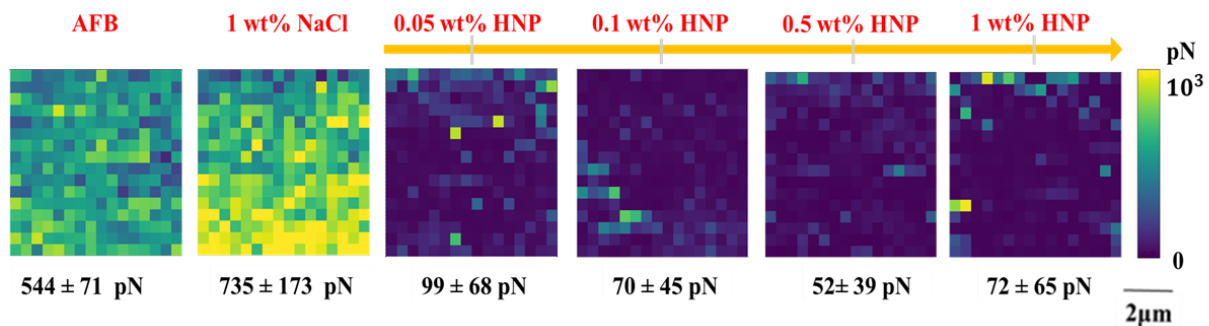
Figure 4.3. Adhesion force maps obtained over a 5 μm x 5μm scan area of mica in the presence of –COOH compound and aqueous media such as brine and HNP solutions

A further reduction in adhesion force was achieved with an increase in nanoparticle concentration, up until 1 wt% HNP which was the optimal concentration. Adhesion force decreased to 144 pN at this concentration – signifying nearly 90% reduction compared to AFB. It is worth stating that there was no increase in adhesion force between 0.5 wt% and 1 wt% HNP as observed in the experiments with non-polar alkane and aromatic compounds which suggests that crude oil composition affect the molecular dynamics of oil release and displacement via EOR using nanosilica dispersions. Even so, these studies reveal the latency of hydrophilic silica nanofluid EOR to recover adsorbed polar and non-polar crude oil molecules from clay-rich TMS formations.

4.1.1.2. Effect of Hydrophilic Silica-based Nanofluids on the Adhesion of Alkane (-CH₃), Aromatic (-C₆H₅) and Carboxylate (-COOH) Compounds to Quartz

Formation mineralogy poses an effect on flow through porous media and EOR in general (Afekare and Radonjic, 2017) but mineralogical heterogeneity effects on silica-based nanofluid EOR is not known to a great detail – let alone fundamental mechanistic insights. Force volume maps presented below show that hydrophilic SiO_2 nanoparticle dispersions can detach molecules of alkane,

aromatic and carboxylate compounds from quartz surfaces to drive nanoscale wettability improvement towards less oil-wet state, as observed on mica substrates. For the case of quartz/-CH_3 interactions (Figure 4.4), mean adhesion force in synthetic brine (AFB) and 1 wt% NaCl measured 425 pN and 244 pN respectively. However, the adhesion force reduced to 208 pN with 0.05 wt% HNP – signifying more than a 50% decrease compared to AFB. A successive increase in nanofluid concentration led to a corresponding reduction in surface energy, indicating further wettability improvement. The least adhesion force (119 pN) was attained with 0.1 wt% or 1000 ppm HNP, which represents a more than 70% reduction compared to AFB. It appears, however, that 0.1 wt% HNP is the optimal silicon dioxide nanofluid concentration because adhesion forces measured 442 pN and 213 pN at 0.5 wt% HNP and 1 wt% HNP. Nonetheless, a significant decrease in adhesion force observed with SiO_2 nanoparticle dispersions presents additional sub-pore scale evidence of its EOR potential in tight oil reservoirs containing predominantly quartz and saturated alkane hydrocarbons.
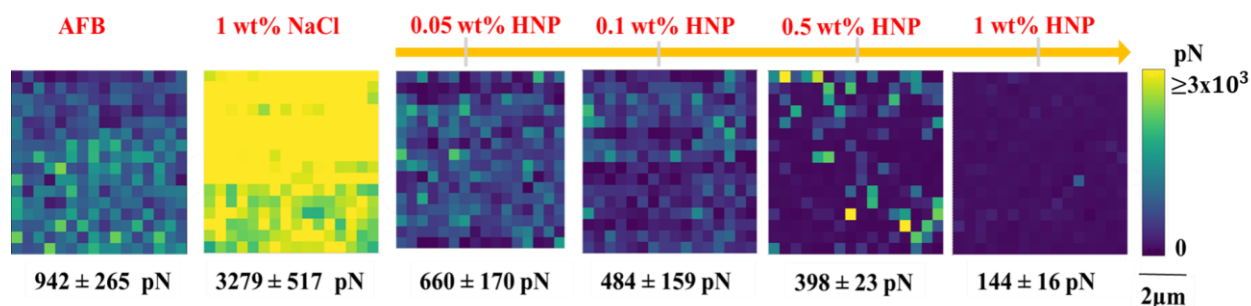

Figure 4.4. Adhesion force maps obtained over a 5 μm x 5 μm scan area of quartz in the presence of–CH_3 compound and aqueous media such as brine and HNP solutions

When quartz was contacted with –C_6H_5 tip, adhesion forces measured 2526 pN and 3858 pN in AFB and 1 wt% NaCl respectively (Figure 4.5). In 0.05 wt% HNP, adhesion force measured 1242 pN – decreasing by 50% compared to AFB brine. Higher concentration of silica nanoparticles led to greater decrease in adhesion: adhesion force measured 404 pN in 1wt% HNP (optimal concentration) which is more than 80% lower than in formation brine.

Figure 4.5. Adhesion force maps obtained over a 5 μm x 5 μm scan area of quartz in the presence of -C$_6$H$_5$ and aqueous media such as brine and HNP solutions

Carboxyl (-COOH) compounds appear to adhere strongly to quartz in brine but less in nanofluid solutions, as shown in Figure 4.6. Adhesion force measured ~26 nN in AFB which is 10x the force attained in quartz/-C$_6$H$_5$ system and 60x the adhesion force in quartz/-CH$_3$ system at the same electrolyte conditions. In 1 wt% NaCl, an adhesion force of ~4 nN was recorded – more than the force obtained in quartz/-C$_6$H$_5$ system and 15x the adhesion force in quartz/-CH$_3$ system. However, 0.05 wt% HNP yielded 644 pN – indicating 98% decrease compared to AFB and suggesting that nanoscale wettability is shifted towards a less oil-wet state. A further reduction in adhesion force was attained with an increase in nanoparticle concentration, up until 0.5 wt% HNP which was the optimal concentration. Adhesion force decreased to 242 pN at this concentration – signifying 99% reduction compared to AFB. As shown in Figure 4.6 also, there was a noticeable increase in adhesion force between 0.5 wt% and 1 wt% HNP, from 242 pN to 495 pN. This sheds more light on nanofluid as an EOR agent and suggests that both rock mineral and crude oil composition affect the molecular dynamics of the oil release and mobilization processes at nanoscale. Even so, these findings reveal the potential of silica nanofluid EOR to recover adsorbed polar and non-polar crude oil species from pore walls in tight rocks such as TMS containing primarily inorganic pores with quartz minerals.
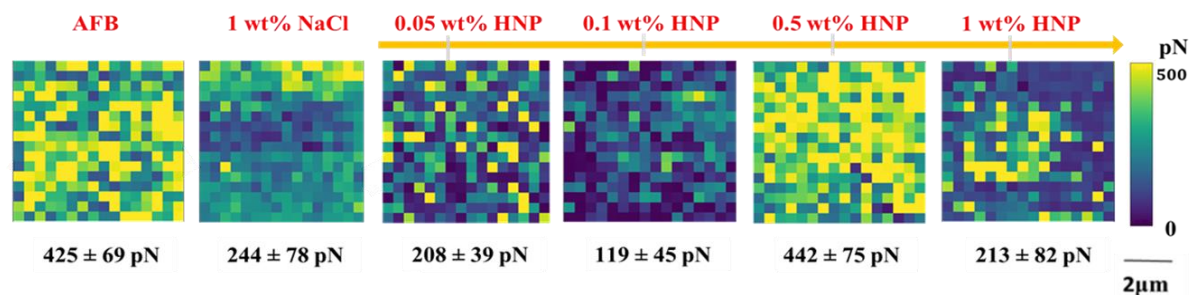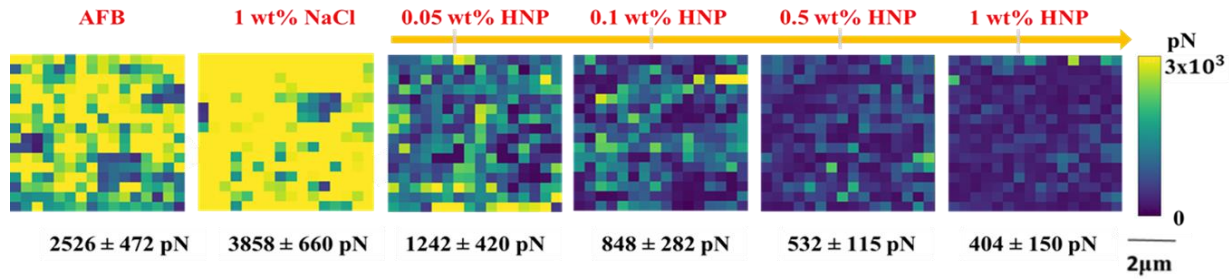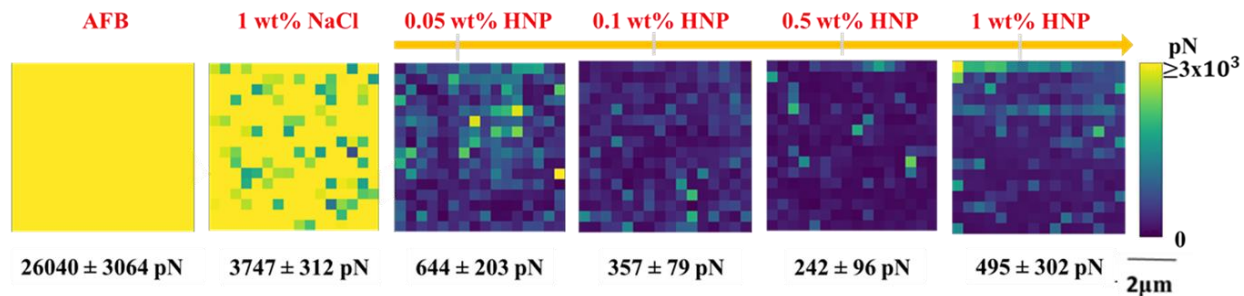
Figure 4.6. Adhesion force maps obtained over a 5 μm x 5 μm scan area of quartz in the presence of–COOH compound and aqueous media such as brine and HNP solutions

4.1.2.   Adsorption of Silica Nanoparticles and Nanoscale Wetting Effects

Adsorption of nanoparticles on the walls of pore bodies in petroleum reservoirs is fundamental to its wettability-altering performance but adsorption of nanosilica materials and impact on rock/fluid interactions is not well understood. If the nanoparticles do not adsorb or adsorb reversibly, there is a high tendency for surface wettability to return to an initially more oil-wet state as previously detached oil molecules may re-attach on pore surfaces during nanofluid injection, which may lead to an increase in oil saturation and poor recovery factor. Thus, the purpose of this study was to test for the reversibility of silicon dioxide nanoparticles by measuring adhesion forces in NaCl and AFB before and after HNP experiments. It is worthy of note that the mineral substrates were rinsed with copious rinses of De-ionized water after HNP treatments and before re-immersion in NaCl and AFB solutions. In such case, there are three different possibilities:

a.   The post-HNP adhesion forces are significantly lower than pre-HNP adhesion forces: This would indicate irreversible adsorption of the SiO_2 nanoparticles and also indicate that

---

Section 4.1.2 was previously published as Afekare, D., 2020. Enhancing Oil Recovery Using Aqueous Dispersions of Silicon Dioxide Nanoparticles: The Search for Nanoscale Wettability Alteration Mechanism, SPE Annual Technical Conference and Exhibition. Society of Petroleum Engineers, Virtual, pp. 19. Reprinted by permission of Society of Petroleum Engineers.

adsorption promotes adhesion force reduction and wettability change towards a less oil-wet (more hydrophilic) state.

b. The post-HNP adhesion forces are significantly higher than pre-HNP adhesion forces: This would indicate irreversible adsorption of the SiO_2 nanoparticles and also indicate that adsorption promotes adhesion force increase and wettability change towards a less water-wet (more hydrophobic) state.

c. The post-HNP adhesion forces are the same as pre-HNP adhesion forces: This would indicate reversible or non-adsorption of the SiO_2 nanoparticles.

The first possibility (point a) was proven, as shown in Figure 4.7. For mica interacting with $-CH_3$ tip, pre-HNP adhesion forces in AFB and 1 wt% NaCl were 400 pN and 442 pN respectively whereas post-HNP adhesion forces were 170 pN and 189 pN respectively- indicating more than 50% decrease (Figure 4.7a). For quartz contacted with $-CH_3$ tip, pre-HNP adhesion forces in AFB and 1 wt% NaCl were 426 pN and 244 pN respectively whereas post-HNP adhesion forces were 278 pN (35% decrease) and 120 pN (50% decrease) respectively (Figure 4.7b).
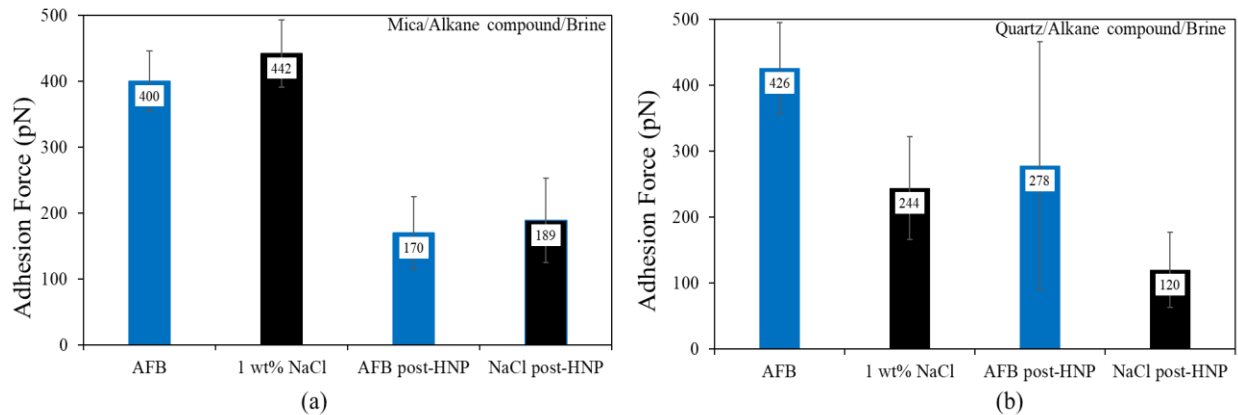

Figure 4.7. Adhesion force measurements obtained in AFB and 1 wt% NaCl before and after nanofluid treatments of (a) mica surfaces and (b) quartz surfaces in contact with alkane ($-CH_3$) compounds

These findings agree with a previous AFM imaging study on mica substrates at elevated temperatures (Afekare et al., 2020b) and SEM micrographs (see Appendix B) which showed that nanoparticles adsorb on quartz surfaces and illite clays (Afekare et al., 2020c). Column floods (Zhang et al., 2015) and adsorption tests (Abhishek et al., 2018) have also confirmed adsorption of nanoparticles on sandstones with clay sites.

4.1.3.   Effect of Nanoparticle Surface Modification with Aminosilanes on Adhesion Force

4.1.3.1.   Effect of Surface-modified Silica-based Nanofluids on the Adhesion of Alkane (-CH3), Aromatic (-C6H5) and Carboxylate (-COOH) Compounds to Mica

The objective of this study is to investigate the impact of silanization of hydrophilic silicon dioxide nanoparticles (HNP) on the adhesion force measured using force spectroscopy. As stated in the methodology section, the nanoparticles were functionalized with APTES to yield corresponding amino-treated nanoparticle dispersions (NNP). The impact of $-NH_2$ group on the wettability performance of SiO_2 nanoparticles has been studied in oil-treated Berea sandstones at the micron-to-core scales but little is known about nanoscale wettability alteration effects – especially in pure mineral systems interacting with crude oil chemical species. In this work, AFM adhesion force data obtained with NNP at 0.1 wt% was compared with results obtained with HNP at 0.1 wt% and 0.5 wt% at the same pH of 6. The pH value was chosen as the reservoir pH in TMS based on geochemistry data was observed to be between 6 and 6.8. Only one type of NNP concentration was considered due to the partial solubility of the modified nanoparticles in NaCl. Figure 4.8 shows force maps with mean adhesion forces recorded when mica was contacted with $-CH_3$ compound, in the presence of HNP and NNP solutions. In the case of mica contacted with $-CH_3$ group, it can be seen that switching from 0.1 wt% HNP to 0.5 wt% HNP (both at pH of 6) slightly decreased adhesion force from 110 to 94 pN, whereas switching to 0.1 wt% NNP increased adhesion force

significantly. Adhesion force in NNP solution is more than 2x force measured in HNP solutions at 0.1 wt% and 0.5 wt%.
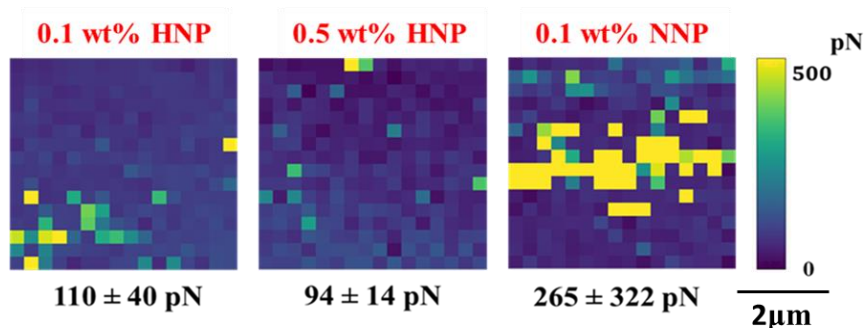
Figure 4.8. Adhesion force maps obtained over a 5 μm x 5 μm scan area of mica in the presence of (a) –CH$_3$ compound, HNP and NNP solutions at a pH of 6

Similarly, for a mica/C$_6$H$_5$ system, an increase in HNP concentration led to a modest reduction in adhesion force (52 pN to 49 pN) whereas switching to 0.1 wt% NNP increased adhesion force to 200 pN:~4x adhesion force recorded in HNP solutions (Figure 4.9).

Figure 4.9. Adhesion force maps obtained over a 5 μm x 5μm scan area of mica in the presence of -C$_6$H$_5$ compound, HNP and NNP solutions at a pH of 6

In the case of mica contacted with surface-active carboxylate (COOH) compounds, adhesion force reduced from 251 pN to 63 pN when switching from 0.1 wt% HNP to 0.5 wt% HNP whereas switching to 0.1 wt% NNP led to an increase in adhesion force to 500 pN, 2x the force measured in 0.1 wt% HNP and nearly 8x the force recorded in 0.5 wt% HNP (Figure 4.10).
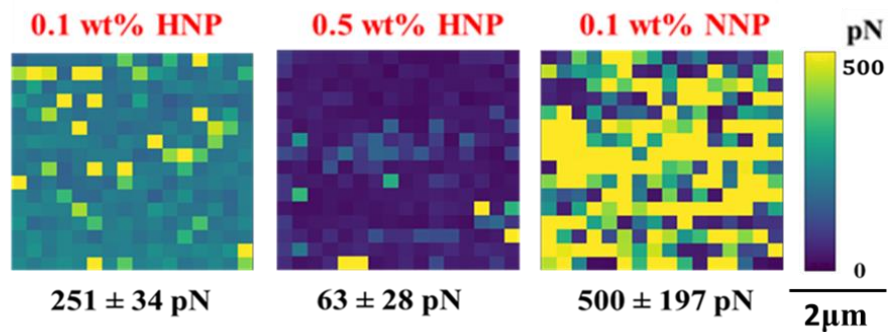
Figure 4.10. Adhesion force maps obtained over a 5 μm x 5μm scan area of mica in the presence of –COOH compound, HNP and NNP solutions at a pH of 6

The increase in surface energies due to silanization of silica nanoparticles can be due to particle surface charge and hydrophobicity of amino group being grafted onto the SiO_2 particle surface. First, the zeta potential of 0.1 wt% NNP measured 12.23 mV, which implies a net positive surface charge. In comparison, the zeta potential of 0.1 wt% HNP and 0.5 wt% HNP measured – 18.75 mV and – 28.1 mV respectively. As a result, adsorption of the NNP particles on mica will steer the mineral substrate towards a less negatively charged state and compress the electrical double layer in the presence of negatively charged functional groups such as carboxylic acid (COOH-) compounds. Second, the presence of NH_2- functionalized silica nanomaterials will render the mica surface more hydrophobic which has the potential to also increase adhesion force when mica is contacted with different crude oil chemical species with hydrophobic groups such as $–CH_3$, $-C_6H_5$ and –COOH compounds.

4.1.3.2.   Effect of Surface-modified Silica-based Nanofluids on the Adhesion of Alkane (-CH_3), Aromatic (-C_6H_5) and Carboxylate (-COOH) Compounds to Quartz

The effect of surface treatment of silica nanoparticles with aminosilanes is consistent for the functional groups tested on muscovite mica in a pH-controlled environment, but the same cannot be said for quartz surfaces. The figures below show force maps with mean adhesion forces recorded when quartz was contacted with $–CH_3$, $-C_6H_5$, and –COOH compounds respectively, in the presence of HNP and NNP solutions. When quartz was contacted with $–CH_3$ group, switching

from 0.1 wt% HNP to 0.5 wt% HNP (both at pH of 6) slightly decreased adhesion force from 840

to 757 pN on average, whereas switching to 0.1 wt% NNP increased adhesion force significantly

to 1033 pN (Figure 4.11).
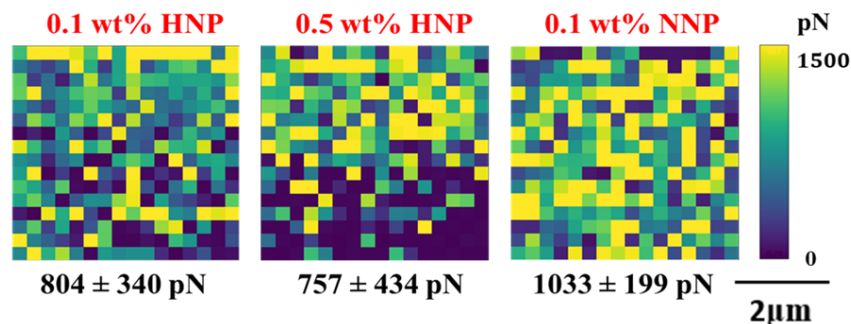
Figure 4.11. Adhesion force maps obtained over a 5 μm x 5μm scan area of quartz in the presence of –CH_3 compound, HNP and NNP solutions at a pH of 6

However, for a quartz/C_6H_5 system, an increase in HNP concentration from 0.1 wt% to 0.5

wt% led to an increase in adhesion force, from 173 pN to 208 pN (possibly due to precipitation

effects) whereas switching to 0.1 wt% NNP decreased adhesion force to 71 pN:~0.3-0.4x adhesion

force recorded in HNP solutions (Figure 4.12).

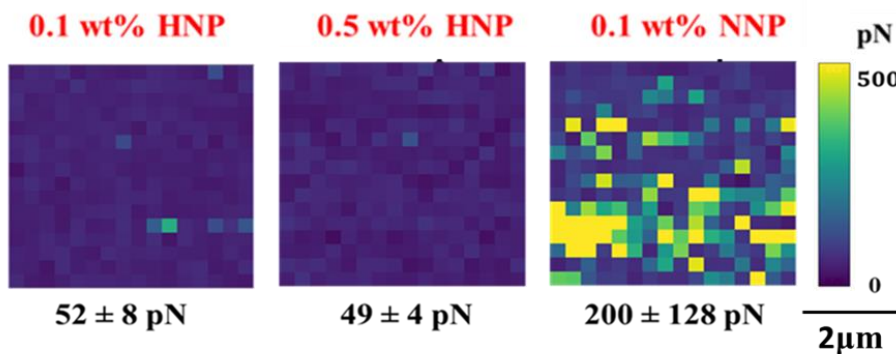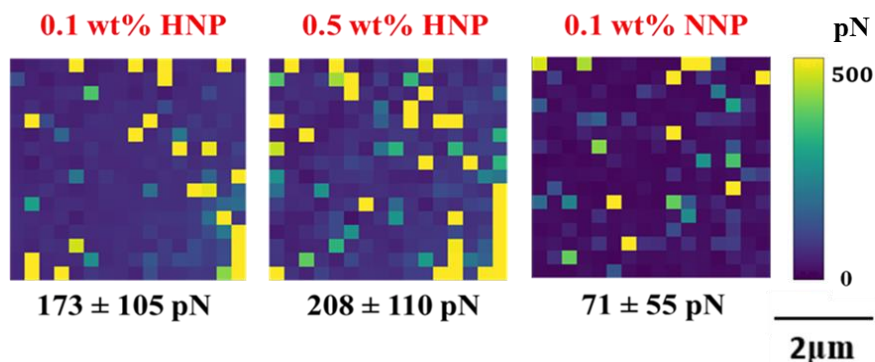Figure 4.12. Adhesion force maps obtained over a 5 μm x 5μm scan area of quartz in the presence of –C_6H_5 compound, HNP and NNP solutions at a pH of 6

In the case of quartz contacted with surface-active carboxylate (COOH) compounds, there

were no notable changes in adhesion force when switching from 0.1 wt% HNP to 0.5 wt% HNP,

whereas switching to 0.1 wt% NNP led to a modest decrease in adhesion force to 58 pN (Figure

4.13). These trends contrast with those of mica/functional group interactions and although the

underlying mechanisms are not known to great detail, it highlights the potential influence of petroleum reservoir mineralogical composition on wettability effects of NH_2-modified silica nanoparticles.
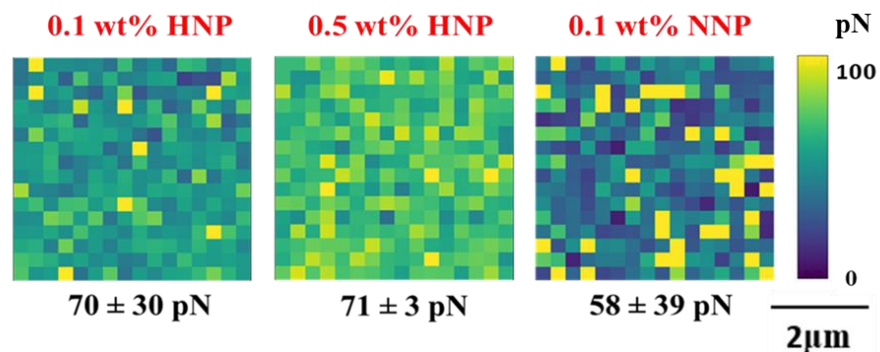
Figure 4.13. Adhesion force maps obtained over a 5 μm x 5μm scan area of quartz in the presence of –COOH compound, HNP and NNP solutions at a pH of 6

4.1.4. Correlation between Adhesion Force, Work of Adhesion and Wettability

The peak adhesion force characterized throughout this study is the point of maximum deflection from the zero base line on the retract portion of the force curve generated under chemical force spectroscopy using AFM (Chandrasekhar and Mohanty, 2018). For a functionalized tip in contact with a mineral substrate (substitute for a rock surface) immersed in a liquid medium, the integral area between the approach and retract portions of the force curve is known as work of adhesion (Afekare et al., 2020b) (see Figure D. 1 in Appendix D). In the context of crude oil/rock/brine (or nanofluid) interactions, this property – also referred to as adhesion energy - is defined as the energy required to separate the oil/rock interface, forming new oil/brine (or nanofluid) interface and brine (or nanofluid)/rock interface (Zhang, 2013). Hypothetically speaking, the swept regions of TMS rocks containing 100% oil will see a gradual reduction in oil saturation (shift toward more water-

Section 4.1.4 was previously published as Afekare, D., Garno, J. and Rao, D., 2020a. Insights into Nanoscale Wettability Effects of Low Salinity and Nanofluid Enhanced Oil Recovery Techniques. Energies, 13(17). Reprinted by permission of Energies MDPI.

wet state) while regions containing a mixture of oil and connate brine (possibly mixed-wet) may observe an increase in the rock relative permeability to oil and also decrease in residual oil saturation.

Injecting dispersions of silicon dioxide nanoparticles into the reservoir can penetrate oil/rock interfaces by forming a wedge film (Bennetzen and Mogensen, 2014; Chengara et al., 2004; Haeri and Rao, 2019). By doing so, fluids containing nanoparticles will advance over the area previously occupied by the oil phase, reducing the work of adhesion to gradually change the system to a less oil-wet state. Since the aim of this study is to simulate rock/oil/brine and rock/oil/nanofluid systems using mineral substrate/functionalized tip/brine and mineral substrate/functionalized tip/nanofluid models respectively, it can be said that the work of adhesion obtained from AFM will give an indication of the wetting effects of nanofluid EOR, in addition to adhesion force measurements. It has been established from modelling and experimental efforts that both properties are directly related. Two of the most popular models on adhesion mechanics were developed by Johnson, Kendall and Roberts (JKR) (Johnson et al., 1971) and by Derjaguin, Muller and Toporov (DMT) (Derjaguin et al., 1975). In terms of percentage changes in adhesion energy, these models were compared with an AFM-derived mathematical expression; elaborate details on derivations of formulae are available in APPENDIX D and a summary of models used is presented in Table 4.1. As shown, the input parameters for all the equations are: adhesion force, spring constant, tip radius, nanoparticle radius and characterization constant. The adhesion force was measured throughout the study and the tip was calibrated using "thermal K" feature of the Keysight AFM force spectroscopy module to obtain the spring constant of 0.08 N/m. The spring constant determined by the manufacturer was also 0.08 N/m. An SEM image of the AFM probe was captured to measure the tip radius of 28 nm (Figure D.2 in Appendix D) and a transmission

electron microscope (TEM) image of the silica nanoparticles was captured to obtain a radius of 8

nm (Figure 3.1). The characterization constant α_{adh} is a function of the substrate material and

mechanical properties (Afekare et al., 2020a; Derjaguin et al., 1975; Johnson et al., 1971). Note

that it is the percentage change that is more meaningful to discuss rather than absolute values since

the DMT and JKR models do not consider exactly the same parameters for calculating W_{adh} as did

this study (see Table 4.1).

Table 4.1. Summary of models used in calculating work of adhesion

Models used	Required Parameters	Source of Parameters	Unit	References
$W_{adh} = \dfrac{F_{adh}^2}{2k_s}$	Adhesion force, F_{adh}	This study	Joule	(Afekare et al., 2020a; Butt et al., 2005)
	Spring constant, k_s	This study; tip manufacturer		
$W_{DMT} = \dfrac{F_{adh} \cdot R}{\alpha_{adh}}$ $R = \dfrac{R_{tip} \cdot R_{NP}}{R_{tip} + R_{NP}}$	Adhesion force, F_{adh}	This study	Joule	(Derjaguin et al., 1975)
	Tip radius, R_{tip}	This study (see Figure D.2)		
	Nanoparticle radius, R_{NP}	This study (see Figure 3.1)		
	Characterization constant, α_{adh}	$\alpha_{adh} = 2$ from Derjaguin and co-authors' work (Derjaguin et al., 1975)		
$W_{JKR} = \dfrac{F_{adh} \cdot R}{\alpha_{adh}}$ $R = \dfrac{R_{tip} \cdot R_{NP}}{R_{tip} + R_{NP}}$	Adhesion force, F_{adh}	This study	Joule	(Johnson et al., 1971)
	Tip radius, R_{tip}	This study (see Figure D.2)		
	Nanoparticle radius, R_{NP}	This study (see Figure 3.1)		
	Characterization constant, α_{adh}	$\alpha_{adh} = 1.5$ from Johnson and co-authors' work (Johnson et al., 1971)		

For the case of hydrophilic silica nanoparticle dispersions (HNP), the maximum decrease in W_{adh} was calculated as a percentage decrease in adhesion energy when switching from synthetic formation brine AFB to the optimal HNP concentration. Note that AFB is the reference fluid and not necessarily the liquid media that yields the highest adhesion, since, in real-life applications, the EOR potential of nanofluids is typically demonstrated by comparing its performance with that of injected formation brine. For tests involving solutions of functionalized nanoparticles NNP, the change in adhesion energy due to surface modification was calculated as a percentage change when switching from 0.1 wt% HNP to 0.1 wt% NNP at a pH of 6.

The adhesion energy obtained in brine media (AFB and I wt% NaCl) when mica and quartz substrates are contacted with $-CH_3$, $-C_6H_5$ and $-COOH$ species were in the order of 10^{-18}J (aJ) to 10^{-15}J (fJ) whereas W_{adh} obtained in nanofluid media were typically less than 10 aJ and down to 10^{-3}aJ (Figure 4.14). The interaction between molecules of alkane compound ($-CH_3$) and mica in AFB requires a pull-off energy of 1 aJ, whereas switching to 0.5 wt% HNP (optimum concentration) depressed W_{adh} to 5.3 x 10^{-3}aJ, equivalent to a 99% maximum reduction. In comparison with JKR and DMT models, the maximum decrease obtained was 98% (Figure 4.14a). A nanofluid concentration of 0.5 wt% HNP also decreased the work of adhesion by 99% when compared to AFB – from 1.9aJ to 1.7 x 10^{-2}aJ - when mica was contacted with an aromatic (C_6H_5) tip. This agrees excellently well with JKR and DMT models which both predicted 98% maximum decrease (Figure 4.14b). When mica was contacted with -COOH group, adhesion energy was generally higher than with alkane and aromatic groups, but the effect of silica nanoparticles was still as considerable. Nanofluids at 1 wt% concentration (optimum) decreased W_{adh} from 5.5aJ (in AFB) to 0.1aJ. This signifies a 98% maximum reduction, which is also in excellent agreement with DMT and JKR forecasts of 97% (Figure 4.14c).
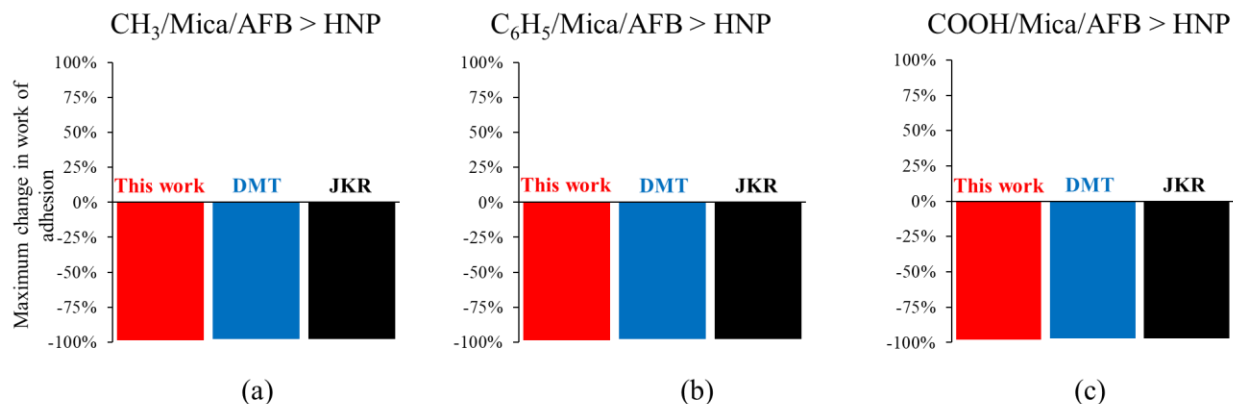
Figure 4.14. Maximum percentage decrease in work of adhesion (W_{adh}) between: (a) -CH$_3$ and mica; (b) -C$_6$H$_5$ and mica; and (c) -COOH and mica obtained herein and based on DMT and JKR models when switching from TMS formation brine (AFB) to hydrophilic SiO$_2$ nanofluids (HNP) at optimal concentration.

The interaction between molecules of alkane compound (-CH$_3$) and quartz in AFB requires a work of adhesion of 1.1aJ, whereas switching to 0.1 wt% HNP (optimum concentration) decreased W_{adh} to 8.9 x 10^{-2} aJ, signifying a 92% maximum reduction (see Figure 4.15). In comparison with JKR and DMT models, the maximum decrease obtained was 94% (Figure 4.15a). A nanofluid concentration of 1 wt% HNP also decreased the work of adhesion by 98% when compared to AFB – from 40 aJ to 1 aJ - when quartz was contacted with an aromatic (C$_6$H$_5$) tip. This agrees well with JKR and DMT models which predicted 97% (Figure 4.15b). When quartz was brought into contact with –COOH group, adhesion energy was again generally higher than with alkane and aromatic groups. Nanofluids at 0.5 wt% HNP concentration (optimum) decreased W_{adh} from 4.2 fJ (in formation brine AFB) to 0.4 aJ, signifying a ~100% reduction which is also in excellent agreement with DMT and JKR forecasts of 100% (Figure 4.15c).
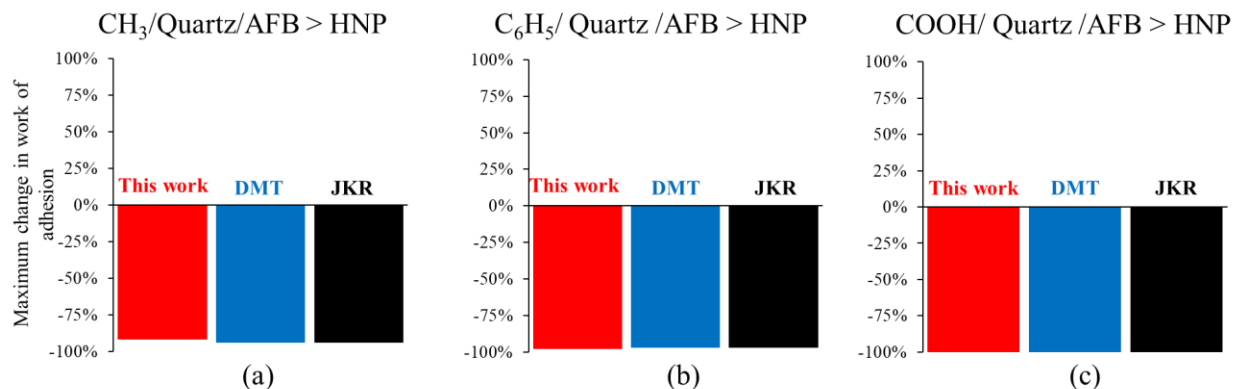
Figure 4.15. Maximum percentage decrease in work of adhesion (W_{adh}) between: (a) -CH$_3$ and quartz; (b) -C$_6$H$_5$ and quartz; and (c) -COOH and quartz obtained herein and based on DMT and JKR models

At a pH of 6, the grafting of aminosilanes onto the surfaces of SiO$_2$ nanoparticles increased the adhesion energy between mica and -CH$_3$ by 480%, when comparing 0.1 wt% HNP (7.6 x 10^{-2} aJ) and 0.1 wt% NNP (0.4 aJ) (see Figure 4.16a). In comparison, the JKR and DMT models forecasted a 181% increase in surface energies due to nanoparticle silanization. The W_{adh} for NNP dispersions was calculated using DMT and JKR equations by accounting for a 1 nm-thick coating of aminosilanes on SiO$_2$ nanoparticles; note that our AFM-derived expression does not require the thickness of APTES, as shown in Table 4.1. For the case of mica in contact with -C$_6$H$_5$ group, adhesion energy again increased by about 1379% when switching from HNP (1.7 x 10^{-2} aJ) to NNP (0.3 aJ) at 0.1 wt% and pH of 6, compared with the 349% increase predicted by DMT and JKR models (see Figure 4.16b). Similarly, the silanization of silica nanoparticles increased the adhesion energy between mica and -COOH group by 297% - from 0.4 aJ with 0.1 wt% HNP to 1.6 aJ with 0.1 wt% NNP at a pH of 6 (see Figure 4.16c). In comparison, DMT and JKR model predicted a 132% increase in adhesion energy.
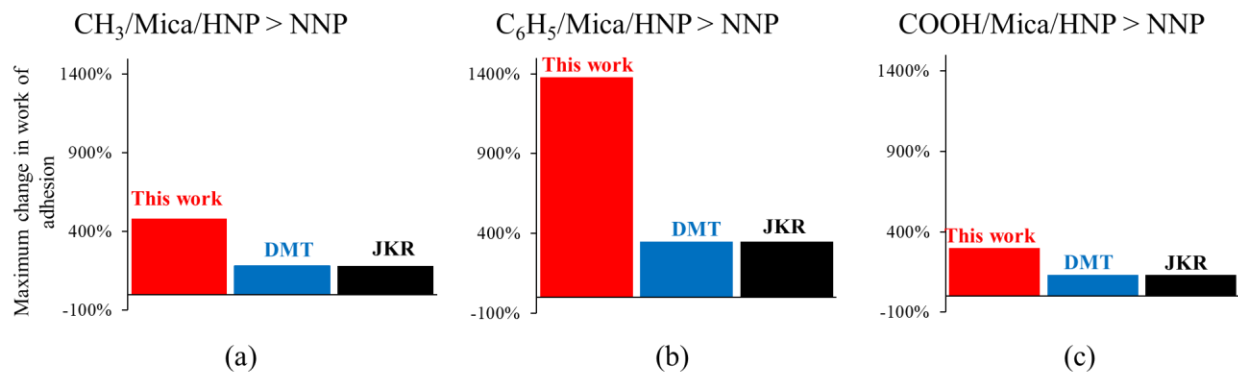
Figure 4.16. Percentage change in work of adhesion (W_{adh}) due to silanization of silica nanoparticles between: (a) -CH_3 and mica; (b) -C_6H_5 and mica; and (c) -COOH and mica obtained herein and based on DMT and JKR models

The inconsistent trend observed for the effect of silica nanoparticle surface functionalization on adhesion forces measured on quartz substrates in contact with functional species is also expressed in changes in work of adhesion (see Figure 4.17). At a pH of 6, the grafting of aminosilanes onto the surfaces of SiO_2 nanoparticles increased the adhesion energy between quartz and -CH_3 by 65%, when comparing 0.1 wt% HNP (4 aJ) and 0.1 wt% NNP (7 aJ) (see Figure 4.17a). In comparison, DMT and JKR models forecasted a 50% increase. However, for the case of quartz in contact with -C_6H_5 group, adhesion energy decreased by 83% when switching from HNP (0.2 aJ) to NNP (3 x10^{-2} aJ) at 0.1 wt% and pH of 6, compared with the 52% decrease predicted by DMT and JKR models (Figure 4.17b). Likewise, the silanization of silica nanoparticles decreased the adhesion energy between quartz and -COOH group by 31%, from 3 x10^{-2} aJ with 0.1 wt% HNP to 2 x10^{-2} aJ with 0.1 wt% NNP at a pH of 6 (Figure 4.17c). In comparison, DMT and JKR model predicted only a 3% decrease in adhesion energy.
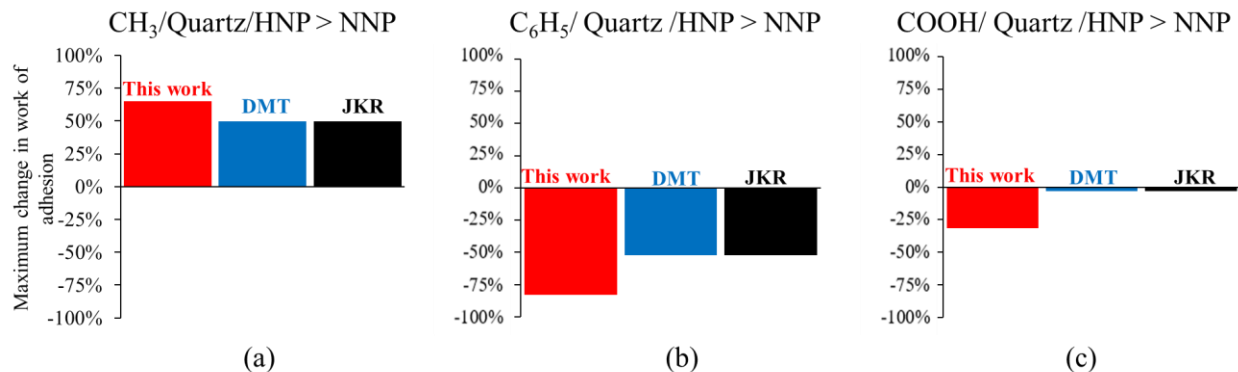
Figure 4.17. Percentage change in work of adhesion (W_{adh}) due to silanization of silica nanoparticles between: (a) -CH$_3$ and quartz; (b) -C$_6$H$_5$ and quartz; and (c) -COOH and quartz obtained herein and based on DMT and JKR models

4.1.5.   Discussions

New insights into the wettability alteration mechanisms of nanofluid EOR at the nanoscale are presented, with concrete scientific evidence in the context of adhesion force and energy. It was shown that hydrophilic silicon dioxide nanoparticles dispersed in salt solutions (NaCl) significantly reduce the adhesion of both charged (COOH) and uncharged (CH$_3$ and C$_6$H$_5$) functional groups to quartz and mica. In all experiments involving unmodified silica nanoparticles, it can be reasonably inferred that an optimal concentration of 0.5 wt% (or 1×10^{15} particles/ml) was found; in certain cases, such as mica/CH$_3$/HNP, mica/C$_6$H$_5$/HNP and quartz/COOH/HNP, increasing nanofluid concentration from 0.5 wt% to 1 wt% HNP increased adhesion force. It was also demonstrated that the grafting to aminosilanes onto the nanoparticles to create a net positive surface charge increased adhesion force of CH$_3$, C$_6$H$_5$ and COOH terminated tips to mica; however, results obtained with quartz substrates were inconsistent. The irreversible adsorption of silica nanoparticles was also observed. In this section, the scientific significance and broad engineering implications of these findings are discussed.

114

The silica nanomaterials used have a radius of 8 nm and a high surface area of 185 m^2/g which means they have sufficiently high surface "free" energies. As the number of nanoparticles in solution increases, the surface energy increases. There is also an energy that arises from the interaction of pure mineral substrates (quartz and clays) and chemical functional groups (CH_3, C_6H_5 and COOH) – known as adhesion energy (or work of adhesion). This property constitutes an energy barrier which must be surmounted to disrupt the interfaces between the mineral surfaces and functional groups, synonymous to rock/oil interfaces. This study, therefore, showed that, due to their surface energies, silica nanoparticles can significantly reduce the adhesion energy barrier for the spontaneous release of crude oil molecules from clay- and quartz-rich rock surfaces. As previously discussed, the adhesion force and energy reductions correspond to the creation of disjoining pressure which aids the development of wetting films of nanofluid dispersions to liberate crude oil species from mineral surfaces (Afekare et al., 2020a). In comparison with TMS brine (AFB), dispersions of hydrophilic silica nanoparticles at optimal concentrations (HNP) decreased adhesion force and energy by 90% and 99% respectively on average when mica substrates were contacted with -CH_3, -C_6H_5 and –COOH terminated tips. Regarding experiments on quartz, HNP at optimal levels also decreased adhesion force and energy by 85% and 97% respectively on average.

The zone of interest in Tuscaloosa Marine Shale for which these silica nanomaterials are being studied as potential EOR reagents is populated with interconnected natural fractures. These fractures contain the oil in place, with about 44% of illite clays and 43% quartz, and which may imply that much of the in-situ hydrocarbons are contained in inorganic pores. As a result, in probing chemical interactions between functional groups and quartz/clay minerals, this study

demonstrates the latency of silica nanoparticles to improve oil production from the inorganic pores in TMS.

The adhesion force measured using the AFM is a resultant of different intermolecular contributions: Van der Waals force F_{vdW}, non-electrostatic adhesion F_{nel}, electrostatic repulsion F_{el} and structural forces F_{str} which may be identified from the approach and retract portions of the force-displacement curves (Afekare et al., 2020a; Afekare et al., 2020b; Heinz and Hoh, 1999). The latter three force components F_{nel}, F_{el} and F_{str} are affected by silica nanoparticles while Van der Waal forces which typically apply to all discrete bodies are insensitive to aqueous chemistry (Afekare et al., 2020a). Figure 4.18 displays a few representative examples of the thousands of force-displacement (F-z) curves obtained, for brevity. Meaningful discussions on surface and intermolecular forces can be made using these graphs and the actual force-distance curves (Figure 4.18d) may be used to calculate these forces (Afekare et al., 2020a; Lorenz et al., 2017).
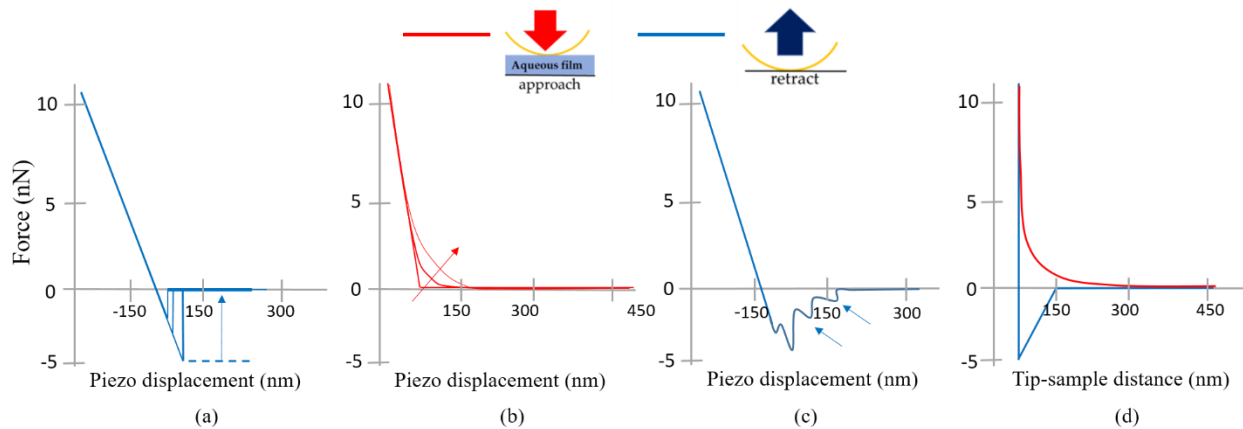
Figure 4.18. Examples of force curves obtained. The force-displacement curves show: (a) non-electrostatic adhesion (blue arrow line); (b) increase in electrostatic repulsion (pointed by red arrow line); (c) structural forces; and (d) the true force-distance curve.

The surface energy of the SiO_2 nanoparticles is directly related to their chemical potential: an increase in the nanoparticle concentration follows an increase in chemical potential gradient at the rock/fluid interface and a subsequent decrease in the non-electrostatic component of the adhesion force, shown in Figure 4.18a. The engineering implication is that silica-based nanofluids

can recover uncharged crude oil molecules like alkane and aromatic compounds from TMS shale rocks. The electrostatic component as observed in Figure 4.18b can be more closely studied by examining the zeta potential of the nanoparticles themselves, as a function of concentration (see Figure 4.19). The isoelectric point of mica and quartz are between 2 and 3, which means that surfaces of these minerals will be positively charged if immersed in solutions of pH < 3 and negatively charged at pH > 3. Considering the pH and zeta potential of nanofluid solutions used, the latter will certainly apply: the zeta potential of HNP solutions ranges from -23 mV to -26 mV with a pH range of 7.5 to 8.5, respectively. It is worthwhile to state that the high salinity of the nanoparticles' dispersant, being 1 wt% NaCl, has a notable impact on the electrophoretic mobility involved in the zeta potential measurements. As shown in Figure 4.19a, the zeta potential increased to the negative with increase in pH and nanofluid concentration which means that silica nanoparticles will therefore promote electrostatic repulsion by coating the substrates and creating sufficient negative surface charges (due to the presence of silanol groups) to repel and dislodge similarly charged molecules such as carboxylic acids (COOH). In a more practical sense, it indicates that silica nanomaterials can improve recovery of shale rocks containing inorganic pores saturated with polar crude oil fractions such as carboxylate compounds. However, as these particles become exceedingly large in number (2×10^{15} particles per ml or 1 wt% HNP), they tend to be confined, ordering themselves in discrete layers and giving rise to a non- Derjaguin, Van der wey, Landeau and Overbeek (DLVO) force known as structural interactions (Figure 4.18c). In this confined state, the interparticle interactions may significantly increase at the expense of particle-surface interactions which may lead to increase in adhesion force at very high concentrations as observed in certain results obtained: mica/CH_3, mica/C_6H_5, and quartz/COOH systems. Yet, previous research suggested that structural interactions are not well understood (Israelachvili,

117

2009) as it was observed to favor the spreading of nanofluids in the context of EOR elsewhere (Wasan et al., 2011). Another possibility is the dependence of structural forces of nanoparticles on length scale. Interparticle interactions at the micron- scales and beyond may favor the formation of "wedges" at the interface between bulk oil droplets and rock surfaces which can promote wettability improvement and adhesion force reduction. However, at the nanoscale, the enhanced interactions of nanoparticles at very high concentrations coupled with the thickness of the particle layers approaching and exceeding that of the organic species may lead to a sudden increase in adhesion force. These may add to the complexity of structural interactions in the context of surface energies, which Wu and colleagues previously reported (Wu et al., 2017).
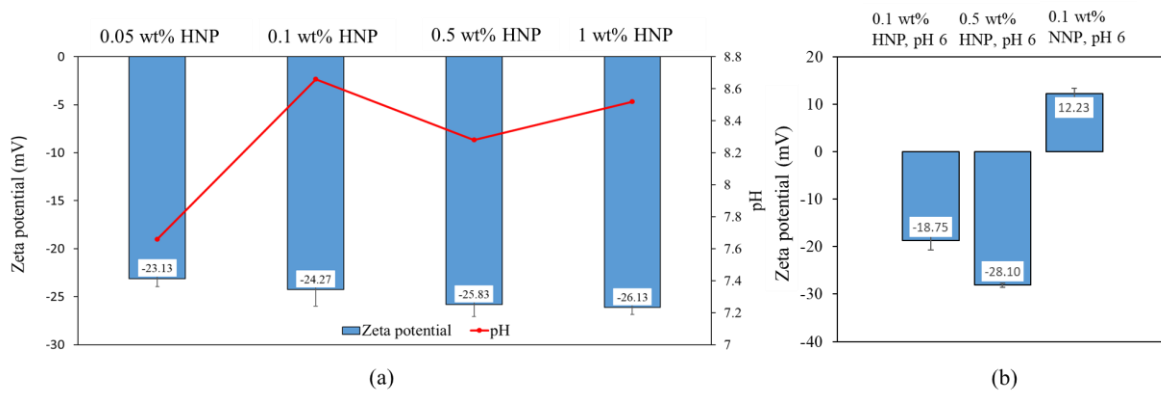
Figure 4.19. Zeta potential measurements of silicon dioxide nanoparticle dispersions: (a) Z-potential of HNP solutions as a function of hydrophilic silica nanoparticle concentration (wt %) and pH; and (b) Z-potential of HNP and NNP solutions at selected concentrations and pH of 6.

The impact of 3-aminopropyltriethoxysilane (APTES)-modified silica nanoparticles on enhancing oil recovery have been studied in the past and conflicting results have ensued, at micron-to-core scales (Alvarez-Berrios et al., 2018; Ngouangna et al., 2020; Ogolo et al., 2012). In addition, the nanoscale effects remain to be seen. For instance, Alvarez and colleagues (Alvarez-Berrios et al., 2018) showed that APTES-modified silica nanoparticles (dispersed in ethanol) reduced the contact angle on aged Berea sandstone core from 106° using brine (oil-wet state) to 97°(intermediate-wet) whereas negatively charged silica NPs (also dispersed in ethanol) shifted

the contact angle from 106° to 69°, signifying wettability alteration from oil- to water-wet state. Ngouangna and co-authors (Ngouangna et al., 2020) compared the oil recovery performance of unmodified and APTES-modified NPs and observed insignificant changes in contact angle, modest IFT changes but significant improvements in core-scale oil recovery. In their work, they observed a change in the surface wettability of an oil-wet sandstone core through a decrease in contact angle from 135° using brine to 54.5° and 54.3° with bare and APTES-modified silica nanoparticle dispersions, respectively. Interfacial tension reduced from 17 mN/m to 5 mN/m and 3 mN/m with bare silica nanoparticles and APTES-modified nanoparticles respectively. However, forced imbibition experiments showed that bare silica nanoparticle dispersions recovered 69.6% of oil in place compared to 62.9% obtained with waterflood, whereas APTES-modified silica nanodispersions yielded 75% recovery.

In furtherance to these reported works, we investigated the nanoscopic effect of APTES coating of silica nanoparticles on adhesion of specific crude oil functional groups such as $-CH_3$, $-C_6H_5$ and $-COOH$ - on surfaces of specific geological minerals such as quartz and clays (replicated using mica). Results showed that, in comparison with unmodified silica nanoparticles (HNP), dispersions of NH_2-modified nanoparticles (NNP) at 0.1 wt% and pH of 6 increased adhesion force and energy by hundreds to thousands of percentages when mica was contacted with CH_3, C_6H_5 and COOH functional species. Regarding experiments on quartz, NNP increased adhesion force and energy compared to HNP for a quartz/CH_3 system but decreased adhesion force and energy for quartz/C_6H_5 and quartz/COOH systems. The amine group from APTES becomes protonated at pH 6, giving rise to positive charges on nanosilica surface as evidenced by the z-potential measurements shown in Figure 4.19b. The z-potential of 0.1 wt% NNP measured 12.23 mV whereas z-potential of 0.1 wt% HNP and 0.5 wt% HNP measured -18.75 mV and -28.1 mV

119

respectively. As a result, there will be a compression of the electric double layer formed between negatively charged functional groups such as COO- and NNP-coated surfaces, which will significantly increase the adhesion force. This statement is bolstered by the result obtained with mica, but not quartz, which could be because the latter tends to be more hydrophobic than the former. The rationale behind the increase in adhesion of uncharged organic groups such as CH_3 and C_6H_5 can be explained in the context of nanoparticle aggregation (see Figure B. 1 in Appendix B) and structural forces. The presence of NH_2 coating screens the charges between silica nanoparticles and promotes aggregation on clays, which in turn causes the multi-layer, self-assembly of these particles. The self-assembly of the particles in confinement may give rise to structural interactions.

A cross-examination of the hundreds of force curves obtained during mica/CH_3/NNP and mica/C_6H_5/NNP experiments identified structural forces (as in Figure 4.18c) which was not observed in similar experiments conducted on quartz since it appears that these particles do not particularly aggregate on quartz, as seen in Figure B. 1. These may explain the contrasting results obtained with NNP solutions when quartz was contacted with functional groups.

Results of force spectroscopy experiments indicated that hydrophilic silica nanoparticles adsorb irreversibly on mica and quartz surfaces, and the broad implication can be discussed in the context of previously conducted forced imbibition experiments. Similar to the AFM experiments we conducted, one way to test the impact of nanoparticle irreversible adsorption at the core scale is to conduct forced imbibition experiments in a sequential manner: inject brine (stage 1) > nanofluids (stage 2) > brine (stage 3). If the nanoparticles adsorb irreversibly in a manner that favors wettability alteration, the cumulative recovery factor obtained at stage 3 should be greater than stage 1 recovery factor. Hendraningrat and Torsaeter (Hendraningrat and Torsæter, 2015)

120

conducted their coreflood experiments in this manner on 4 initially water-wet (WW) cores, 1 intermediate-wet (IW) core and oil-wet (OW) sandstone cores - all originally saturated with the same type of degassed oil. The average stage 1 recovery obtained from the WW cores was 54.3%, with cumulative average recovery of 59.8% and 68.7% obtained after stages 2 and 3 respectively. For the IW core, the stage 1 recovery obtained was 53%, with cumulative recovery of 55% and 71% obtained after stages 2 and 3 respectively. Similarly, for the OW core, the stage 1 recovery obtained was 46%, with cumulative recovery of 48% and 73% obtained after stages 2 and 3 respectively. The same group of researchers (Hendraningrat and Torsæter, 2014) performed another series of tests using identical rocks and fluids and reported similarly convincing results. Stage 1 average recovery factor recorded from 3 IW cores was 57%, with a cumulative 62% recovery after stage 2 and 66% recovery after stage 3. The recovery factor obtained from an OW core after stage 1 was 61%, with a cumulative 68% recovery after stage 2 and 72% recovery after stage 3. All the cores used in both reported studies contained predominantly quartz (93%) while the oil samples used contained 75.1% saturates, 22.6% aromatics, 1.9% resins and 0.4% asphaltene fractions. The permeability and porosity ranges are 100-400 mD and 15-17% respectively. These reports provide a concrete basis to suggest that the adhesion force changes observed in our study at the nanoscale translate to a decrease in residual oil saturation and incremental oil recovery at the core-scale, in the context of silica nanoparticle treatments.

Overall, results from this work provide fundamental basis for the field-scale recovery increments in shale oil reservoirs recently reported (Syfan et al., 2018), in addition to other lab-scale observations (Agi et al., 2018; Hendraningrat et al., 2013a). This study demonstrated an optimistic potential of nanofluids to recover additional oil from TMS which has potentially 7 billion barrels of recoverable oil (John et al., 1997). Based on the convincing scientific evidence

coupled with practical engineering implications and discussions presented herein, conceptual models of effects of silicon dioxide nanoparticles on adhesion of chemical functional species in crude oil to quartz and clay surfaces was designed, as presented in Figure 4.20 and Figure 4.21.

Adhesion force = high ↑↑   Adhesion force = low ↓

Brine   Quartz/Muscovite mica (clay substitute)   R = Terminal group: $-CH_3$, $-C_6H_5$, $-COOH$

(−) Hydrophilic SiO_2 nanoparticles
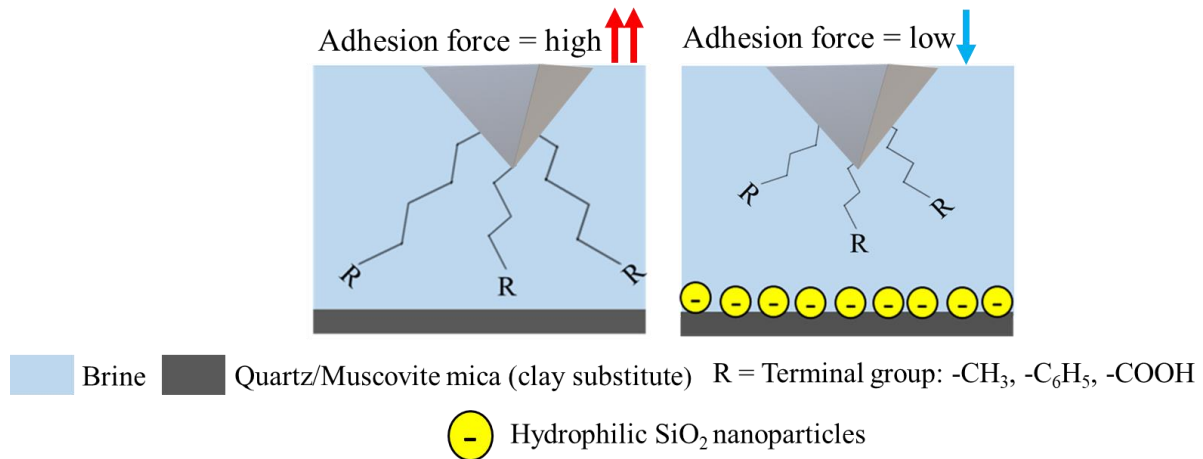
Figure 4.20 Conceptual model of the effect of hydrophilic silicon dioxide nanoparticles on adhesion of chemical functional species to quartz and model clay surfaces

Adhesion force, F_{adh} is sum of:
- Van der Waals force, F_{VdW}
- Non-electrostatic adhesion F_{nel}
- Electrostatic repulsion, F_{el}
- Structural force, F_{str}

SiO_2 nanoparticles + APTES

Adhesion force = high ↑↑   Adhesion force = low ↓   Adhesion force increases ↑

Brine   Muscovite mica (clay substitute)   (−) Hydrophilic SiO_2 nanoparticles

R = Terminal group: $-CH_3$, $-C_6H_5$, $-COOH$ (+) SiO_2 nanoparticles with APTES

Figure 4.21. Conceptual model of the effect of hydrophilic silicon dioxide nanoparticles with aminosilanes functionalization on adhesion of chemical functional species to model clay surfaces

In the context of Young dupre equation (Rao, 2003; Young, 1805), adhesion force is a function of surface wettability effects in terms of contact angle and fluid/fluid interfacial effects in terms of interfacial tension. This AFM study places emphasis on adhesion force changes leading to modification of surface wettability because the adhesion force is only measured after the functionalized tip contacts the mineral substrate in nanofluid media. However, how the nanoparticles behave at liquid/liquid interfaces compared to solid/liquid interfaces remains to be found. In the next section, results of contact angle and interfacial tension measurements obtained at the micron-scale are presented and discussed.

4.2. Micron-Scale Characterization of Nanofluid Enhanced Oil Recovery

4.2.1.   Effect of Hydrophilic Silica-based Nanofluids (HNP) on Interfacial Tension

The experimental results showed that hydrophilic silicon dioxide nanoparticles modestly influence IFT in pure oil systems as well as crude oil from the TMS formation, as displayed in Figure 4.22. As shown, undecane recorded the highest IFT while TMS recorded the least, consistent with all aqueous phases. The interfacial tension for decane (-CH_3)/AFB and decane/NaCl measured 33.9 mN/m and 40.61 mN/m, whereas switching to HNP 0.05 wt% decreased IFT to 37.24 mN/m. However, the decane/0.05 wt% HNP IFT is 10% higher than decane/AFB IFT. A subsequent increase in nanofluid concentration followed a slight decrease in IFT: the lowest IFT of 32.43 mN/m was obtained with 1 wt% HNP, which is only a 4% decrease from decane/AFB IFT.
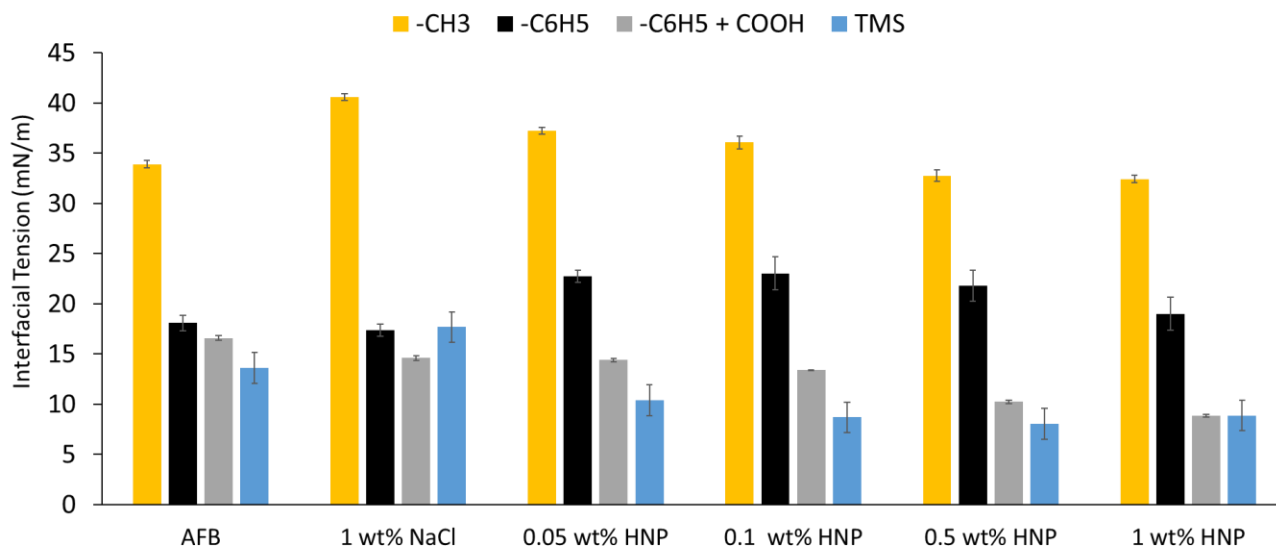
Figure 4.22. Interfacial tension measurements across oil/aqueous phases at room conditions.

Next, ethylbenzene (-C_6H_5)/AFB and ethylbenzene (-C_6H_5)/NaCl IFT measured 18.08 mN/m and 17.37 mN/m compared with ethylbenzene/0.05 wt% HNP IFT which measured 22.75 mN/m – 25% higher than ethylbenzene/AFB IFT. A successive increase in nanofluid concentration led to reduction of IFT but not sufficiently low enough to be less than the IFT measured in brine – either AFB or 1 wt% NaCl. The IFT obtained for ethylbenzene/1 wt% HNP was 19 mN/m, which is still 5% higher than ethylbenzene/AFB IFT. The addition of undecanoic acid to ethylbenzene to simulate a mixture containing –COOH group in addition to –C_6H_5 led to a generally lower interfacial tension for all the aqueous solutions tested and the effect of hydrophilic silica nanoparticles on IFT is more significant than with undecane (-CH_3) and ethylbenzene (-C_6H_5). For convenience, the mixture of ethylbenzene and undecanoic acid is denoted as C_6H_5 + COOH. As shown in Figure 4.22, C_6H_5 + COOH/AFB and C_6H_5 + COOH/NaCl IFT measured 16.6 mN/m and 14.61 mN/m respectively, whereas switching to 0.05 wt% HNP decreased IFT to 14.4 mN/m. As expected, a subsequent increase in nanofluid concentration followed a noticeable decrease in IFT: C_6H_5 + COOH/1 wt% HNP IFT measured 8.83 mN/m, signifying close to a 50% reduction in IFT compared to C_6H_5 + COOH/AFB system.

124

The IFT values and trends obtained with TMS crude oil are similar to those obtained with the C_6H_5 + COOH mixture. As shown in Figure 4.22, TMS/AFB and TMS/NaCl IFT measured 13.6 mN/m and 17.68 mN/m respectively, whereas switching to 0.05 wt% HNP decreased IFT to 10.38 mN/m – representing more than a 20% decrease in IFT compared to TMS/AFB system. As expected, a subsequent increase in nanofluid concentration led to a corresponding decrease in IFT: AFB/1 wt% HNP IFT measured 8.88 mN/m, signifying close to a 35% reduction in IFT compared to TMS/AFB system. Note that the lowest IFT of 8.06 mN/m was obtained with 0.5 wt% HNP, compared to 1 wt% HNP which increased IFT to 8.88 mN/m. In summary, these findings reveal the effect of hydrophilic silica nanoparticles at liquid/liquid interfaces carrying specific functional groups such as $-CH_3$, $-C_6H_5$ and COOH and TMS crude oil which is a complex mixture of organic compounds.

4.2.2. Effect of Aminosilanes-Treated Silica-based Nanofluids (NNP) on Interfacial Tension

The grafting of aminosilanes onto silica nanoparticles is known to enhance adsorption of particles at liquid/liquid interfaces and consequently impact interfacial tension (Ngouangna et al., 2020; Ogolo et al., 2012). The oil/water interface typically has a negative charge due to hydroxyl ion adsorption, and the introduction of positively charged functionalized particles will tend to neutralize the interface charge, leading to a significant reduction in IFT. This was confirmed in this study, as shown in Figure 4.23. At a pH of 6, undecane/NNP (at 0.1 wt%) measured IFT of 7.2 mN/m compared to undecane/HNP which measured 17. 28 mN/m and 17.34 mN/m at 0.1 wt% and 0.5 wt% respectively. In other words, at the same pH of 6 and 0.1 wt% concentration, the grafting of aminosilanes onto the surfaces of silica nanoparticles reduced IFT by nearly 60% when these nanoparticles interact with undecane ($-CH_3$) solution.
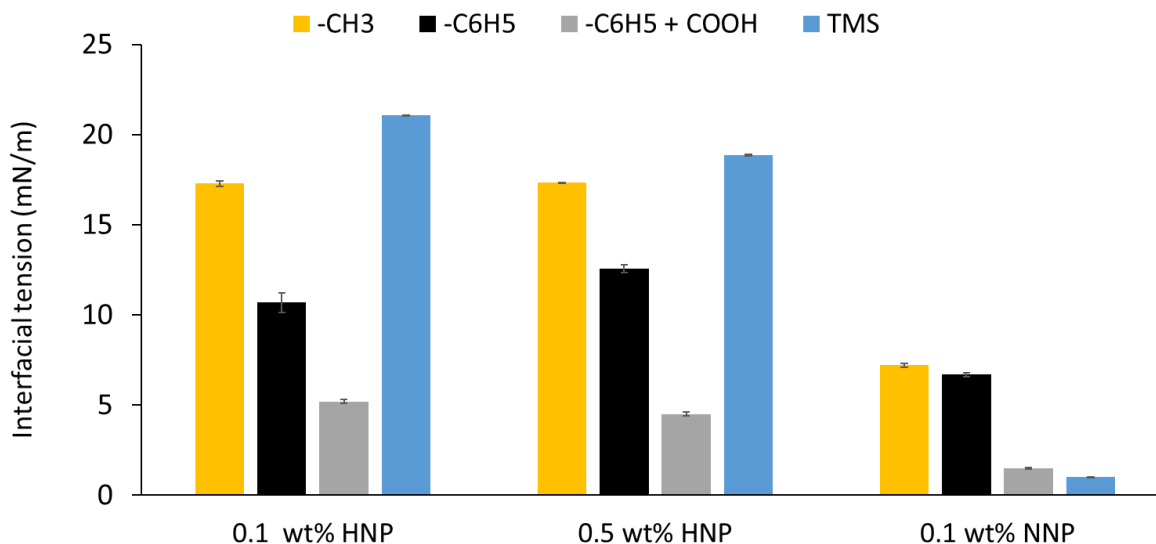
Figure 4.23. Interfacial tension of oil/aqueous phases at room conditions. All nanofluid solutions have a pH of 6.

Similarly, ethylbenzene/0.1 wt% NNP IFT measured 6.7 mN/m compared to ethylbenzene/HNP which measured 10.68 mN/m and 12.55 mN/m at 0.1 wt% and 0.5 wt% respectively. This means that, at the same pH of 6 and 0.1 wt% concentration, the grafting of aminosilanes onto the surfaces of silica nanoparticles reduced IFT by nearly 40% when these nanoparticles interact with ethylbenzene (-C_6H_5) solution.

For a mixture of ethylbenzene and undecanoic acid (C_6H_5 + COOH), IFT values were generally lower just as it was observed when brine solutions such as AFB and 1 wt% NaCl and selected concentrations (0.05 wt% - 1 wt%) of HNP were tested (see Figure 4.23). The IFT measured in 0.1 wt% NNP was 1.5 mN/m, which was lower than those obtained with 0.1 wt% HNP (5.2 mN/m) and 0.5 wt% HNP (4.5 mN/m). In other words, at the same pH of 6 and 0.1 wt% concentration, the grafting of aminosilanes onto the surfaces of silica nanoparticles reduced IFT by more than 70% when these nanoparticles interact with a solution carrying COOH and C_6H_5 functional groups.

The most notable effect was observed with TMS crude oil: IFT measured in 0.1 wt% HNP and 0.5 wt% HNP were 21.05 mN/m and 18.85 mN/m, whereas functionalized nanoparticles NNP at 0.1 wt% concentration yielded an IFT of 1 mN/m. In other words, at the same pH of 6 and 0.1 wt% concentration, the grafting of aminosilanes onto the surfaces of silica nanoparticles reduced IFT by more than 95% when these nanoparticles interact with actual TMS crude oil - a complex mixture of organic compounds - posing significant implications for enhancing oil recovery.

Overall, this study systematically demonstrates the effect of silica nanoparticle functionalization with 3-aminopropyltriethoxysilane (APTES) on interfacial tension effects with pure hydrocarbon compounds carrying certain functional groups such as $-CH_3$, $-C_6H_5$ and COOH, and crude oil from TSM reservoir containing hundreds to thousands of chemical species. Further, all interfacial tension measurements obtained with TMS crude oil serve as key input variables for the modeling of capillary pressure and relative permeability curves used in compositional core-scale simulation of nanofluid-assisted CO_2 EOR.

4.2.3.   Effects of Silica-based Nanofluids (HNP & NNP) on Contact Angle

In addition to evaluating fluid/fluid interactions, the enhanced recovery potential of silica nanoparticle dispersions can be investigated in the context of rock/fluid interactions using the well-established DDDC technique for measuring advancing contact angle. Contact angle results obtained using TMS oil, rocks and aqueous solutions such as brine AFB, HNP and NNP dispersions are presented in Table 4.2 and the associated three-phase contact line graphs are presented in Figure 4.24, Figure 4.25 and Figure 4.26. As shown in Figure 4.24 and Table 4.2, the advancing and reducing contact angle measured on TMS rock surface in contact with a droplet of TMS oil in the presence of AFB brine were 45° and 40° respectively, signifying a water-wet system. The advantage of monitoring the TPCL movement to capture the true representative

127

advancing contact angle is illustrated in Figure 4.24: it was not until the normalized TPCL movement ratio changed that the advancing contact angle of 45° was obtained, after 240 mins of contact time and over 24 hrs aging time.

Figure 4.24. The monitoring of TPCL movement to obtain DDDC advancing contact angle on TMS rock in contact with TMS oil droplet in AFB solution at ambient conditions

In 1 wt% NaCl solution, the advancing and reducing contact angle measured were 55° and 45° respectively (see Figure 4.25 and Table 4.2), signifying a less water-wet system which agrees with nanoscale adhesion force measurements whereby adhesion forces measured between functionalized tips and mica in AFB were significantly less than those measured in NaCl solution. The benefit of monitoring the TPCL movement to capture the true representative advancing contact angle is also illustrated in Figure 4.25: it was not until the normalized TPCL movement ratio changed from 1.74 to 1.725 that the advancing contact angle of 55° was obtained, after 240 mins of contact time and over 24 hrs aging time.
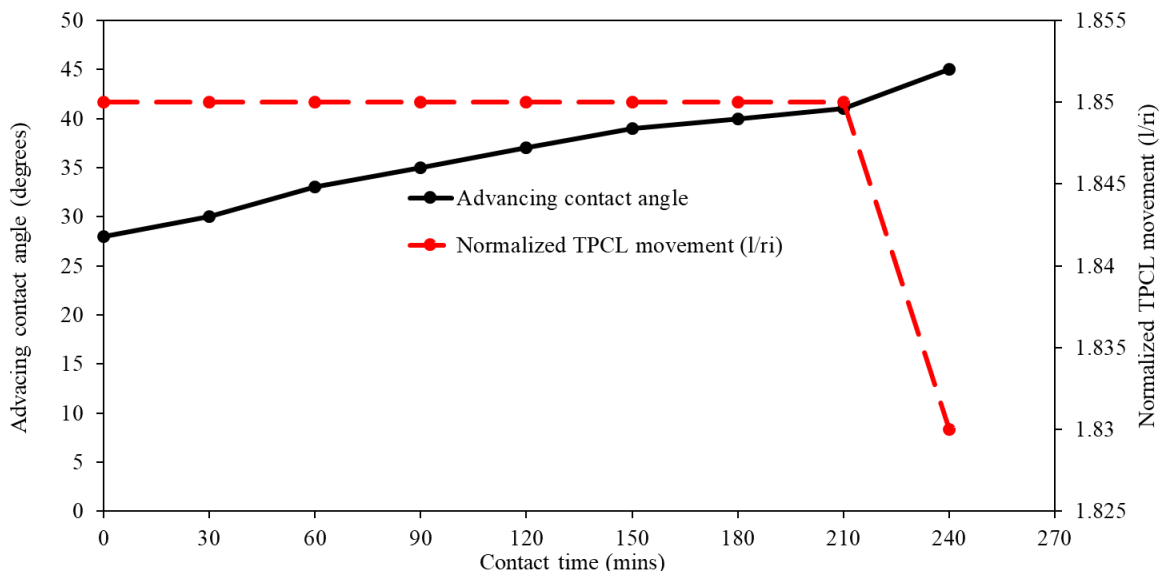
Figure 4.25. The monitoring of TPCL movement to obtain DDDC advancing contact angle on TMS rock in contact with TMS oil droplet in 1 wt% NaCl solution at ambient conditions

However, a drastic reduction in contact angle was observed in the presence of hydrophilic silica nanoparticle dispersions. At all concentrations tested, the TMS oil droplet failed to stick to the rock surface, which means both the advancing and receding contact angles can be safely assumed to be zero (see Table 4.2), indicating wettability change from water-wet to perfectly water-wet. Even though two separate contact angle tests were conducted on TMS rock in contact with crude oil when surrounded by AFB, 1 wt% NaCl and NNP fluids for reproducibility, five oil droplets were released from the needle in each HNP solution to adequately confirm the non-adhesion to the rock surface. The red arrow in the image column points to one of the oil droplets which on multiple occasions failed to adhere to the TMS rock surfaces in hydrophilic silica-based nanofluid media. The non-sticking of the oil droplets was also observed in 0.1 wt% and 0.5 wt% HNP at a pH of 6.

However, the grafting of aminosilanes enhanced the adhesion of TMS oil droplet on the rock surface to a noticeable degree and modified the surface wettability from perfectly water-wet

to strongly water-wet state. In the presence of NNP, a 20° advancing contact angle and a 5° receding contact angle were achieved, as seen in Figure 4.26 and Table 4.2. Figure 4.26 shows that, even though the advancing contact angle appeared to stabilize at 15° between 0 and 60 mins contact time, the true measurement of 20° was only captured after the TCPL movement was observed at a contact time of 150 mins.
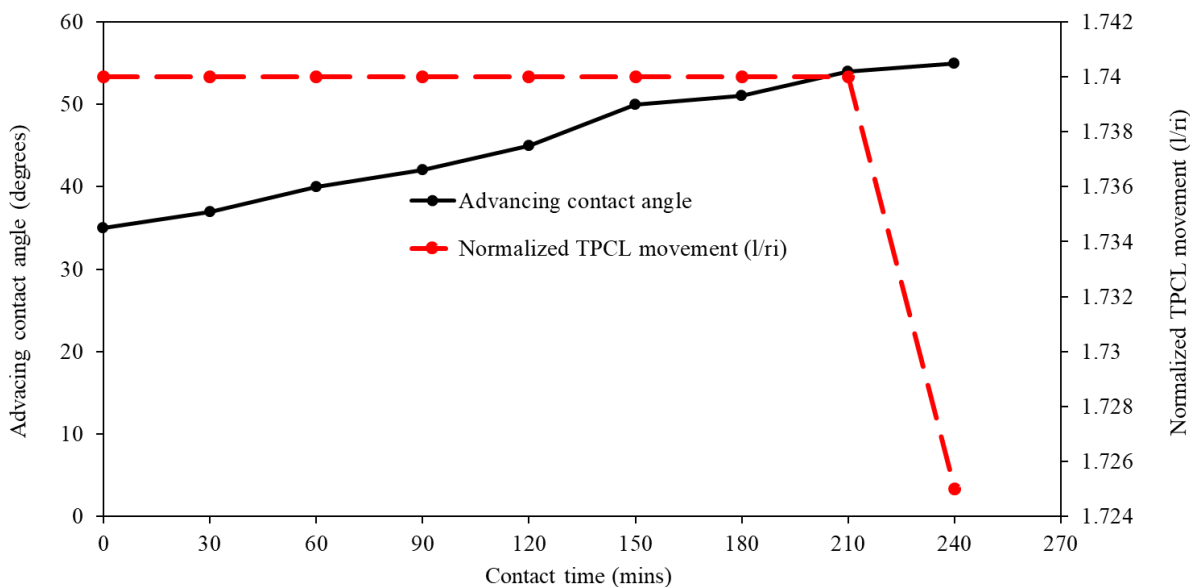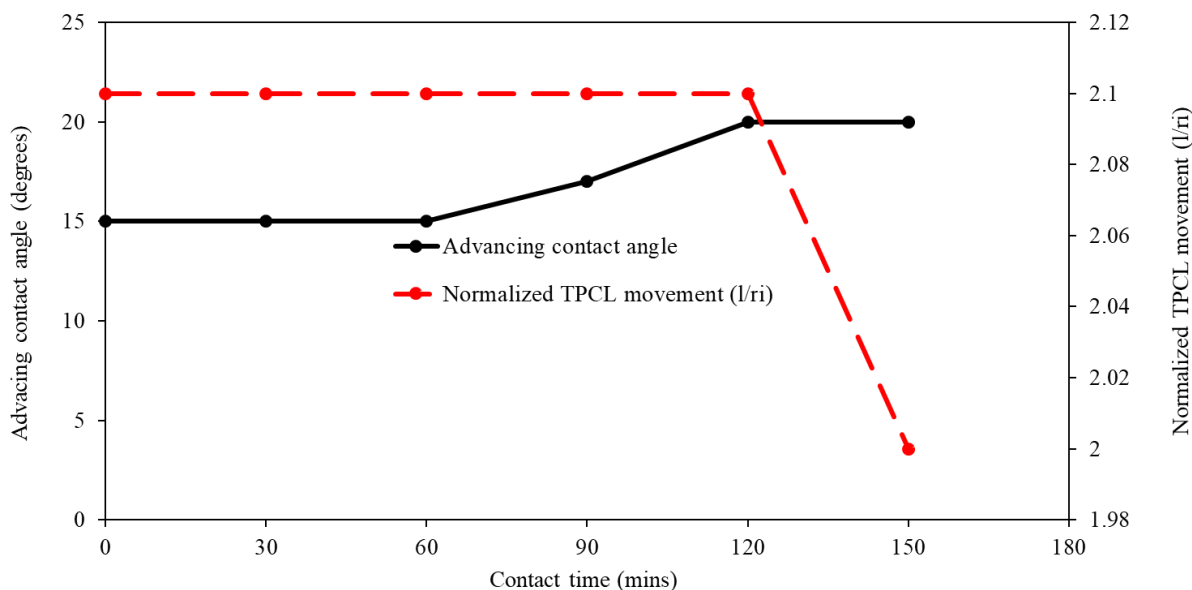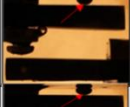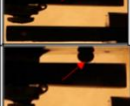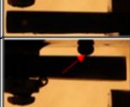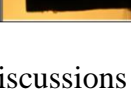

Figure 4.26. The monitoring of TPCL movement to obtain DDDC advancing contact angle on TMS rock in contact with TMS oil droplet in 0.1 wt% HNP at a pH of 6 and at ambient conditions

Resultantly, the adhesion force from Young-Dupre equation (equation 2.7) was determined for AFB, 1 wt% NaCl, HNP and NNP solutions. The proportionality constant was assumed to be 1 and the radius of the needle used is 0.94 mm. As seen in Table 4.2, the adhesion force in TMS rock/oil/AFB and TMS rock/oil/NaCl were calculated to be 0.732 μN and 2.222 μN respectively. The non-sticking of oil droplets on the rock surfaces in HNP also resulted in a zero-adhesion force, and the subsequent treatment of HNP with aminosilanes mildly increased adhesion force to 0.053 μN at a pH of 6. In general, the DDDC studies helped reveal the original wettability state of TMS

and subsequent changes by virtue of hydrophilic and surface-modified silica nanoparticle treatments. These measurements coupled with IFT data also serve as important variables used to predict capillary pressure and relative permeability curves for TMS HRZ.

Table 4.2 Results of DDDC contact angle measured on TMS rock surfaces contacted with crude oil in the presence of brine and nanofluid media. Multiple tests were conducted for reproducibility.

Experiment	Image	Advancing contact angle, θ_a° (test 1)	Receding contact angle, θ_r° (test 1)	Advancing contact angle, θ_a° (test 2)	Receding contact angle, θ_r° (test 2)	IFT (γ), mN/m	Adhesion force, $F_{adh} = R\gamma(\cos\theta_r - \cos\theta_a)$, μN
TMS rock/ TMS oil/ AFB		45	40	45	40	13.6	0.753
TMS rock/ TMS oil/1 wt% NaCl		55	45	55	45	17.68	2.222
TMS rock/TMS oil/0.05 wt% HNP		0	0	0	0	10.38	0
TMS rock/TMS oil/0.1 wt% HNP		0	0	0	0	8.69	0
TMS rock/TMS oil/0.5 wt% HNP		0	0	0	0	8.06	0
TMS rock/TMS oil/1 wt% HNP		0	0	0	0	8.88	0
TMS rock/TMS oil/0.1 wt% HNP pH 6		0	0	0	0	21.05	0
TMS rock/TMS oil/0.5 wt% HNP pH 6		0	0	0	0	18.85	0
TMS rock/TMS oil/0.1 wt% NNP pH 6		20	5	20	5	1	0.053

4.2.4.   Discussions

The purpose of this study was to differentiate the effect of silica nanoparticles on liquid/liquid interfacial activity from rock/fluid interactions and correlate observations with nanoscale findings (discussed in section 4.1.5). To do so systematically, single-component hydrocarbons – namely undecane and ethylbenzene – and a mixture of ethylbenzene and undecanoic acid were selected

for IFT tests. These organic compounds were selected because they are chemically similar to the thiols used for nanoscale studies, carrying the same functional groups (see Figure 3.7). In preserving this resemblance, one can relate the adhesion force variation observed at the nanoscale to the interfacial tension characterized at the micron-scale herein to further understand the oil release mechanisms of silica nanoparticles. In addition, IFT and contact angle measurements were made using actual TMS rock and oil in the presence of brine and silica nanofluid media. These properties serve as key variables to examine the core-scale potential of nanofluid-enhanced CO_2 EOR in the context of capillary pressure and relative permeability modelling. In this section, the scientific significance and practical engineering implications of these findings are discussed.

Results showed that hydrophilic nanosilica dispersions had a negligible effect of interfacial tension with pure hydrocarbon systems such as undecane ($-CH_3$) and ethylbenzene ($-C_6H_5$). The finding on undecane/HNP is in tandem with a study conducted by Jiang and colleagues (Jiang et al., 2017) to examine the impact of silica nanoparticles on reducing decane/nanofluid interfacial tension. In their study, different sizes (10-150 nm) and concentrations (0.01 wt% - 0.05 wt%) of silica nanoparticles were tested - none of which changed the decane/water IFT by up to 1 mN/m. Further, that the addition of undecanoic acid to ethylbenzene generally lowered interfacial tension for all the aqueous solutions tested is in close agreement with another study in which the addition of organic acids such as cyclohexane carboxylic acid and cyclohexane pentanoic acid to n-decane significantly lowered IFT (compared to water) by 20 mN/m (Sayed et al., 2019). Another research group (Guo and Errington, 2019) employed Monte Carlo simulations to investigate the effects of acetic acid on water-octane system and they showed that, in terms of number of molecules adsorbed, acetic acid had strong affinity towards the octane-water interface leading to a reduction of octane/water IFT.

The effect of surface-active carboxylates may also explain why IFT measurements using TMS crude oil were significantly lower than those obtained with the pure compounds, since it contains surface-active components such as asphaltenes and resins. Carboxylic acid is majorly found in asphaltenes and resins. In terms of IFT reduction, an optimal concentration of hydrophilic silica nanoparticles was found to be 0.5 wt%: the lowest IFT of 8.06 mN/m was obtained with 0.5 wt% HNP, compared to 1 wt% HNP which increased IFT to 8.88 mN/m. The contrasting behavior observed between 0.5 wt% HNP and 1 wt% HNP may be due to the emergence of structural interactions which was partly responsible for increasing adhesion force between 0.5 wt% to 1 wt% HNP at the nanoscale. Yet, how large the IFT reduction effect of hydrophilic silica nanoparticles is on capillary pressure, relative permeability, capillary number and residual oil saturation remains to be seen.

The grafting of aminosilanes onto the surface of silica nanoparticles had an evident impact on interfacial tension. As evidenced by the z-potential measurements shown in Figure 4.19b, the amine group from APTES becomes protonated at pH 6, giving rise to positive charges on nanosilica surface. The oil/water interface typically has a negative charge due to hydroxyl ion adsorption, and the introduction of positively charged functionalized particles will tend to neutralize the interface charge, leading to a significant reduction in IFT. Of more practical importance is the attainment of a 1 mN/m interfacial tension between TMS crude oil and 0.1 wt% NNP at a pH of 6. This implies that APTES-functionalized silica nanoparticles can sufficiently disrupt oil/water interface to reduce oil/water capillary pressure, increase oil relative permeability and accelerate oil production in TMS producing zones such as the HRZ.

The DDDC contact angle measurements helped reveal the true wetting state of TMS HRZ under focus in this study and the wettability modification effects of silica nanoparticles at the

133

micron scale. Following the movement of the TPCL, the TMS rock/oil/brine (AFB) advancing

contact angle measured 45°, indicating that TMS HRZ is water wet. Results also showed that

hydrophilic silica nanoparticles steered from a water-wet state to a perfectly water-wet state; no

oil droplet adhered to the rock surface in the presence of hydrophilic silica nanofluids. However,

switching to silica nanoparticles functionalized with aminosilanes caused a modest sticking effect

of the TMS oil droplet to the rock surface, resulting in a contact angle of 20°.The Young-dupre

equation was used to calculate corresponding adhesion forces of 0.8 μN, 0 μN and 0.1 μN with

AFB, HNP and NNP solutions respectively. Because the TMS rock comprises of 44% clay and

43% quartz, it can be said that these results agree with nanoscale force spectroscopy studies

performed on mica (clay substitute) and quartz contacted with $-CH_3$, $-C_6H_5$ and $-COOH$ groups

which are the dominant functional groups found in TMS crude oil. Recall that, from the AFM

study (Section 4.1), adhesion force of non-polar and polar functional groups to pure minerals

significantly decreased in the order of pN when switching from AFB to HNP, whereas NNP led to

a higher adhesion force due to the role of surface charge and hydrophobicity.

Discussions on the role of surface and intermolecular forces presented in the context of

nanoscale evidences (section 4.1.5) also hold true herein. While the IEP of TMS is unknown, one

can assume a similarity with mica and quartz since both minerals constitute > 80% of the rock. As

such, TMS rocks become more negatively charged as hydrophilic silica nanoparticles adsorb on

the surface, which helps to significantly lower advancing water contact angle and decrease

adhesion force. Besides electrostatic interactions, the surface free energies of the nanoparticles

also create a chemical potential gradient at the rock/fluid interface that favors wettability alteration

towards a more water-wet state. However, from this study, it appears that 0.05 wt% HNP (or 1 x

10^{14} particles per ml) was sufficient to reduce both contact angle and adhesion force to zero and

correspondingly yield a perfectly water-wet system. In a similar sense, TMS immersed in NNP solution with +12 mV at a pH of 6 will be positively charged, which will compress electric double layer, increase the advancing contact angle and increase adhesion force.

The impact of 3-aminopropyltriethoxysilane (APTES)-modified silica nanoparticles on enhancing oil recovery have been studied in the past and conflicting results have ensued, at micron-to-core scales (Alvarez-Berrios et al., 2018; Ngouangna et al., 2020; Ogolo et al., 2012). For instance, Alvarez and colleagues (Alvarez-Berrios et al., 2018) showed that APTES-modified silica nanoparticles (dispersed in ethanol) reduced the contact angle on aged Berea sandstone core from 106° using brine (oil-wet state) to 97°(intermediate-wet) whereas negatively charged silica NPs (also dispersed in ethanol) shifted the contact angle from 106° to 69°, signifying wettability alteration from oil- to water-wet state. Ngouangna and co-authors (Ngouangna et al., 2020) compared the oil recovery performance of unmodified and APTES-modified NPs and observed insignificant changes in contact angle, modest IFT changes but significant improvements in core-scale oil recovery. In their work, they observed a change in the surface wettability of an oil-wet sandstone core through a decrease in contact angle from 135° using brine to 54.5° and 54.3° with bare and APTES-modified silica nanoparticle dispersions, respectively. Interfacial tension reduced from 17 mN/m to 5 mN/m and 3 mN/m with bare silica nanoparticles and APTES-modified nanoparticles, respectively. However, forced imbibition experiments showed that bare silica nanoparticle dispersions recovered 69.6% of oil in place compared to 62.9% obtained with waterflood, whereas APTES-modified silica nanodispersions yielded 75% recovery.

In a similar wettability characterization study on Berea sandstone cores and a crude oil sample obtained Texas, some authors found that hydrophilic silica nanoparticles dispersed in 0.3 wt% NaCl increased aged Berea surface wettability towards water-wet whereas silica

nanoparticles treated with APTES rendered the surface less water wet (Alvarez et al., 2018). In their study, the contact angle in water phase for an aged Berea/water/air system without nanoparticles was 106.32°, whereas hydrophilic silica NPs decreased contact angle to 68.84° and APTES-treated nanoparticles increased the contact angle to 96.88°.

Largely, this study has shown that hydrophilic silica nanoparticles can improve recovery in TMS through wettability modification whereas amino-treated silica nanoparticles can improve recovery through IFT reduction. Based on the convincing fundamental evidence coupled with broad engineering implications presented in this section, conceptual mechanistic models of effects of silicon dioxide nanoparticles on IFT in pure and complex hydrocarbon compounds and advancing contact angle measured on TMS rocks in contact with TMS oil droplets are presented in Figure 4.27 and Figure 4.28.

As shown in Figure 4.27, dispersions of hydrophilic silica nanoparticles have minimal impact on oil/brine interfacial tension whereas the functionalization of the nanoparticles with APTES may lead to a significant decrease in IFT. In terms of advancing contact angle (see Figure 4.28), the coating of TMS rock with hydrophilic nanoparticles can effectively reduce advancing contact angle and create a more water-wet state, whereas APTES-modified nanoparticles steer the surface towards less water-wet.
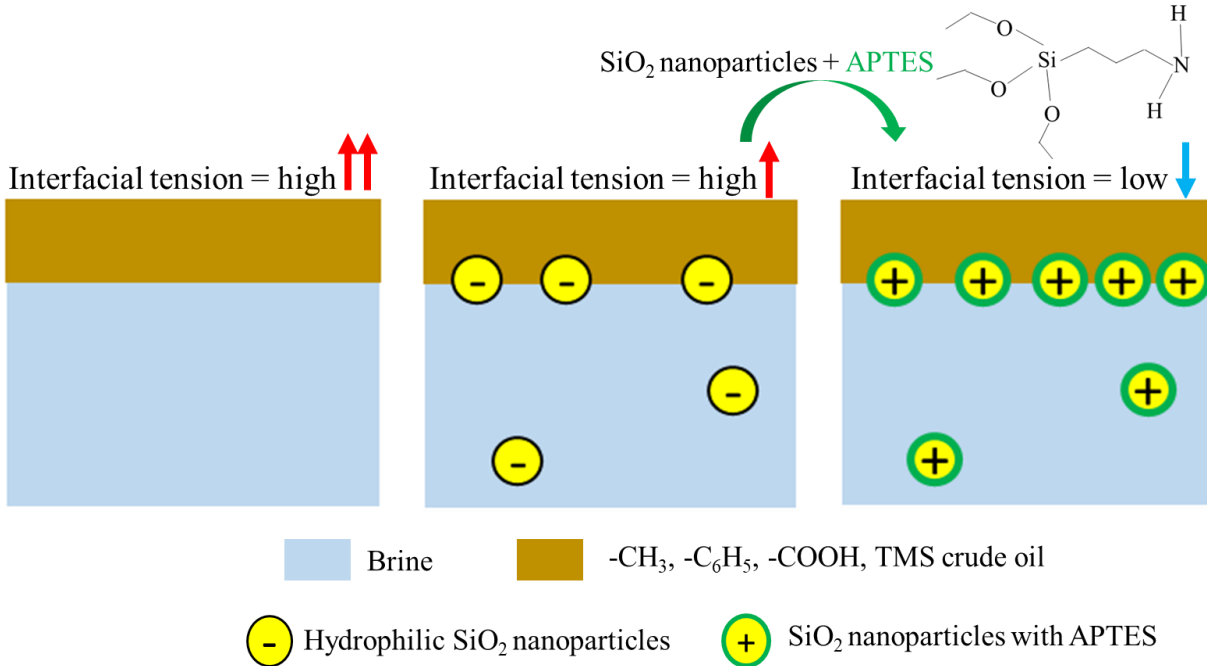
Figure 4.27. Conceptual model of the effect of hydrophilic and APTES-modified silicon dioxide nanoparticles on interfacial tension measured across the interface between nanofluids and hydrocarbon compounds with $–CH_3$, $-C_6H_5$, $–COOH$ functional groups as well as TMS crude oil
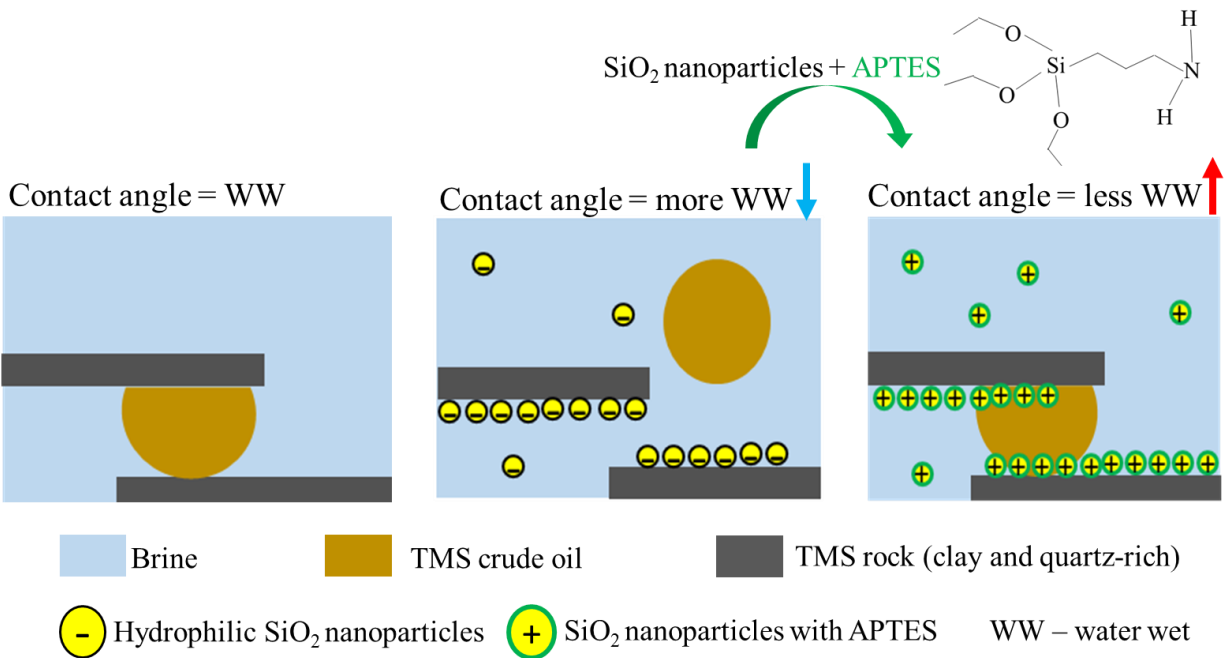
Figure 4.28. Conceptual model of the effect of hydrophilic and APTES-modified silicon dioxide nanoparticles on advancing contact angle measured on TMS rock surfaces contacted with TMS crude oil droplets in nanofluid media

In addition to cost and environmental impact, the benefits of the APTES modification may boil down to the impact of IFT decrease (compared to contact angle changes) on residual oil saturation, relative permeability and capillary pressure. The next section discusses how the latter two multiphase flow parameters can be deduced from IFT and contact angle measurements to explore the core-scale potential of nano-assisted CO_2 EOR. The core-scale characterization aspect also employs reservoir rock and fluid characterization to investigate the microscopic sweep efficiency obtainable with CO_2 and nanofluid injection in matrix-dominated and fractured-dominated regions in TMS HRZ.

4.3. Core-Scale Characterization of Nanofluid-Assisted CO_2 Enhanced Oil Recovery

4.3.1.   High-pressure CO_2 coreflood EOR in low-permeability TMS core

Assuming they contain significant volumes of hydrocarbons in place, the low-permeability regions in TMS HRZ (0.1 mD or less) are amenable to CO_2 EOR, due to favorable gas injectivity, oil viscosity reduction and the ability of CO_2 to alter the phase behavior of the in-situ oil. This is confirmed from results of high-pressure CO_2 injection EOR in the low-permeability core shown in Figure 4.29. The original dry weight of the core was 64.6483 g. After flooding the core with TMS oil, the measured weight was 64.7850 g. The final weight measured after CO_2 injection was 64.7400 g. Inputting these values in equation 3.1 led to a recovery factor of 32.92%.
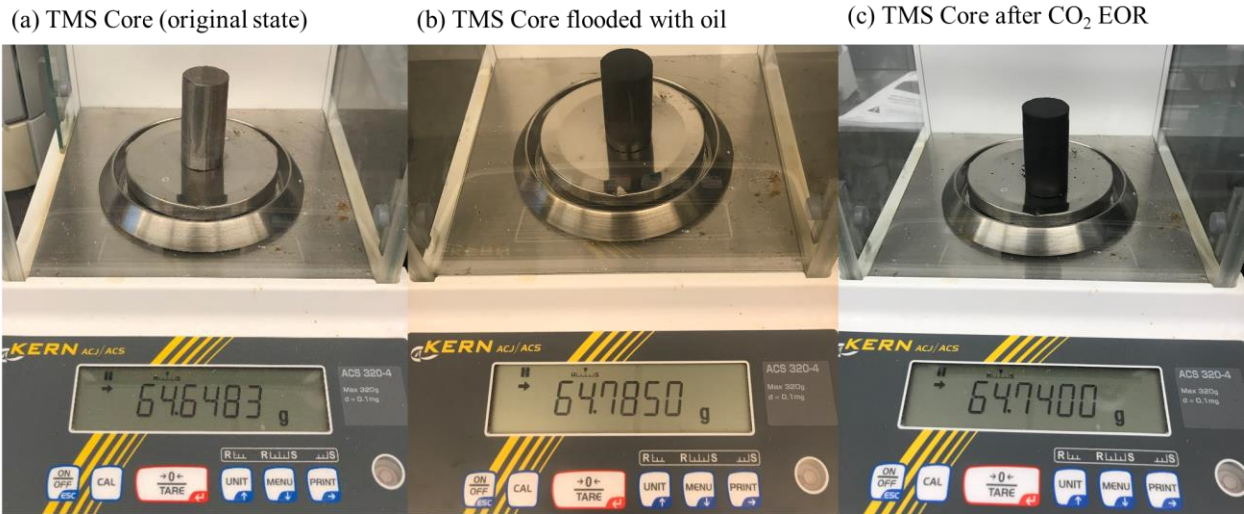
Figure 4.29. Weight measurements of low-permeability TMS core at different stages of the CO_2 EOR process: (a) original state of TMS core, (b) TMS core flooded with oil (before CO_2 injection) and (c) TMS core after CO_2 EOR

Images of the core were taken before and after CO_2 injection, for the purpose of visual inspection (see Figure 4.30). The subjection of the TMS core to confining pressure during oil flooding coupled with the fissility of the TMS shale may have caused the core to split along its bedding planes, as seen in Figure 4.30a&b.
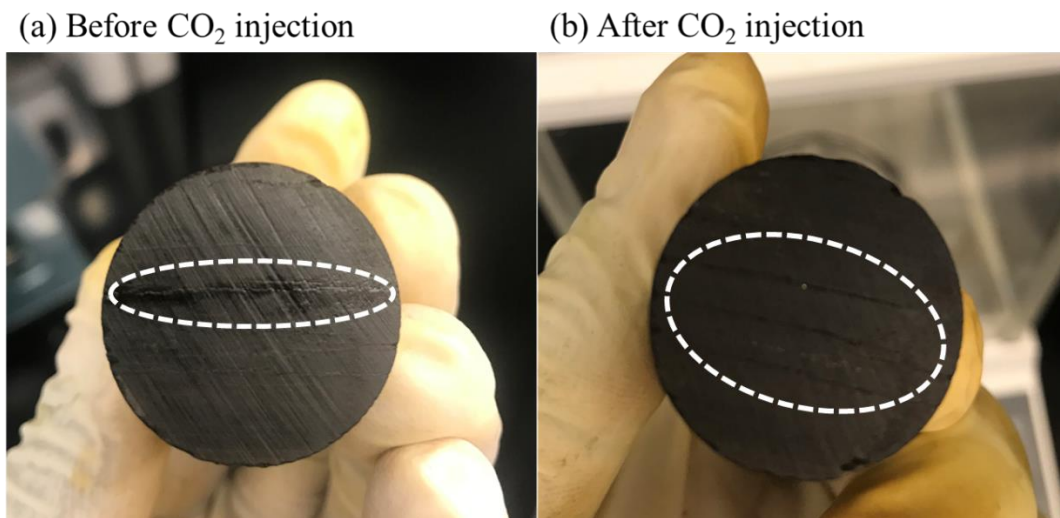
Figure 4.30. Snapshot images of the inlet face of the core before and after CO_2 injection. The splitting of the rock along bedding planes is visible in the areas circled by the ellipse with dash white lines

Figure 4.30a indicates the possible expulsion (to a certain degree) of oil through an opening before CO_2 injection. However, it appears that CO_2 injection led to the formation of more splits, as seen in Figure 4.30b, and no expulsion of oil either from the inlet or outlet face of the core was visually observed.

4.3.2. Reservoir Fluid Characterization

The pressure-temperature diagram for TMS oil based on reservoir fluid characterization done using CMG WinProp is shown in Figure 4.31. Likewise, regression models of PVT properties such as gas-oil ratio, oil formation volume factor, oil viscosity, z factor, gas formation volume factor and gas viscosity with good fit to experimental data are presented in Figure 4.32. The figure only shows some of the PVT properties, for brevity; other properties such as specific gravity and density were also modelled and matched with experimental data.

These PVT analyses reveal that TMS is a black oil reservoir, with an initial reservoir pressure and temperature of 7497 psia and 260°F respectively, and saturation pressure of 1417 psia. The cricondenbar and cricondentherm are 1875 psia and 885°F respectively.
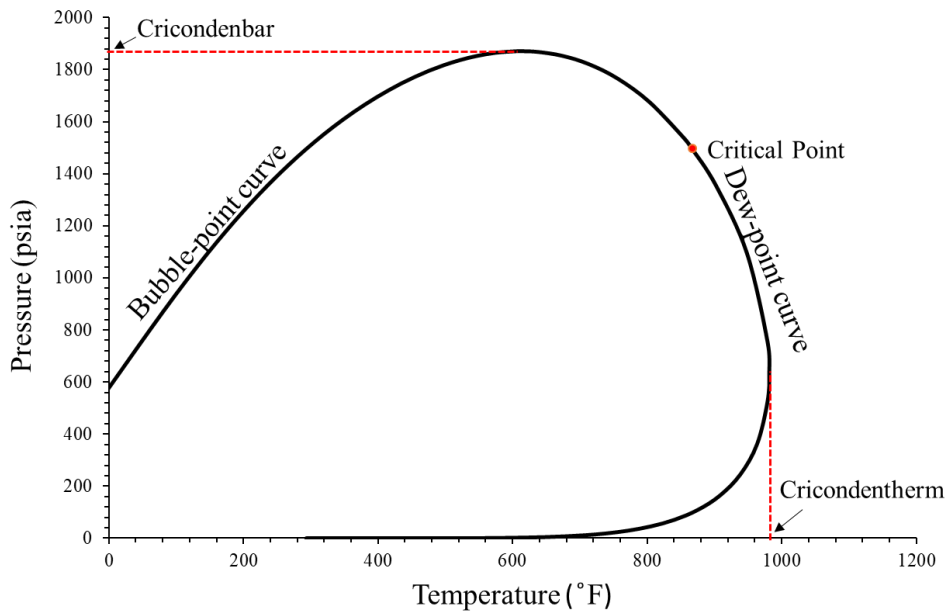
Figure 4.31. Pressure-Temperature diagram obtained through reservoir fluid characterization of TMS in CMG WinProp
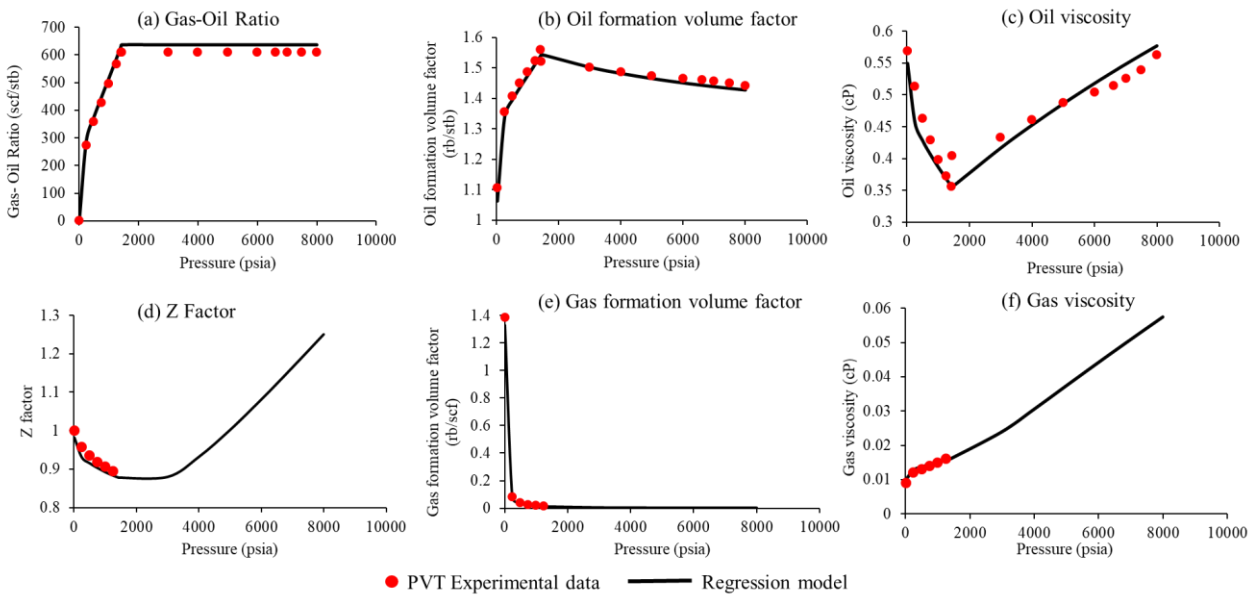
Figure 4.32. Regression models of significant PVT parameters compared with experimental data based on TMS reservoir fluid characterization performed using CMG WinProp

4.3.3. Capillary Pressure and Relative Permeability Curves for Tight and Fractured Zones in TMS HRZ

Next, the path to obtaining relative permeability and capillary pressure from coupling the Leverett J Function and Purcell model can be diagrammatically described using Figure 4.33. In accordance with the workflow presented in section 3.3.4.3 (see Figure 3.20), the J function was obtained for the 4 samples (S20-S23) retrieved from the HRZ in TMS based on Lohr and Hackley's (2018) study, and a fit was derived (green line overlaying the S23 scatter plot in Figure 4.33a). The oil/AFB capillary pressure for tight and fractured zones are shown in Figure 4.33b, while Figure 4.33c&d are the $1/Pc^2$ function and K_r graphs respectively.

As shown in Figure 4.33d, the K_{rw} model for high (dash blue line) and low (solid blue line) permeability regions is in excellent agreement with log-based water relative permeability data (blue scatter plot), confirming the existence of a water-wet state and a dual-permeability rock system. As revealed, the models reasonably predict the rock permeability to water both within the tight pores and through the interconnected fractures. Notice that all four graphs in Figure 4.33 have a starting residual water saturation point of 0.1 which was the value for the residual pseudo-wetting phase saturation obtained for the mercury injection porosimetry experiments (Lohr and Hackley, 2018). The well logging data obtained from TMS was analyzed and it was discovered that the average irreducible water saturation across TMS HRZ is also 0.1.
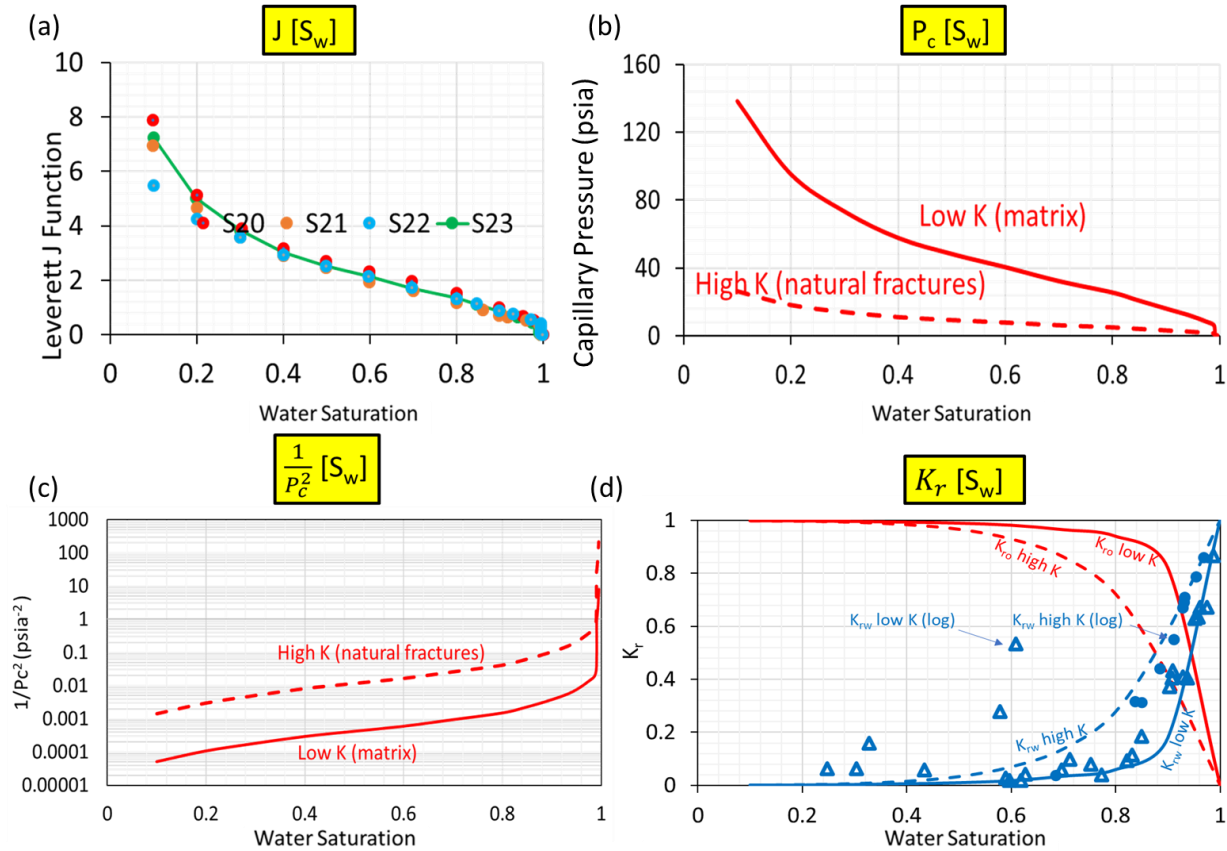
Figure 4.33. Results obtained: (a) J function for TMS HRZ samples; (b) oil/AFB capillary pressure; (c) $1/P_c^2$ function for oil/AFB; and (d) relative permeability curves for oil and AFB phases

Next, the oil/gas capillary pressure curves and relative permeability curves were derived for the low- permeability and high-permeability regions in TMS HRZ, as shown in Figure 4.34 and Figure 4.35 respectively. Note that these curves were derived based on CO_2/brine contact angle and IFT measurements (Lohr and Hackley, 2018) which makes them applicable to compositional simulation of CO_2 EOR in TMS. Figure 4.34 illustrates the effect of permeability on oil/gas capillary pressure: the capillary pressure in the high-permeability region is in the range of 0-3 psia over the entire oil saturation, whereas it becomes slightly higher in the low-permeability zone, in the range of 0-14 psia within the same oil saturation range. It is also noticed that the oil/gas capillary pressure both for the low- and high-permeability zones are significantly lower than the oil/water capillary pressures (shown in Figure 4.33b) due to the higher degree of interactions -such

as compositional variations and mass transfer - between oil and gas phases compared to oil and water phases.
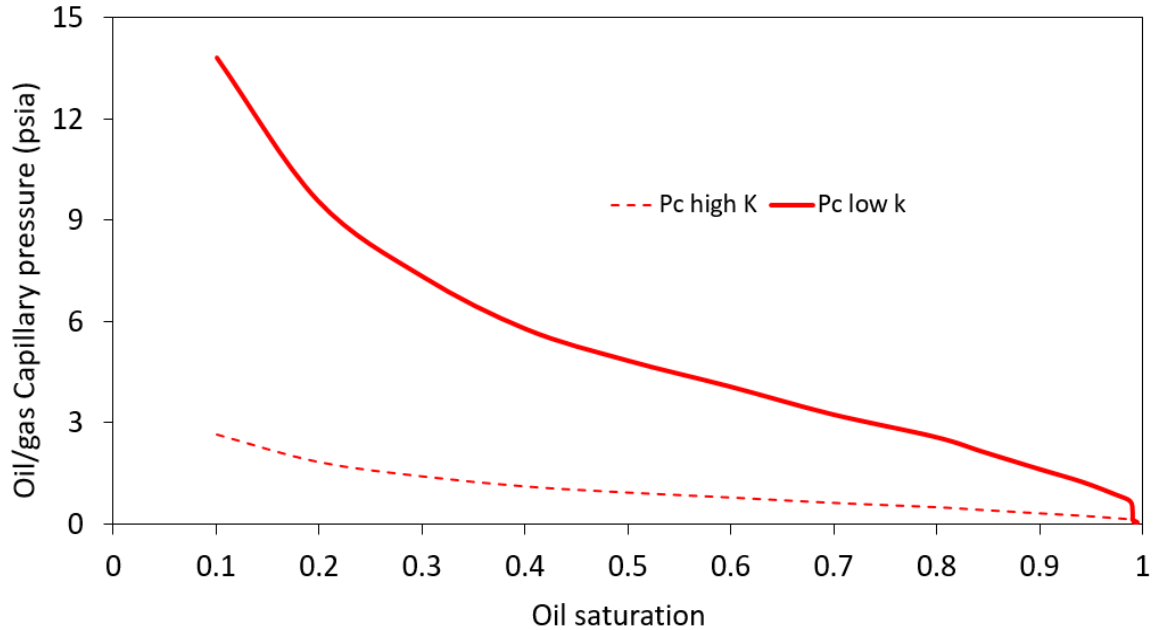
Figure 4.34. Gas/oil capillary pressure curves for low- permeability and high-permeability regions in TMS HRZ

Correspondingly, the oil/gas relative permeability curves for the low-permeability region differs slightly from those of the fractured region, as shown in Figure 4.35. Within the range of oil saturation, the rock relative permeability to oil in the low-permeability region is slightly slower than that in the high-permeability region due to effect of pore confinement. This will make the gas relative permeability in the low-permeability region also slightly higher than in the low-permeability region, as shown in Figure 4.35. It is worthwhile to note that, even at significant level of oil saturation, say 0.3, the oil relative permeability remains low and close to zero while the gas relative permeability remains high and close to 1 within the TMS HRZ.
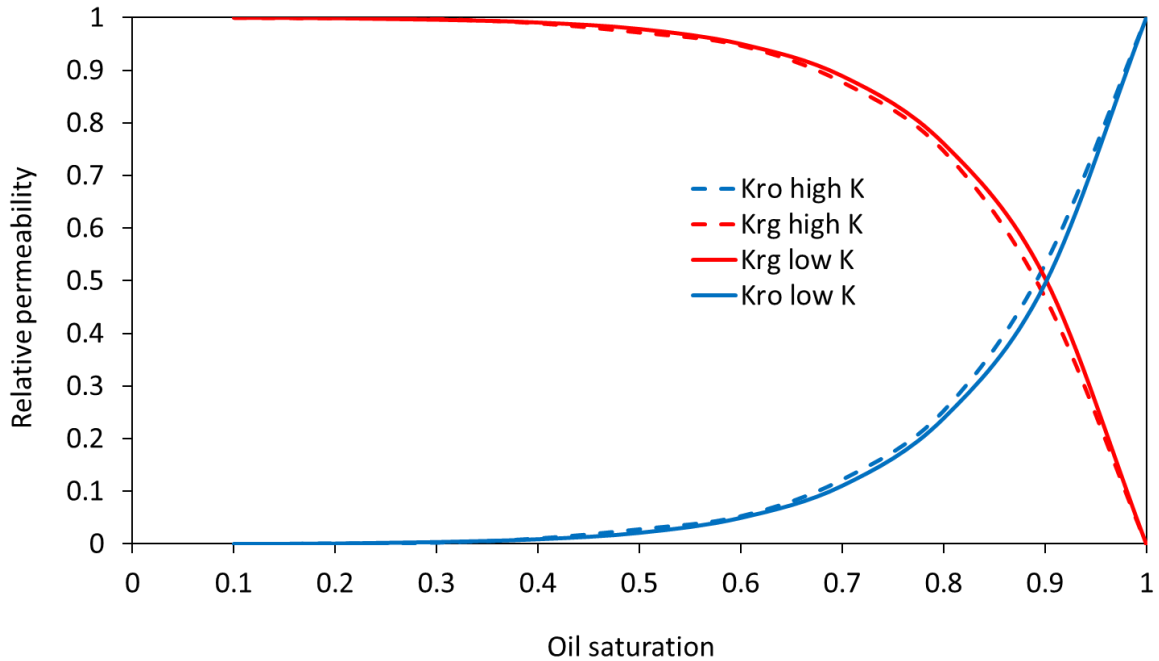
Figure 4.35. Gas/oil relative permeability curves for low- permeability and high-permeability regions in TMS HRZ

The oil/water capillary pressure curves for AFB brine and dispersions of hydrophilic and APTES-functionalized silica nanoparticles in the high-permeability regions of TMS HRZ are presented in Figure 4.36. Note that 0.5 wt% HNP was identified as optimal hydrophilic silica-based nanofluid concentration based on nano-to-micron scale studies and it is the basis for which the capillary pressure curves and relative permeability curves are displayed. Similarly, capillary pressure and relative permeability curves for 0.1 wt% HNP at pH of 6 and 0.1 wt% NNP at pH of 6 are presented to reveal effects of APTES modification. As shown, 0.5 wt% HNP decreased the oil/water capillary pressure compared to AFB due to significant changes in advancing contact angle (45° to 0°) and also a modest reduction in IFT (13.6 mN/m to 8.06 mN/m), as reported in the previous section. With 0.1 wt% NNP at a pH of 6, the oil/water capillary pressure decreased even further due to significantly lower IFT of 1 mN/m compared to 0.5 wt% HNP and AFB. The highest oil/water capillary pressure across the entire range of water saturation was obtained with 0.1 wt% HNP at a pH of 6, due to its high IFT of 21.05 mN/m compared to other fluids mentioned.
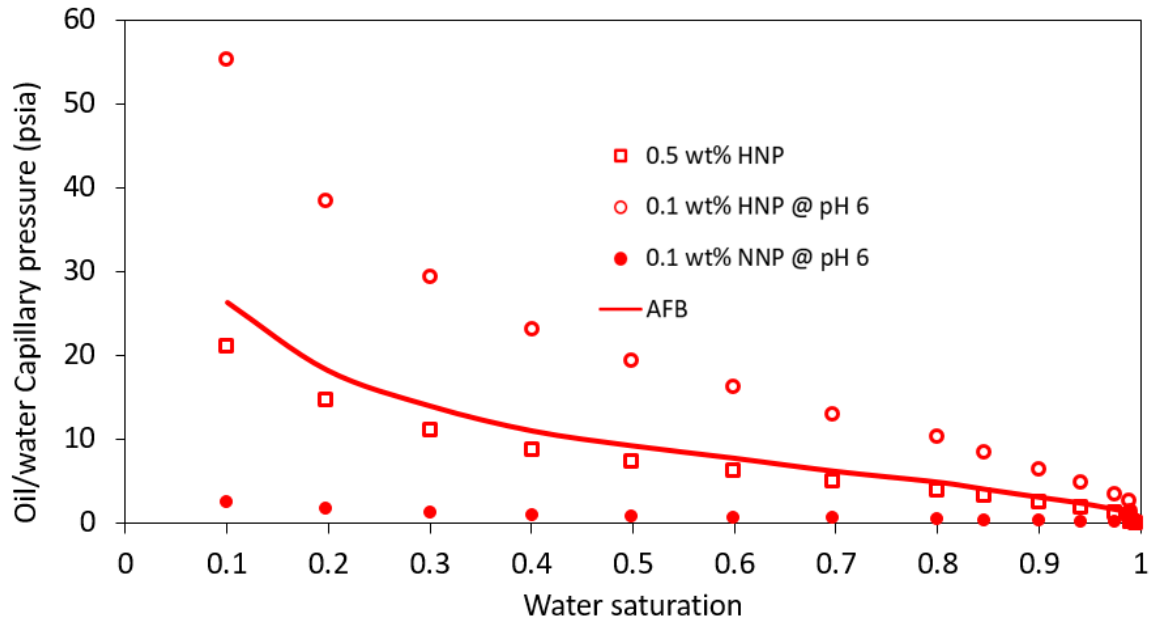
Figure 4.36. Oil/water capillary pressure curves for brine (AFB), hydrophilic silica-based nanofluids (HNP) and APTES silica-based nanofluids (NNP) in TMS HRZ high permeability regions.

Consequently, both 0.5 wt% HNP and 0.1 wt% NNP at pH of 6 increased oil relative permeability and decreased water relative permeability compared to AFB, as seen in Figure 4.37. Dispersions of APTES-modified silica nanoparticles (0.1 wt% NNP at pH of 6) increased oil relative permeability and reduced water relative permeability the most, also due to significant reduction in IFT. Over the range of water saturation, the second highest and lowest set of oil and water relative permeability values respectively were obtained with 0.5 wt% HNP due to its impact on wettability from contact angle measurements. It appears that AFB and 0.1 wt% HNP at pH of 6 have nearly the same oil/water relative permeability curves across the entire range of water saturation, mainly due to high IFT measured in both media.
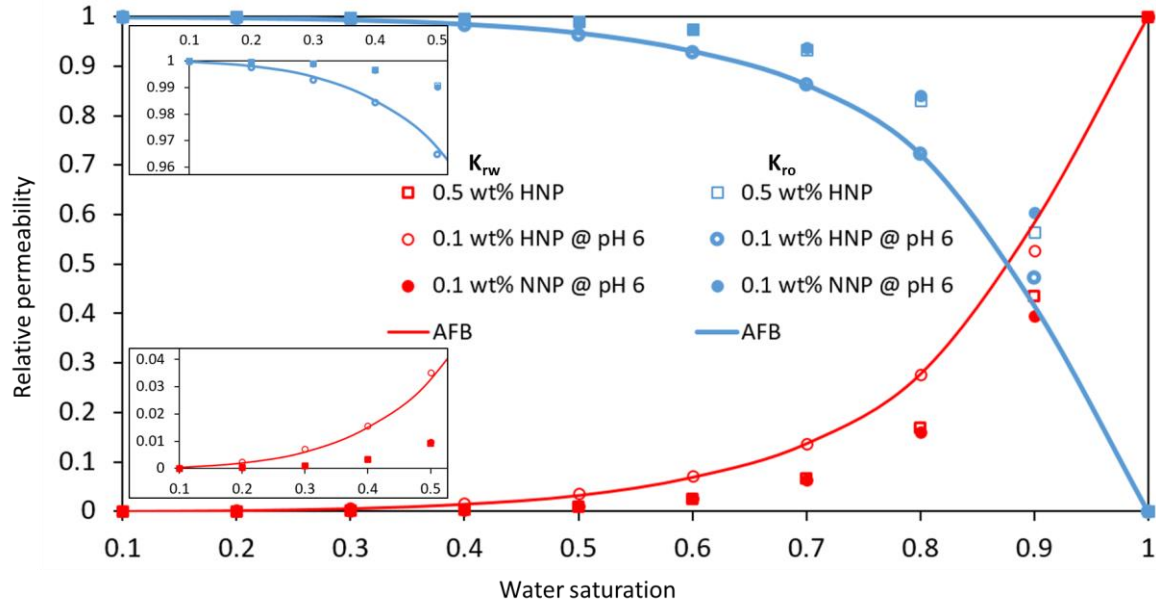
Figure 4.37. Oil/water relative permeability curves for brine (AFB), hydrophilic silica-based nanofluids (HNP) and APTES silica-based nanofluids (NNP) in TMS HRZ high permeability regions

4.3.4. Core-scale EOR Simulation Results

Following the completion of the models, CO_2 EOR and nanofluid-assisted CO_2 EOR processes were simulated. A tight rock model was used for CO_2 EOR while the fractured model was used for CO_2 EOR augmented with nanofluid injection. Simulation results show that injecting CO_2 into a low-permeability TMS rock system (0.07 mD) can recover at least 30% of oil-in-place, as seen in Figure 4.38, and the recovery profile shows that it took about 0.99 day to obtain the maximum recovery of 30.92 %. This result is in excellent agreement with the recovery factor of 32.92% obtained from coreflood experiment, and also indicates that the oil/gas capillary pressure and relative permeability curves modeled – among other input parameters - can reliably be used for CO_2 EOR simulation with a high confidence level.
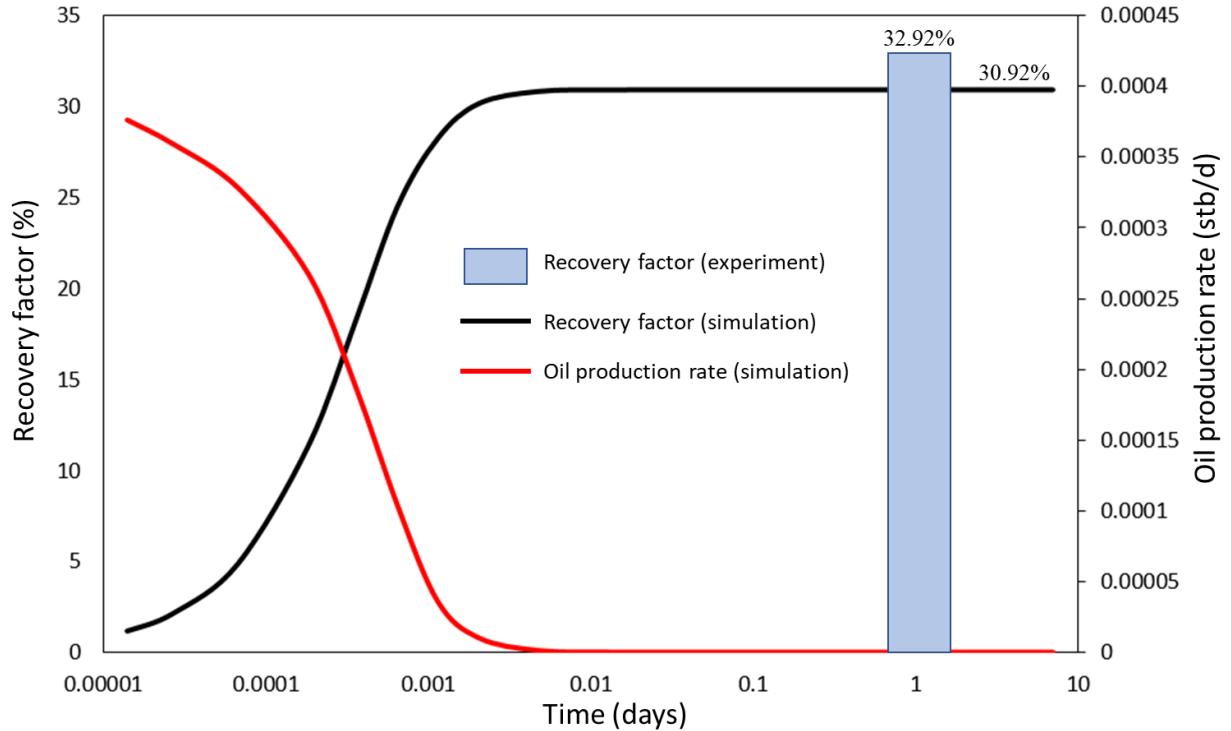
Figure 4.38. Recovery profile for CO_2 injection EOR in the low-permeability TMS core

A closer look at the oil displacement mechanism of the immiscible CO_2 injection in the low-permeability TMS model was taken by examining the change in mole fraction of the hydrocarbon components in the oil phase (see Figure 4.39). As shown, at immiscible conditions, CO_2 injection can enhance oil recovery by vaporizing the lighter hydrocarbons, namely C_1-C_4, in addition to N_2 and CO_2 which are present in the oil phase. The notable decrease in mole fraction of these oil components gave rise to a corresponding increase in mole fraction of the intermediate to heavy components, namely C_5 to C_{30} - and beyond – as shown in Figure 4.39.
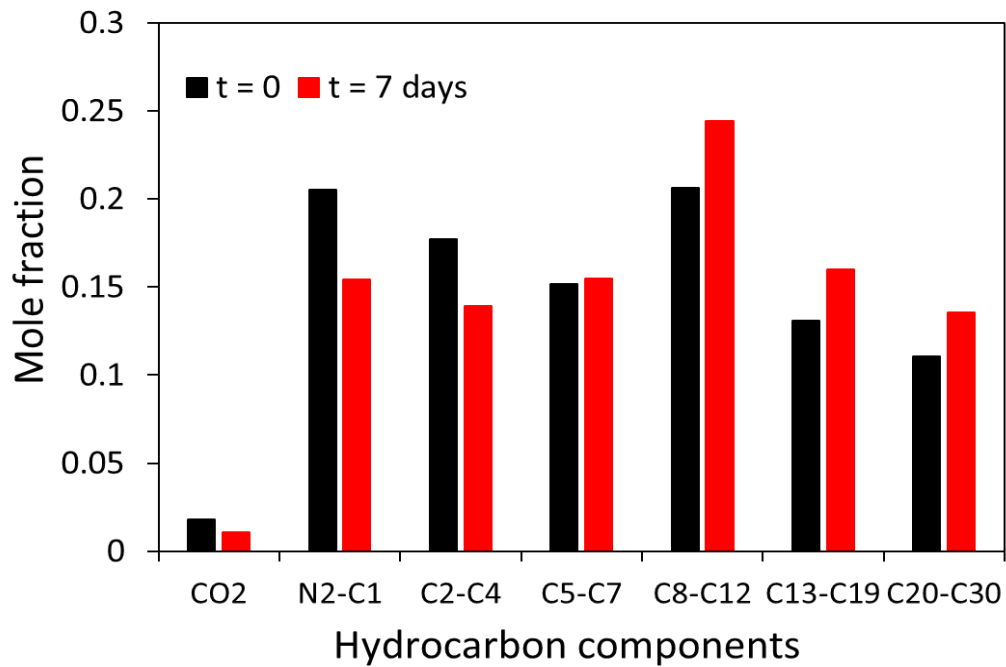
Figure 4.39. A plot of mole fraction of hydrocarbon components in the oil phase during CO_2 injection shows the effect of immiscible CO_2 EOR on the vaporization of light hydrocarbon components.

A sensitivity analysis study shows that the injection pressure has a significant effect on oil recovery obtainable via CO_2 injection due to the effect of miscibility , as seen in Figure 4.40. Increasing the injection pressure from 1000 psi to 2000 psi significantly increased recovery efficiency, from 31% to 100% as CO_2 became miscible with the oil, eliminating oil/gas interfacial tension and capillary pressure.
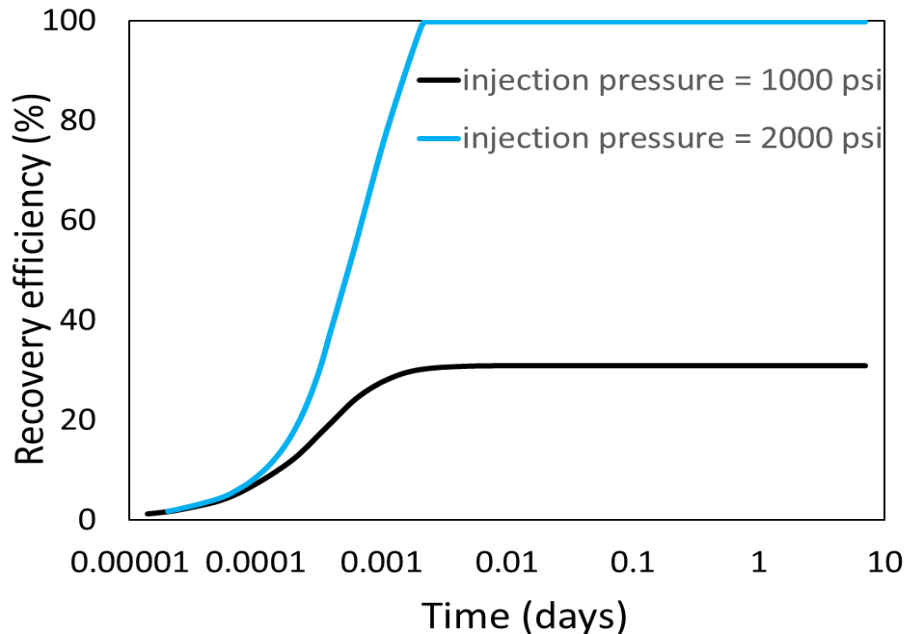
Figure 4.40. Sensitivity study on injection pressure shows that increasing CO_2 injection pressure from 1000 psi to 2000 psi can improve recovery factor from 31% to 100% due to miscibility attainment

The development of miscibility at 2000 psi in terms of the interactions of CO_2 with the hydrocarbon components can also be studied by examining the mole fraction profiles of the components along the entire length of the TMS core, from point of injection to production (see Figure 4.41 and Figure 4.42). As shown in Figure 4.41, the profile of CO_2 mole fraction in the oil phase before start of CO_2 injection was at equilibrum conditions; however, a sudden increase in mole fraction of CO_2 in oil – especially near the injector - was observed after 30 s of CO_2 injection. The profile appears to relax after 1 min of CO_2 injection was observed, which because some of the oil components also goes into the CO_2 phase as miscibility is being developed. As shown, nearly all of the CO_2 in the oil phase were completely expelled into injected CO_2 gas to attain complete miscibility after 1 min 30 s of CO_2 injection. Correspondingly, a significant change in the mole fraction profile for the hydrocarbon components was noticed, as shown in Figure 4.42. A sharp decrease in mole fractions of the light and intermediate hydrocarbon components in the oil phase,

150

namely C_1 to C_4, and iC_5 to C_{12} respectively, especially near the injector, was observed after 30 s of CO_2 injection. This led to a corresponding increase in the mole fractions of the heavy ends, such as C_{13}-C_{19} and C_{20}-C_{30}. After 1 min of CO_2 injection, more light and intermediate components were vaporized into the injected CO_2 and produced, leaving behind the heavier hydrocarbons. Over, at complete miscibility, all of the components were produced, as CO_2 eliminated oil/gas interfacial tension and capillary pressure. However, it is recommended to perform minimum miscibility pressure experiments using the Vanishing Interfacial Tension (VIT) technique reduce the uncertainty associated with this study and support the simulation results on CO_2 injection at immiscible and miscible conditions presented herein. Nonetheless, these findings clearly show the potential of CO_2 injection in low-permeability TMS and some underlying drive mechanisms for oil displacement.
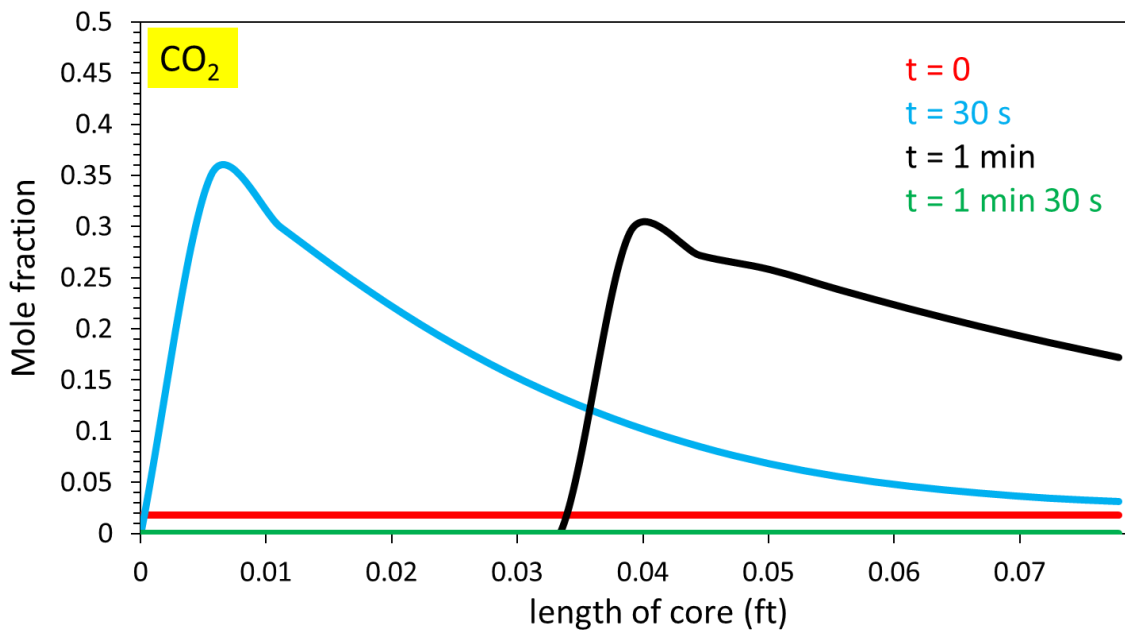
Figure 4.41. The mole fraction profile of CO_2 in the oil phase along the length of the low-permeability TMS core during CO_2 injection at 2000 psi.
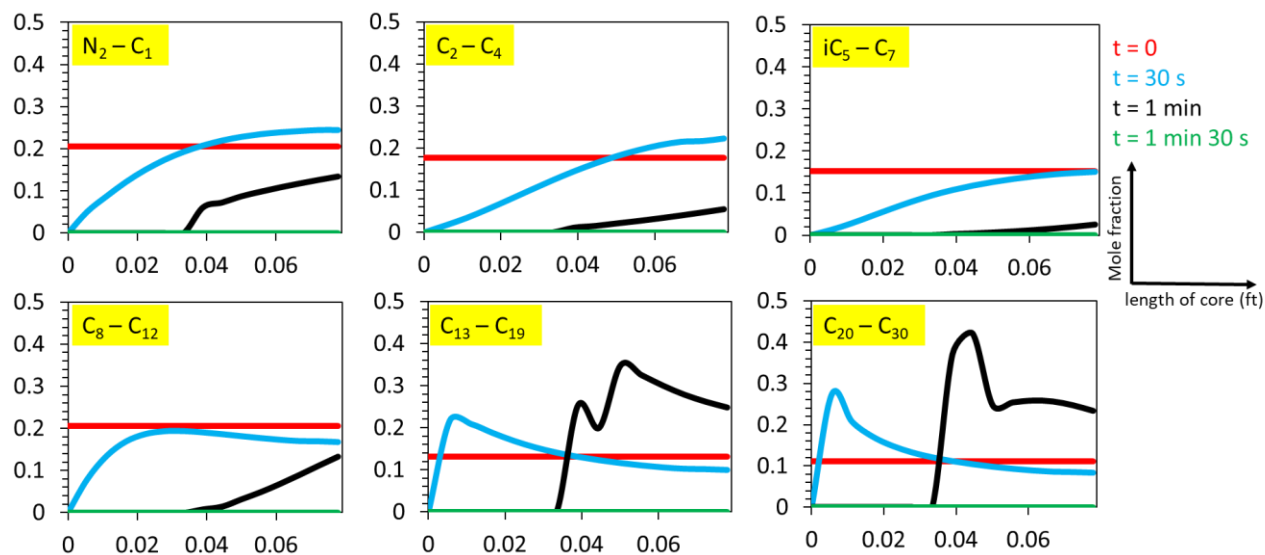
Figure 4.42. The mole fraction profile of the hydrocarbon components in the oil phase along the length of the low-permeability TMS core during CO_2 injection at 2000 psi

In the high-permeability core, recovery profiles obtained with CO_2 EOR and nanofluid-assisted CO_2 EOR were compared with primary production "do nothing" scenario as in the case of a hydraulic fractured well. As shown in Figure 4.43, an ultimate recovery of 23.34% was obtained with primary production and it was observed that the recovery profile plateaued after less than a day of production. CO_2 injection increased recovery by close to 70%, leading to an ultimate recovery of 90.57% after 14 days. When CO_2 was injected for 7 days followed by 7 days of AFB brine injection, the recovery factor was 90.29%, producing 0.26% of oil-in-place less compared to stand-alone CO_2 injection. Similarly, nanofluid-assisted CO_2 EOR provided marginal increases in oil recovery compared to brine-assisted CO_2 EOR or CO_2 EOR. A 7-day CO_2 injection period followed by a 7-day period of 0.5 wt% HNP injection led to a recovery factor of 90.75%. Switching from 0.5 wt% HNP to 0.1 wt% HNP at a pH of 6 during the post-CO_2 injection phase increased recovery factor to 90.86%. Similarly, after CO_2 injection for 7 days, the injection of APTES-modified silica nanoparticle dispersions (0.1 wt% NNP, pH 6) over the same time span, in place of 0.1 wt% HNP at pH of 6, led to an ultimate recovery of 90.86%. For the EOR injection scenarios

examined, it is generally observed that there was a rapid acceleration of oil production during the CO_2 injection phase, similar to what was observed in the case of the "do nothing" scenario.
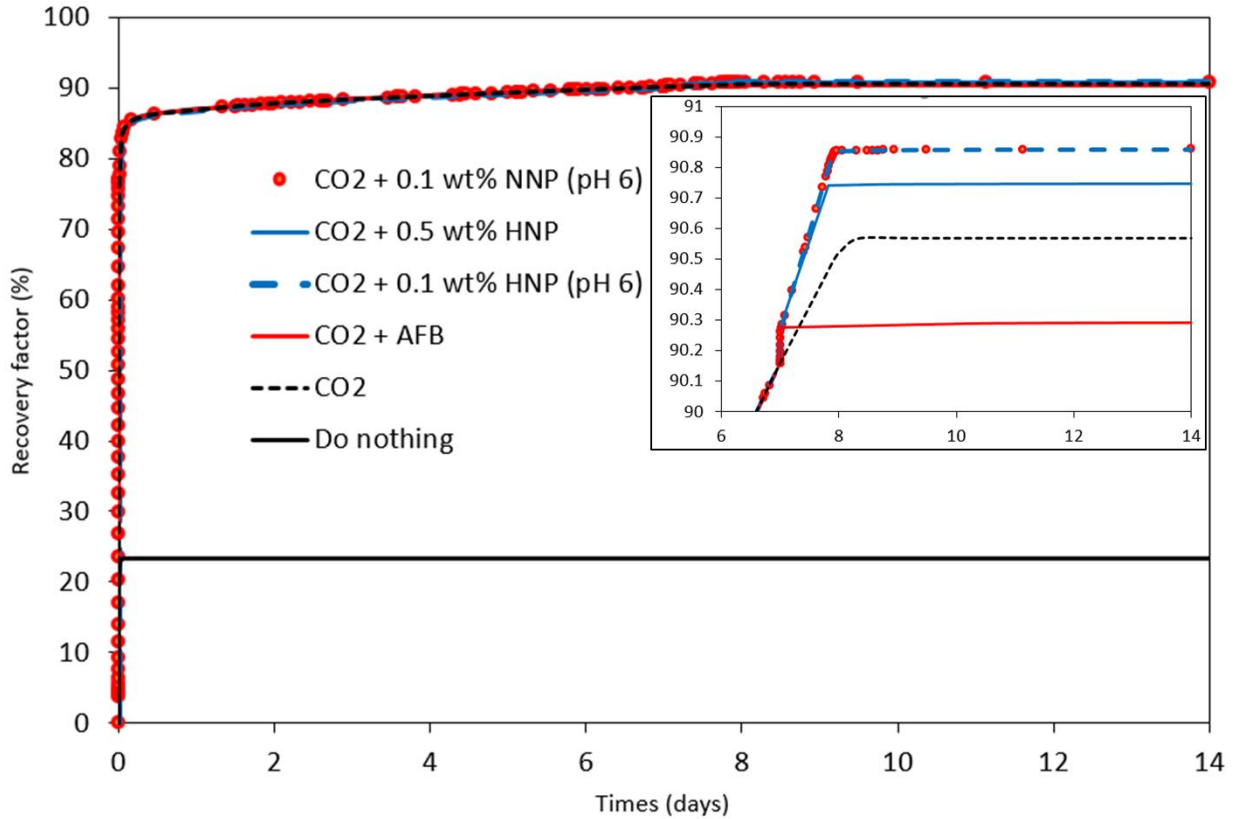
Figure 4.43. Oil recovery profile using nanofluid-assisted CO_2 EOR for the high-permeability TMS core

4.3.5.   Discussions

In this study, a core-scale investigation of nanofluid-assisted CO_2 EOR in the most productive oil-bearing zone of the Tuscaloosa Marine Shale was conducted. A high-pressure CO_2 injection EOR experiment was performed in a tight TMS rock, and compositional simulation of CO_2 and nano-CO_2 EOR process in tight and fractured rock systems were conducted following comprehensive equation-of-state fluid characterization and modelling of capillary pressure and relative permeability curves. In this section, the results are discussed in view of the applicability of CO_2 EOR and nano-enhanced CO_2 EOR in TMS and the importance of a systematic multi-scale investigation.

The recovery factor obtained from the high-pressure CO_2 coreflood experiment in the tight TMS rock was 32.92% which indicates that CO_2 injection has a promising potential in the TMS HRZ with the poorest reservoir quality, in terms of porosity and permeability. In the context of shale oil recovery in the US industry, ultimate recovery estimates via hydraulic fracturing and horizontal drilling in most US tight oil reservoirs are no more than 10% and this study shows that CO_2 injection can provide up 3x this value. It was also observed that the injection of CO_2 accentuated the splitting of TMS core along bedding planes but it remains to be known whether these "cracks" considerably affect the performance of CO_2 injection at field scale – especially if the cracks become extensive and are in concert with hydraulic fractures created across the sandface in horizontal wells. It is also possible that this may be of less of an issue at the field scale, due to effects of overburden pressure and reservoir compaction.

Reservoir fluid properties have a significant impact on fluid phase behavior, so it is important to adequately characterize the fluids in TMS using relevant laboratory data. The Peng-Robinson equation-of-state were tuned using experimental PVT data from differential liberation, constant composition expansion and reservoir fluid composition experiments and excellent match was obtained between the PVT models and lab data (see Figure 4.32). The oil viscosity data was also excellently matched with the Jossi-Stiel-Thodos (JST) correlation.

Next, the workflow displayed in Figure 3.20 was implemented to model capillary pressure and relative permeability curves as a function of micron-scale experimental data such as IFT, DDDC contact angle and special core analyses conducted elsewhere (Lohr and Hackley, 2018). The resulting relative permeability curves were then compared with log-based relative permeability data for the water phase, for the low-permeability and high-permeability regions in TMS. The relative permeability curves showed that the TMS HRZ is strongly water-wet, having

the K_{ro}/K_{rw} crossover point (> 0.5) and initial water saturation criteria according to Craig's rule of thumb (see Figure 2.2 and Figure 4.33). The existence of a strongly water-wet pore network in TMS was also observed during an NMR study performed elsewhere (Besov et al., 2017) and from DDDC advancing contact angle of 45° measured at the micron-scale in this study. The close match obtained between the modelled relative permeability curves and the log-derived water relative permeability data is indicative of: the reliability of the workflow designed herein; the similarity of the AFB brine composition and the actual in-situ formation water composition; and the accuracy of IFT and contact angle measurements. Characterization of shale wettability is a research area of growing interest (Arif et al., 2021) and this study contributes meaningfully to the existing body of knowledge.

It is seen that the oil/water (AFB) capillary pressure for the low-permeability zone is in the range of 0-150 psia because the arithmetic average permeability for this zone is 0.02 mD. As reported by a group of authors (Lohr and Hackley, 2018), absolute permeability in TMS HRZ in Mississippi location is in the range of 0.000004 - 0.002 mD and the resulting capillary pressure is in the range of 700 – 6000 psia. It is also noticed that the oil/gas capillary pressure both for the low- and high-permeability zones (Figure 4.34) are significantly lower than the oil/water capillary pressures (shown in Figure 4.33b) due to the higher degree of interactions -such as compositional variations and mass transfer - between oil and gas phases compared to oil and water phases.

When TMS rock/oil/brine (or nanofluid) systems were studied at the micron scale, hydrophilic silica dioxide nanoparticle dispersions significantly impacted the water advancing contact angle while APTES-modified dispersions significantly reduced interfacial tension, so it is expected that these will translate to a change in capillary pressure and relative permeability curves at the core scale. This was confirmed in Figure 4.36 and Figure 4.37. The optimal concentration

of hydrophilic silica-based nanofluid which is 0.5 wt% HNP as identified from nano-to-micron scale resulted in lower capillary pressure compared to AFB due to reduction in IFT and contact angle. However, NNP at 0.1 wt% and pH of 6 resulted in the lowest capillary pressure due to the largest decrease in IFT obtained with surface-functionalized silica nanoparticles, from 14 mN/m in AFB to 1 mN/m. On the other hand, unmodified silica nanoparticles (0.1 wt% HNP, pH of 6) resulted in a higher IFT to 21 mN/m which further increased capillary pressure even more than AFB. Correspondingly, silica-based nanofluids increased oil relative permeability and reduced water relative permeability compared to AFB.

A recovery factor of 30.92% was obtained with CO_2 EOR core-scale simulation in a low-permeability TMS core, which is in excellent agreement with the recovery factor of 32.92% obtained from the high-pressure coreflood experiment. The simulation result showed that recovery profile plateaued after ~1 day of CO_2 injection, exactly how long the coreflood experiment lasted for and further indicating the technical feasibility of CO_2 injection in low-permeability regions of TMS HRZ. In an actual field development scenario, the invasion of silica nanoparticles in pores with nanometer size distribution may lead to severe permeability impairment, which explains why injection of nanofluids in the low-permeability model were not simulated. The SEM micrographs obtained in this study confirms the possible existence of a fractal pore morphology in the low-permeability TMS rock (see Figure B. 2 in Appendix B). Pores of 222 nm – 778 nm in diameter were characterized on the surface of the TMS rock, but subsequent cutting using focused ion beam to obtain a cross-sectional image revealed the presence of smaller pores, which can be small as 49 nm in diameter. As such, the injection of silica nanoparticles of 16 nm in diameter may potentially lead to severe permeability impairment.

In a strongly water-wet high-permeability reservoir, water occupies the smaller pores, forming extensive and continuous films on pore surfaces which aid imbibition and leads to rapid displacement of the oil phase from the bigger pores to production wells. The water-wetting phase also favors the interaction of CO_2 with the oil at the center of the pores and accelerate oil production during CO_2 EOR. As shown in Figure 4.43, oil recovery efficiency profiles of the high-permeability model after primary production and EOR generally reveal a steep initial production phase followed by a plateau phase as in the case of primary production – or "do nothing" – scenario or a gradual phase as in the cases of CO_2 and nanofluid-assisted CO_2 injection scenarios. The steep initial phase is primarily caused by the strongly-water wet state of the TMS model; in an oil-wet reservoir, the oil recovery efficiency gradually increases with pore volume of fluid injected over time before reaching a plateau (Todd and Somerville, 2014). Figure 4.43 revealed the advantage of CO_2 EOR scenario over the do-nothing scenario: the former generated a recovery factor of 90.57% compared to 23.34% obtained with the latter. However, the initial water-wet state of the high permeability TMS model masked the potential benefits of injecting brine after CO_2 injection and injecting nanofluids in place of brine (post-CO_2 injection). AFB-assisted CO_2 injection recovered 90.29% oil-in-place (OIP) and silica nanoparticle dispersions (0.5 wt% HNP, 0.1 wt% HNP at pH of 6 and 0.1 wt% NNP at pH of 6) recovered between 90.75% and 90.86% of oil in place. Therefore, the existence of an initially oil-wet state is an important criterion for screening naturally fractured shale oil reservoirs such as TMS for the field-scale deployment of silica-based nanofluid EOR.

A mineral known to promote oil wetness is calcite. The IEP of calcite is between 7-11, which implies that calcite surfaces will be positively charged at typical reservoir conditions such as in TMS where the pH is less than 7. The negative charges carried by COO^- in crude oil binds to

Ca^{2+} at the calcite surface, forming organometallic complexes and promoting oil wettability. As such, calcite mineral mainly found in carbonate reservoirs are known to be mostly oil-wet (Afekare and Radonjic, 2017), which suggests that carbonate rocks or carbonate-rich shale reservoirs can be excellent candidate reservoirs for hydrophilic silica-based nanofluid EOR or nanofluid-assisted CO_2 EOR, as previously shown (Haeri and Rao, 2019). The silica nanoparticles can render the positively charged calcite surface negatively charged, which will promote electrostatic repulsion from negatively charged crude oil molecules and shift wettability towards less oil wet. In this study, a closer examination of the relative permeability data obtained from well logs identified some outlier data points: very low water relative permeability values of 0.02-0.2 were observed at water saturation range of 0.2-0.4, as shown in Figure 4.44. The mineralogical data from TMS HRZ revealed that these areas contain significant amounts of calcite (10-24%) compared to the zone of focus in this study which predominantly contains clays and quartz (87%), with trace amounts of calcite (<5 %).

A broader look at the entire well logging data for the TMS (within and outside HRZ) revealed a strong correlation between the calcite content and relative permeability to water (see Figure E. 1 in Appendix E). Within the HRZ where the reservoir has very low calcite content (0 - 5%), the initial water saturation was high (0.6), and majority of the water relative permeability curve are in the region of 0.6-1 in terms of water saturation. This may indicate a cross-over saturation point of greater than 0.5 and thus confirm water-wetness. However, calcite content appears significant outside the HRZ. In these regions with high calcite content, from 10% to say 95%, the initial water saturation was significantly lower (0.2-0.4) and the relative permeability data points were between 0.2 and 0.7 in terms of water saturation, which may suggest a change in wettability state from water-wet to oil wet. Thus, it is recommended to comprehensively study

areas in TMS with notable presence of calcite mineral in the context of nanofluid-assisted CO_2 EOR.
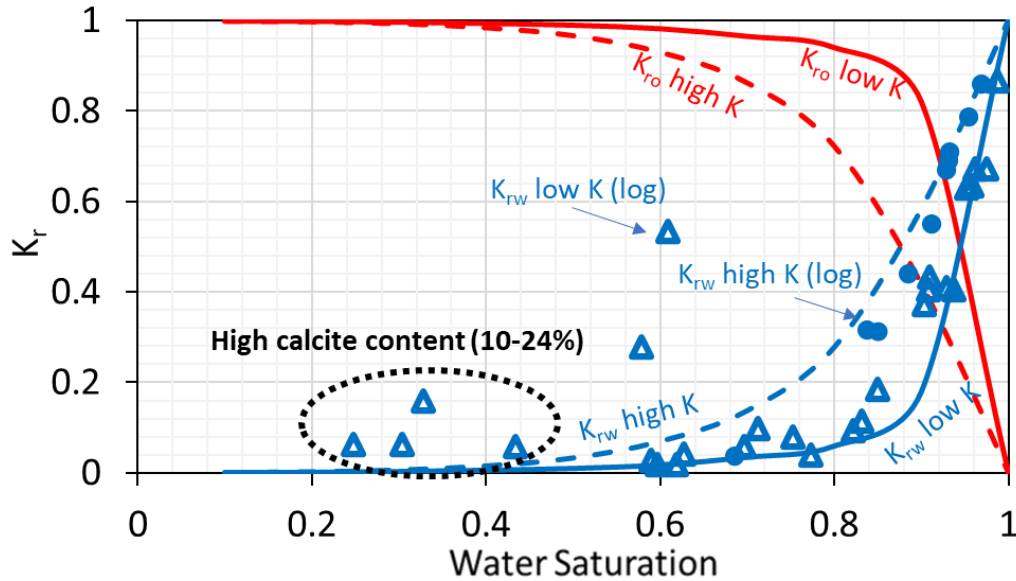
Figure 4.44. The log-derived relative permeability data obtained in TMS HRZ shows the effect of effect of calcite content on relative permeability to water

Another reason for the marginal incremental recovery obtained could be because a change in residual oil saturation – which is a direct indication of microscopic displacement - was not implemented in the simulator. These results can be corroborated with recovery data from coreflood experiments in high-permeability TMS cores which were not performed due to the non-availability of high-permeability cores from the sampled well. As some researchers (Tovar et al., 2014) have shown, using fractured pieces of available low-permeability TMS rocks with glass beads, for example, could replicate a high-permeability shale rock system but the fissile nature of TMS and the potential permeability damage from invasion of nanoparticles constitute significant operational constraints.

Overall, using Tuscaloosa Marine Shale as a case example, this study has shown that the core-scale potential of nanofluid-assisted CO_2 EOR in naturally fractured shale oil reservoirs can

be adequately investigated based on sufficient reservoir fluid and rock characterization as well as multiscale, physics-based modelling of relative permeability and capillary pressure curves for oil, gas and water phases.

5. CONCLUSIONS AND FUTURE WORK

5.1. Conclusions

In this study, a systematic nano-to-core scale characterization of nanofluid-assisted CO_2 EOR was performed, using a series of high-resolution analytical tools, precise material characterization and wettability measurement techniques, mathematical models and core-scale multiphase flow simulation software.

Consequently, the following conclusions are drawn:

- The objective of the nanoscale study to investigate the wettability alteration performance of silicon dioxide nanoparticles at the nanoscale and expand current scientific understanding in the context of nanofluid EOR was successfully met. At the nanoscale:

  o Atomic force microscope investigations performed at ambient conditions showed that aqueous dispersions of hydrophilic silicon dioxide nanoparticles (HNP) can effectively improve nanoscale wettability alteration (towards less water-state) by significantly decreasing rock-oil adhesion force (by over 70%) and work of adhesion (by over 95%) required to spontaneously desorb alkane (-CH_3), aromatic (-C_6H_5) and carboxylate (-COOH) compounds predominantly found in TMS crude oil from pure mineral surfaces of mica (clay substitute) and quartz. On the basis of force spectroscopy evaluations, 0.5 wt% HNP was found to be the optimal nanofluid concentration for hydrophilic silica nanoparticles. The broad implication is that silica nanoparticle dispersions can recover non-polar and polar crude oil species from shale rock surfaces predominantly containing clays and quartz minerals.

o In a pH-controlled environment (pH of 6), the grafting of aminosilanes (APTES; containing the $-NH_2$ group) onto the surface of hydrophilic silica nanoparticles generally led to an increase in adhesion force and surface energies compared to bare nanosilica materials, AFM studies showed. Compared to 0.1 wt% HNP at pH of 6, APTES-modified silica nanoparticles (0.1 wt% NNP) increased adhesion force of $-CH_3$, $-C_6H_5$ and $-COOH$ functional groups to mica by 140-700%, and in turn increased adhesion energy by 300-1400%. The same cannot be said for quartz, however, which indicates that mineralogical composition plays a significant role in nanoscale wetting effects. APTES-modified silica nanoparticles increased adhesion force of $-CH_3$ species to quartz by 35% whereas it decreased adhesion force of $-C_6H_5$ to species and $-COOH$ species to mica by over 65% and almost 20% respectively. In turn, the adhesion energy between $-CH_3$ species and quartz increased by 65% whereas adhesion energy decreased between $-C_6H_5$ species and mica and $-COOH$ species and mica by over 80% and over 30% respectively.

o A deeper look into the elemental force curves from AFM studies showed that adhesion force is a resultant of different intermolecular forces such as electrostatic repulsion, non-electrostatic adhesive force, and structural interactions. As such, hydrophilic silica nanoparticles effectively decreased adhesion force by increasing electrostatic repulsion and reducing the non-electrostatic adhesive force component. The zeta potential and pH data supported the increased electrostatic repulsion effects: with a z-potential range of -23 mV and – 26 mV at pH of 57.5 to 8.5, the HNP solutions will render the quartz and mica surfaces negatively charged

since both minerals have an IEP of 2-3. Resultantly, the electric double layer expands in the presence of similarly charged molecules such as those of carboxylate (–COOH⁻) compounds. The surface free energies of the hydrophilic silica nanoparticles led to the creation of a chemical potential gradient at the rock/fluid interface which reduced the non-electrostatic component of adhesion force. On the other hand, APTES-modified silica nanoparticles increased adhesion force compared to unmodified hydrophilic silica nanoparticles partly by reducing electrostatic repulsion. The positive charges on surfaces of the modified nanoparticles (zeta potential of +12 mV at pH of 6) will render the mica and quartz surfaces positively charged, compress the electric double layer and increase adhesion force of negatively charged species as carboxylate (–COOH⁻) compounds. The increase in adhesion force of functional species to mica at high concentration of HNP media and increase in adhesion force due to silanization of silica nanoparticles can be partly attributed to emergence of structural forces. As these nanoparticles become exceedingly large in number (2 x 10^{15} particles per ml or 1 wt% HNP), they tend to be confined, ordering themselves in discrete layers and exhibiting structural forces. The structural forces favor interparticle interactions at the expense of chemical interactions between the nanoparticles and the mineral substrates, thus increasing adhesion force. The presence of –NH₂ group screens the interparticle charges to promote aggregation, self-assembly and structural forces. Structural forces are complex in nature and require more thorough research in the context of surface forces and thermodynamics of wetting films.

- Hydrophilic silica nanoparticles irreversibly adsorb on pure minerals of mica and quartz and on TMS rocks, as AFM data and SEM micrographs showed. AFM force measurements showed that silicon dioxide nanoparticles irreversibly adsorb on quartz and clay surfaces in a manner that has the potential to augment the performance of brine-alternate-nanofluid EOR treatments at nano to core scales and reduce the amount of nanofluids to be injected. Yet, the adsorption and aggregation of silica nanoparticles on shale rocks, as seen from SEM micrographs, can pose a formation damage concern.

- The objective of the micron-scale characterization study to differentiate the impact of silica nanoparticles on rock/fluid interactions (surface wettability effects) and fluid/fluid interactions (interfacial tension effects) was successfully fulfilled. At the micron-scale:

  - Hydrophilic silica nanoparticles (HNP) showed a great potential for enhancing oil recovery in quartz- and clay-rich shale oil reservoirs through wettability modification but not through interfacial tension reduction. Results from optical tensiometer tests conducted at ambient conditions showed that HNP solutions generally had a modest effect on interfacial tension when micron-sized droplets of single-component hydrocarbons carrying $-CH_3$, $-C_6H_5$, and $-COOH$ functional groups as well as actual TMS crude oil were tested in nanofluid media. compared to artificially prepared brine AFB, the optimal HNP concentration of 0.5 wt% decreased $-CH_3$/HNP IFT from 34 mN/m to 33 mN/m, increased $-C_6H_5$/HNP IFT from 18 mN/m to 22 mN/m, decreased $-COOH + C_6H_5$/HNP IFT from 17 mN/m to 10 mN/m and TMS oil/HNP IFT from 14 mN/m to 8 mN/m. However, precise micron-scale wettability characterization using the dual-drop dual-crystal

technique showed that hydrophilic silica nanoparticles (HNP) at 0.05-1 wt% reduced advancing contact angle measured between the TMS oil droplet, the shale rock surface and AFB brine from 45° (water-wet state) to 0 (perfectly water-wet state): the oil droplet on contacting the shale rock surface immediately retracted and migrated upwards towards the oil/water interface.

o In a pH-controlled environment (pH 6), the grafting of aminosilanes onto the surface of hydrophilic silica nanoparticles (NNP) led to a further reduction in IFT but a lower decrease in advancing contact angle compared to HNP at 0.1 wt% concentration. As such, these APTES-modified silica nanoparticles showed a great potential for enhancing oil recovery in quartz- and clay-rich shale oil reservoirs through wettability modification and interfacial tension reduction. Results from optical tensiometer tests at ambient conditions showed that, compared to AFB brine, 0.1 wt% NNP decreased –CH_3/HNP IFT from 34 mN/m to 7 mN/m, increased -C_6H_5/HNP IFT from 18 mN/m to 7 mN/m, decreased –COOH + C_6H_5/HNP IFT from 17 mN/m to 2 mN/m and TMS oil/HNP IFT from 14 mN/m to 1 mN/m. The DDDC results showed that NNP reduced TMS rock/oil/brine advancing contact angle from 45° in brine (water-wet state) to 20° (more water-wet state).

o From the Young-Dupre equation, the resulting adhesion force calculations for the TMS oil/rock/nanofluid are in excellent agreement with nanoscale adhesion force measurements for pure minerals and functional groups. Hydrophilic silica nanoparticle dispersions at all concentrations tested decreased adhesion force of TMS crude oil to the shale rock surface (0.753 μN to 0); at the nanoscale, HNP

solutions significantly reduced adhesion force of $-CH_3$, $-C_6H_5$ and $-COOH$ groups to mica and quartz surfaces. compared to HNP solutions, dispersions of APTES-modified silica nanoparticles (NNP) increased adhesion force of TMS crude oil to TMS shale rock; at the nanoscale, NNP generally increased adhesion force of $-CH_3$, $-C_6H_5$ and $-COOH$ functional groups especially to mica (clay substitute) surfaces. The TMS shale contains 44% clays and 43% quartz, and with the former being more reactive, it appears that clay minerals on TMS predominantly dictate the response to the oil release mechanisms of silica nanoparticles.

o The observed impacts of silica nanoparticles on fluid/fluid and rock/fluid interactions directly linked to surface and intermolecular forces observed at the nanoscale. Hydrophilic silica nanoparticles effectively decreased adhesion force by reducing contact angle, which is in turn effectively reduced by increasing electrostatic repulsion and reducing the non-electrostatic adhesive force component. The zeta potential and pH data supported the increased electrostatic repulsion effects: with a z-potential range of -23 mV and $-$ 26 mV at pH of 57.5 to 8.5, the HNP solutions will render TMS rock surfaces negatively charged since the main minerals - namely quartz and clays - have an IEP of 2-3. Resultantly, the electric double layer expands in the presence of similarly charged molecules in TMS oil such as those of carboxylate ($-COOH^-$) compounds. Carboxylate compounds are highly surface-active and significant control the response of crude oil compounds to interfacial effects. As such, the contact angle effects observed with TMS crude oil can be linked to the $-COOH$ compounds present. The surface free energies of the hydrophilic silica nanoparticles led to the creation of a chemical

166

potential gradient at the rock/fluid interface which reduced the non-electrostatic component of adhesion force. On the other hand, compared to unmodified hydrophilic silica nanoparticles, APTES-modified silica nanoparticles increased adhesion force partly by increasing advancing contact angle. The increase is contact angle arises partly by reduction in electrostatic repulsion at the TMS rock/fluid interface. The positive charges on surfaces of the modified nanoparticles (zeta potential of +12 mV at pH of 6) will render the mica and quartz surfaces positively charged, compress the electric double layer and increase adhesion force of negatively charged species as carboxylate ($-COOH^-$) compounds in TMS crude oil. The positive charges on the nanoparticles' surfaces is also primarily responsible for the notable effect on IFT reduction: the oil/water interface has a negative charge (due to hydroxyl ion adsorption), and the introduction of positively charged functionalized particles will tend to neutralize the interface charge, leading to a significant reduction in IFT.

- The objective of the core-scale study to evaluate nanofluid-enhanced CO_2 EOR for TMS using nano-to-micron scale data in conjunction with reservoir rock and fluid characterization was successfully achieved. At the core scale:
  - A customized, high-pressure (1000 psi) coreflood experiment was successfully conducted to evaluate CO_2 EOR potential in a low-permeability (0.07 mD) TMS core. A recovery factor of 33% was obtained, which indicates that immiscible CO_2 injection has promising potential to recover a significant amount of oil-in-place in shale oil reservoirs.

167

o   CMG WinProp, a commercially available fluid property characterization software, was used to perform comprehensive reservoir fluid characterization for TMS. The Peng-Robinson Equation-of-state was tuned to accurately match laboratory results of PVT experiments such as differential liberation, constant composition expansion, reservoir fluid composition, flash expansion and separator tests. Consequently, accurate regression models of PVT properties such as oil and gas formation volume factor, z factor, gas viscosity, bubble point pressure and gas oil ratio were obtained. The Jossi-Thodos-Steidel correlation was used to adequately model oil viscosity. The TMS was identified as a black oil reservoir, with bubble point pressure of 1417 psia, initial reservoir pressure and temperature of 7497 psia and 260°F respectively.

o   An extensive TMS reservoir rock characterization study was conducted, using available formation evaluation and well logging data, to delineate the most profilic hydrocarbon-bearing zone in TMS – known as the high-resistivity zone (HRZ) – and evaluate the main petrophysical properties which are permeability and porosity. The HRZ was delineated between from 15289.5' – 15467.5' TVD using the deep, medium and shallow resistivity logs as well as the total organic content data. The permeability-porosity relationship exhibits a strong correlation, with $R^2 = 0.8$. Two distinct regions were identified: the low-permeability region, with average porosity of 0.08 and 0.02 mD respectively; and the high-permeability region, with average porosity of 0.13 and 1 mD respectively. The main geologic minerals identified from the TMS HRZ were quartz, illite and kaolinite clays, which agrees strongly with the XRD results obtained from this study.

o The Leverett J Function and Purcell Model were successfully coupled to derive three-phase capillary pressure curves and relative permeability curves for the low-permeability and high-permeability regions of TMS HRZ as a function of porosity, permeability, as well as interfacial tension and advancing contact angle measured at the micron-scale. The resulting oil/water relative permeability curves were compared with well logging data for the rock relative permeability to water and an excellent match was obtained. The TMS HRZ both within the high-permeability and low-permeability regions were confirmed to be water-wet, which is in excellent agreement with the DDDC- measured advancing contact angle at the micron scale. Compared to brine AFB, hydrophilic and APTES-modified silica nanoparticles showed great potential to enhance oil recovery in the high-permeability regions of TMS HRZ by reducing the oil/water capillary pressure, increasing the oil relative permeability and decreasing water relative permeability.

o Using CMG GEM software package, a core-scale compositional simulation of CO_2 EOR in a low-permeability TMS model was conducted at typical reservoir conditions of 1000 psi and 260°F. Results showed that immiscible CO_2 EOR can improve recovery by up to 31% of oil in place, which strongly agrees with the recovery factor of 33% obtained with high-pressure coreflood experiment of CO_2 EOR. The petrophysical properties, multiphase flow parameters and operational constraints defined in the model were based on the actual properties of the rock and lab conditions set for the coreflood experiments, which makes the comparison justifiable. The experimental and simulation results also confirm that CO_2 EOR can significant volumes of oil-in-place in the TMS HRZ with the poorest reservoir

169

quality, in terms of porosity and permeability by vaporizing light hydrocarbon components. Increasing the injection pressure from 1000 psi to 2000 psi can significantly improve recovery efficiency and aid miscibility development.

o Using CMG GEM software package, different EOR scenarios using CO_2 and silica nanoparticle dispersions were simulated in a high-permeability TMS model at typical reservoir conditions (1000 psi and 260°F) and compared against primary production. Results showed that primary production, which may occur using hydraulically fractured horizontal well for example, can recover 23% of oil in place and immiscible CO_2 EOR can recover up to 91% oil in place by accelerating production due to the water-wet nature of TMS, and altering the phase behavior of in-situ oil components. The combination of CO_2 and silica-based nanofluids provided a marginal increase in recovery (less than 1%) compared to either stand-alone CO_2 EOR or CO_2-alternate-brine injection primarily due to the initial water-wet state of the high-permeability TMS model. Thus, in the context of nanofluid-assisted CO_2 EOR, this study helped reveal an important criterion for taking science to the field: the existence of an initially oil-wet state.

5.2. Suggestions for Future Work

In this research, the enhanced oil recovery potential of silica nanoparticle dispersions were systematically studied across length scales in conjunction with CO_2 EOR at the core scale for potential applications in shale oil reservoirs such as TMS. Oil release mechanisms at the micron and nano scales such as wettability alteration and fluid/fluid interactions were studied in view of surface adhesion forces, interfacial tension measurements and advancing contact angle measurements. Multi-scale, physics-based models were derived for relative permeability and

capillary pressure curves and core-scale experiment and simulations were used to investigate nano-assisted CO_2 EOR in low-permeability and high-permeability TMS systems.

Despite the comprehensive study, analyses and meaningful observations which led to a contribution of relevant and original knowledge in petroleum engineering, certain gaps and limitations were not addressed. Thus, this study has paved way for subsequent research which can be performed to expand the existing body of knowledge in the area of nanofluid and CO_2 EOR for shale oil reservoirs. As a result, the following suggestions are raised, in view of future research directions:

- At the nanoscale, AFM force spectroscopy offer fundamental-level information that can be supplemented with molecular-level simulations as well as other material characterization techniques, for broad EOR screening. For example, pore size profile of rocks will ultimately determine what size and concentration of injected nanoparticles to prevent permeability damage, but this may be less of an issue if reservoir target zones contain highly conductive natural fractures in concert with hydraulic fractures, such as in the case of TMS HRZ. Additional research is required in establishing demarcation boundaries for oil-wet, intermediate-wet and water-wet states in the context of adhesion force measurements. Furthermore, the AFM experiments conducted herein were at room temperature and pressure conditions, and even though adhesion is typically not a pressure-dependent property, theoretical models of surface forces have identified temperature as a controlling factor (Hilner et al., 2016). In the context of shale oil recovery, molecular dynamic simulation studies have identified the adsorption of typical crude oil compounds such as alkane and aromatic hydrocarbons on kerogen, a principal component of the organic pore network in shale reservoirs. A forward approach will therefore be to conduct

force spectroscopy investigations on kerogen surfaces contacted with a range of functional groups in the presence of nanofluid media.

- At the micron scale, this work investigated the effect of silica nanoparticles on interfacial tension and contact angle measurements using the DDDC technique at ambient conditions. A more comprehensive study on the impact of pressure and temperature is recommended to expand the understanding of the performance of silica-based nanofluid EOR at typical shale reservoir subsurface conditions. Performing DDDC contact angle measurements on pure minerals such as quartz and mica and correlating the data to the same measurements on actual TMS rock surfaces will further reveal the contribution of mineralogical composition to surface wettability changes.

- At the core scale, oil displacement mechanisms of CO_2 EOR in shale oils, such as diffusivity, soaking and miscibility, can be studied to enlarge current scientific understanding and further strengthen the case for field applications. The extremely fissile nature of the TMS core samples provided for this study placed an operational restriction on their use in high-pressure high-temperature experiments. Therefore, it is recommended to obtain less fissile shale rocks from several wells and perform coreflood EOR studies to explicitly reveal the potential of CO_2, brine and nanofluid injection. A more comprehensive study on relative permeability and capillary pressure to include hysteresis effects is also recommended to understand the impact of drainage and imbibition paths in the context of multiphase flow through shale porous media.

- Pertinent to reservoir fluid characterization, it is not uncommon for shale reservoirs to have different types of fluid windows (from black oil to wet gas) and thus a variety of PVT datasets, but commercially available simulators such as CMG WinProp can only analyze

172

1-2 sets of PVT data at a time. Thus, machine learning algorithms such as multivariate linear regression, principal component analysis and discriminant analysis can be used to adequately characterize reservoir fluids in shale.

- The understanding of the TMS geology and reservoir architecture is currently limited, as revealed by literature survey and from personal communications with geologists working on TMS. More extensive reservoir characterization, including special core analyses, formation evaluation and geomechanical effects are required to delineate the hydrocarbon-bearing zones, pore size distribution and the impact of stresses on porosity and permeability profiles in TMS. Calcite mineral is known to favor oil wetness and this study has revealed the presence of varying amounts of calcite outside the TMS HRZ. Thus, to identify the initial wetting states of TMS in these zones and study the wettability modification effects of silica-based nanofluid EOR, it recommended to use core samples from the zones with significant amount of calcite mineral.

- In general, research on the use of nanoparticles for oilfield applications only began in just over a decade ago. Thus, an extensive study on a variety of other types of eco-friendly nanoparticles with functionalization of environmentally compatible chemicals such as chitosan-based polyelectrolyte complexes offer a forward approach in nanodispersion EOR research.

APPENDIX A. TMS RESERVOIR FLUID CHARACTERIZATION

Table A. 1. Differential Liberation (DL) Data Obtained from TMS Well PVT Analyses at 260°F

Oil Properties							
Pressure		Liquid Density	Liquid Compress.	Liquid Viscosity	Liberated GLR, R_l	Solution GLR, R_{sd}	Oil FVF, B_{od}
(psia)		(g/cm^3)	(V/V/psi) x 10^6	(cP)	(scf/bbl)	(scf/bbl)	(vol/resid. vol)
9,000		0.746		0.563	0	610	1.442
8,000		0.741	6.84	0.539	0	610	1.451
7,497	Reservoir	0.739	7.07	0.526	0	610	1.457
7,000		0.736	7.34	0.514	0	610	1.462
6,603	FBHP	0.734	7.66	0.504	0	610	1.466
6,000		0.730	8.14	0.488	0	610	1.474
5,000		0.723	9.19	0.461	0	610	1.487
4,000		0.716	10.34	0.433	0	610	1.503
3,000		0.707	12.20	0.404	0	610	1.521
1,417	Saturation	0.690	15.36	0.356	0	610	1.559
1,250		0.699	13.25	0.372	44	566	1.523
1,000		0.708	11.80	0.398	114	496	1.486
750		0.716	10.49	0.429	182	428	1.450
500		0.727	9.40	0.463	252	358	1.408
250		0.739	8.55	0.513	336	274	1.355
15.025		0.770		0.569	610	0	1.107
15.025	at 60 °F	0.851	API = 34.6 °				1.000
Vapor Properties							
Pressure	Gas Density	Gas Z Factor	Incr. Gas Gravity	Cum. Gas Gravity	Gas FVF, B_g	Gas FVF, B_g	Total FVF, B_t	Calc. Gas Viscosity
(psia)	(g/cm^3)	(vol/vol at std)	(Air = 1.00)	(Air = 1.00)	(res bbl /mmscf)	(res cu ft / scf)	(vol/resid. vol)	(cP)
1,250	0.071	0.895	0.850	0.850	2,653	0.01489	1.641	0.016
1,000	0.058	0.906	0.867	0.861	3,357	0.01885	1.869	0.015
750	0.045	0.919	0.908	0.878	4,540	0.02549	2.277	0.014
500	0.032	0.935	0.981	0.907	6,926	0.03888	3.152	0.013
250	0.019	0.957	1.181	0.976	14,187	0.07966	6.125	0.012
15.025	0.002	1.000	2.464	1.644	246,654	1.38486	151.646	0.009

Table A. 2. Constant Composition Expansion (CCE) Data Obtained from TMS Well PVT Analyses

Pressure		Relative Volume	Oil Density	Oil Compressibility	Y-Function
(psia)		(V / V_{sat})	(g/cm^3)	$(DV/V/Dpsi) \times 10^6$	$(P_{sat}-P)/P(V/V_{sat}-1)$
9,000		0.924	0.746		
8,000		0.931	0.741	6.84	
7,497	Reservoir	0.934	0.739	7.07	
7,000		0.938	0.736	7.34	
6,603	FBHP	0.940	0.734	7.66	
6,000		0.945	0.730	8.14	
5,000		0.954	0.723	9.19	
4,000		0.964	0.716	10.34	
3,000		0.976	0.707	12.20	
1,417	Saturation	1.000	0.690	15.36	
1,000		1.208			2.00
800		1.415			1.86
600		1.791			1.72
400		2.624			1.57
200		5.317			1.41

Table A. 3. Reservoir Fluid Composition from Wellhead Zero Flash. Flash Summary (5000 Psia and 260°F to Atmospheric Pressure and 80°F)

		GOR	390	scf/stb	Vapor Gravity	1.115	(Air = 1.00)		
		FVF	1.346	Vsat/Vstd	API Gravity	38.4	°API at 60°F (Water Free)		
Component		Atm. Vapor	Atm. Liquid	Atm. Liquid	MWt.	Specific Gravity	Reservoir Fluid	Reservoir Fluid	
(Symbol / Name)		(mole %)	(mole %)	(weight %)		(Water = 1.0)	(mole %)	(weight %)	
N2	Nitrogen	1.279	0.000	0.000	28.01	0.809	0.515	0.116	
CO2	Carbon Dioxide	4.497	0.000	0.000	44.01	0.818	1.809	0.639	
H2S	Hydrogen	0.000	0.000	0.000	34.08	0.801	0.000	0.000	

	Sulfide						
C1	Methane	49.656	0.046	0.004	16.04	0.300	20.003	2.575
C2	Ethane	13.246	0.234	0.038	30.07	0.356	5.468	1.319
C3	Propane	14.851	1.210	0.285	44.10	0.507	6.698	2.370
iC4	i-Butane	2.242	0.512	0.159	58.12	0.563	1.208	0.563
nC4	n-Butane	6.979	2.589	0.805	58.12	0.584	4.355	2.031
iC5	i-Pentane	2.313	2.277	0.879	72.15	0.624	2.291	1.327
nC5	n-Pentane	1.995	3.345	1.291	72.15	0.631	2.802	1.622
iC6	i-Hexanes	0.869	3.048	1.405	86.18	0.664	2.171	1.501
nC6	n-Hexane	0.447	2.220	1.023	86.18	0.664	1.507	1.042
C6	Methylcyclopentane	0.327	2.022	0.910	84.16	0.754	1.340	0.905
C6	Benzene	0.050	0.308	0.129	78.11	0.883	0.204	0.128
C6	Cyclohexane	0.159	1.378	0.620	84.16	0.783	0.888	0.599
C7	Heptanes	0.412	5.841	3.130	100.20	0.688	3.657	2.940
C7	Methylcyclohexane	0.210	3.257	1.711	98.19	0.775	2.031	1.600
C7	Toluene	0.036	2.716	1.339	92.14	0.874	1.638	1.211
iC8	Iso-Octane	0.051	0.119	0.073	114.23	0.697	0.092	0.084

C8	Octanes	0.183	5.395	3.296	114.23	0.707	3.298	3.023
C8	Ethyl Benzene	0.008	0.529	0.300	106.17	0.874	0.319	0.272
C8	m&p-Xylene	0.024	0.885	0.503	106.17	0.868	0.539	0.459
C8	o-Xylene	0.006	0.322	0.183	106.17	0.885	0.195	0.166
C9	Nonanes	0.085	5.773	3.961	128.26	0.722	3.485	3.586
C10	Decanes	0.075	6.943	4.978	134.05	0.779	4.180	4.496
C11	Undecanes		5.124	4.029	147.00	0.790	3.063	3.612
C12	Dodecanes		4.570	3.936	161.00	0.801	2.732	3.529
C13	Tridecanes		4.789	4.483	175.00	0.812	2.862	4.019
C14	Tetradecanes		4.068	4.134	190.00	0.823	2.432	3.707
C15	Pentadecanes		3.467	3.821	206.00	0.833	2.072	3.425
C16	Hexadecanes		2.864	3.401	222.00	0.840	1.712	3.049
C17	Heptadecanes		2.548	3.230	237.00	0.848	1.523	2.896
C18	Octadecanes		2.389	3.208	251.00	0.853	1.428	2.876
C19	Nonadecanes		2.145	3.017	263.00	0.858	1.282	2.705
C20	Eicosanes		1.636	2.406	275.00	0.863	0.978	2.158
C21	Heneicosanes		1.417	2.205	291.00	0.868	0.847	1.978
C22	Docosanes		1.341	2.188	305.00	0.873	0.802	1.962

C23	Tricosanes		1.146	1.949	318.00	0.878	0.685	1.748
C24	Tetracosanes		1.023	1.811	331.00	0.882	0.611	1.624
C25	Pentacosanes		0.955	1.763	345.00	0.886	0.571	1.580
C26	Hexacosanes		0.825	1.584	359.00	0.890	0.493	1.420
C27	Heptacosanes		0.791	1.583	374.00	0.894	0.473	1.419
C28	Octacosanes		0.712	1.478	388.00	0.897	0.426	1.325
C29	Nonacosanes		0.654	1.407	402.00	0.900	0.391	1.261
C30+	Triacontanes Plus		6.567	21.345	607.53	1.012	3.925	19.134
Total		100.000	100.000	100.000			100.000	100.000
Calculated Molecular Weight		32.06	186.94				124.63	
Measured Molecular Weight			186.94					

Table A. 4. Compositional Groupings of TMS Reservoir Oil Based on Normal-to-Normal Carbon Distribution

Group	Mole %	Weight %	MW	SG	T_b
Total Fluid	100.000	100.000	124.63	0.766	N/A
C7+	51.173	84.895	206.77	0.851	N/A
C10+	33.487	69.922	260.24	0.879	1,123
C20+	10.201	35.607	435.03	0.947	1,409
C30+	3.925	19.134	607.53	1.012	1,613

APPENDIX B. SCANNING ELECTRON MICROSCOPE RESULTS

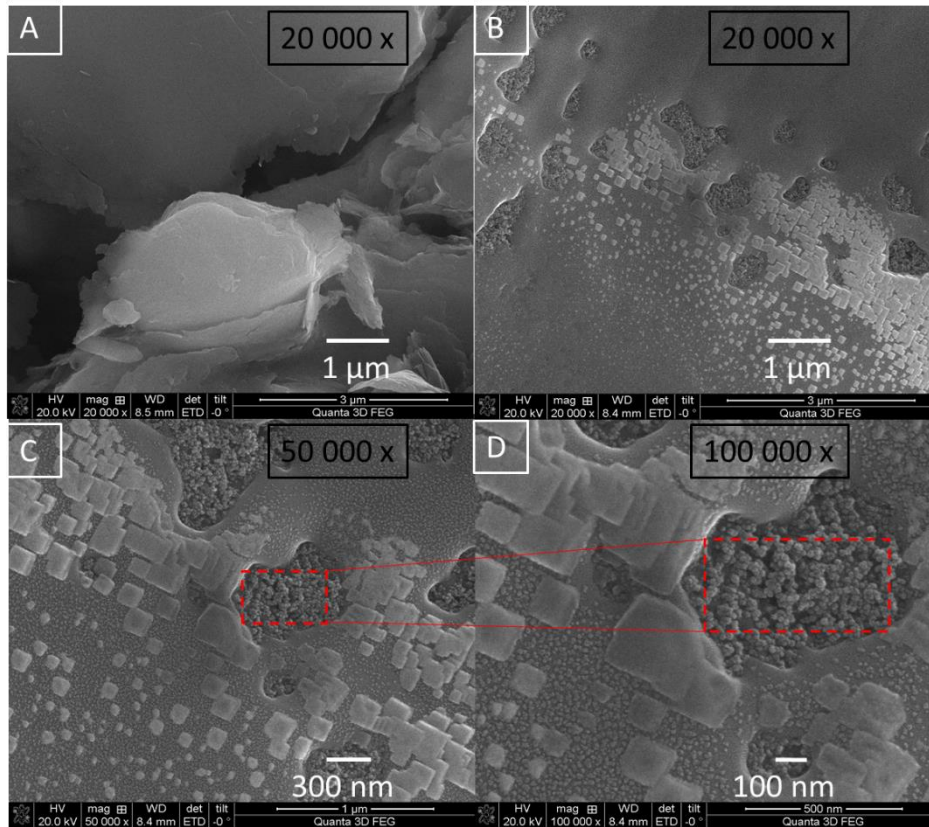Figure B. 1. SEM Micrographs of TMS surfaces without nanoparticles (A) at 20 000 x magnification; with nanoparticles at 20 000 (B), 50 000 x (C) and 100 000 x (D).
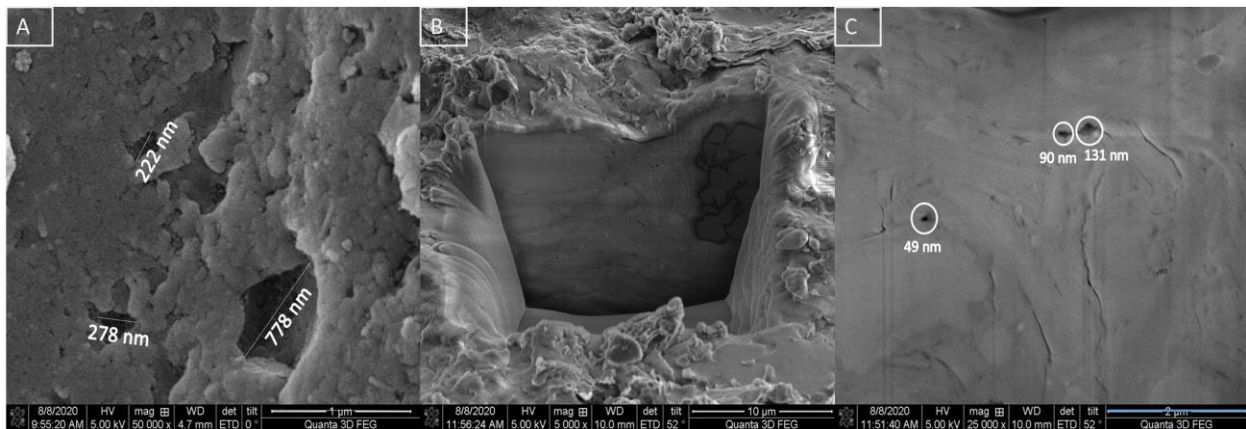

Figure B. 2. Evaluation of TMS pore morphology using SEM: larger pores were characterized on surfaces of preserved rock pieces, after which (B) a focused ion beam cross-section image of the rock was obtained to characterize () smaller pores

APPENDIX C. STEP-BY-STEP GUIDE ON FORCE VOLUME SPECTROSCOPY

This tutorial describes the steps involved in conducting force volume spectroscopy experiments in liquid media. The volume spectroscopy is an extension of force spectroscopy which can be used to characterize the force of interaction between an AFM tip and a sample surface (e.g. mica) in an aqueous environment. This process is followed after the scanning probe system has been prepared for contact mode imaging.

The initial setup for contact mode imaging requires a one-piece nose cone assembly. Conductive tips with a resonance frequency of 17-67 kHz, spring constant of 0.08 – 0.32 N/m and gold coating have been used for contact mode experiments. However, other types of probes may be used.

To setup the SPM for contact mode:

1. Insert the nose cone assembly into scanner

2. Insert a force spectroscopy compatible probe into the nose cone assembly

3. Place the scanner into the microscope and connect its cables to secure in place

4. Align the laser on the cantilever by monitoring through the PicoView software's camera view as well as the detector plate

5. Insert and align the photodetector. The detector is well-aligned when the red dot is well centered and the sum is around 0 V.

6. Prepare the sample and mount onto the sample plate. The sample must be electrically and magnetically insulated from the sample plate to ensure accurate data. For instance it has been observed that the AFM tip directly interacts with the sample plate if the sample itself is a quartz substrate (a conductive material) placed in a liquid cell. In this case, a mica

substrate – or another non-conductive material can be placed on the sample plate before the actual sample is attached.

7. Next, in the PicoView software select **Mode > Contact AFM**

8. If not previously done, select **Controls > Camera view** and observe the tip and sample in the camera window

9. Viewing the window, raise the sample using the **Close** switch on the HEB until the tip very close to, but not touching the sample

10. Next you will "approach" the sample to bring the tip and sample in contact. Key steps involved in this process are:

    a. Note the **Deflection** reading on the HEB front panel, or in PicoView's Laser Alignment window (both should display very similar values, if not same). This is the current cantilever deflection (V).

    b. In PicoView's Servo window, enter a **Setpoint** value slightly more positive than the current Deflection reading. For instance, it is recommended to set the deflection to about -0.2 V to – 0.3 V while maintaining a Setpoint of 0 V, force spectroscopy measurements in air.

    c. Enter representative values for the **I** and **P Gains**. Values between 5-10 have been used.

    d. Now click **Approach** in the PicoView toolbar to contact the sample with the tip.

11. The next step is calibrate the tip by determining the deflection sensitivity and spring constant. The main steps involved are:

    a. Select **Controls > Spectroscopy**

    b. In the resulting window, choose the plot type to be **Force vs Distance**

c. In the Spectroscopy basic tab, click on the 1 button or alternatively the play button to do a single sweep and generate a force curve. It is advisable to do this force curve on a rigid surface like freshly cleaved mica or clean quartz

d. In the resulting window, right click on the approach portion of the curve (red line) – particularly the steep portion which is the contact regime – and **Add Ruler**. Stretch the line as much as possible by moving the endpoints to obtain a representative portion of the contact regime.

e. Right click again and select **Deflection sensitivity (nm/V).** This value is automatically updated in the Advanced tab. For a gold-coated silicon nitride tip on mica in air, an average of 60 nm/V has been recorded.

f. The tip will need be to away from the sample surface to obtain the spring constant. Click on **Withdraw** in the PicoView toolbar**.**

g. In the advanced tab, click **Thermal K**

h. Check for the key parameters and ensure they are correct: acquisition time of 1.0 s, averages of 10, and temperature of 20°C.

i. Click the **Full Span** in the thermal K window

j. Click the **Plot** button. A thermal K plot should appear, with properly pre-defined ranges in which the resonance frequency can be seen. You can adjust this range by dragging the red and green circles.

k. Click the **Compute** button. The software will acquire the chosen number of scans and frequency averages within the chosen range. A best fit curve will be obtained and the integral area under it is used to output the spring constant which will be displayed.

l. More scans may be needed to allow convergence of the averages to a value so one or more additional computations may be required. Click **Compute** again.

m. Once a stable value is obtained, click the **Apply** button so that the spring constant K is registered in the force spectroscopy window

12. Having done calibrations in air, the next step is run the actual force volume spectroscopy experiments in liquids. The previous steps were also useful to determine the closeness of the tip to the sample which may not be easy to identify if a liquid cell is used. The following steps are involved:

    a. Manually lower the sample by using the **Open** switch on the HEB, and remove the sample plate. Also remove the scanner and photodiode detector and safely place elsewhere.

    b. Now place the liquid cell on top of the sample and pin to plate properly. Ensure the sample is well positioned between the plate and the cell so it properly contacts the tip.

    c. Fill the cell with de-ionized water to check if there are leaks around its periphery. Once checked, replace the water with the actual solution of interest. It is advised to use a hand syringe for filling the cell with liquids and also emptying the cell.

    d. Place the system under the AFM and ensure it's well positioned

    e. Carefully re-install the scanner and photodiode detector and follow steps 4-5

    f. Ensure the mode selected in the PicoView software remains **Contact**

    g. In the servo dialog box, check that I and P Gains are properly set. In liquids, a value of 5 has been used.

    h. A Setpoint of **1.5V** has been used and is therefore recommended.

i. Maximize the **Range (µm)** by entering **999** and the software will adjust to the maximum value possible

APPENDIX D. MATHEMATICAL DERIVATION OF WORK OF ADHESION

For a system of interacting bodies such as a sphere and a plane, both JKR and DMT models described adhesion force (N) in the form of:

$$|F_{adh}| = \alpha_{adh}\pi R W_{adh}$$
<div align="right">D. 1</div>

where α_{adh} is adhesion characterization parameter, R is radius of sphere/plane or sphere/sphere area, depending on the system configuration (nm), and W_{adh} is the work of adhesion (N/m). Differences between JKR and DMT models are that α_{adh} is 1.5 (for soft surfaces such as rubber and gelatin) in the former and 2 (hard surfaces such as steel) in the latter. It is known that the JKR model applies to large spheres with a high surface energy and low elastic moduli whereas DMT theory is more suited for small spheres with a low surface energy and high elastic moduli (Leite et al., 2012). Yet, the boundaries for classifying the magnitude of these parameters are not well known.

With AFM force spectroscopy, the work of adhesion can be directly obtained from force-displacement curves (see Figure D. 1) and as was also reported in a previous study (Afekare et al., 2020b). As shown in Figure D. 1, W_{adh} is the colored area (in yellow) between the approach and retract curves as the AFM tip interacts with a surface.
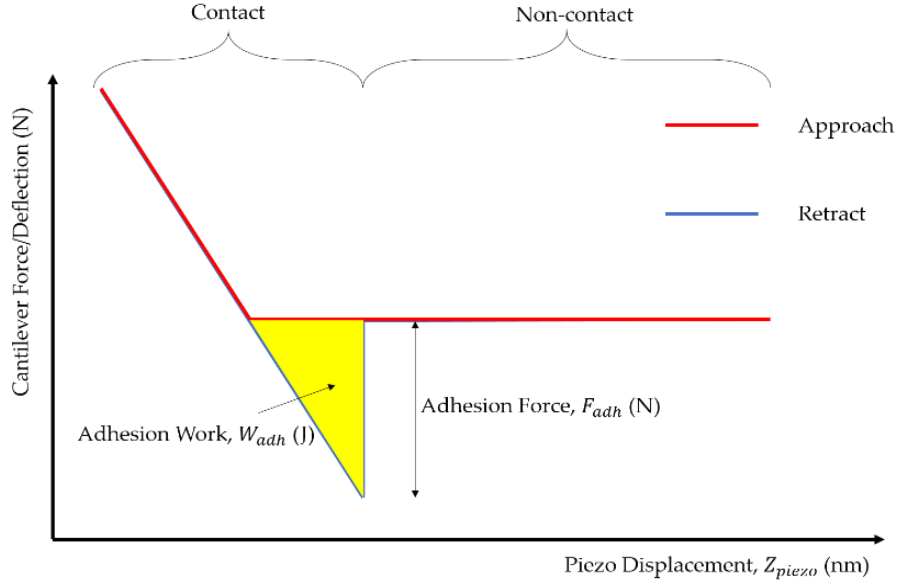
Figure D. 1. Typical force-displacement curve using AFM force spectroscopy

Let the total adhesion force measured under AFM be F_{adh}, with spring constant k_s, cantilever deflection z_{can}, piezo displacement z_{piezo}, true sample-tip separation D and work of adhesion W_{adh}. It then follows that (Butt et al., 2005):

$$F_{adh} = k_s z_{can}$$
<div align="right">D. 2</div>

$$D = z_{can} + z_{piezo}$$
<div align="right">D. 3</div>

At contact regime, $D = 0$ so that z_{can} equals z_{piezo} in magnitude but opposite in sign. W_{adh} from Figure D. 1 is equivalent to the area of a triangle expressed as:

$$W_{adh} = \frac{F_{adh} z_{piezo}}{2}$$
<div align="right">D. 4</div>

or

$$W_{adh} = -\frac{F_{adh} z_{can}}{2}$$
<div align="right">D. 5</div>

Ignoring the negative sign in equation D. 6 (since W_{adh} is a physical property) and substituting z_{can} from equation D. 2 gives (Butt et al., 2005):

$$W_{adh} = \frac{F_{adh}^2}{2k_s}$$

D. 7

where F_{adh} is in N, z_{can}, z_{piezo} and D are in m, k_s is in N/m and W_{adh} is in J. This expression provides a convenient means of obtaining adhesion work based on the adhesion force and spring constant, both of which can be obtained from the force-displacement curve. It also eliminates the need to transform hundreds to thousands of force-displacement curves ($F(z_{piezo})$) obtained per adhesion map to force-distance curves ($F(D)$) (Lorenz et al., 2017). The spring constant was measured to be 0.08 N/m which is the same as provided by the tip manufacturer.

To compare data obtained herein with JKR and DMT models, the adhesion force and the tip radius must be known. An SEM image of the tip cleaned under UV light was obtained (Figure D.2) and the tip radius measured ~28 nm. The measured radius becomes an applicable parameter R in equation D. 1 when the tip directly interacts with the mineral substrate, for instance in brine solutions. However, in the presence of nanoparticles adsorbed on the surface, there are two spheres involved – the tip and the nanomaterial. Several authors have maintained that, for a sphere-sphere interaction, R becomes the product of tip radius (28 nm) and nanoparticle radius (8 nm) divided by their sum (Israelachvili, 2009) which is approximately 6 nm, if we assume that the tip apex always contacts an SiO_2 nanoparticle on approaching the mica substrate.
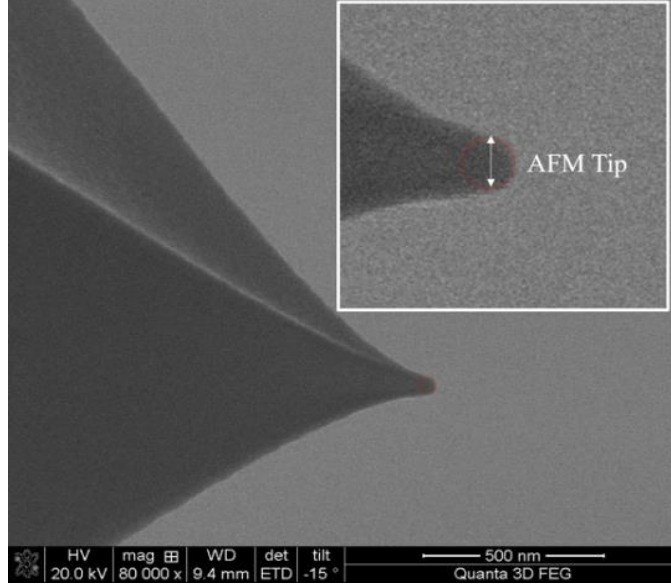
Figure D.2. SEM micrograph of a gold-coated silicon nitride tip (in dark grey) used for AFM experiments. The area in the micrograph containing the tip apex was magnified (white box on the top right) to obtain a radius of ≈ 28 nm

To compare DMT and JKR adhesion mechanics models with results from this work, the W_{adh} in equation D. 1 (N/m or J/m^2) and equation D. 7 (J) should have the same units. Consequently, equation D. 1 was multiplied by πR^2 assuming the tip has a circular surface area and rearranged so that work of adhesion becomes:

$$W_{adh} = \frac{F_{adh}R}{\alpha_{adh}}$$

D. 8

Next, equations D. 7 and D. 8 were applied to obtain adhesion work values (10^{-18}J or 1aJ) for all experiments performed in brine solutions and nanofluids. Note that the DMT and JKR equations require adhesion forces to be known, which were obtained using AFM force spectroscopy in this study. For these experiments, it was calculated as the percentage reduction in W_{adh} from artificial formation brine (AFB) to the optimum nanofluid concentration, which was 0.5 wt% HNP in the presence of -CH$_3$ and -C$_6$H$_5$ tips and 1 wt% HNP in the presence of COOH groups. Note that the reference (high case) solution here is AFB and not necessarily the solution that generates the highest adhesion force.

188

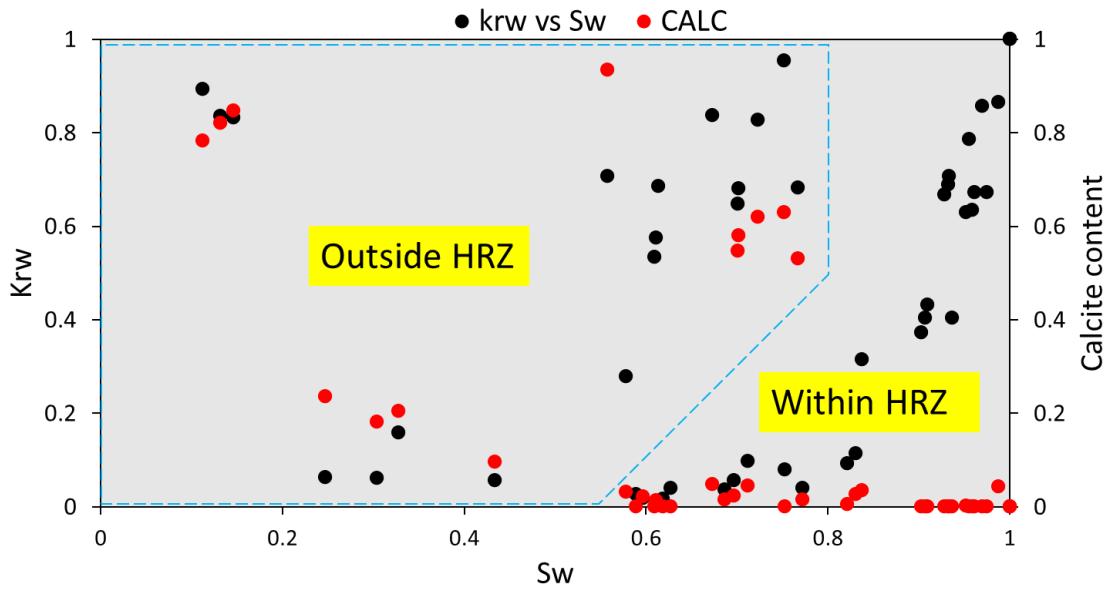# APPENDIX E. EFFECT OF CALCITE CONTENT ON RELATIVE PERMEABILITY

Figure E. 1. A plot of relative permeability to water (left vertical axis) and calcite content (right vertical axis) versus water saturation (horizontal axis) indicates possibility of dual wettability in TMS. As shown, the calcite content has a direct impact on water permeability curves.

APPENDIX F. PUBLISHERS' GRANTS OF PERMISSION

The following provides details on request for permission to reprint previously published works

and grants of permission:

To: Dayo A Afekare <dafeka1@lsu.edu>
Cc: Alan Wegener <awegener@aapg.org>
Subject: Re: Permission for Publication Re-use

Dayo—

Alan has kindly forwarded your e-mail on to me.

Your 2020 URTeC paper can certainly be used in your Ph.D. dissertation. The only requirement we have is that you publish full reference information for the URTeC paper, and you include the following text on the first page of content from your URTeC paper, "reprinted with permission from URTeC, whose permission is required for further use".

If you have any additional questions or if I can assist you in any way, please don't hesitate to let me know.

Kind regards and best wishes for your dissertation,
Beverly

Beverly K. Molyneux
Managing Editor, Technical Publications
918.560.2670
molyneux@aapg.org
publications@aapg.org
wiki@aapg.org

From: Dayo A Afekare <dafeka1@lsu.edu>
Date: Wednesday, January 6, 2021 at 12:14 PM
To: Alan Wegener <awegener@aapg.org>
Subject: Permission for Publication Re-use

Dear Alan,

Happy New Year! I hope this finds you well.

My name is Dayo Afekare, Petroleum Engineering PhD student at Louisiana State University. I am trying to request permission to use the contents of my 2020 URTEC paper titled: "URTEC-2020-3271-MS Application of Force Spectroscopy to Evaluate Rock-Fluid Interactions at the Nanoscale" in my PhD dissertation. I humbly ask that you please assist.

Looking forward to your response.

RE: Publication Rights

BB   **Barbara Barnett** <bbarnett@spe.org>
11/9/2020 12:55 PM

To: Dayo A Afekare

Hello Dayo,

Thank you for your email and interest in complying with SPE copyright policy. I have approved your republication request at no cost. If I can be of further assistance, please let me know.

Sincerely,

Barbara Barnett
Retail Sales Coordinator
Society of Petroleum Engineers (SPE)
222 Palisades Creek Drive
Richardson, TX 75080
Phone: 972-952-1107
Fax: 972-952-9435
Email: bbarnett@spe.org
Website: www.spe.org

From: Dayo A Afekare <dafeka1@lsu.edu>
Sent: Thursday, November 05, 2020 4:47 PM
To: Permissions <permissions@spe.org>
Cc: Service <service@spe.org>
Subject: FW: Publication Rights

> **CAUTION:** This email originated from outside of SPE.

Dear Sir/Madam,

I hope this meets you well. My name is Dayo Afekare, Petroleum Engineering PhD student at Louisiana State University. Per the email below, I am currently trying to request return of one-time journal publication rights to enable the resubmission of my 2020 ATCE paper titled: "SPE-204259-STU Enhancing Oil Recovery Using Aqueous Dispersions of Silicon Dioxide Nanoparticles: The Search for Nanoscale Wettability Alteration Mechanism" to a journal. I was wondering what information is being requested for under the "Reuse Content Details" section (see attached). Please let me know.

Looking forward to your response.

Regards,

LSU
Dayo A. Afekare

Angela Zhang <angela.zhang@mdpi.com>
12/29/2020 3:51 AM

To: Dayo A Afekare Cc: energies@mdpi.com

Dear Dr. Afekare,

Thank you very much for your question.

You do not need to get any permission from our journal to use your published paper in your PhD dissertation. Hope my answer can help you.

I wish you a Merrier 2021 in advance.

Kind regards,

Ms. Angela Zhang
Assistant Editor

/Energies/ (IF: 2.702; CiteScore: 3.8; https://nam04.safelinks.protection.outlook.com/?url=http%3A%2F%2Fwww.mdpi.com%2Fjournal%2Fenergies&data=04%7C01%7Cdafeka1%40lsu.edu%7C9ffe9d54fa554a2b76fd08d8abdf5d8d%7C2d4dad3f50ae47d983a09ae2b1f466f8%7C0%7C0%7C637448323147011385%7CUnknown%7CTWFpbGZsb3d8eyJWIjoiMC4wLjAwMDAiLCJQIjoiV2luMzIiLCJBTiI6Ik1haWwiLCJXVCI6Mn0%3D%7C1000&sdata=%2FimyqectBpcOV3talAFFnLzikdTLBgSFw%2BO4F7n9HfI%3D&reserved=0)
LinkedIn: https://nam04.safelinks.protection.outlook.com/?url=https%3A%2F%2Fch.linkedin.com%2Fin%2Fenergies&data=04%7C01%7Cdafeka1%40lsu.edu%7C9ffe9d54fa554a2b76fd08d8abdf5d8d%7C2d4dad3f50ae47d983a09ae2b1f466f8%7C0%7C0%7C637448323147011385%7CUnknown%7CTWFpbGZsb3d8eyJWIjoiMC4wLjAwMDAiLCJQIjoiV2luMzIiLCJBTiI6Ik1haWwiLCJXVCI6Mn0%3D%7C1000&sdata=TAMet%2FJUbZ%2FPTRuOASsp4HduHLZXemeQYXdrMW%2F0sew%3D&reserved=0
Twitter: @energies_MDPI
Editor's Choice: https://nam04.safelinks.protection.outlook.com/?url=https%3A%2F%2Fwww.mdpi.com%2Fjournal%2Fenergies%2Feditors_choice&data=04%7C01%7Cdafeka1%40lsu.edu%7C9ffe9d54fa554a2b76fd08d8abdf5d8d%7C2d4dad3f50ae47d983a09ae2b1f466f8%7C0%7C0%7C637448323147021374%7CUnknown%7CTWFpbGZsb3d8eyJWIjoiMC4wLjAwMDAiLCJQIjoiV2luMzIiLCJBTiI6Ik1haWwiLCJXVCI6Mn0%3D%7C1000&sdata=hKJyEJasyxDDqjZY5PeW%2BCzeZ6rh7hy3xDng%2BzyxLrk%3D&reserved=0
--

On 2020/12/29 1:35, Dayo A Afekare wrote:
> Season's Greetings MS. Zhang,
>
> Hope you are doing great. I'd like to include my published paper in
> my PhD dissertation and I was wondering if I'll need any special
> permission from your journal. Kindly let me know.
>
> Best,

REFERENCES

2018. Lousiana State Department of Natural Resources: Strategic Online Natural Resources Information Systtem.

Abdallah, W., Buckley, J., Carnegie, A., Edwards, J. and Fordham, E., 2007. Fundamentals of Wettability. OilField Review: 44-45.

Abhishek, R., Hamouda, A.A. and Murzin, I., 2018. Adsorption of silica nanoparticles and its synergistic effect on fluid/rock interactions during low salinity flooding in sandstones. Colloids and Surfaces A: Physicochemical and Engineering Aspects, 555: 397-406.

Afekare, D., Garno, J. and Rao, D., 2020a. Insights into Nanoscale Wettability Effects of Low Salinity and Nanofluid Enhanced Oil Recovery Techniques. Energies, 13(17).

Afekare, D., Gupta, I. and Rao, D., 2020b. Nanoscale investigation of silicon dioxide nanofluids and implications for enhanced oil recovery – An atomic force microscope study. Journal of Petroleum Science and Engineering, 191: 107165.

Afekare, D.A., Garno, J.C. and Rao, D.N., 2020c. Application of Force Spectroscopy to Evaluate Rock-Fluid Interactions at the Nanoscale, SPE/AAPG/SEG Unconventional Resources Technology Conference. Unconventional Resources Technology Conference, Virtual, pp. 20.

Afekare, D.A. and Radonjic, M., 2017. From Mineral Surfaces and Coreflood Experiments to Reservoir Implementations: Comprehensive Review of Low-Salinity Water Flooding (LSWF). Energy & Fuels, 31(12): 13043-13062.

Agi, A., Junin, R. and Gbadamosi, A., 2018. Mechanism governing nanoparticle flow behaviour in porous media: insight for enhanced oil recovery applications. International Nano Letters, 8(2): 49-77.

Ahmadi, K. and Johns, R.T., 2008. Multiple Mixing-Cell Method for MMP Calculations, SPE Annual Technical Conference and Exhibition. Society of Petroleum Engineers, Denver, Colorado, USA.

Akinluyi, O. and Hazlett, R., 2018. Enhanced-Oil-Recovery Potential for Lean-Gas Reinjection in Zipper Fractures in Liquid-Rich Basins. SPE Journal, 23(03): 625-639.

Al Matroushi, M., Pourafshary, P. and Al Wahaibi, Y., 2015. Possibility of Nanofluid/Gas Alternating Injection as an EOR Method in an Oil Field, Abu Dhabi International Petroleum Exhibition and Conference.

Al-Menhali, A.S., Menke, H.P., Blunt, M.J. and Krevor, S.C., 2016. Pore Scale Observations of Trapped CO2 in Mixed-Wet Carbonate Rock: Applications to Storage in Oil Fields. Environmental Science & Technology, 50(18): 10282-10290.

Alfarge, D., Wei, M. and Bai, B., 2018. A Parametric Study on the Applicability of Miscible Gases Based EOR Techniques in Unconventional Liquids Rich Reservoirs, SPE Canada Unconventional Resources Conference. Society of Petroleum Engineers, Calgary, Alberta, Canada.

Alharthy, N. et al., 2018. Enhanced Oil Recovery in Liquid-Rich Shale Reservoirs: Laboratory to Field. SPE Reservoir Evaluation & Engineering, 21(01): 137-159.

Alhosani, A. et al., 2021. Pore-scale characterization of carbon dioxide storage at immiscible and near-miscible conditions in altered-wettability reservoir rocks. International Journal of Greenhouse Gas Control, 105: 103232.

Alvarez, J.O., Saputra, I.W.R. and Schechter, D.S., 2018. The Impact of Surfactant Imbibition and Adsorption for Improving Oil Recovery in the Wolfcamp and Eagle Ford Reservoirs. SPE Journal, 23(06): 2103-2117.

Alvarez-Berrios, M.P., Aponte-Reyes, L.M., Aponte-Cruz, L.M., Loman-Cortes, P. and Vivero-Escoto, J.L., 2018. Effect of the surface charge of silica nanoparticles on oil recovery: wettability alteration of sandstone cores and imbibition experiments. International Nano Letters, 8(3): 181-188.

Aminzadeh-Goharrizi, B. et al., 2012. Effect of Nanoparticles on Flow Alteration During CO2 Injection, SPE Annual Technical Conference and Exhibition. Society of Petroleum Engineers, San Antonio, Texas, USA, pp. 13.

Amott, E., 1959. Observations Relating to the Wettability of Porous Rock. Society of Petroleum Engineers.

Andersen, S.I. et al., 2016. Detection and Impact of Carboxylic Acids at the Crude Oil–Water Interface. Energy & Fuels, 30(6): 4475-4485.

Anderson, W.G., 1986. Wettability Literature Survey － Part 2: Wettability Measurement. . JPT, J. Pet. Technol. , 38(98): 1246 － 1262.

Andrew, M., Bijeljic, B. and Blunt, M.J., 2014. Pore-scale contact angle measurements at reservoir conditions using X-ray microtomography. Advances in Water Resources, 68: 24-31.

Arif, M., Zhang, Y. and Iglauer, S., 2021. Shale Wettability: Data Sets, Challenges, and Outlook. Energy & Fuels, 35(4): 2965-2980.

Babadagli, T., 2001. Scaling of concurrent and countercurrent capillary imbibition for surfactant and polymer injection in naturally fractured reservoirs. . SPE Journal: 465–478.

Bachu, S., Shaw, J.C. and Pearson, R.M., 2004. Estimation of Oil Recovery and CO2 Storage Capacity in CO2 EOR Incorporating the Effect of Underlying Aquifers, SPE/DOE Symposium on Improved Oil Recovery. Society of Petroleum Engineers, Tulsa, Oklahoma.

Basu, S. and Sharma, M.M., 1997. Characterization of Mixed-Wettability States in Oil Reservoirs by Atomic Force Microscopy. SPE Journal, 2(04): 427-435.

Basu, S. and Sharma, M.M., 1999. Investigating the Role of Crude-Oil Components on Wettability Alteration Using Atomic Force Microscopy.

Bennetzen, M.V. and Mogensen, K., 2014. Novel Applications of Nanoparticles for Future Enhanced Oil Recovery, International Petroleum Technology Conference. International Petroleum Technology Conference, Kuala Lumpur, Malaysia, pp. 14.

Besov, A. et al., 2017. Application of Laboratory and Field NMR to Characterize the Tuscaloosa Marine Shale. Petrophysics, 58(03): 221-231.

Bjørlykke, K., 2010. Unconventional Hydrocarbons: Oil Shales, Heavy Oil, Tar Sands, Shale Gas and Gas Hydrates. In: K. Bjorlykke (Editor), Petroleum Geoscience: From Sedimentary Environments to Rock Physics. Springer Berlin Heidelberg, Berlin, Heidelberg, pp. 459-465.

Borrok, D.M., Yang, W., Wei, M. and Mokhtari, M., 2019. Heterogeneity of the mineralogy and organic content of the Tuscaloosa Marine Shale. Marine and Petroleum Geology, 109: 717-731.

Brooks, R.H. and Corey, A.T., 1966. Properties of Porous Media Affecting Fluid Flow. Journal of Irrigation and Drainage Division: 61.

Bui, L.H., Tsau, J.-S. and Willhite, G.P., 2010. Laboratory Investigations of CO2 Near Miscible Application in Arbuckle Reservoir, SPE Improved Oil Recovery Symposium. Society of Petroleum Engineers, Tulsa, Oklahoma, USA, pp. 9.

Butt, H.-J., Cappella, B. and Kappl, M., 2005. Force measurements with the atomic force microscope: Technique, interpretation and applications. Surface Science Reports, 59(1): 1-152.

Carpenter, C., 2015. A Study of Wettability-Alteration Methods With Nanomaterials Application. Journal of Petroleum Technology, 67(12): 74-75.

Chandrasekhar, S. and Mohanty, K.K., 2018. Effect of brine composition on oil-rock interaction by atomic force microscopy. Journal of Petroleum Science and Engineering, 164: 289-301.

Chen, H.L., Lucas, L.R., Nogaret, L.A.D., Yang, H.D. and Kenyon, D.E., 2001. Laboratory Monitoring of Surfactant Imbition With Computerized Tomography. SPE Reservoir Evaluation & Engineering, 4(01): 16-25.

Chen, Z., 2007. Reservoir Simulation - Mathematical Techniques in Oil Recovery. Society for Industrial and Applied Mathematics.

Chengara, A., Nikolov, A.D., Wasan, D.T., Trokhymchuk, A. and Henderson, D., 2004. Spreading of nanofluids driven by the structural disjoining pressure gradient. Journal of Colloid and Interface Science, 280(1): 192-201.

Christensen, J.R., Stenby, E.H. and Skauge, A., 2001. Review of WAG Field Experience. SPE Reservoir Evaluation & Engineering, 4(02): 97-106.

Craig, F.F., 1971. The Reservoir Engineering Aspects of Waterflooding, SPE Monograph Series. 3.

Cuiec, L.E., Bourbiaux, B. and Kalaydjian, F., 1994. Oil Recovery by Imbibition in Low-Permeability Chalk. SPE Formation Evaluation, 9(03): 200-208.

da Silva, F.V. and Belery, P., 1989. Molecular Diffusion in Naturally Fractured Reservoirs: A Decisive Recovery Mechanism, SPE Annual Technical Conference and Exhibition. Society of Petroleum Engineers, San Antonio, Texas, pp. 14.

Derjaguin, B.V., Muller, V.M. and Toporov, Y.P., 1975. Effect of contact deformations on the adhesion of particles. Journal of Colloid and Interface Science, 53(2): 314-326.

Ding, Y., Zheng, S., Meng, X. and Yang, D., 2018. Low Salinity Hot Water Injection with Addition of Nanoparticles for Enhancing Heavy Oil Recovery under Reservoir Conditions, SPE Western Regional Meeting. Society of Petroleum Engineers, Garden Grove, California, USA, pp. 18.

Donaldson, E.C., Thomas, R.D. and Lorenz, P.B., 1969. Wettability Determination and Its Effect on Recovery Efficiency. Society of Petroleum Engineers Journal, 9(01): 13-20.

Dong, C. and Hoffman, B.T., 2013. Modeling Gas Injection into Shale Oil Reservoirs in the Sanish Field, North Dakota, SPE/AAPG/SEG Unconventional Resources Technology Conference. Unconventional Resources Technology Conference, Denver, Colorado, USA, pp. 10.

Drelich, J., Long, J. and Yeung, A., 2007. Determining Surface Potential of the Bitumen-Water Interface at Nanoscale Resolution using Atomic Force Microscopy. The Canadian Journal of Chemical Engineering, 85(5): 625-634.

Duan, Q., Yang, X. and Chen, J., 2017. Hydraulic properties of a low permeable rupture zone on the Yingxiu-Beichuan Fault activated during the Wenchuan earthquake, China: Implications for fluid conduction, fault sealing, and dynamic weakening mechanisms. Tectonophysics, 721: 123-142.

Ehrlich, R., Hasiba, H.H. and Raimondi, P., 1974. Alkaline Waterflooding for Wettability Alteration-Evaluating a Potential Field Application. Journal of Petroleum Technology, 26(12): 1335-1343.

EIA, 2017. World Energy Outlook 2017, World Energy Outlook.

El-Amin, M.F., Kou, J. and Sun, S., 2017. A Multiscale Time-Splitting Discrete Fracture Model of Nanoparticles Transport in Fractured Porous Media, SPE Kingdom of Saudi Arabia Annual Technical Symposium and Exhibition. Society of Petroleum Engineers, Dammam, Saudi Arabia, pp. 12.

El-Amin, M.F., Sun, S. and Salama, A., 2013. Enhanced Oil Recovery by Nanoparticles Injection: Modeling and Simulation, SPE Middle East Oil and Gas Show and Conference. Society of Petroleum Engineers, Manama, Bahrain, pp. 10.

Enomoto, C.B. et al., 2018. Petroleum geology data from Mesozoic rock samples in the eastern U.S. Gulf Coast collected 2011 to 2017: U.S. Geological Survey data release.

Espinoza, D.A., Caldelas, F.M., Johnston, K.P., Bryant, S.L. and Huh, C., 2010. Nanoparticle-Stabilized Supercritical CO2 Foams for Potential Mobility Control Applications, SPE Improved Oil Recovery Symposium. Society of Petroleum Engineers, Tulsa, Oklahoma, USA, pp. 13.

Falode, O. and Manuel, E., 2014. Wettability Effects on Capillary Pressure, Relative Permeability, and Irredcucible Saturation Using Porous Plate. Journal of Petroleum Engineering, 2014: 465418.

Ferno, M.A., Haugen, A. and Graue, A., 2012. Surfactant Prefloods for Integrated EOR in Fractured, Oil-Wet Carbonate Reservoirs, SPE Annual Technical Conference and Exhibition. Society of Petroleum Engineers, San Antonio, Texas, USA, pp. 13.

Fernø MA, Hauge LP, Rognmo AU, Gauteplass J and A., G., 2015. Flow visualization of CO2 in tight shale formations at reservoir conditions. Geophys Res Lett.

Ghanaatian, S., 2014. The Application of Nanofluids for Enhanced Oil Recovery: Effects on Interfacial Tension and Coreflooding Process AU - Joonaki, E. Petroleum Science and Technology, 32(21): 2599-2607.

Ghazanfari M. H. , Khodabakhsh M., Kharrat R. , Rashtchian D. and S., V., 2006. Unsteady State Relative Permeability and Capillary Pressure

Estimation of Porous Media.

Ghedan, S.G., 2009. Global Laboratory Experience of CO2-EOR Flooding. Society of Petroleum Engineers.

Gherabati, S.A., Browning, J., Male, F., Ikonnikova, S.A. and McDaid, G., 2016. The impact of pressure and fluid property variation on well performance of liquid-rich Eagle Ford shale. Journal of Natural Gas Science and Engineering, 33: 1056-1068.

Gong, X., Tian, Y., McVay, D.A., Ayers, W.B. and Lee, J., 2013. Assessment of Eagle Ford Shale Oil and Gas Resources, SPE Unconventional Resources Conference Canada. Society of Petroleum Engineers, Calgary, Alberta, Canada, pp. 26.

Gonzalez, J.W., Perozo, A.E. and Medina, F.X., 2016a. Quantification of the Distribution of Initial Water Saturation through Leverett J Function to Calculate Hydrocarbon Reserves, SPE Latin America and Caribbean Heavy and Extra Heavy Oil Conference. Society of Petroleum Engineers, Lima, Peru, pp. 14.

Gonzalez, J.W., Perozo, A.E. and Medina, F.X., 2016b. Quantification of the Distribution of Initial Water Saturation through Leverett J Function to Calculate Hydrocarbon Reserves. Society of Petroleum Engineers.

Gruesbeck, C. and Collins, R.E., 1982. Entrainment and Deposition of Fine Particles in Porous Media. Society of Petroleum Engineers Journal, 22(06): 847-856.

Guo, W. and Errington, J.R., 2019. Effect of Carboxylic Acid on the Wetting Properties of a Model Water–Octane–Silica System. Langmuir, 35(20): 6540-6549.

Gupta, S.P. and Trushenski, S.P., 1979. Micellar Flooding - Compositional Effects on Oil Displacement. Society of Petroleum Engineers Journal, 19(02): 116-128.

Hackley, P.C. et al., 2020. Oil-source rock correlation studies in the unconventional Upper Cretaceous Tuscaloosa marine shale (TMS) petroleum system, Mississippi and Louisiana, USA. Journal of Petroleum Science and Engineering, 190: 107015.

Haeri, F. and Rao, D.N., 2019. Precise Wettability Characterization of Carbonate Rocks To Evaluate Oil Recovery Using Surfactant-Based Nanofluids. Energy & Fuels, 33(9): 8289-8301.

Haeri, M.F., 2018. Experimental Evaluation of Surfactant-based Nanofluids on Wettability Alteration and Oil Recovery, Louisiana State University.

Hassenkam, T. et al., 2012. Observation of the Low Salinity Effect by Atomic Force Adhesion Mapping on Reservoir Sandstones, SPE Improved Oil Recovery Symposium. Society of Petroleum Engineers, Tulsa, Oklahoma, USA, pp. 14.

Hawthorne, S.B., Miller, D.J., Jin, L. and Gorecki, C.D., 2016. Rapid and Simple Capillary-Rise/Vanishing Interfacial Tension Method To Determine Crude Oil Minimum Miscibility Pressure: Pure and Mixed CO2, Methane, and Ethane. Energy & Fuels, 30(8): 6365-6372.

Heinz, W.F. and Hoh, J.H., 1999. Spatially resolved force spectroscopy of biological surfaces using the atomic force microscope. Nanotechnology.

Helset, H.M., Nordtvedt, J.E., Skjaeveland, S.M. and Virnovsky, G.A., 1998. Three-Phase Relative Permeabilities from Displacement Experiments with Full Account for Capillary Pressure. SPE Reservoir Evaluation & Engineering, 1(02): 92-98.

Hendraningrat, L., Li, S. and Torsaeter, O., 2013a. Enhancing Oil Recovery of Low-Permeability Berea Sandstone through Optimised Nanofluids Concentration, SPE Enhanced Oil Recovery Conference. Society of Petroleum Engineers, Kuala Lumpur, Malaysia, pp. 10.

Hendraningrat, L., Li, S. and Torsater, O., 2013b. A Coreflood Investigation of Nanofluid Enhanced Oil Recovery in Low-Medium Permeability Berea Sandstone, SPE International Symposium on Oilfield Chemistry. Society of Petroleum Engineers, The Woodlands, Texas, USA, pp. 14.

Hendraningrat, L., Li, S. and Torsater, O., 2013c. Effect of Some Parameters Influencing Enhanced Oil Recovery Process using Silica Nanoparticles: An Experimental Investigation, SPE Reservoir Characterization and Simulation Conference and Exhibition. Society of Petroleum Engineers, Abu Dhabi, UAE, pp. 10.

Hendraningrat, L., Li, S. and Torsæter, O., 2013d. A coreflood investigation of nanofluid enhanced oil recovery. Journal of Petroleum Science and Engineering, 111: 128-138.

Hendraningrat, L., Shidong, L., Suwarno and Torsaeter, O., 2012. A Glass Micromodel Experimental Study of Hydrophilic Nanoparticles Retention for EOR Project (Russian), SPE Russian Oil and Gas Exploration and Production Technical Conference and Exhibition. Society of Petroleum Engineers, Moscow, Russia, pp. 12.

Hendraningrat, L. and Torsæter, O., 2014. Effects of the Initial Rock Wettability on Silica-Based Nanofluid-Enhanced Oil Recovery Processes at Reservoir Temperatures. Energy & Fuels, 28(10): 6228-6241.

Hendraningrat, L. and Torsæter, O., 2015. Metal oxide-based nanoparticles: revealing their potential to enhance oil recovery in different wettability systems. Applied Nanoscience, 5(2): 181-199.

Heshmati, M. and Piri, M., 2018. Interfacial boundary conditions and residual trapping: A pore-scale investigation of the effects of wetting phase flow rate and viscosity using micro-particle image velocimetry. Fuel, 224: 560-578.

Hilner , E. et al., 2016. The effect of Ionic strength on oil adhesion in sandstone - the search for the low salinity mechanism. Scientific Reports, 5(9933).

Hirasaki, G. and Zhang, D.L., 2004. Surface Chemistry of Oil Recovery From Fractured, Oil-Wet, Carbonate Formations. SPE Journal, 9(02): 151-162.

Hoo, C.M., Starostin, N., West, P. and Mecartney, M.L., 2008. A comparison of atomic force microscopy (AFM) and dynamic light scattering (DLS) methods to characterize nanoparticle size distributions. Journal of Nanoparticle Research, 10(1): 89-96.

IPE, 2005. Reservoir Simulation Handbook, Heriot-Watt University.

Israelachvii, J.N., 2009. Intermolecular and Surface Forces.

Israelachvili, J.N., 2009. Intermolecular and Surface Forces. Elsevier, USA.

J., T., 2011. Near miscible carbon dioxide application in Arbuckle reservoirs to improve oil recovery. , TORP IOR Conference. Wichita, Kansas, USA, .

Jahanbakhsh, A. and Sohrabi, M., 2015. A New Approach for Simultaneous Estimation of Relative Permeability and Capillary Pressure from Coreflood Experiments, SPE Annual Technical Conference and Exhibition. Society of Petroleum Engineers, Houston, Texas, USA, pp. 13.

Javadpour, F., Moravvej Farshi, M. and Amrein, M., 2012. Atomic-Force Microscopy: A New Tool for Gas-Shale Characterization. Journal of Canadian Petroleum Technology, 51(04): 236-243.

Jennings, H.Y., 1967. The effect of temperature and pressure on the interfacial tension of benzene-water and normal decane-water. Journal of Colloid and Interface Science, 24(3): 323-329.

Jia, B., Tsau, J.-S. and Barati, R., 2018. Role of molecular diffusion in heterogeneous, naturally fractured shale reservoirs during CO_2 huff-n-puff. Journal of Petroleum Science and Engineering, 164: 31-42.

Jia, B., Tsau, J.-S. and Barati, R., 2019. A review of the current progress of CO2 injection EOR and carbon storage in shale oil reservoirs. Fuel, 236: 404-427.

Jiang, H.-F. et al., 2008. A CO2 i mmiscible displacement experimental study aiming at Fuyang extra-low permeability layer at the Daqing Changhing peripheral. Geoscience, 22(4): 659-663.

Jiang, R., Li, K. and Horne, R., 2017. A Mechanism Study of Wettability and Interfacial Tension for EOR Using Silica Nanoparticles, SPE Annual Technical Conference and Exhibition. Society of Petroleum Engineers, San Antonio, Texas, USA, pp. 17.

Jiang, Z. et al., 2016. Basic characteristics and evaluation of shale oil reservoirs. Petroleum Research, 1(2): 149-163.

Jin, B., Bi, R. and Nasrabadi, H., 2017a. Molecular simulation of the pore size distribution effect on phase behavior of methane confined in nanopores. Fluid Phase Equilibria, 452: 94-102.

Jin, L. et al., 2017b. Utilization of Produced Gas for Improved Oil Recovery and Reduced Emissions from the Bakken Formation, SPE Health, Safety, Security, Environment, & Social Responsibility Conference - North America. Society of Petroleum Engineers, New Orleans, Louisiana, USA.

Jin, L., Ma, Y. and Jamili, A., 2013. Investigating The Effect of Pore Proximity on Phase Behavior And Fluid Properties in Shale Formations, SPE Annual Technical Conference and Exhibition. Society of Petroleum Engineers, New Orleans, Louisiana, USA, pp. 16.

Jin, Z. and Firoozabadi, A., 2016. Thermodynamic Modeling of Phase Behavior in Shale Media. SPE Journal, 21(01): 190-207.

John, C.J., Jones, B.L., Harder, B.J. and Bourgeois, R.J., 2005. Exploratory Progress towards Proving the Billion Barrel Potential of the Tuscaloosa Marine Shale. Gulf Coast Association of Geological Studies, pp. 367-372.

John, C.J., Jones, B.L., Moncrief, J.E., Bourgeois, R. and Harder, B.J., 1997. An Unproven Unconventional Seven Billion Barrel Oil Resource- the Tuscaloosa Marine Shale, BRI Bulletin.

John, C.J., Jones, B.L., Moncrief, J.E., Bourgeois, R. and Harder, B.J., 2006. An Unproven Unconventional Seven Billion Barrel Oil Resource- the Tuscaloosa Marine Shale, BRI Bulletin.

Johns, R.T. and Garmeh, G., 2010. Upscaling of Miscible Floods in Heterogeneous Reservoirs Considering Reservoir Mixing. SPE Reservoir Evaluation & Engineering, 13(05): 747-763.

Johnson, K.L., Kendall, K. and Roberts, A.D., 1971. Surface Energy and the Contact of Elastic Solids. Proceedings of the Royal Society of London Series A, 324: 301-313.

Joslin, K., Ghedan, S.G., Abraham, A.M. and Pathak, V., 2017. EOR in Tight Reservoirs, Technical and Economical Feasibility, SPE Unconventional Resources Conference. Society of Petroleum Engineers, Calgary, Alberta, Canada, pp. 18.

Ju, B. and Fan, T., 2009. Experimental study and mathematical model of nanoparticle transport in porous media. Powder Technology, 192(2): 195-202.

Ju, B., Fan, T. and Ma, M., 2006. Enhanced oil recovery by flooding with hydrophilic nanoparticles. China Particuology, 4(1): 41-46.

Kaasa, A.T., 2013. Investigation of How Silica Nanoparticle Adsorption Affects Wettability in Water-wet Berea Sandstone. , Norwegian University of Science and Technology, Norway.

Kafili Kasmaei, A. and Rao, D.N., 2015. Is Wettability Alteration the Main Cause for Enhanced Recovery in Low-Salinity Waterflooding?

Kamath, J., Meyer, R.F. and Nakagawa, F.M., 2001. Understanding Waterflood Residual Oil Saturation of Four Carbonate Rock Types, SPE Annual Technical Conference and Exhibition.

Kang, S.M., Fathi, E., Ambrose, R.J., Akkutlu, I.Y. and Sigal, R.F., 2010. CO2 Storage Capacity of Organic-Rich Shales, SPE Annual Technical Conference and Exhibition. Society of Petroleum Engineers, Florence, Italy, pp. 17.

Kazemi, H., Gilman, J.R. and Elsharkawy, A.M., 1992. Analytical and Numerical Solution of Oil Recovery From Fractured Reservoirs With Empirical Transfer Functions (includes associated papers 25528 and 25818). SPE Reservoir Engineering, 7(02): 219-227.

Khezrnejad, A., James, L.A. and Johansen, T.E., 2014. Water Enhancement Using Nanoparticles in Water Alternating Gas (WAG) Micromodel Experiments, SPE Annual Technical Conference and Exhibition. Society of Petroleum Engineers, Amsterdam, The Netherlands.

Kneuer, C. et al., 2000. Silica nanoparticles modified with aminosilanes as carriers for plasmid DNA. International Journal of Pharmaceutics, 196(2): 257-261.

Kong, X. and Ohadi, M., 2010. Applications of Micro and Nano Technologies in the Oil and Gas Industry - Overview of the Recent Progress, Abu Dhabi International Petroleum Exhibition and Conference. Society of Petroleum Engineers, Abu Dhabi, UAE, pp. 11.

Koons, C.B., Bond, J.G. and Peirce, F.L., 1974. Effects of Depositional Environment and Postdepositional History on Chemical Composition of Lower Tuscaloosa Oils1. AAPG Bulletin, 58(7): 1272-1280.

Kovscek, A.R., Tang, G.-Q. and Vega, B., 2008. Experimental Investigation of Oil Recovery From Siliceous Shale by CO2 Injection, SPE Annual Technical Conference and Exhibition. Society of Petroleum Engineers, Denver, Colorado, USA, pp. 17.

Kulkarni, M.M. and Rao, D.N., 2005. Experimental investigation of miscible and immiscible Water-Alternating-Gas (WAG) process performance. Journal of Petroleum Science and Engineering, 48(1): 1-20.

Kumar, K., Dao, E.K. and Mohanty, K.K., 2005. Atomic Force Microscopy Study of Wettability Alteration, SPE International Symposium on Oilfield Chemistry. Society of Petroleum Engineers, The Woodlands, Texas, pp. 11.

Lake, L.W., Johns, R., Bossen, B. and Pope, G., 2014. Fundamentals of enhanced oil recovery. Society of Petroleum Engineers, Richardson, Texas, x, 479 pages pp.

Lashgari, H.R., 2014. Development of a four-Phase Thermal-Chemical Reservoir Simulator for Heavy Oil. .

Lashkarbolooki, M. and Ayatollahi, S., 2018. Investigating injection of low salinity brine in carbonate rock with the assist of works of cohesion and adhesion and spreading coefficient calculations. Journal of Petroleum Science and Engineering, 161: 381-389.

Leite, F.L., Bueno, C.C., Da Róz, A.L., Ziemath, E.C. and Oliveira, O.N., 2012. Theoretical Models for Surface Forces and Adhesion and Their Measurement Using Atomic Force Microscopy. International Journal of Molecular Sciences, 13(10).

Leverett, M.C., 1941. Capillary Behavior in Porous Solids. Transactions of the AIME, 142(01): 152-169.

Li, K. and Horne, R.N., 2006. Comparison of methods to calculate relative permeability from capillary pressure in consolidated water-wet porous media. Water Resources Research, 42(6).

Li, L. and Sheng, J.J., 2017. Nanopore confinement effects on phase behavior and capillary pressure in a Wolfcamp shale reservoir. Journal of the Taiwan Institute of Chemical Engineers, 78: 317-328.

Li, S., Genys, M., Wang, K. and Torsæter, O., 2015. Experimental Study of Wettability Alteration during Nanofluid Enhanced Oil Recovery Process and Its Effect on Oil Recovery, SPE Reservoir Characterisation and Simulation Conference and Exhibition. Society of Petroleum Engineers, Abu Dhabi, UAE, pp. 11.

Li, S. and Torsæter, O., 2015a. Experimental Investigation of the Influence of Nanoparticles Adsorption and Transport on Wettability Alteration for Oil Wet Berea Sandstone, SPE Middle East Oil & Gas Show and Conference. Society of Petroleum Engineers, Manama, Bahrain, pp. 16.

Li, S. and Torsæter, O., 2015b. The Impact of Nanoparticles Adsorption and Transport on Wettability Alteration of Water Wet Berea Sandstone, SPE/IATMI Asia Pacific Oil & Gas Conference and Exhibition. Society of Petroleum Engineers, Nusa Dua, Bali, Indonesia, pp. 11.

Liang, S. et al., 2019. Oil detachment by modified nanoparticles: A molecular dynamics simulation study. Computational Materials Science, 170: 109177.

Lin, W., 2016. A Review on Shale Reservoirs as an Unconventional Play – The History, Technology Revolution, Importance to Oil and Gas Industry, and the Development Future. Acta Geologica Sinica - English Edition, 90(5): 1887-1902.

Liu, K., Ostadhassan, M., Jabbari, H. and Bubach, B., 2016. Potential Application of Atomic Force Microscopy in Characterization of Nano-pore Structures of Bakken Formation, SPE Low Perm Symposium. Society of Petroleum Engineers, Denver, Colorado, USA, pp. 10.

Liu, X. and Civan, F., 1993. Characterization and Prediction of Formation Damage in Two-Phase Flow Systems, SPE Production Operations Symposium. Society of Petroleum Engineers, Oklahoma City, Oklahoma, pp. 18.

Lohr, C.D. and Hackley, P.C., 2018. Using mercury injection pressure analyses to estimate sealing capacity of the Tuscaloosa marine shale in Mississippi, USA: Implications for carbon dioxide sequestration. International Journal of Greenhouse Gas Control, 78: 375-387.

Lorenz, B. et al., 2017. Salinity-Dependent Adhesion Response Properties of Aluminosilicate (K-Feldspar) Surfaces. Energy & Fuels, 31(5): 4670-4680.

Lowry, E. and Piri, M., 2018. Effects of chemical and physical heterogeneity on confined phase behavior in nanopores. Microporous and Mesoporous Materials, 263: 53-61.

Lu, J., Milliken, K., Reed, R.M. and Hovorka, S., 2011. Diagenesis and sealing capacity of the middle Tuscaloosa mudstone at the Cranfield carbon dioxide injection site, Mississippi, U.S.A. Environmental Geosciences, 18(1): 35-53.

Ma, S., Morrow, N.R. and Zhang, X., 1995. Generalized Scaling Of Spontaneous Imbibition Data For Strongly Water-Wet Systems, Technical Meeting / Petroleum Conference of The South Saskatchewan Section. Petroleum Society of Canada, Regina, pp. 19.

Ma, Y., Jin, L. and Jamili, A., 2013. Modifying van der Waals Equation of State to Consider Influence of Confinement on Phase Behavior, SPE Annual Technical Conference and Exhibition. Society of Petroleum Engineers, New Orleans, Louisiana, USA, pp. 12.

Maghzi, A., Mohammadi, S., Ghazanfari, M.H., Kharrat, R. and Masihi, M., 2012. Monitoring wettability alteration by silica nanoparticles during water flooding to heavy oils in five-spot systems: A pore-level investigation. Experimental Thermal and Fluid Science, 40: 168-176.

Mahzari, P., Mitchell, T., Jones, A. and Oelkers, E., 2019. A New Mechanism for Enhanced Oil Recovery by CO2 in Shale Oil Reservoirs, EAGE IOR, Pau, France.

Manrique, E.J., Muci, V.E. and Gurfinkel, M.E., 2007. EOR Field Experiences in Carbonate Reservoirs in the United States.

Mascle, M., Youssef, S., Deschamps, H. and Vizika, O., 2019. In-Situ Investigation of Aging Protocol Effect on Relative Permeability Measurements Using High-Throughput Experimentation Methods. Petrophysics, 60(04): 514-524.

Mattax, C.K., J., 1962. Imbibition Oil Recovery from Fractured, Water-Drive Reservoir. *Society of Petroleum Engineers Journal*, 2(2): 177-184.

Meissner, F.F., 1991. A Geological - Mechanical Basis for creating fractured reservoir in the Bakken formation, in W.B. ed, Geology and Horizontal Drilling of the Bakken Formation: Montana Geological Society.

Metin, C.O., Baran Jr., J.R. and Nguyen, Q.P., 2012. Adsorption of surface functionalized silica nanoparticles onto mineral surfaces and decane/water interface. J Nanopart Res, 14.

Miranda, C.R., Lara, L.S.d. and Tonetto, B.C., 2012. Stability and Mobility of Functionalized Silica Nanoparticles for Enhanced Oil Recovery Applications, SPE International Oilfield Nanotechnology Conference and Exhibition. Society of Petroleum Engineers, Noordwijk, The Netherlands, pp. 11.

Mirchi, V., 2018. Pore-Scale Investigation of the Effect of Surfactant on Fluid Occupancies during Low-Salinity Waterflooding in Oil-Wet Carbonates, SPE Annual Technical Conference and Exhibition.

Moore, T.F. and Slobod, R.L., 1955. Displacement of Oil by Water-Effect of Wettability, Rate, and Viscosity on Recovery, Fall Meeting of the Petroleum Branch of AIME.

Morrow, N.R., 1976. Capillary Pressure Correlations For Uniformly Wetted Porous Media. . Journal of Canadian Petroleum Technology 15(4).

Morsy, S. and Sheng, J.J., 2014. Imbibition Characteristics of the Barnett Shale Formation, SPE Unconventional Resources Conference. Society of Petroleum Engineers, The Woodlands, Texas, USA, pp. 8.

Morsy, S., Sheng, J.J. and Ezewu, R.O., 2013a. Potential of Waterflooding in Shale Formations, SPE Nigeria Annual International Conference and Exhibition. Society of Petroleum Engineers, Lagos, Nigeria, pp. 9.

Morsy, S., Sheng, J.J., Gomaa, A.M. and Soliman, M.Y., 2013b. Potential of Improved Waterflooding in Acid-Hydraulically- Fractured Shale Formations, SPE Annual Technical Conference and Exhibition. Society of Petroleum Engineers, New Orleans, Louisiana, USA, pp. 12.

Morsy, S.S., Sheng, J.J. and Soliman, M.Y., 2013c. Improving Hydraulic Fracturing of Shale Formations by Acidizing, SPE Eastern Regional Meeting. Society of Petroleum Engineers, Pittsburgh, Pennsylvania, USA, pp. 15.

Mousavi, M.A. and Bryant, S.L., 2007. Geometric Models of Porosity Reduction Mechanisms in Tight Gas Sands, Rocky Mountain Oil & Gas Technology Symposium. Society of Petroleum Engineers, Denver, Colorado, U.S.A., pp. 13.

Muecke, T.W., 1979. Formation Fines and Factors Controlling Their Movement in Porous Media. Journal of Petroleum Technology, 31(02): 144-150.

Mullen, M.J. et al., 2010. Does the Presence of Natural Fractures Have an Impact on Production? A Case Study from the Middle Bakken Dolomite, North Dakota, SPE Annual Technical Conference and Exhibition. Society of Petroleum Engineers, Florence, Italy, pp. 15.

Nakornthap, K. and Evans, R.D., 1986. Temperature-Dependent Relative Permeability and Its Effect on Oil Displacement by Thermal Methods. SPE Reservoir Engineering, 1(03): 230-242.

Neshat, S.S. and Pope, G.A., 2018. Three-Phase Relative Permeability and Capillary Pressure Models With Hysteresis and Compositional Consistency. SPE Journal, 23(06): 2394-2408.

Nečas, D. and Klapetek, P., 2012. Gwyddion: an open-source software for SPM data analysis. Central European Journal of Physics, 10(1): 181-188.

Ngouangna, E.N. et al., 2020. Influence of (3–Aminopropyl) triethoxysilane on silica nanoparticle for enhanced oil recovery. Journal of Molecular Liquids, 315: 113740.

Nguyen, D., Phan, T., Hsu, T.-P. and Phan, J., 2017. Adhesion and surface energy of shale rocks. Colloids and Surfaces A: Physicochemical and Engineering Aspects, 520: 712-721.

NOAA, 1999. Database of Hazardous Materials. CAEMO Chemicals.

Ogolo, N.A., Olafuyi, O.A. and Onyekonwu, M.O., 2012. Enhanced Oil Recovery Using Nanoparticles, SPE Saudi Arabia Section Technical Symposium and Exhibition. Society of Petroleum Engineers, Al-Khobar, Saudi Arabia, pp. 9.

Pathak, M., 2018. Storage Mechanisms of Oil and Gas in Shales. In: R. Sorkhabi (Editor), Encyclopedia of Petroleum Geoscience. Springer International Publishing, Cham, pp. 1-6.

Phi, T. and Schechter, D., 2017. CO2 EOR Simulation in Unconventional Liquid Reservoirs: An Eagle Ford Case Study, SPE Unconventional Resources Conference. Society of Petroleum Engineers, Calgary, Alberta, Canada, pp. 16.

Phillips, Z.D., Halverson, R.J., Strauss, S.R., Layman, J. and Green, T.W., 2007. A Case Study in the Bakken Formation: Changes to Hydraulic Fracture Stimulation Treatments Result in Improved Oil Production and Reduced Treatment Costs, Rocky Mountain Oil & Gas Technology Symposium. Society of Petroleum Engineers, Denver, Colorado, U.S.A., pp. 9.

Pope, G.A. et al., 2000. Modeling Relative Permeability Effects in Gas-Condensate Reservoirs With a New Trapping Model. SPE Reservoir Evaluation & Engineering, 3(02): 171-178.

Purcell, W.R., 1949. Capillary Pressures - Their Measurement Using Mercury and the Calculation of Permeability Therefrom. Journal of Petroleum Technology, 1(02): 39-48.

Qian, C., Telmadarreie, A., Dong, M. and Bryant, S., 2020. Synergistic Effect between Surfactant and Nanoparticles on the Stability of Foam in EOR Processes. SPE Journal, 25(02): 883-894.

Rao, D., 2003. The concept, characterization, concerns and consequences of contact angles in solid-liquid-liquid systems, Contact Angle, Wettability and Adhesion, London: CRC Press pp. 1-20.

Rao, D., 2004. The concept, characterization, concerns and consequences of contact angles in solid-liquid-liquid systems, Contact Angle, Wettability and Adhesion, London: CRC Press pp. 1-20.

Rao, D.N., 2002. Measurements of dynamic contact angles in solid–liquid–liquid systems at elevated pressures and temperatures. Colloids and Surfaces A: Physicochemical and Engineering Aspects, 206(1): 203-216.

Rao, D.N., Ayirala, S.C., Kulkarni, M.M. and Sharma, A.P., 2004. Development of Gas Assisted Gravity Drainage (GAGD) Process for Improved Light Oil Recovery, SPE/DOE Symposium on Improved Oil Recovery. Society of Petroleum Engineers, Tulsa, Oklahoma, pp. 12.

Rao, D.N. and Girard, M.G., 1996. A New Technique For Reservoir Wettability Characterization. Journal of Canadian Petroleum Technology, 35(01): 10.

Reuters, 2013. Insight: The fight for North Dakota's fracking-water market.

Rilian, N.A., Sumestry, M. and Wahyuningsih, W., 2010. Surfactant Stimulation to Increase Reserves in Carbonate Reservoir "A Case Study in Semoga Field", SPE EUROPEC/EAGE Annual Conference and Exhibition. Society of Petroleum Engineers, Barcelona, Spain, pp. 9.

Roustaei, A., Moghadasi, J., Bagherzadeh, H. and Shahrabadi, A., 2012. An Experimental Investigation of Polysilicon Nanoparticles' Recovery Efficiencies through Changes in Interfacial Tension and Wettability Alteration, SPE International Oilfield Nanotechnology Conference and Exhibition. Society of Petroleum Engineers, Noordwijk, The Netherlands, pp. 7.

Rücker, M. et al., 2020. Relationship between wetting and capillary pressure in a crude oil/brine/rock system: From nano-scale to core-scale. Journal of Colloid and Interface Science, 562: 159-169.

Saini, D. and Rao, D.N., 2009. Line Tension-Based Modification of Young's Equation for Rock-Oil-Brine Systems. SPE Reservoir Evaluation & Engineering, 12(05): 702-712.

San, J., Wang, S., Yu, J., Lee, R. and Liu, N., 2016. Nanoparticle Stabilized CO_2 Foam: Effect of Different Ions, SPE Improved Oil Recovery Conference. Society of Petroleum Engineers, Tulsa, Oklahoma, USA, pp. 12.

Sarkar, A.K., 1988. Fines Migration in Two-Phase Flow, University of Texas at Austin.

Sarkar, A.K. and Sharma, M.M., 1990. Fines Migration in Two-Phase Flow. Journal of Petroleum Technology, 42(05): 646-652.

Sayed, A.M., Olesen, K.B., Alkahala, A.S., Sølling, T.I. and Alyafei, N., 2019. The effect of organic acids and salinity on the interfacial tension of n-decane/ water systems. Journal of Petroleum Science and Engineering, 173: 1047-1052.

Sharma, M.M. and Filoco, P.R., 2000. Effect of Brine Salinity and Crude-Oil Properties on Oil Recovery and Residual Saturations. SPE Journal, 5(03): 293-300.

Sheng, J.J., 2013a. Chapter 5 - Surfactant–Polymer Flooding. In: J.J. Sheng (Editor), Enhanced Oil Recovery Field Case Studies. Gulf Professional Publishing, Boston, pp. 117-142.

Sheng, J.J., 2013b. Chapter 12 - Surfactant Enhanced Oil Recovery in Carbonate Reservoirs. In: J.J. Sheng (Editor), Enhanced Oil Recovery Field Case Studies. Gulf Professional Publishing, Boston, pp. 281-299.

Sheng, J.J., 2014. Critical review of low-salinity waterflooding. Journal of Petroleum Science and Engineering, 120: 216-224.

Sheng, J.J., 2017. Critical review of field EOR projects in shale and tight reservoirs. Journal of Petroleum Science and Engineering, 159: 654-665.

Sheng, J.J. and Chen, K., 2014. Evaluation of the EOR potential of gas and water injection in shale oil reservoirs. Journal of Unconventional Oil and Gas Resources, 5: 1-9.

Sheng, J.J. et al., 2015. Screening of the EOR Potential of a Wolfcamp Shale Oil Reservoir, 49th U.S. Rock Mechanics/Geomechanics Symposium. American Rock Mechanics Association, San Francisco, California.

Sheshdeh, M.J., 2015. A Review Study of Wettability Alteration Methods with Regard to Nano-Materials Application, SPE Bergen One Day Seminar. Society of Petroleum Engineers, Bergen, Norway, pp. 12.

Shuler, P.J., Tang, H., Lu, Z. and Tang, Y., 2011. Chemical Process for Improved Oil Recovery From Bakken Shale, Canadian Unconventional Resources Conference. Society of Petroleum Engineers, Calgary, Alberta, Canada, pp. 8.

Sigmund, P.M., 1976a. Prediction of Molecular Diffusion At Reservoir Conditions. Part 1-Measurement And Prediction of Binary Dense Gas Diffusion Coefficients. Journal of Canadian Petroleum Technology, 15(02): 11.

Sigmund, P.M., 1976b. Prediction of Molecular Diffusion At Reservoir Conditions. Part II - Estimating the Effects Of Molecular Diffusion And Convective Mixing In Multicomponent Systems. Journal of Canadian Petroleum Technology, 15(03): 11.

Smalley, P.C. et al., 2018. Screening for EOR and Estimating Potential Incremental Oil Recovery on the Norwegian Continental Shelf, SPE Improved Oil Recovery Conference. Society of Petroleum Engineers, Tulsa, Oklahoma, USA, pp. 16.

Song, C. and Yang, D., 2017. Experimental and numerical evaluation of CO2 huff-n-puff processes in Bakken formation. Fuel, 190: 145-162.

SONRIS, 2018. State of Louisiana Department of Natural Resources: Louisiana Energy Facts and Figures.

Sorrell, S., Speirs, J., Bentley, R., Brandt, A. and Miller, R., 2009. Global Oil Depletion: An assessment of the evidence for a near-term peak in global oil production.

Stimpson, B.C. and Barrufet, M.A., 2017. Constructing Oil/Gas Capillary Pressure and Relative Permeability Curves From a Distribution of Pores in Shale Reservoirs, SPE/AAPG/SEG Unconventional Resources Technology Conference. Unconventional Resources Technology Conference, Austin, Texas, USA, pp. 20.

Sun, J., Zou, A., Sotelo, E. and Schechter, D., 2016. Numerical simulation of CO2 huff-n-puff in complex fracture networks of unconventional liquid reservoirs. Journal of Natural Gas Science and Engineering, 31: 481-492.

Sun, X. and Mohanty, K.K., 2005. Estimation of Flow Functions During Drainage Using Genetic Algorithm. SPE Journal, 10(04): 449-457.

Syfan, F.E. et al., 2018. Enhancing Delaware Basin Stimulation Results Using Nanoparticle Dispersion Technology, SPE Hydraulic Fracturing Technology Conference and Exhibition. Society of Petroleum Engineers, The Woodlands, Texas, USA, pp. 24.

Taber, J.J., 1969. Dynamic and Static Forces Required To Remove a Discontinuous Oil Phase from Porous Media Containing Both Oil and Water. Society of Petroleum Engineers Journal, 9(01): 3-12.

Tajmiri, M. and Ehsani, M.R., 2016. The Potential Of CuO Nanoparticles to Reduce Viscosity and Alter Wettability at Oil- Wet and Water- Wet Rocks in Heavy Oil Reservoir, SPE Annual Technical Conference and Exhibition. Society of Petroleum Engineers, Dubai, UAE, pp. 12.

Tangparitkul, S., Charpentier, T.V.J., Pradilla, D. and Harbottle, D., 2018. Interfacial and Colloidal Forces Governing Oil Droplet Displacement: Implications for Enhanced Oil Recovery. Colloids and Interfaces, 2(3).

Theloy, C. and Sonnenberg, S.A., 2013. Integrating Geology and Engineering: Implications for Production in the Bakken Play, Williston Basin, SPE/AAPG/SEG Unconventional Resources Technology Conference. Unconventional Resources Technology Conference, Denver, Colorado, USA, pp. 12.

Tissot, B.P. and Welte, D.H., 1984. Petroleum Formation and Occurence. Springer-Verlag Berlin Heidelberg, New York - Tokyo.

Todd, A. and Somerville, J., 2014. Reservoir Engineering Handbook. Heriot Watt University.

Todd, H.B. and Evans, J.G., 2016. Improved Oil Recovery IOR Pilot Projects in the Bakken Formation, SPE Low Perm Symposium. Society of Petroleum Engineers, Denver, Colorado, USA, pp. 22.

Torsater, O., Engeset, B., Hendraningrat, L. and Suwarno, S., 2012. Improved Oil Recovery by Nanofluids Flooding: An Experimental Study, SPE Kuwait International Petroleum Conference and Exhibition. Society of Petroleum Engineers, Kuwait City, Kuwait, pp. 9.

Tovar, F.D., Eide, O., Graue, A. and Schechter, D.S., 2014. Experimental Investigation of Enhanced Recovery in Unconventional Liquid Reservoirs using CO2: A Look Ahead to the Future of Unconventional EOR, SPE Unconventional Resources Conference. Society of Petroleum Engineers, The Woodlands, Texas, USA, pp. 9.

Treiber, L. and Owens, W.A., 1972. Laboratory Evaluation of the Wettability of Fifty Oil-Producing Reservoirs. SPEJ, Soc. Pet. Eng. J. , 12(6): 531 − 540.

Vega, B., O'Brien, W.J. and Kovscek, A.R., 2010. Experimental Investigation of Oil Recovery From Siliceous Shale by Miscible CO2 Injection, SPE Annual Technical Conference and Exhibition. Society of Petroleum Engineers, Florence, Italy, pp. 21.

Wan T and H., L., 2018. Exploitation of fractured shale oil resources by cyclic CO2 injection. Petroleum Science, 15(552).

Wang, D., Butler, R., Liu, H. and Ahmed, S., 2011. Flow-Rate Behavior and Imbibition in Shale. SPE Reservoir Evaluation & Engineering, 14(04): 485-492.

Wang, D., Butler, R., Zhang, J. and Seright, R., 2012. Wettability Survey in Bakken Shale With Surfactant-Formulation Imbibition. SPE Reservoir Evaluation & Engineering, 15(06): 695-705.

Wang, S., Javadpour, F. and Feng, Q., 2016. Molecular dynamics simulations of oil transport through inorganic nanopores in shale. Fuel, 171: 74-86.

Wang, X., Luo, P., Er, V. and Huang, S.-S.S., 2010. Assessment of CO2 Flooding Potential for Bakken Formation, Saskatchewan, Canadian Unconventional Resources and International Petroleum Conference. Society of Petroleum Engineers, Calgary, Alberta, Canada, pp. 14.

Wasan, D., Nikolov, A. and Kondiparty, K., 2011. The wetting and spreading of nanofluids on solids: Role of the structural disjoining pressure. Current Opinion in Colloid & Interface Science, 16(4): 344-349.

Wasan, D.T. and Nikolov, A.D., 2003. Spreading of nanofluids on solids. Nature, 423(6936): 156-159.

Wilke CR and P., C., 1955. Correlation of diffusion coefficients in dilute solutions. AICHE J, 1: 264–70.

Wood, T. and Milne, B., 2011. Waterflood potential could unlock billions of barrels: Crescent Point Energy .

Wu, J. et al., 2017. Effect of specific functional groups on oil adhesion from mica substrate: Implications for low salinity effect. Journal of Industrial and Engineering Chemistry, 56: 342-349.

Xie, X., Weiss, W.W., Tong, Z.J. and Morrow, N.R., 2005. Improved Oil Recovery from Carbonate Reservoirs by Chemical Stimulation. SPE Journal, 10(03): 276-285.

Xu, L. and Fu, Q., 2012. Ensuring Better Well Stimulation in Unconventional Oil and Gas Formations by Optimizing Surfactant Additives, SPE Western Regional Meeting. Society of Petroleum Engineers, Bakersfield, California, USA, pp. 7.

Yang, G., Fan, Z. and Li, X., 2018. Determination of Confined Fluid Phase Behavior Using Modified Peng- Robinson Equation of State, SPE/AAPG/SEG Unconventional Resources Technology Conference. Unconventional Resources Technology Conference, Houston, Texas, USA, pp. 15.

Yang, H.D. and Wadleigh, E.E., 2000. Dilute Surfactant IOR - Design Improvement for Massive, Fractured Carbonate Applications, SPE International Petroleum Conference and Exhibition in Mexico. Society of Petroleum Engineers, Villahermosa, Mexico, pp. 10.

Yellig, W.F. and Metcalfe, R.S., 1980. Determination and Prediction of CO2 Minimum Miscibility Pressures (includes associated paper 8876).

Young, T., 1805. III. An essay on the cohesion of fluids. Philosophical Transactions of the Royal Society of London, 95: 65-87.

Yu, W., Lashgari, H.R., Wu, K. and Sepehrnoori, K., 2015. CO2 injection for enhanced oil recovery in Bakken tight oil reservoirs. Fuel, 159: 354-363.

Yu, W. and Sepehrnoori, K., 2018. Chapter 8 - CO2 Injection for Enhanced Oil Recovery in Tight Oil Reservoirs. In: W. Yu and K. Sepehrnoori (Editors), Shale Gas and Tight Oil Reservoir Simulation. Gulf Professional Publishing, pp. 333-376.

Zarragoicoechea, G.J. and Kuz, V.A., 2004. Critical shift of a confined fluid in a nanopore. Fluid Phase Equilibria, 220(1): 7-9.

Zeng, T., S. Miller, C. and Mohanty, K., 2018. Application of Surfactants in Shale Chemical EOR at High Temperatures, SPE Improved Oil Recovery Conference. Society of Petroleum Engineers, Tulsa, Oklahoma, USA, pp. 14.

Zhang, J., 2013. Work of Adhesion and Work of Cohesion. In: Q.J. Wang and Y.-W. Chung (Editors), Encyclopedia of Tribology. Springer US, Boston, MA, pp. 4127-4132.

Zhang, T. et al., 2015. Investigation of Nanoparticle Adsorption During Transport in Porous Media. SPE Journal, 20(04): 667-677.

Zhang, Y., Song, C., Zheng, S. and Yang, D., 2012. Simultaneous Estimation of Relative Permeability and Capillary Pressure for Tight Formations from Displacement Experiments, SPE Canadian Unconventional Resources Conference.

Zhang, Y., Yu, W., Li, Z. and Sepehrnoori, K., 2018. Simulation study of factors affecting CO2 Huff-n-Puff process in tight oil reservoirs. Journal of Petroleum Science and Engineering, 163: 264-269.

Zheng, S., Sharma, M., Watts, R. and Ahmad, Y., 2020. A Nanoparticle Assisted CO Huff-N-Puff Field Test in the Eagle Ford Shale, SPE Improved Oil Recovery Conference. Society of Petroleum Engineers, Tulsa, Oklahoma, USA, pp. 17.

Zhou, Y. et al., 2020. Development of silicon quantum dots based nano-fluid for enhanced oil recovery in tight Bakken cores. Fuel, 277: 118203.

Zuloaga-Molero, P., Yu, W., Xu, Y., Sepehrnoori, K. and Li, B., 2016. Simulation Study of CO2-EOR in Tight Oil Reservoirs with Complex Fracture Geometries. Scientific Reports, 6: 33445.

VITA

Dayo Akintan Afekare was born in Lagos, Nigeria to Taiwo Sunday Afekare (father) and Temitope Gloria Afekare (mother). Dayo received his bachelor's degree in Petroleum & Gas Engineering from the University of Lagos (Nigeria) in 2012, completed a compulsory 1-year National Youth Service Corp (NYSC) program in 2014 and received a master's degree in petroleum engineering from Heriot-Watt University (United Kingdom) in 2015. Dayo arrived at the United States in 2016 to enroll in the Petroleum Engineering Ph.D. program at Louisiana State University, with enthusiasm and curiosity for interdisciplinary, fundamental research. He anticipates graduating with his Ph.D. degree in May 2021 and will be joining DuPont de Nemours, Inc. as a Ph.D. Scientist/Engineer and Research Investigator upon completion.